Max Burian, Dipl.-Ing.

Nanostructure of organic/inorganic photosystems

Doctoral Thesis

to achieve the university degree of

Doktor der technischen Wissenschaft

submitted to

Graz University of Technology

Supervisor

Ass.Prof. Dipl.-Ing. Dr.techn. Heinz Amenitsch

Institute of Inorganic Chemistry

Graz, May 2018

Eidesstattliche Erklärung

Ich erkläre an Eides statt, dass die vorliegende Arbeit selbstständig verfasst, andere als die angegebenen Quellen/Hilfsmittel nicht benützt, und die den benutzten Quellen wörtlich und inhaltlich entnommenen Stellen als solche kenntlich gemacht habe. Das in TUGRAZonline hochgeladene Textdokument ist mit der vorliegenden Dissertation identisch.

Affidavit

I declare that I have authored this thesis independently, that I have not used other than the declared sources/resources, and that I have explicitly indicated all material which has been quoted either literally or by content from the sources used. The text document uploaded to TUGRAZonline is identical to the present doctoral thesis.

Date/Datum Signature/Unterschrift

«Cosa è una furia transforma?»

C.M.

Acknowledgements

First off, I express my deepest gratitude to my supervisor Heinz Amenitsch for his scientific visions, ideas and guidance throughout the last years. I am grateful for giving me the freedom to follow my own interests and I sincerely appreciate giving me the trust to manage my collaborations and projects independently. And of course for the countless, fruitful conversations at day and night.

Right after, I warmly thank my friends and colleagues of the (current and past) AustroSAXS family, (sorted alphabetically) Andrea, Barbara, Benedetta, Christian, Kruno, Marcel, Marco Bogar, Marco DeMarco, Richard and Sigrid for the enduring encouragement and the entertaining moments throughout the years.

On a scientific note, I thank all collaborators that have contributed to the success of this work, including (sorted alphabetically): Angela Chemelli, Nicola Demitri, Luka Dordevic, Stefan Freunberger, Ivan Khalakhan, Manfred Kriechbaum, Nadia Marino, Francesco Rigodanza, Andrea Sartorel and Zois Syrgiannis. Special acknowledgement goes to Mauro Carraro for his constructive comments on improving this manuscript and his time and efforts evaluating the final work. I further thank all other colleagues for their collaboration in projects not directly related to this work, including (sorted alphabetically): Carina Karner, Christian Koczwara, Rainer Lechner and Christian Prehal.

On a bureaucratic note, I thank Frank Uhlig and his supportive team, particularly (listed alphabetically) Resi Koller, Sonja Heyn and Barbara Seibt, for the assistance in dealing with the peculiar nature of the TUG administration.

On a personal note, I thank my friends for the entertaining hours off the clock, my companion Romana for her endless encouragement and empathy and my parents for their invaluable support throughout the years.

Abstract

Water oxidation driven by solar light is an attractive strategy towards clean and renewable energy production. The grand pursuit in this regard is the rationalization of an artificial analogue of the oxygen evolving photosystem II found in nature – a supramolecular complex whose characteristic functionality is attributed to the structural separation of light absorption and the chemical reaction center. While a series of artificial analogues of the photosystem II are known today, their respective structural motifs on the intermolecular level have not been elucidated so far. This work presents the first investigation on the nanostructure of organic/inorganic photosystems used for solar driven water oxidation. The functional corner stone of this thesis is the Ru polyoxometalate reaction center RuPOM, which was paired with the strongly absorbing photosensitizers perylene bisimides as well as Ru-bipyridine and Ru-dendrimeric coordination compounds. In a first step, the isolated constituents were studied by means of small angle X-ray scattering (SAXS), complemented by a series of microscopic and spectroscopic techniques. Specific methodological advancements in the evaluation of SAXS data were made, which yield detailed information for the particular cases of scattering from perylene-fibers and weakly interacting Ru-dendrimeric compounds. This knowledge is then utilized to describe three selected photoactive systems involving RuPOM and to derive respective structural models. In particular for the case of RuPOM paired with perylene bisimides, the nanostructural motif presents a striking resemblance to the natural photosystem II, where a corolla-like hetero-molecular arrangement was found as a structural building-block. The findings reported in this work will aid towards a better understanding of the complex nature of hetero-molecular light-harvesting systems – a necessary prerequisite in the design of new and optimized artificial photosystems.

Kurzfassung

Die Spaltung von Wasser mittels Sonnenlicht ist ein vielversprechender Ansatz zur Gewinnung sauberer und erneuerbarer Energie. Eine der diesbezüglich großen Herausforderungen ist die Realisierung eines künstlichen Abbildes des natürlichen, Sauerstoff erzeugenden Photosystems II: ein supramolekularer Komplex dessen Funktionsweise auf die strukturelle Aufteilung von Lichtabsorption und chemischer Reaktion zurückzuführen sind. Auch wenn bereits einige künstliche Abbilder dieses Systems existieren, so gibt es in Bezug auf dessen strukturellen Eigenschaften lediglich Hypothesen. Diese Arbeit beinhaltet die erste Untersuchung der Nanostruktur von organisch/anorganischen Photosystemen welche zur Sonnenlicht-getriebenen Erzeugung von Sauerstoff dienen. Der funktionelle Mittelpunkt ist dabei das molekulare Ru polyoxometalat Reaktionszentrum RuPOM, das mit diversen, stark absorbierenden Photosensibilisatoren, wie Perylen-Bisimiden, Ru-Pyridin und anderwärtig dendrimerisierten Ru Koordinationskomplexen, kombiniert wird. In einem ersten Schritt, wurden die einzelnen Bestandteile mittels Röntgenkleinwinkelstreuung (RKWS) untersucht, wobei ergänzend eine Reihe an mikro- und spektroskopischen Techniken zur Hilfe gezogen wurden. Spezielle methodische Entwicklungen zur Auswertung experimenteller RKWS Daten geben nun detaillierte Einsicht in Perylen-basierten Fasersystemen und schwach interagierenden Ru-Dendrimer Komplexen. Gestützt durch diese Erkenntnis wurden im Folgenden drei auf RuPOM basierende, photokatalytische Systeme untersucht, sodass entsprechende nano-strukturelle Modelle aufgestellt werden konnten. In dem speziellen Fall von RuPOM mit Perylene-Bisimid zeigt die gefundene Nanostruktur erstaunliche Ähnlichkeit zum natürlichen Photosystem II, wobei in beiden Fällen das katalytische Reaktionszentrum von photosensibilisierenden Molekülen zylindrisch umschlossen wird. Die aus dieser Arbeit gewonnene Erkenntnis ist ein wichtiger Baustein um das komplexe Verhalten von hetero-molekularen Systemen zur Licht-getrieben Sauerstofferzeugung besser zu verstehen, wobei gerade dieses Verständnis die Voraussetzung für die Entwicklung neuer, optimierter, künstlicher Photosysteme ist.

Contents

Contents ..... **xiii**

List of Abbreviations ..... **xvii**

1 Introduction and objective **1**

2 Literature **3**

2.1 Scattering theory 3

2.1.1 Kinematic scattering approximation 5

2.1.2 Small angle X-ray scattering 6

2.1.3 Modelling of SAXS data 8

2.2 Compounds 10

2.2.1 Perylene bisimides 10

2.2.2 Ruthenium-polybipyridine and -dendrimeric coordination compounds 13

2.2.3 Ruthenium polyoxometalate 16

3 Results and discussion **21**

3.1 SAXS methodology – dummy atom modelling of stacked and helical nanostructures 22

3.1.1 Introduction 22

3.1.2 A structural simplification – the projection scheme 23

3.1.3 Computational implementation 26

3.1.4 Verification of the algorithm 28

3.1.5 Summary & concluding remarks 32

3.2 SAXS methodology – weak inter-molecular aggregation in Ru/Os-dendrimeric photosensitizers 33

3.2.1 Introduction 33

3.2.2 Derivation - aggregation number estimated from the PDDF 34
3.2.3 Application to experimental data 37
3.2.4 Summary & concluding remarks 39
3.3 Nanostructure of perylene-bisimides (PBI) in aqueous media 40
3.3.1 Introduction 40
3.3.2 Theoretical considerations 40
3.3.3 In-solution structure – a concentration series 42
3.3.4 Hydrogelation of PBI – a multiscale model 45
3.3.5 Long-range charge transfer – a structure/function correlation 49
3.3.6 Summary & concluding remarks 51
3.4 Nanostructure of Ru_4POM based water oxidation systems 53
3.4.1 Introduction 53
3.4.2 Nanostructure of Ru_4POM/Ru(bpy) and Ru_4POM/Ru_4dend 54
3.4.3 Nanostructure of Ru_4POM/PBI1 57
3.4.4 Summary & concluding remarks 62
4 Conclusion 65
5 Experimental 67
5.1 Materials 67
5.2 Methods 69
5.3 SAXS Model functions 73
5.3.1 Fitting of PBI1 73
5.3.2 Fitting of PBI2 75
5.4 Crystal structures 77
6 Bibliography 85
7 List of publications 99

Appendix A: publications related to this work..... 101

A1: Dummy atom modelling of stacked and helical nanostructures from solution scattering data..... 103

A2: Aggregation-induced energy transfer in a decanuclear, mixed-metal Os(II)/Ru(II) polypyridine light-harvesting antenna dendrimer..... 129

A3: Structural and Optical Properties of a Perylene Bisimide in Aqueous Environment 149

A4: Inter-backbone charge transfer as prerequisite for long-range conductivity in perylene bisimide hydrogels..... 159

A5: Ruthenium based photosensitizer/catalyst supramolecular architectures in light driven water oxidation..... 173

A6: Artificial Quantasomes: Hierarchical Organization of Perylene-Bisimides and Polyoxometalates for Photo-assisted Water Oxidation..... 185

List of Abbreviations

AFM	atomic force microscopy
cryoTEM	transmission electron microscopy under cryogenic conditions
DA	dummy atom
DLS	dynamic light scattering
dPDDF	derivative of the pair distance distribution function
GISAXS	grazing incidence small angle neutron scattering
ISC	inter system crossing
MLCT	metal ligand charge transfer
PBI	perylene bisimide
PDDF	pair distance distribution function
POM	polyoxometalate
PTCDA	perylene-3,4:9,10-tetracarboxylic dianhydride
QY	quantum yield
Ru_4POM	tetra-Ru(IV)-oxo centered di-γ-decatungstosilicate
Rubpy	Ru(II)-tris(2,2-bipyridine)
Ru-dend	Ru-centered dendrimeric compound
SEA	sacrificial electron acceptor
SANS	small angle neutron scattering
SAXS	small angle X-ray scattering
SEM	scanning electron microscopy
WAXS	wide angle X-ray scattering
XRD	X-ray diffraction

1 Introduction and objective

Harvesting solar energy is a promising strategy to transition the global energy land-scape from linear fossil-consumption to a circular, renewable system.[1] While nature has been pursuing this strategy to maintain a nourishing H_2O/CO_2 equilibrium, the solar conversion efficiency of green-plants is limited to a few percent[2] – a value much too low to satisfy the rapidly growing energy demands of the world's population.[3] The only option to overcome the natural bottlenecks and efficiency-losses is an engineered photosystem,[4] aiming at the theoretical conversion-efficiency limit of 7%.[2] Driven by this prospect, the re-design of the natural photosystem, including its single components as well as their ensemble properties, is the scientific challenge behind artificial photosynthesis.[1]

One of the characteristic aspects of natural light harvesting systems is the functional and structural separation of: a) the absorption of light, so transforming a photon into an excited-state electron and b) the chemical reaction, so using the excited-state electron to drive a chemical reaction.[5,6] Artificial analogues of such antenna systems follow the same concept,[7–9] pairing a) light absorbing molecular groups, such as conjugated polymers,[10–12] porphyrins[13,14] and dendrimers[15,16], with b) an often inorganic catalytic redox reaction center.[15–23] To this extent, polyoxometalate (POM) compounds are highly-promising candidates as molecular reaction centers in catalytic water splitting systems, fueled by electrical energy or solar light.[17,20,24,25]

The modular separation of the functional constituents requires charge-transfer between them – a mechanism that is governed by the intermolecular structure of the working system.[26–31] In the case of POM paired with strongly absorbing, organic sensitizer molecules, a few cases of autonomous solar water splitting systems, particularly focusing on the production of O_2, have been reported.[15,16,32] Yet, the intermolecular structure of these systems is only subject to speculations with very little experimental evidence. Reaching the full potential of these systems, in particular optimizing the underlying charge-transfer processes, therefore requires a comprehensive, multiscale understanding of the nanostructure of such artificial photosystems and its constituents.

Scattering techniques are particularly ideal to study such nanosystems designed for the solar splitting of H_2O. Starting from the single-molecular building-blocks, wide angle X-ray scattering (WAXS) and single-crystal X-ray diffraction (XRD) determine the inter-atomic, structural motif. Small angle X-ray and neutron scattering (SAXS and SANS, respectively) give insight on the slightly larger, supra-molecular level – the length-scale on which charge-transfer phenomena between pairing molecules occur. These techniques give an extensive, yet non-trivial to interpret, toolset for the structural characterization of artificial water-splitting photosystems in their working environment: in aqueous solution.

The objective of this work is to investigate structural aspects of POM based water splitting systems and their single constituents, in particular the Ru centered polyoxometalate Ru_4POM, perylene-bisimides or dendrimeric compounds, using scattering techniques. The following subtasks were identified:

- Development and implementation of a fitting algorithm for SAXS data that allows modelling of fiber-like systems, such as π-π-stacked perylenes in aqueous media.
- Development of a mathematical strategy on the evaluation of SAXS data from weakly interacting molecular systems, such as low-concentrated solutions of Ru/Os dendrimeric compounds.
- Characterization of the nanostructure of amphiphilic perylene-bisimides in the solute and hydrogel state as well as possible effects on charge transfer properties.
- Structural characterization of Ru_4POM based water oxidation systems, using Ru-bipyridine/dendrimeric as well as perylene bisimide photosensitizers.

2 Literature

The following chapter provides the scientific basis for this thesis. The first section discusses the principle concepts of small angle x-ray scattering (SAXS) necessary for the evaluation of experimental SAXS data and to draw attention towards the limitations of current evaluation methods. The second section focuses on the chemical, optical and structural properties of the compounds used in this work and how these aspects are relevant to understand the nanostructure of respective systems in water.

2.1 Scattering theory

Scattering is a fundamental physical process that applies to particles (e.g. electrons, neutrons and photons) and waves (e.g. phonons and electromagnetic waves). The following sub-sections will exclusively deal with the scattering principles of electromagnetic waves, in particular of X-rays.

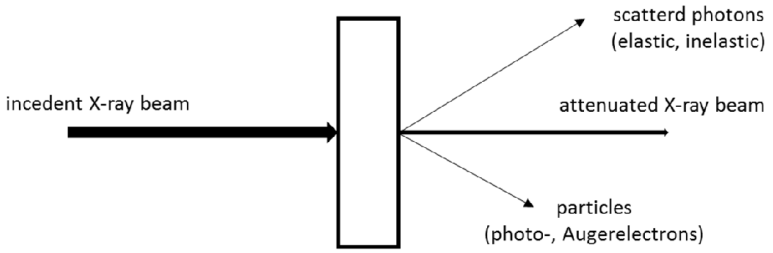

Fig. 2.1-1: Illustration of the interaction between X-rays and matter. The relative magnitude of the processes depends on the energy of the incident beam. All three contributions, scattered photons, emitted particles and the transmitted beam, are valuable probes for condensed matter studies.

When X-rays interact with matter, a series of processes based on the interaction between photons and electrons (and partially phonons) can occur (see Fig. 2.1-1). While, all of the involved processes attenuate the incident beam, the magnitude of each contribution depends on the energy of the light. In the region of medium-energy X-rays (with an energy of 8-16 keV), the majority of the photons are attenuated by condensed matter due to photoelectric absorption: the incoming photon is fully absorbed by an electron, kicking it from an atomic

orbital into vacuum. In turn, the absorbed energy is released from the system by emitting either fluorescence light or Auger electrons.[33]

A fraction of the incident photons is inelastically or elastically scattered by electrons. Inelastic scattering, also called Compton scattering, involves energy to be transferred from the incident photon to an electron, or vice-versa. Hence, the scattered photon now has a different wavelength compared to the incident one. As a consequence of this change in wavelength, the phase information between the incoming and outgoing photon is lost, making the process *incoherent*. As a consequence, Compton scattering will give a constant *background scattering* contribution independent of the scattering angle.[33]

Elastic scattering, also called Thompson scattering in the classical description, is energetically speaking neutral as the entire energy of the incident photon is transferred to the emitted one. Regarding the physical properties of the incident and scattered wave, the conservation of energy yields that the magnitude of the corresponding wave vectors $\vec{k}$ and $|\vec{k}'|$ must be conserved, such that $|\vec{k}| = |\vec{k}'| = 2\pi/\lambda$.[33,34] The elastic scattering process does however change the trajectory of the incident wave, where the angle between scattered and incident path is denoted as 2θ (see Fig. 2.1-2a). The mathematical description of the outgoing wave is known as the Thomson equation – a formalism that is independent of the wave energy and hence wavelength. The consequences of this phenomena, in particular in the case of small angle scattering, will be discussed in the following section.[33]

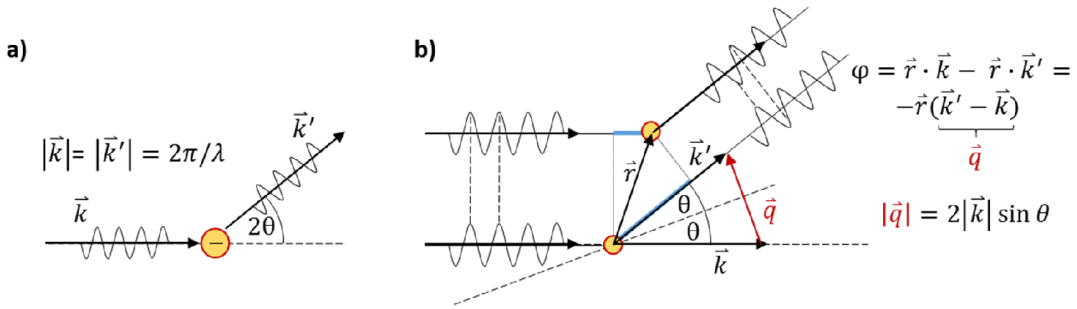

Fig. 2.1-2: The elastic scattering process of coherent electromagnetic waves. a) Illustration of the scattering at a single electron, where the magnitude of the wave vector $\vec{k}$ is conserved. **b)** Illustration of the scattering of a two-electron system, resulting in the phase difference φ between the two independently scattered waves and its relation to the scattering vector $\vec{q}$.

2.1.1 Kinematic scattering approximation

X-rays are a powerful medium to determine the atomic scale structure of condensed matter by means of scattering. To properly describe such a scattering experiment in illustrative and analytic terms, a series of assumptions have to be made. First, the X-rays must be monochromatic. Second, they require a fixed phase-relation over a distance significantly larger than the structural motif that is to be studied (transversal and lateral coherence). Third, the scattered intensity must be weak compared to the incident beam such that no secondary scattering occurs – an assumption known as *the kinematic scattering approximation*. Fourth, the distance between the sample and the detector must be large such that incident and scattered wave can be seen as plane waves.[33] During the experiment, the scattered intensity I is then measured as a function of the scattering angle 2θ. The incident and the scattered waves are mathematically described using the complex form, where the wave amplitudes are defined as $A(\vec{q}) = A_0 e^{i\varphi}$ where φ denotes the wave phase.[33–35]

The most fundamental (yet purely theoretical) example of a scattering experiment is the elastic scattering of a coherent X-ray wave by two electrons: one placed at the origin and one placed at the distance $\vec{r}$ (see Fig. 2.1-2b). Both electrons produce an independent, coherent, scattered wave. While these scattered wave amplitudes are identical for both electrons (see Thompson scattering), they are emitted at different positions. Consequently, the waves scattered at each electron undergo a different optical path length of $\vec{r}\cdot\vec{k} - \vec{r}\cdot\vec{k}' = -\vec{r}\cdot\left(\vec{k}' - \vec{k}\right) = -\vec{r}\cdot\vec{q}$, leading to either constructive or destructive wave interference at the detection point. The wave emitted by the two-electron-system, so the sum of both independent waves, now has a phase according to $\varphi = -\vec{q}\cdot\vec{r}$, where $\vec{q} = \vec{k}' - \vec{k}$ is the scattering vector. The corresponding vector construction shown in Fig. 2.1-2b also gives the geometrical relation between the scattering vector magnitude and the scattering angle according to $|\vec{q}| = 2\left|\vec{k}\right|\sin\theta = \frac{4\pi}{\lambda}\sin\theta$. [33,34]

The example-case of the two-electron system could, in theory, be expanded to condensed matter, such as atoms and molecules, by evaluating the phase of all electron pairs. Considering the fact that a) this includes an enormous amount of electrons that b) cannot be precisely localized, it is more convenient to introduce the number electron density $\rho(\vec{r})$, describing the electron density distribution in real space. Using a volume integral, the scattering amplitude of such an arbitrary electron cloud is then written as[34,35]

$$A(\vec{q}) = \iiint \rho(\vec{r})\, e^{-i\vec{q}\cdot\vec{r}} dV. \qquad (2.1.1\text{-}1)$$

such that the scattering intensity at a given point in $\vec{q}$-space is calculated using the complex conjugate $A(\vec{q})^*$ of $A(\vec{q})$ as[33]

$$I(\vec{q}) = A(\vec{q}) \cdot A(\vec{q})^* = \iiint \iiint \rho(\vec{r})\, e^{-i\vec{q}\cdot\vec{r}}\, \rho(\vec{r})\, e^{i\vec{q}\cdot\vec{r'}} dV\, dV'. \qquad (2.1.1\text{-}2)$$

According to these equations, the scattering amplitude (or its complex conjugate) is the direct (or inverse) Fourier transform of the electron density distribution in real-space. This mathematical property is particularly useful as there exist analytic solutions for simple geometries of $\rho(\vec{r})$, such as e.g. spheres.[34,36] The consequences of this relation will be discussed with further detail in the following subsections.

In the case of scattering from atoms, the electron density distribution is not trivial such that the Fourier transform cannot be readily calculated.[33,37] In the following, atoms (and not electrons) are considered to be the smallest scattering center, where the scattering of each atom is given by the *atomic formfactor* $f_0(q)$. The scattering from an assembly of atoms is then, written as[33,38,39]

$$I(\vec{q}) = f_0(\vec{q})^2 \sum_n e^{i\vec{q}\vec{r}_n} \sum_m e^{-i\vec{q}\vec{r}_m} = f(Q)^2 \sum_n \sum_m e^{i\vec{q}(\vec{r}_n - \vec{r}_m)}. \qquad (2.1.1\text{-}3)$$

While the double sum over all possible atom-pair distances in a real, condensed matter system might not be feasible, the formalism denoted in equation 2.1.1-3 has advantages that will become apparent in subsection 2.1.3 on modelling of SAXS data. First, however, assumptions that apply to the special case of small angle scattering will be introduced.

2.1.2 Small angle X-ray scattering

As the terminology implies, the experimental technique of small angle x-ray scattering (SAXS) studies scattering phenomena in the low-angular regime ($2\theta < 10°$). In the angular reciprocal space, in which the scattering intensity is experimentally recorded, small angles correspond to dimensions larger than 1 nm). The majority of systems that are studied on this scale area a) (statistically) isotropic and b) uncorrelated (on the large scale). As a consequence of these properties the scattering problem can be simplified, as follows.[34,35]

In regard of attribute a, it can be assumed that the electron density distribution depends only on the magnitude of $\vec{r}$. The phase defining dot-product $\vec{q} \cdot \vec{r}$ can then be rewritten using the respective magnitudes $q \equiv |\vec{q}|$ and $r \equiv |\vec{r}|$ and the respective angle ω between them as $q \cdot r \cdot \cos\omega$. By performing the spherical average over α the well-known Debye formalism is derived, such that e.g. equation 2.1.1-3 can be rewritten as[34,39]

$$I(q) = f(Q)^2 \sum_n \sum_m \frac{\sin qr_{mn}}{qr_{mn}} \tag{2.1.2-1}$$

where r_{mn} denotes the distance between the m-th and the n-th atom. This simple equation will become very helpful for the modelling of condensed matter systems.

In regard of attribute b, the spherical averaged electron density distribution $\rho(r)$ becomes independent (hence uncorrelated) at large distances such that it approaches a constant mean value $\hat{\rho}$ for r $\rightarrow \infty$. As the Fourier transform of a constant in real-space yields a delta function in reciprocal-space, this constant electron density distribution yields no structural information (yet, the delta function magnitude corresponds to the integral sum in real space). The real-space structure can hence be represented by the finite region (with volume V) where $\rho(r) \neq \hat{\rho}$. By defining the electron-density difference $\Delta\rho(r) = \rho(r) - \hat{\rho}$, the correlation function $\gamma(r)$, which denotes the mean magnitude of electron density fluctuations at a given distance r, can be introduced ($\gamma(r) \equiv \gamma(0) = \widehat{\Delta\rho}^2 and\, \gamma(r \rightarrow \infty) = 0$). Using the correlation function, equation 2.1.1-3 can be rewritten as[34,35,38]

$$I(q) = V \int_0^\infty 4\pi\, r^2\, \gamma(r) \frac{\sin qr}{qr}\, dr. \tag{2.1.2-2}$$

The scattering intensity measured in a SAXS experiment is hence the Fourier transform of the correlation function.

Equation 2.1.2-2 together with the inherent properties of the correlation function reveals an outstanding fact: its integral for $q = 0$ gives $I(0) = V^2\widehat{\Delta\rho}^2$. Hence, the forward scattering intensity relates quadratic to a) the total scattering volume and b) the mean electron density difference.[34,38] Considering now the example of scattering from a single particle with homogenous electron density different to the background $\Delta\rho$, the scattering intensity can be expressed in geometry-dependent and -invariant terms, such that[34,36]

$$I_{particle}(q) = \Delta\rho^2\, V^2 |F(q)|^2 \tag{2.1.2-3}$$

Here, $F(q)$ denotes the particle formfactor - a term that only depends on the particle shape (as $I_{particle}(0) = \Delta\rho^2\, V^2, F(0) = 1$). In mathematic terms, the particle formfactor denotes the normalized Fourier transform of the particle shape, which can be calculated analytically and/or numerically for a series of simple geometries.[36,40] The resulting formalisms then depend on a series of structural parameters that can in turn be determined by comparison of the experimental scattering data with modeled patterns – the principle idea of SAXS data modelling.

2.1.3 Modelling of SAXS data

The scattering intensity recorded in an e.g. solution-SAXS experiment only yields spherical and statistical averaged information. A *direct* approach to evaluate such data, so e.g. calculating the correlation function by a discrete inverse Fourier transform of equation 2.1.2-2 directly from the scattering data, yields precise but no direct information on the scatterers in the comprehensible real space.[41–43] For most systems, an *indirect* approach, so modelling the sample in real space and comparing the corresponding model scattering I_{model} with the experimental pattern I_{exp} in reciprocal space, allows a more detailed evaluation. Similarity of the scattering curves, and hence agreement of model and experimental data, is quantitatively measured by the chi-square χ^2.[36,40]

For structurally speaking "simple" systems, one can reduce the scatterer's shape to a model geometry, e.g. a sphere, cylinder, cube, etc… For such shapes, parametric mathematical models can be derived, such that only single structural parameters determine the theoretical scattering pattern, is a common technique. Accounting for particle interactions or periodicity by means of a Structure factor $S(q)$ and the particle concentration c, the model pattern then reads[34–36,40]

$$I_{model}(q) = c\Delta\rho^2\, V^2 |F(q)|^2 S(q). \qquad (2.1.3\text{-}1)$$

For systems where the exact shape of the building-blocks is not known, more complex modelling methods are required. A widely used technique to circumvent shape-constraints is the pair distance distribution function (PDDF).[34,35] Equation 2.1.2-2 can be simplified by merging the two structurally dependent terms (r^2 and $\gamma(r)$) into the PDDF $P(r)$, such that

$$I(q) = V \int_0^\infty 4\pi\, P(r) \frac{\sin qr}{qr}\, dr\,, \qquad P(r) = \gamma(r)\, r^2. \tag{2.1.3-2}$$

Inversion of the above relation yields

$$P(r) = \frac{1}{2\pi^2} \int_0^\infty I(q)\, qr \sin qr\; dq. \tag{2.1.3-3}$$

The PDDF may be interpreted as a histogram of all distances that appear inside a given particle, weighted by the corresponding electron densities. In theory, the PDDF can be calculated directly from the scattering data. Yet, the low-angular truncation of an experimental scattering curve causes artefacts in the Fourier transform of equation 2.1.3-3 that dominate the PDDF and render it useless.[34,35] While the extrapolation to $q = 0$ by the Guinier approximation reduces this problem, indirect methods have proven themselves useful, in particular if experimental smearing effects (due to beam-divergence or collimation effects) are non-negligible. Here, the PDDF is described in real-space by a set of (often cubic-spline) functions for which the Fourier transform is analytically known.[44–47] The sum of the transform function is then (after convolution with smearing effects) optimized against the experimental pattern by iteratively altering their real-space counterpart. The PDDF is hence computed in an *indirect* manner.

Instead of modelling a 1D probability distribution in real space, such as the PDDF, computational advancements of the last decades have made 3D modelling approaches feasible.[48–51] For highly monodisperse systems,[52] the particle shape is represented by a set of dummy atoms (DA), of equal size and electron density, which are distributed in a finite real-space volume. By evaluation of the Debye equation (see equation 2.1.2-1) over the DA configuration, the scattering intensity can readily be calculated.[51] Again, iterative modelling of the real-space configuration while fitting theoretical to experimental pattern then yields a plausible 3D configuration that represents the particle shape. However, as the numerical complexity of the Debye formula scales quadratic with the number of DAs in a configuration, large systems require a significant computational overhead and hence time. Current fitting algorithms rely on the spherical harmonics approximation[35,53] to reduce the numerical complexity to a linear dependence in regard of the configurations size.[48–50,53–55] The drawback of this approximation is that it breaks down for highly asymmetric geometries, such as fiber-

like structures or helices (see Fig. 2.1.3-1 for the example of an artificial seemingly-endless helix constructed of DAs).

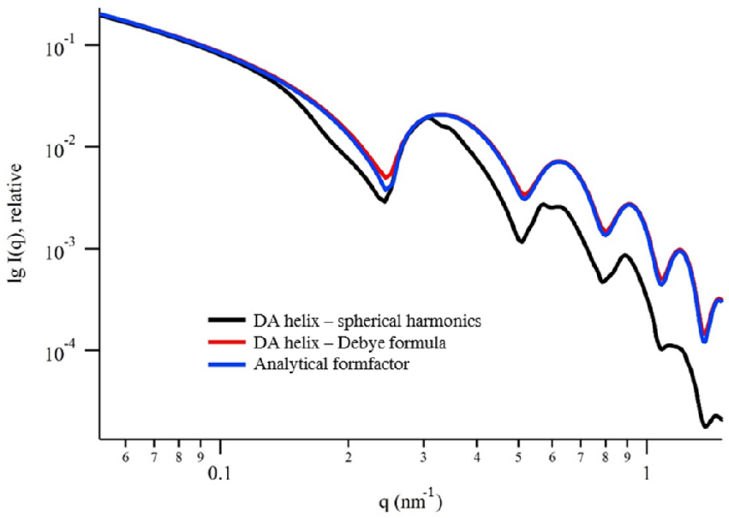

Fig. 2.1.3-1: Limitations of the spherical harmonics approximation for the calculation of DA models. Here, the analytically available model (blue) of a seemingly endless helix (pitch = 50 nm, inner diameter = 10 nm, outer diameter = 20 nm, helical tape-width = 2 nm – see literature[56] for the analytical model) is compared to the scattering curve computed from an artificial DA model (15000 DAs) that representing the same geometry. The red trace denotes the result obtained by evaluating the Debye formula (see equation 2.1.2-1) and the black trace denotes the result obtained from the spherical harmonics approximation (CRYSOL[54]). Obviously, the latter cannot reproduce the correct scattering pattern.

2.2 Compounds

2.2.1 Perylene bisimides

Dating back to the first synthesis more than 100 years ago,[57,58] perylene bisimide (PBI) compounds are wide-spread industrial dyes and pigments.[59,60] The enduring success of PBIs is attributed to: i) a strong visible absorption, ii) a high thermal, photo, and oxidative stability and iii) a general high insolubility.[59,61] On an academic note, PBIs exhibit a fluorescence quantum yield (QY) near unity[62,63] as well as a low reduction potential,[64,65] enabling their use as an n-type semiconductor[66–68] and as an electron acceptor in photoinduced charge transfer reactions.[69–72] Not surprisingly, a variety of applications based on PBIs are reported in literature, such as e.g. light emitting diodes,[73–76] photovoltaic cells,[65,77–80] field-effect transistors[58,68,81,82] and opto-active chemical sensors.[83–86] As the literature on PBIs is very extensive, the following will exclusively address aspects relevant to PBI in aqueous systems.

The majority of PBIs are synthesized by condensation reaction of the insoluble perylene-3,4:9,10-tetracarboxylic dianhydride (PTCDA) with anilines and aliphatic primary amines in protic solvents at temperatures >100°C (see Fig. 2.2.1-1 – scheme 1).[87–89] This approach leads to reaction yields above 90% and allows for simple tuning of the PBI solubility depending on the substituted amine group (*tail-functionalization*).[58,61] As the reaction occurs symmetrically, that is both anhydride positions are equally converted, the perylene core remains planar, making it prone to π-π-stacked aggregation in polar solvents.[58,61,90–92] In order to further increase the solubility of PBI, the PTCDA bay-position may be pre-functionalized (prior to the imide condensation) with either X,Y=Br or X,Y = Cl (*bay-functionalization*, see Fig. 2.2.1-1 – scheme 2, 2*):[58,87,93] the strong polarity of either substituent causes torsion of the aromatic core, which hence disrupts the face-to-face π-π-stacking and reduces the overall hydrophobicity[87,94] (further functionalization of b-PBI with e.g. organic groups is possible by nucleophilic substitution at the –Cl or –Br position)[58,61].

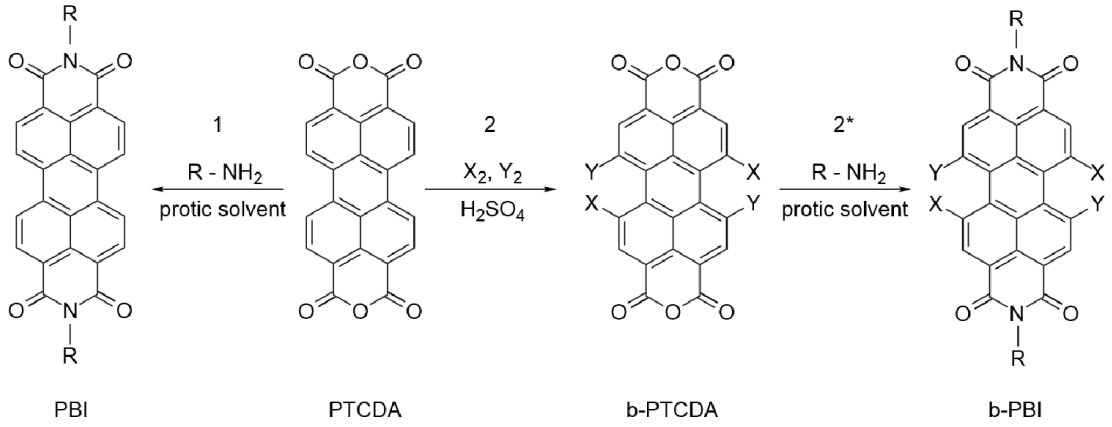

Fig. 2.2.1-1: Synthetic reactions to form functionalized PBI from the dianhydride base-compound PTCDA.

PBIs exhibit a characteristic UV/Vis absorption fingerprint: the strong conjugation between the electron-rich perylene core and the electron-withdrawing imide groups shifts the S^0-S^1 absorption from ~440 to 525 nm (compared to perylene)[90,95] and causes a fine vibronic structure (see Fig. 2.2.1-2a).[96–98] The optical fluorescence is almost mirror like to the absorption spectrum (see Fig. 2.2.1-2a), whereas its high QY (even in water >90%)[99,100] is attributed to a low-lying triplet state, such that S^1-T^1 intersystem crossing (ISC) is very unlikely (QY-ISC < 0.01% - see Fig. 2.2.1-2b).[90,101] DFT calculations of the highest occupied and the lowest unoccupied molecular orbital (HOMO and LUMO, respectively) visualize an electronic symmetry along the molecular long-axis, which defines the direction of the absorption

transition dipole (see Fig. 2.2.1-2c).[102–104] Both N atoms are central on the symmetry-axis such that a change of their interaction (e.g. by symmetric substitution) with the conjugate core is expected to affect LUMO and HOMO in equal manner.[58,90,103] Indeed, imide substitution by tail-functionalization has little effect on the HOMO-LUMO band-gap and the vibronic structure (hence, the optical absorption spectrum remains inert).[58,90,103] Yet, even modestly electron rich imide substituents such as alkylated phenyl groups[105] enable electron-transfer to the perylene core and hence quench the fluorescence.[106,107] Imide substitution is hence a feasible option to include PBIs in photo-induced charge-transfer cascades.

In contrast, bay-*functionalization* strongly affects the molecular energy landscape by: i) destabilization and expansion of the π-conjugated molecular orbitals (red-shifted absorption) and ii) torsion of the perylene core due to steric interaction (blue-shifted absorption).[61,103,108–110] The final properties of a given bay-substituted compound hence depends on the relative magnitude of these contributions such that definition of general rules is highly complex and not feasible.[61,90,110]

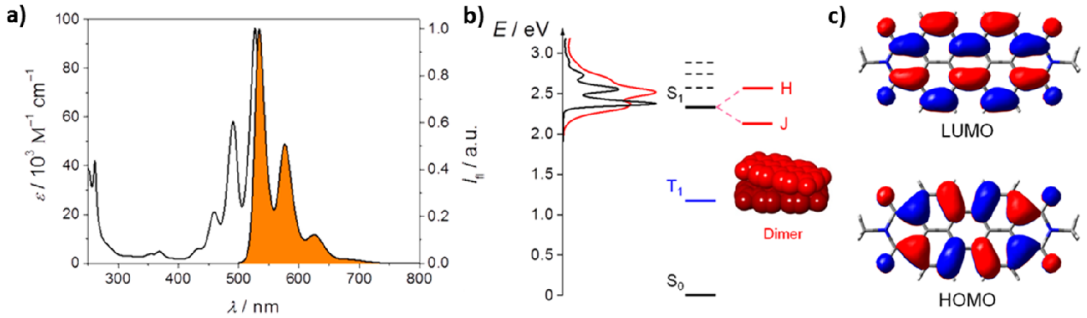

Fig. 2.2.1-2: Electronic and optical properties of PBIs. a) Characteristic UV/Vis absorption (black line) and fluorescence (orange filling) spectra. **c)** Simplification of a Jablonski diagram, showing the singlet (S_1) and triplet (T_1) states of PBI in its monomeric (black) and its rotationally displaced π-π-stacked dimeric (red) state. The left axis sows the corresponding UV/Vis absorption spectra. **c)** DFT (B3LYP/6-31++G**) calculated LUMO and HOMO. Adapted with permission from *F.Würthner, et.al.*[90] Copyright (2016) American Chemical Society.

The strong hydrophobic nature of PBIs is the driving force for molecular aggregation in polar media, in particular in water: mutual shielding of the (rigid) perylene core results in widely studied π-π-stacked arrangements, such as fibers or helices.[66,98,108,111–115] In such a configuration, the close vicinity of the π-conjugated cores (π-π-stacking-distance = 0.34 nm)[58,90] leads to exciton coupling between the chromophores.[116,117] The consequence of this effect is the splitting of the excited singlet state (S_1) into an H- and J-band (see Fig. 2.5b), shifting the absorption maximum to lower or higher wavelengths, respectively.[112,114,118,119] As

the exciton coupling is governed by the relative alignment of the transition dipole moments, the molecular arrangement determines the magnitude and form of the coupling. The absorption spectrum of self-assembled PBIs hence gives valuable information on the relative position and alignment of neighboring perylene cores.

In this regard, numerous studies characterize the molecular structure of PBI self-assemblies by means of their optical fingerprint.[83,97,99,113,120–122] While this approach, for the above reasons, is very sensitive to the detailed relative arrangement of the π-conjugated cores,[98,112,114,115,122] it yields no information on the larger scale: e.g., UV/Vis absorption might elucidate how PBIs arrange within a π-π-stacked column[112,123–126] but it reveals no information on the inter-columnar structural motif. Contrary to the broad literature on PBI superstructure, only few works provide a comprehensive model ranging over multiple length-scales,[127–130] such that most "structural investigations" are based on chemically feasible models without experimental evidence.[120,131–135]

2.2.2 Ruthenium-polybipyridine and -dendrimeric coordination compounds

Over the last decades, a broad family of Ru-polypyridine and –dendrimeric compounds has emerged around one of the most studied and understood photoactive coordination compounds, the Ru(II)-tris(2,2-bipyridine) ($[Ru(bpy)_3]^{2+}$ = Rubpy – see Fig. 2.6).[136–139] Rubpy presents a unique combination of i) chemical stability, ii) redox properties, iii) luminescence and iv) excited state reactivity and lifetime.[136,137] Attributes (i-iii) have led to immense interest of application driven research such that Rubpy has been implemented in countless sensing and energy conversion devices.[140–145] The last attribute (iv), however, has made Rubpy to a model system for photo-induced metal to ligand charge transfer (MLCT) mechanisms from which invaluable insight on intra-molecular charge-transfer mechanisms has been gained.[146–152] Dendrimeric derivatives of Rubpy subsequently evolved in efforts to optimize and tailor the above molecular properties.[137,138]

A facile synthesis of Rubpy is based on a simple Ru-reduction of $Ru(III)Cl_3$, in the presence of excess bpy (and hydrophosphorous acid (H_3PO_2) as reducing agent) in water at boiling temperature, to Ru(II)bpy (see Fig. 2.2.2-1 - top).[153] This electrophilic condensation reaction principle can be applied to other ligands containing a 2,2-bipyridinic motif and hence offers a modular approach for Ru centered dendrimeric complexes.[154] By exchanging bpy with a ligand with a double 2,2-bipyradinic motif (e.g. 2,3-Bis(2-pyridyl)pyrazine) the final complex

presents two free N atoms, which can further link with an only partially substituted poly-bipyridinic Ru complex (see Fig. 2.2.2-1 – bottom).[138,155] This "polymerization" method allows construction of seemingly endless dendrimeric compounds.[137,138,156] The following, however, will mainly focus on properties of the Rubpy and only briefly address similarities with dendrimeric compounds.

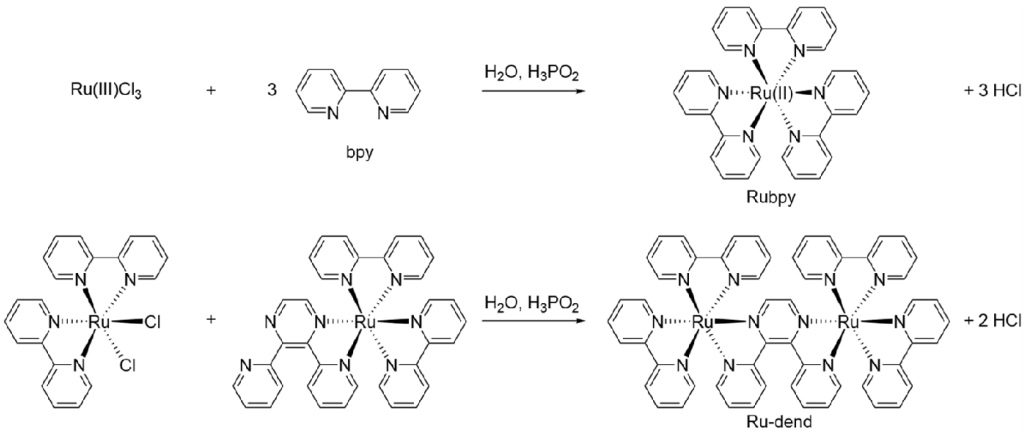

Fig. 2.2.2-1: Synthetic reactions to form Rubpy and corresponding dendrimeric derivatives.

Contrary to PBIs (see Fig. 2.2.1-2a), Rubpy presents a more complex band-structure and hence optical absorption spectrum (see Fig. 2.2.2-2a). This is caused by the interplay between the (Ru) metal center and the bivalent π-conjugate nature of the organic ligands (ground-state donors and excited state acceptors).[136,138] Depending on the photon-energy, an optical absorption can hence lead to one of the following three phenomena (see Fig. 2.2.2-2a): i) a metal-centered (MC) excitation @330 nm, ii) a ligand-centered (LC) excitation @ 285 nm or iii) a metal to ligand charge transfer (MLCT) @ 452 and 244 nm.[136] Upon excitation of the MLCT band, the excited electron (after passing through the singlet S_1 state[152]) remains in in the triplet T_1 state,[138] in which it can remain for up to 580 ns (in water).[157] The system then returns to its ground state via either radiation-less decay-phenomena or via a phosphorescent emission at 610 nm (with a quantum yield around 4% in water - see Fig. 2.2.2-2b).[136,138] Related phenomena occur in dendrimeric compounds: The MLCT band is significantly broadened (multiple MLCT phenomena) and the maximum is generally redshifted to approx. 510 nm whereas secondary charge-transfer processes between neighboring metal centers occurs.[138,139] However, recombination of the excited state electrons in pure Ru dendrimeric compounds is only allowed at the peripherial metal centers, which hence determine the

emission spectra.[138,158] Substitution of the center Ru with Os forms an energetic sink, such that all excited electrons recombine at the center metal (usually at approx. 820 nm).[138,139,158]

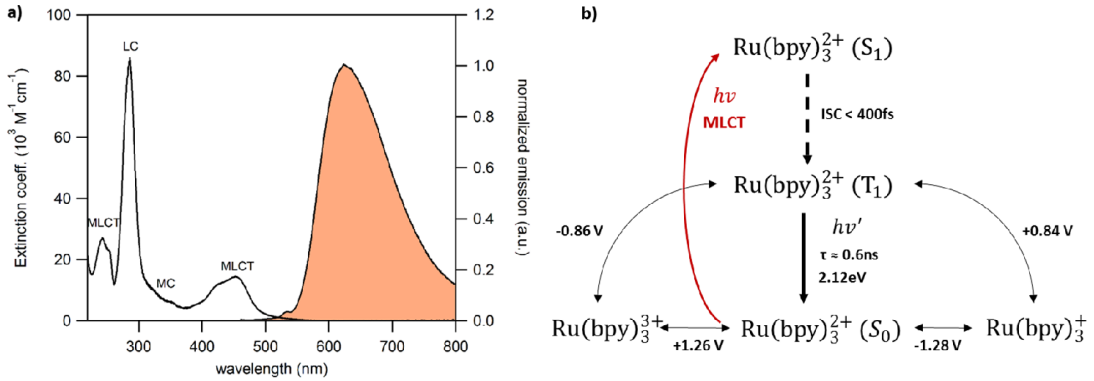

Fig. 2.2.2-2: Optical and redox properties of Rubpy. a) Characteristic UV/Vis absorption (black line) and fluorescence (orange filling) spectra. The excited state phenomena linked to the absorption bands are labeled accordingly.[136,137] **b)** Possible electron transfer processes of Rubpy in its ground and excited state. The specified potentials refer to aqueous solution vs SCE.[137]

The long excited-state T_1 life-time is of exceptional interest for inter-molecular energy and charge transfer reactions, in particular in regard of the redox properties of Rubpy. In its ground state, a potential of approx. ±1.27 V oxidizes or reduces the $Ru(bpy)_3^{2+}$ to $Ru(bpy)_3^{3+}$ or $Ru(bpy)_3^{+}$, respectively (vs saturated calomel electrode (SCE) in aqueous solution).[137,159] From its T_1 state, however, $Ru(bpy)_3^{2+}$ yields an opposing reduction and oxidation potential of approx. ±0.85 V, respectively.[137,160,161] In other words, while $Ru(bpy)_3^{2+}$ might be stable in the unexcited state, photo-excitation can turn the molecule into an reducing and oxidizing agent, depending on the presence of other reactants. The most commonly used system utilizing these attributes is the combination of Rubpy with the strongly oxidizing persulfate ion ($S_2O_8^{2-}$):[136,137,162] here a single excitation forms two reduced $Ru(bpy)_3^{3+}$, which then in-turn oxidize an electron-donating species, such as e.g. an O_2 evolving water splitting catalyst.[15] Interestingly, the reduction or oxidation of Rubpy occurs exclusively on the bpy ligands, which quenches the MLCT absorption and causes a general red-shift.[136,159] This advantageous combination of reversible redox properties, ionization of the structurally widely separated bpy ligands paired with the long excited-state lifetime makes Rubpy ideal electron-acceptor and electron-donor in photochemical reactions. Equally, dendrimeric compounds are very rich in redox properties, where each organic linker or peripheral bpy gives rise to additional redox states (generally, the potentials of the core constituents are lower compared to the peripheral relatives).[138,139,163]

On a structural note, Rubpy can be fully dissolved in water by choice of the proper counter-ion.[136,137] So far, the scientific interest on solute state studies of pure Rubpy is limited (only recently, theoretical work has elucidated the ion distribution around Rubpy in water).[164] Interestingly, Rubpy is known to form ion-pairs upon salt-exchange, leading to a quenched triplet state by radiationless energy transfer between the constituents – hence, an obvious correlation between the inter-molecular structure and the molecular functionality exists.[136,165–167] This situation is even more drastic for dendrimeric compounds: a single study by Campagna et.al. in 1995 suggested molecular aggregation in acetonitrile for concentrations above 10^{-6} M.[168] Even though the authors hypothesized about possible inter-molecular charge-transfer (as they are known for the ion-paired Rubpy "mother-compound"), so far nobody has reported evidence of such phenomena.

2.2.3 Ruthenium polyoxometalate

Polyoxometalates (POMs) are a class of oligomeric, often three-dimensional, aggregates of d^0 metal cations (usually M(IV-VII)) linked via oxygen-bridges.[169–171] The structural and compositional diversity of POM compunds[172–174] is equally broad as their potential use, including applications in life-science,[169,173,175,176] electronic devices[173,177–179] and catalysis.[17,173,180–182] Importantly, POMs exhibit both electron-donating (given by the abundant oxygen shell) and electron-accepting (given by the unfilled orbitals of the central metal atom) properties depending on the solvent condition,[170,174] making them well dispersible in aqueous media.[171,183,184] In the following, the focus will be set on a specific POM that has attracted attention due to its outstanding water-oxidation capabilities: the tetra-Ru(IV)-oxo centered di-γ-decatungstosilicate $[Ru_4(\mu\text{-}O)_4(\mu\text{-}OH)_2(H2O)_4(\gamma\text{-}SiW_{10}O_{36})_2]^{10-}$, from hereafter referred to as Ru_4POM.[185]

Ru_4POM is synthesized by reaction of the K_8 γ-$SiW_{10}O_{36}$ POM with pentachlororuthenate(IV), $Ru_2OCl_{10}^{4-}$, in aqueous solution (see Fig. 2.2.3-1).[185] At mild temperatures (70°C), $Ru_2OCl_{10}^{4-}$ acidifies the solvent and forms the tetranuclear ruthenium(IV) aqua-ion $[Ru_4O_6(H_2O)_n]^{4+}$,[186,187] which subsequently reacts with the SiW_{10} POM ion. The Ru_4POM is then precipitated by addition of excess CsCl.[185] Structurally speaking, the γ-SiW_{10} units are slightly prolate (a x b x c = 1.0 x 0.8 x 0.6 nm) – they connect to the electrophilic Ru_4O_8 core in a 90° twisted orientation (see Fig. 2.2.3-1). The encapsulated Ru-center includes a total of 10 O-atoms, of which 6 provide the structural cohesion between the Ru(IV) atoms and the remaining 4 are

exposed to the solvent. These peripheral O-atoms are the key-sites for aqueous catalysis reactions (note, that hydrogen atoms are omitted so far).[17,185,188,189]

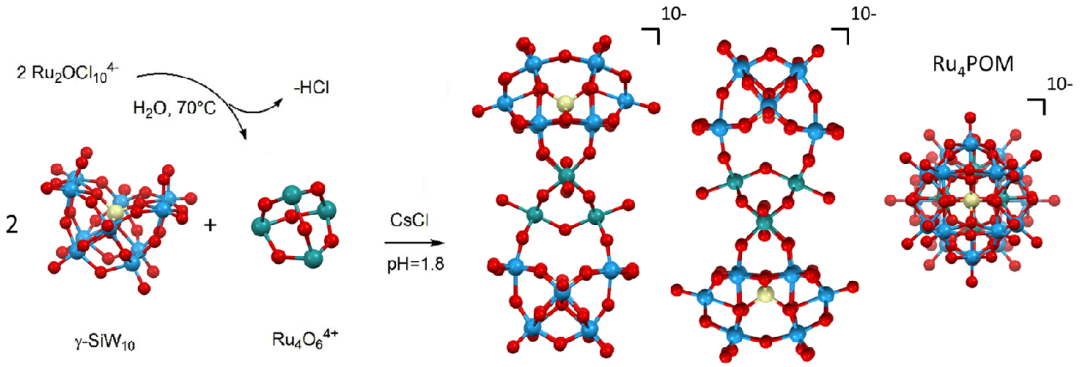

Fig. 2.2.3-1: Simplified reaction scheme and molecular structure of the Ru_4POM molecule (hydrogens omitted for clarity). Adapted with permission from A.*Sartorel, et.al.*[185] Copyright (2008) American Chemical Society.

The production of O_2 from water, is a four electron process following the reaction $2H_2O \rightarrow 4H^+ + 4e^- + O_2$, where the total free energy is 4.92 eV (at pH 0 and room temperature).[188] Correspondingly, Ru_4POM consists of four separate Ru reaction sites, of which each one may mediate the $4e^-/4H^+$ process.[185,189] In its ground state (S_0), all Ru atoms are in a Ru(IV)-H_2O bound state.[185,188] Step-wise oxidation of the all Ru(IV) atoms results in a symmetric Ru(V)-OH coordination (S_4). Further oxidation will now occur only on a single Ru site, following: i) formation of a Ru(V)-oxyl (S_5) (noting that a Ru(VI)-oxo cannot be outruled) and ii) subsequently forming a Ru(V)-OOH^- (S_6^*) and Ru(V)-OO^- (S_7) (see Fig. 2.2.3-2a).[188] The critical step in this energy-cascade is the formation of the O-O bond, after which oxygen evolution is thermodynamically possible (see Fig. 2.2.3-2a).[188] In this catalytic cycle, Ru_4POM acts as a charge mediator such that addition of the e.g. primary oxidizing agent Ce(IV) (in the form of ceric ammonium nitrate), results in spontaneous oxygen evolution.[17,190]

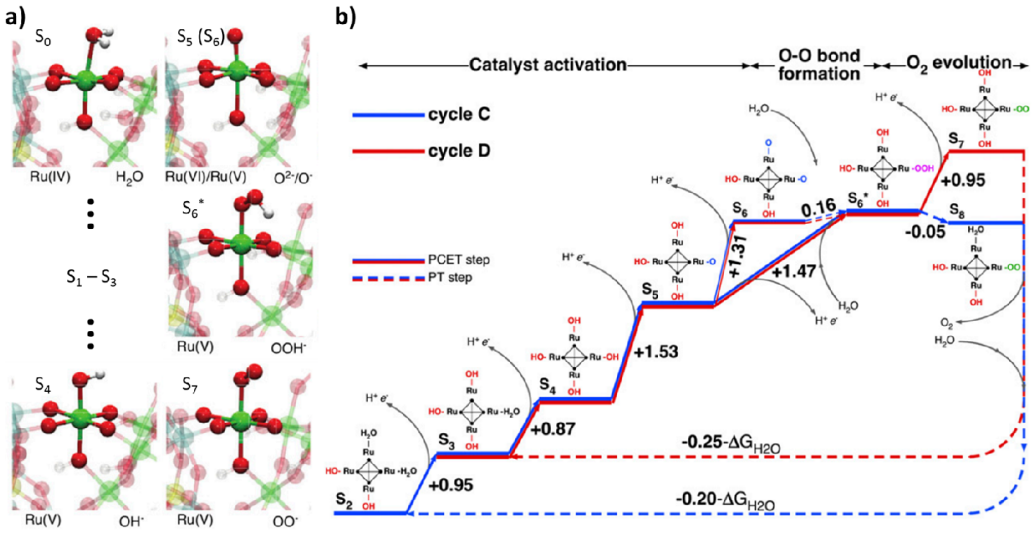

Fig. 2.2.3-2: Oxygen evolution at the Ru reaction centers of Ru_4POM. a) Atomistic model of the coordination environment around a single Ru center along the energy pathway ($S_0 \rightarrow S_7$). **b)** Free energy diagram of the reversible oxygen evolution cycles. $\Delta G(H_2O)$ is the free energy change in the reaction $2H_2O \rightarrow O_2 + 2H_2$ at pH = 0 and room temperature. Adapted with permission from S.*Piccinin, et.al.*[188] Copyright (2013) National Academy of Sciences.

However, Ce(IV) can be replaced by a photo-generated oxidizing agent, such as $Ru(bpy)_3^{3+}$, formed from $Ru(bpy)_3^{2+}$ either in the presence of the sacrificial electron acceptor (SAE) persulfate ($S_2O_8^{2-}$)[15,18,32] (see Fig.2.2.2-2b) or immobilized on a biased TiO_2 electrode.[18,189] The full reaction scheme for the first case, that is Ru_4POM + $Ru(bpy)_3^{2+}$ + $S_2O_8^{2-}$, is shown in Fig. 2.2.3-3a. Here, the excited triplet state of $Ru(bpy)_3^{2+}$ is first oxidized by the SAE, initiating a cascade of follow-up reactions, and subsequently reduced by hole-transfer to the Ru_4POM[15,32] – a reaction scheme in analogue to the natural photosystem II.[16,191] Exchanging $Ru(bpy)_3^{2+}$ with a Ru-dendrimeric (Ru_4dend) compound may reverse this scheme, such that the excited state chromophore is first quenched by hole transfer to Ru_4POM and only subsequently oxidized by the SAE (see Fig. 2.2.3-3b).[16] While, the choice of photo activated oxidizing agent might change the reaction, both systems are outstanding examples for solar water oxidation (with a solar-to-O_2 quantum yield of 9%[32] and 60%[24] in case of $Ru(bpy)_3^{2+}$ and Ru_4dend, respectively).

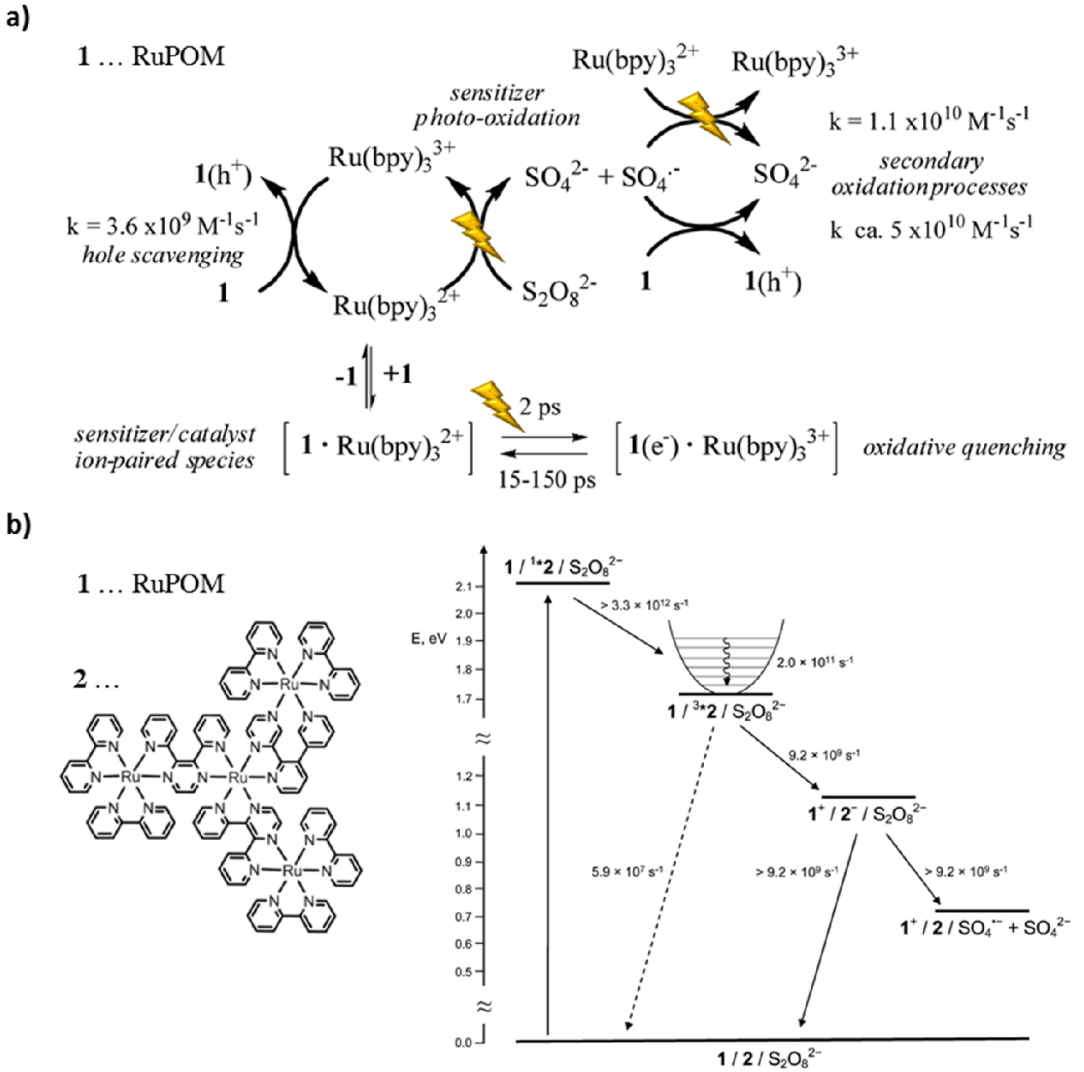

Fig. 2.2.3-3: Reaction schemes of photosensitized oxygen evolution via Ru4POM working in two different directions. a) Reduction scheme of Ru4POM (**1**) + $Ru(bpy)_3^{2+}$ + persulfate as SAE: the sensitizer is first oxidized by the SAE and only subsequently reduced by hole scavenging from Ru4POM. The yellow spark indicates process that require optical excitation. Adapted with permission from *M.Natali, et.al.*[15] Copyright (2012) American Chemical Society. **b)** Energy-level diagram of Ru4POM (**1**) + a Ru-dendrimer (**2**) + persulfate as SAE: here the sensitizer is first reduced by the catalyst and only subsequently oxidized by the SAE. Adapted with permission from *M.Natali, et.al.*[16] Copyright (2015) American Chemical Society.

Even though the Ru4POM + $Ru(bpy)_3^{2+}$ system has been studied quite extensively,[15,18,24,32] some aspects, in particular in regard of the molecular arrangement, are subject to speculation. As it is shown in Fig- 2.2.2-3a, hole scavenging between Ru4POM and $Ru(bpy)_3^{2+}$ is counteracted by an oxidative quenching process within, what is termed, the "ion-paired species" between the anionic Ru4POM and the cationic $Ru(bpy)_3^{2+}$.[15,18,24] This effect occurs at high catalyst concentrations (Ru4POM:$Ru(bpy)_3^{2+}$>0.5:1) and can lead to complete suppression of the

system.[15] On the contrary, the ion-pairing of Ru_4POM and Ru_4dend is termed responsible for the fast hole scavenging process, which further initiates the energy-cascade towards oxygen production.[16,192] Even though these phenomena are suggested to be the result of a constrained, tightly linked molecular arrangement, no information on the nanostructure of these systems in the solute state is available in the literature.

3 Results and discussion

The following chapter summarizes the methodological and experimental results of this thesis. The first subsection discusses a new approach towards DA modelling of SAXS data for the specific case of highly elongated structures, such as fibers or helices. The second subsection will present a model free formalism to determine the aggregation number of weakly interaction molecular systems such as Ru and Os-dendrimeric compounds. The third subsection presents experimental results on the detailed nanostructure of PBI based systems in water, in particular in regard of its effect on long-range conductivity. In the final fourth subsection, recent results on the nanostructure of super-molecular organic/inorganic oxygen-evolving water-splitting systems are discussed.

Some of the following subchapters contain not original content – they might be reproduced and/or adapted from the corresponding publications without direct indication. At the beginning of each subsection, reference to the original publications is given. Corresponding reprints may be found in Appendix A.

3.1 SAXS methodology – dummy atom modelling of stacked and helical nanostructures

See Appendix A1 for an adapted reprint of the original publication.

3.1.1 Introduction

As already mentioned in the previous chapter (see subchapter 2.1.3 Modelling of SAXS data), there exist three major approaches to evaluate solution SAXS data. Which one of the following is to be chosen strongly depends on the type of system that is studied: i) the pair distance distribution function (PDDF), which can be seen as a methodological "universalist", ii) parametric model fitting, which requires a discrete structural model of the system (derived from other methods such as TEM) and a corresponding analytical description and iii) dummy atom (DA) modelling, which is only applicable for highly monodisperse systems. For the case of elongated systems, such as e.g. π-π-stacked PBI fibers, all three approaches bear significant disadvantages: i) the PDDF does not contain detailed information on the fiber cross-section (unless radial symmetry and axial homogeneity is assumed, as shown by Glatter, et.al.[193]), ii) only a few parametric models for highly idealized geometries exist[194,56,195,196] and iii) current DA modelling implementations (based on the spherical harmonics approximation) fail (see Fig. 2.1.3-1) for structures with aspect ratios above approx. 1:5.[197] The goal was hence to overcome these limitations and provide a computational tool to reconstruct the structural motif of stacked and/or helical nanostructures from solution SAXS data.

The following subchapters will focus on helical motifs as model examples, as helical structures are rich in information content. E.g., as the helical *pitch* is generally larger than the helical strand/tape cross-section and even the helical diameter, corresponding scattering features are spread in reciprocal (angular) space: the low-q regime will contain information on the helical length and pitch, the mid-q regime will contain information on the radial cross-section (diameter) and the high-q regime will contain information on the helical *tape* cross-section. It can hence be assumed that a computational toolset capable of resolving all these structural features inherent to helical motifs can also be used on simpler geometries, such as fiber-like structures.

3.1.2 A structural simplification – the projection scheme

The methodological novelty of this work is based on the fact that rod-like and helical systems often possess a certain structural motif, a building block, which recurs along the elongation direction. Hence, only this building block is of interest for shape reconstruction. One can hence define a building block of N_{BB} dummy atoms (DAs) aligned parallel to the z-axis (see Figure 1). The entire rod-like structure is then constructed by multiplication of the building block M times along the z-direction, with a stacking distance corresponding to the building block's height H_{BB} (see Fig. 3.1.2-1). Evaluation of the Debye formula (see equation 2.1.2-1) of this stacked representation by means of the Debye formula now includes redundant terms, as distinct motifs inside the structure become recurrent. For instance, the single building block motif must evaluated at each repetition along z – hence the same computation must be performed a total of M times. It is, however, sufficient to calculate the scattering intensity of the building block only once and scale it by the number of stacks.

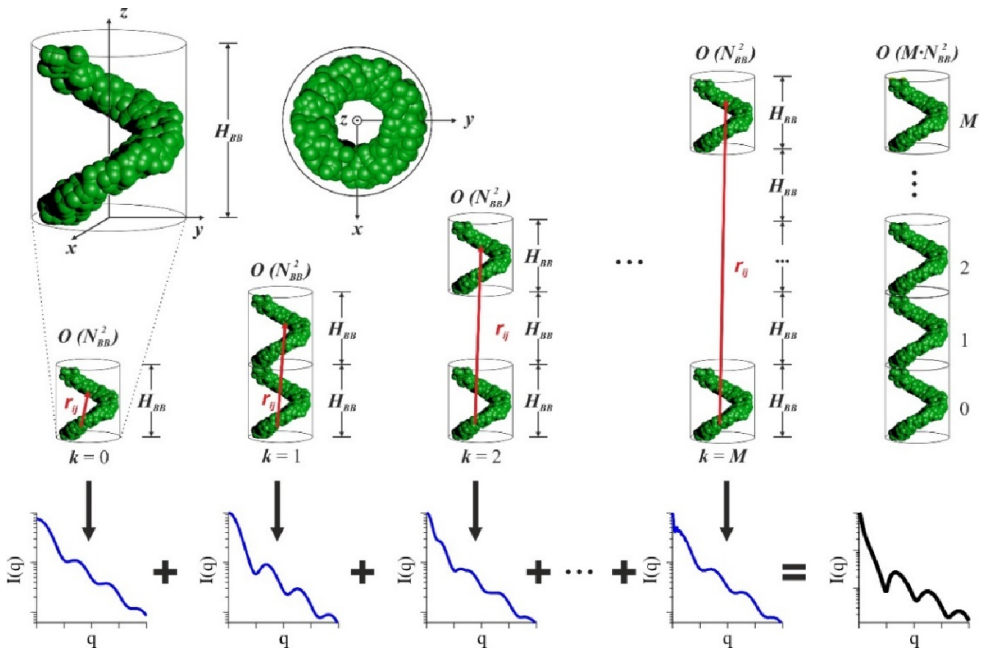

Fig. 3.1.2-1: Projection-scheme, visualized using the example of a single-strand helix. For such seemingly-endless geometries, there exists a building-block (see upper left corner) that is recurrent along the z-axis (see full helix on the right). For a full body consisting of M stacked building-blocks, one finds distinct structural motifs, such as e.g. the building-block itself, neighboring building-blocks, single-spaced building-blocks, etc.. The scattering intensity of the full geometry can hence be calculated by summing up the contributions of these structural motifs, scaled by their recurrence. This bypasses the demand of an actual DA model representing the full structure as solely projections of the building block instead of actual stacked duplicates, are evaluated, hence the term projection scheme.

Including now all structural motifs (such as single-, double-, triple-, etc.. spaced building-blocks), the Debye formula can be adjusted to neglect numerical redundancies, resulting in

$$I(q) = f_{DA}(q)^2 \left[M \sum_{i=1}^{N_{BB}} \sum_{j=1}^{N_{BB}} \frac{\sin\left(q\left|\boldsymbol{r_j} - \boldsymbol{r_i}\right|\right)}{q\left|\boldsymbol{r_j} - \boldsymbol{r_i}\right|} + 2 \sum_{k=1}^{M-1} (M - k) \sum_{i=1}^{N_{BB}} \sum_{j=1}^{N_{BB}} \frac{\sin\left(q\left|\left(\boldsymbol{r_j} + k * H_{BB}\boldsymbol{e_z}\right) - \boldsymbol{r_i}\right|\right)}{q\left|\left(\boldsymbol{r_j} + k * H_{BB}\boldsymbol{e_z}\right) - \boldsymbol{r_i}\right|} \right] \quad (3.1.2\text{-}1)$$

where $\mathbf{e_z}$ denotes the unit vector along the **z**-axis (elongation/stacking direction). This formalism reduces the calculation of the scattering intensity to the sum of structural motifs found inside of the stacked model (see scheme in Fig. 3.1.2-1) and further bypasses the demand of a DA model representing the full structure as solely projections of the building block instead of all stacked duplicates, are evaluated; hence the term projection scheme. Its benefit, compared to the standard Debye formula, is a reduction of the mathematical complexity from $O((M \cdot N_{BB})^2)$ to $O(M \cdot N_{BB}^2)$, which drastically speeds up the computation.

A careful look at equation 3.1.2-1 yields that the DA configuration representing the building-block motif is not sufficient to calculate the scattering intensity: in addition, the stacking-distance H_{BB} must be specified. This stacking-distance may be determined from the derivative of the PDDF (dPDDF) as shown in the following.

As given by Glatter,[198] the PDDF can be calculated for any given assembly of spheres. Hence, an arbitrary stacked structure of e.g. 10 linear-stacked spheres can be constructed, of which the PDDF may readily be calculated (see Fig. 3.1.2-2). From this calculation, a series of observations may be made: as the system contains of 10 spheres the corresponding PDDF presents 10 peaks. The first peak (see blue trace in Fig. 3.1.2-2) relates to the mean shape of all involved spheres – it is hence the *intra*-building-block PDDF. The following nine peaks (see red traces Fig. 3.1.2-2) are caused by the repetitive nature of the system as for each possible sphere-to-sphere distance a new peak is found – they are hence *inter*-building-block PDDFs. From these inter-building-block PDDFs, in particular the distance between them, information on the stacking distance can be obtained. A straight-forward measurement of the peak-distance might, however, lead to misdetermination as the exact peak shapes and therefore

positions are distorted due to: 1) a linear high-r decay in the PDDF[35] (dashed line in Fig. 3.1.2-2) and 2) overlap of neighboring peak-contributions.[198] A direct measurement of the peak positions in the PDDF might therefore result in misdetermination of the stacking-distance.

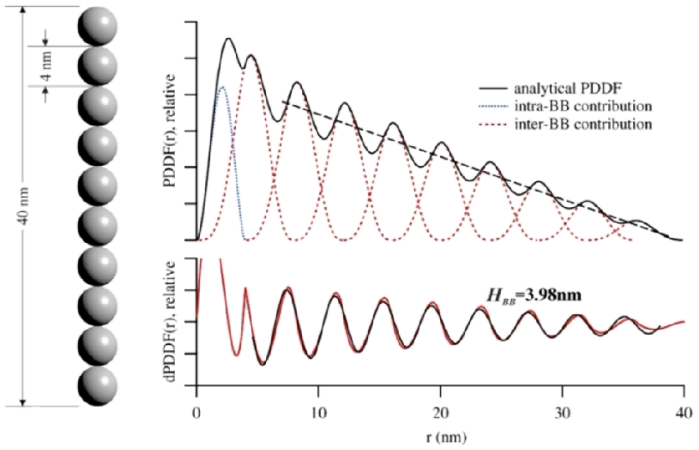

Fig. 3.1.2-2: Analytical investigation of phenomena occurring in the PDDF and dPDDF using a model-case of 10 spheres with diameter of 4 nm and a stacking distance of 4 nm. An illustration of the model used as input for the calculation of the PDDF is shown on the left. The calculated PDDF on the right shows distinct peaks, correlating to the intra- and inter-building-block contributions (blue and red, respectively). The dashed black line shows the linear nature of the high-r decay, characteristic for 1D extended geometries. The damped sine-function fit of the numerically calculated dPDDF on the bottom is in good agreement (H_{BB} =3.98 nm compared to input stacking distance of 4 nm).

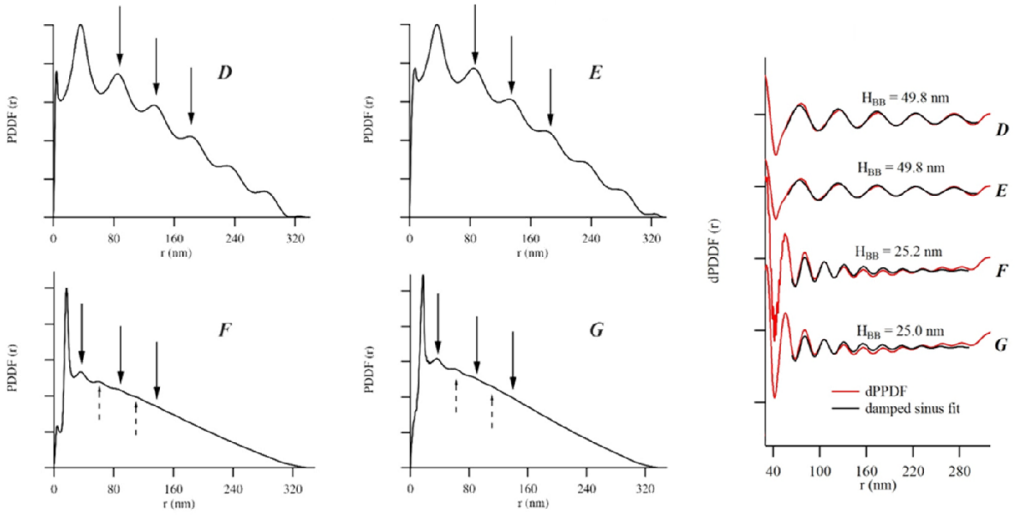

Fig. 3.1.2-3: PDDFs (left) and dPDDFs (right) of model scattering curves from helical motifs. The letters relate to the following models: **D**) single-strand and **F**) double-strand helix with 5 nm tape-width; **E**) single-strand and **G**) double-strand helix with 1 nm tape-width (in all cases, the helical pitch is 50 nm and the diameter is 20 nm) – see . Only weak oscillations in the PDDF relate to the repetitive nature of the models. The dPDDF amplifies these effects – corresponding damped sinus fits give outstanding agreement between the determined stacking distance (denoted as H_{BB}) with the initial model dimensions.

An approach to circumvent this issue is to calculate the derivative of the PDDF (dPDDF), as this numerically easy operation suppresses the mentioned decay distortion (see dPDDF in Fig. 3.1.2-2). The resulting dPDDF can then be fitted by a damped sinusoidal function

$$f(r) = y_0 + A * \sin\left(\frac{2\pi}{H_{BB}} * r \ + \varphi_0\right) e^{-\tau r} \qquad (3.1.2\text{-}2)$$

in which the period is directly related to the mean stacking distance (the other parameters y_0, A, φ_0 and τ are equally determined but yield no relevant information). For model calculations of stacked (see Fig. 3.1.2-2) and helical (see Fig. 3.1.2-3) systems, this approach yields an error in the determination of the stacking distance of <1%.

3.1.3 Computational implementation

The projection scheme reduces the complexity of the reconstruction process by *M*-fold, as only a single building-block instead of the entire structure is to be reconstructed. Hence, the DA modelling occurs only within the building-block. Here, the building-block motif is represented by a DA configuration *X* of which the scattering intensity I_{calc} is calculated according to equation (3.1.2-1). Optimization of this geometry is achieved by minimizing the chi-square

$$\chi^2 = \frac{1}{N_{exp}} \sum_{m}^{N_{exp}} \left(\frac{I_{exp}(q_m) - I_{calc}(q_m)}{\sigma_{\exp}(q_m)} \right)^2 , \qquad (3.1.3\text{-}1)$$

where $\sigma_{\exp}(q_m)$ denotes the experimental error and N_{exp} the number of datapoints. Throughout the fitting-algorithm, the configuration *X* is gradually altered whereas the effect of the structural change on the χ^2 is monitored. Current DA modelling implementations achieve this by "activating" or "deactivating" single DAs on a fixed grid (by setting is electron density to either 0 or 1).[49,50,199] The disadvantages of this approach are: i) limited spatial resolution of the model (if grid is chosen too coarse) and ii) excessive amounts of DAs (if grid is chosen too fine). Departing from this common practice, an algorithm was developed based on *free-floating* DAs: here an initial building-block volume is randomly filled with a fixed number of DAs that are set free at the beginning. The configuration X is then optimized by randomly moving single DAs and checking for improvement of χ^2.

This change in paradigm, so moving from a fixed-grid to a grid-free algorithm, requires a reconsideration of some of the fitting restraints currently employed to avoid unfeasible DA

configurations. DA modelling faces the general problem of uniqueness: as models consist of $>10^3$ DAs, the information content given by the scattering data is highly overdetermined by a given configuration. Fitting of the scattering data without restraints can therefore lead to physically unfeasible results, in particular in regard of model homogeneity and compactness. Current algorithms control and optimize these two properties during the fitting process by means of a looseness penalty regularization term as a quantitative measure of the DAs' local vicinity: by counting and maximizing the number of contacting neighbors of each DA, a compact and homogeneous configuration is achieved.[48,49,200] This technique is adapted in two manners. For one, the d_{N12} parameter, denoting the distance between a given DA and its 12 (close-packed-limit) next neighbors, is introduced. Similar to the looseness penalty, the d_{N12} quantifies the local vicinity of each DA, acting as a homogeneity classifier for the algorithm to decide if a given DA position is accepted or not. For the other, a radial compactness parameter RC(X) is introduced as a regularization term $(0 < RC(X) < 1)$ in the minimization procedure, keeping DA close to the (radial) center of mass of the configuration. Hence, the fitting algorithm in fact minimizes the goal function

$$f(X) = \chi^2 + |\beta| * RC(X) \tag{3.1.3-2}$$

instead of χ^2 alone according to equation 3.1.3-1.

In addition, the choice of a grid-free DA algorithm brings challenges for which no readily available solutions exists so far, such that new concepts must be introduced in order to: a) allow model scalability over different length-scales, b) generate a random movement depending on the current annealing temperature and c) obtain a hard-contact limit for neighboring DAs. The following briefly discusses computational solutions to these challenges.

In regard of a), model scalability is achieved using an estimated diameter D_X from the (radial) radius of gyration $R_{G,X}$ such that

$$D_X = 2\sqrt{2} * R_{G,X} = 2\sqrt{2} * \sqrt{\frac{1}{N_{BB}} \sum_{i=1}^{N_{BB}} x_i^2 + y_i^2} \quad . \tag{3.1.3-3}$$

Along the z-axis, a continuity condition is introduced (see Fig. 3.1.2-1) such that DAs leaving the building block in the vertical direction are re-projected back inside the building-block volume.

In regard of b), random DA movements are generated depending on the current temperature T of the fitting process and on the helical nature of the system γ, ($0 < \gamma < 1$, default 0.3). In mathematical terms, the random movement generator reads

$$\boldsymbol{r_{rand}}(T) = \begin{pmatrix} D_X\, T\, \left[Rand_x + \gamma\, T \cos\left(\frac{2\pi\, z_i}{H_{BB}}\right)\right] \boldsymbol{e_x} \\ D_X\, T\, \left[Rand_y + \gamma\, T \sin\left(\frac{2\pi\, z_i}{H_{BB}}\right)\right] \boldsymbol{e_y} \\ \alpha\, H_{BB}\, T * Rand_z\, \boldsymbol{e_z} \end{pmatrix} \quad (3.1.3\text{-}4)$$

where a random number generator $Rand$ returns any value between $-1 < Rand_{x,y,z} < 1$ every time when called and $\alpha = 0.1$ scales the movement along the z-direction in order to maintain axial homogeneity. As T is stepwise reduced throughout the fitting process, also the movements become smaller until the structure eventually "freezes".

In regard of c), a hard contact limit is derived from the $\langle d_{N12,X} \rangle$ parameter (here, $\langle d_{N12,X} \rangle$ denotes the mean d_{N12} parameter of configuration X), such that DA are not allowed to come closer than $0.1 * \langle d_{N12,X} \rangle$.

On a computational note, the fitting algorithm is written in C++ and implemented in Qt based, standalone computer program. After specifying the stacking distance H_{BB} and a starting diameter, the initial fitting volume is randomly filled. Upon start of the fitting procedure, the algorithm undergoes N_k iterations: starting from a temperature T_0 the system cools down as defined by the quenching coefficient q_T ($0 < q_T < 1$) such that the current temperature at a given iteration k is $T_k = T_0 \cdot q_T^k$ (default values: $N_k = 100$, $T_0 = 1$ and $q_T = 0.99$). In each k-iteration, all DAs are randomly moved using the random movement generator (see equation 3.1.3-4) and considering the hard-contact restriction. If the movement leads to improvement of the goal function (see equation 3.1.3-2), the movement is accepted – if not, each DA undergoes a total of 100 tires until moving to the next DA in a random sequence. Additionally, every 10th k-iteration, antifragile[201] movements are forced onto each DA atom, forcing the algorithm away from the local convergence minimum.

3.1.4 Verification of the algorithm

In order test and confirm the developed algorithm, a series of test geometries were reconstructed. For each model case, the scattering intensity was calculated according to the literature, (see Table 3.1.4-1 for exact model dimensions), which was then used as input for

the fitting algorithm. Here, 500-800 DAs per building-block were used, resulting in computation times for each run between 20-60 minutes on a standard workstation. The reconstructions are shown in Fig. 3.1.4-1. In order to evaluate the stability and reproducibility of the reconstruction algorithm, each reconstruction was repeated 8 times and subsequently analyzed using DAMAVER: as a result, the mean normalized spatial discrepancy (<NSD>) as a measure of similarity between the independent reconstructions of each model, is obtained (<NSD> = 0 for identical configurations).

Table 3.1.4-1: Detailed dimensions of the models shown in Fig. 3.1.4-1 – explanation of the model variables can be found in the corresponding references. (Feigin & Svergun, 1987)[35]; (Pringle & Schmidt, 1970)[56]; (Guinier & Fournet, 1955)[38]; (Kawaguchi, 2001)[202]

	Model					
Parameter	**A**	**B**	**C**	**D**	**E**	**F**
Reference	[1]	[1]	[1]	[2]	[2]	[2]
R_o **(nm)**	10	10	-	10	10	10
R_i **(nm)**	0	5	-	5	0	5
a; b (nm)	-	.	8; 20	-	-	-
L = c (nm)	1000	1000	1000	1000	1000	1000
P (nm)	-	-	-	50	50	50
ω (°)	-	-	-	45	6	45
φ (°)	-	-	-	-	-	180

For all model calculations, the structural motifs were successfully reconstructed. Reconstructions ***A*** and ***B*** show a circular cross-section in agreement with the initial model, while in the case the cylindrical shell, the empty core is present. Also reconstruction ***C*** shows a clear rectangular cross-section. However, the sharp corners are not fully resolved, which is most likely the effect of insufficient resolution from the scattering data ($d_{res} \approx 1.6$ nm compared to the rectangular cross section: $a\ x\ b = 4\ x\ 20$ nm). In cases ***D-G***, the helical fingerprints (single or double-strand nature) are well resolved in the reconstructed models. ***D*** and ***E*** as well as ***F*** and ***G*** present noticeable differences in their cross-sections, allowing to distinguish between helical filament (empty core) and helical tape (filled core). Reproducibility analysis shows that the <NSD>, so the similarity between independent reconstructions, of ***A-G*** gradually increases from $1.01 - 1.37$ with model complexity. On absolute scale, these values are higher than common fixed-grid programs ($0.4 < \langle \mathrm{NSD} \rangle < 0.7$).[197] However, for other grid free programs, significantly higher values ($1 < \langle \mathrm{NSD} \rangle$) are

commonly reported.[199] As reference, eight randomly filled, artificial cylinders and single-strand helices ($N_{DA} = 700$) yield a <NSD> of 1.03 ± 0.01 and 1.06 ± 0.01, respectively. The reported values from the reconstruction are hence feasible.

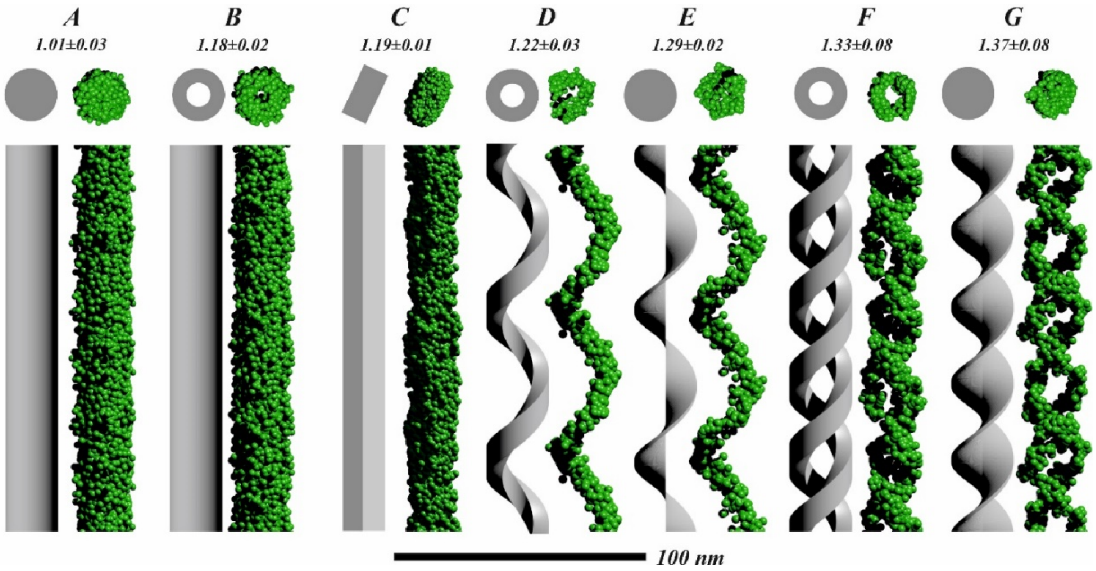

Fig. 3.1.4-1: Theoretical models and corresponding 3D reconstructions of the fitting algorithm. The numbers below the labels denote the mean normalized spatial discrepancy (<NSD>), obtained from eight independent reconstructions (random artificial cylinder: <NSD> = 1.03 ± 0.01, random artificial single-strand helix: <NSD> = 1.06 ± 0.01). The PDDFs and dPDDFs used to determine the stacking-distance between the building-block can be found in Fig. 3.1.2-3. See reprint of the publication in Appendix A1 for the corresponding scattering curves.

A further model example was calculated from the crystal-structure of a Br bay-substituted PBI (PBI1-Br_2), which forms asymmetrically, "wing-like", π-π-stacked columns (see Fig. 3.1.4-2 left). From this crystal-structure-based column (with length of approx. 14 nm) the theoretical scattering pattern was calculated using FoXS[203] and subsequently used as input for the fitting algorithm (here the artificial error band was calculated according to $\sigma(q) = 0.1\sqrt{I(q)}$). As shown in Fig. 3.1.4-2 right, the triangular cross-section in its shape and size is clearly present in the reconstruction. The full details of the tail-functionalized ligands cannot be resolved due to insufficient resolution provided by the scattering curve ($d_{res} \approx 0.4\,nm$).

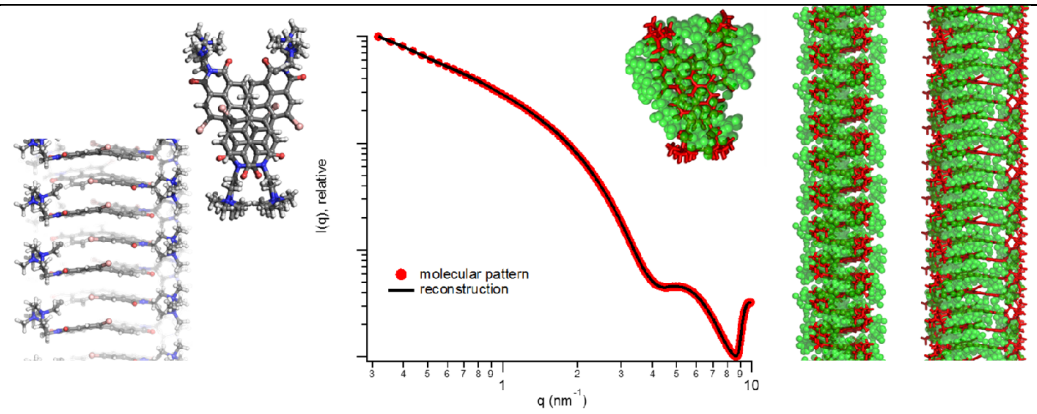

Fig. 3.1.4-2: Reconstruction from the scattering pattern of a π-π-stacked Br-PBI column. Left: Orthogonal snapshots of the π-π-stacked column isolated from the crystal structure of a Br bay-substituted PBI, showing a clear, "wing-like" cross-section. Middle: theoretical scattering pattern of the crystal-structure column (red dots) compared to the fitting result. Right: Comparison of the reconstruction (green) with the theoretical model used as input (red).

As final confirmation, the reconstruction algorithm was applied to the experimental dataset of a self-assembled peptide double-strand-helix.[204] In a first step, the stacking-distance of 53 nm was determined from a corresponding dPDDF (see Fig. 3.1.4-3 top). The corresponding real-space reconstruction (see Fig. 3.1.4-3 middle) presents two independent tapes within the building block. However, the two tapes do not appear to be symmetric along the *z*-direction, suggesting a displacement angle of $\varphi \neq 180°$ between them. The cross-section of the helical-tapes presents a rough surface that does not allow more detailed interpretation, as typical for such random-movement DA models. Nevertheless, comparison of the reconstruction with the model according to the previously published dimensions is in good agreement.[204] Further, 16 independent reconstructions were performed and averaged using DAMAVER.[205] For one, the <NSD> of 1.27± 0.02 is in good agreement with the previously determined reference values and hence confirm reproducibility of the reconstruction. For the other, in the superimposed and averaged models (see Fig. 3.1.4-3 right), the structural motif becomes even clearer.

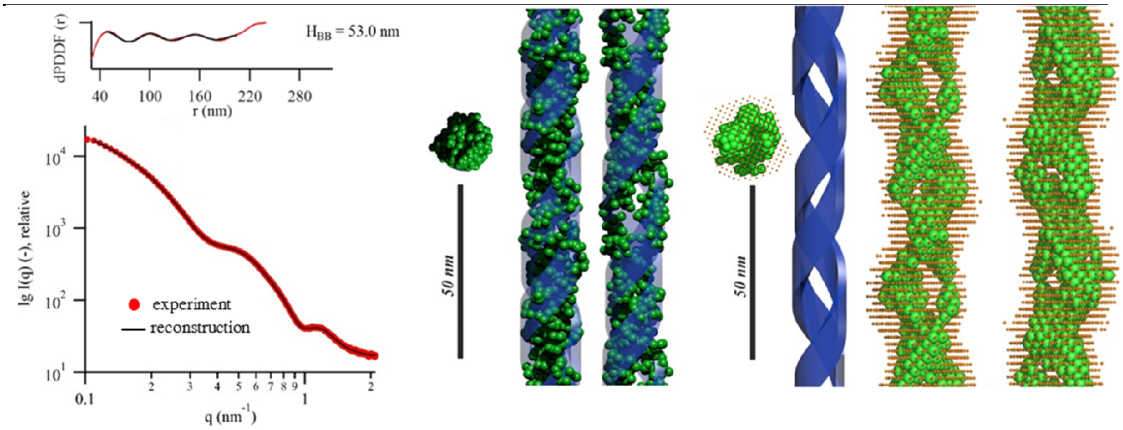

Fig. 3.1.4-3: Verification of the reconstruction algorithm using experimental scattering data. Left: Experimental scattering pattern and corresponding fit together with the dPDDF used to determine the stacking-distance. Middle: Orthogonal views of the model reconstructed from the scattering pattern (green), compared to previously published structure (blue). Right: Analysis of uniqueness and repeatability of the reconstruction by means of 16 independent reconstructions, which were aligned and superimposed using DAMAVER. The dots denote positions of the full DAMAVER model whereas the green spheres correspond to the 50% occupancy representation. The theoretical models are shown in blue.

3.1.5 Summary & concluding remarks

In summary, the above work presents a new method to reconstruct the structural motif of elongated, rod-like systems from solution scattering data. A series of reconstructions from model calculations and experimental data were made to test the algorithms functionality and reproducibility. At this point, it should be noted, that the algorithm can also be used for the case of M=1 stacks, so for globular particles, making it applicable for a broad range of samples.

However, a critical aspect on model resolution shall not remain unmentioned. DA modelling always provides only one of many possible configurations that describe a given scattering pattern – a unique solution does not exist. Equally, the reconstructed models should always be inspected with caution, in particular if the information content provided by the scattering curve (= angular range) is limited. For this purpose, a multi-core mode in the software runs a separate reconstruction on every core, such that a reproducibility analysis using e.g. DAMAVER[205] is facilitated. The <NSD> obtained from such a model comparison is a stable indicator of reproducibility, such that reconstruction series with high <NSD> should be treated with caution.

3.2 SAXS methodology – weak inter-molecular aggregation in Ru/Os-dendrimeric photosensitizers

See Appendix A2 for an adapted reprint of the original publication.

3.2.1 Introduction

One of the most common applications of SAXS is the structural characterization of colloidal nano-systems, including inorganic nano-crystals, proteins and molecules in solution. Here, the concentration of the colloidal solutions is chosen such that particle interaction can be neglected. In mathematical terms, this sets the structure factor $S(q) = 1$ such that, according to equation 2.1.3-1, the measured scattering is defined only by the form-factor scattering, so the shape of the colloid. However, colloidal solutions exhibit a concentration dependent behavior: depending on the solubility of the dissolved species, particle-interaction will occur at increasing concentrations. In mathematical terms, this yields $S(q) \neq 1$ such that the interaction-depended scattering features are not constant over q. Using parametric models that describe both particle shape and interaction, it is possible to disentangle the structure- and form-factor contributions, in particular for simple globular particle geometries. If, however, the systems become more complex, e.g. if intercalation effects occur, the exact particle shape cannot be determined or the scattering is generally weak, corresponding models may not be available or applicable. The goal was hence to derive a general shape-independent formalism that gives an estimate on the magnitude of inter-molecular aggregation by means of the aggregation number, so the number fraction of particles that are aggregated.

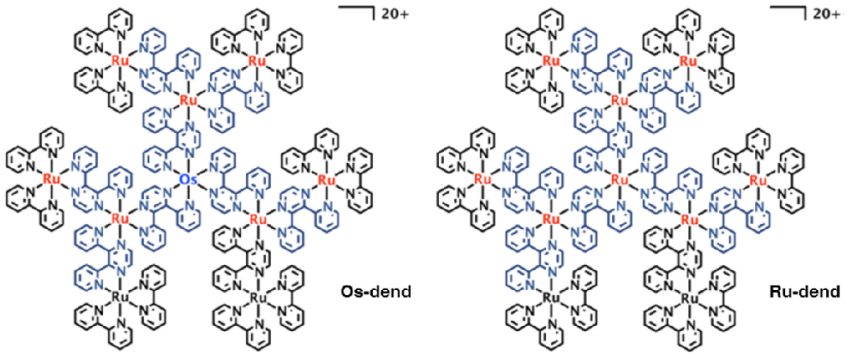

Fig. 3.2.1-1: Os- and Ru-dendrimeric compounds used in this work.

The following subchapters will focus on low concentrated systems (30 µM in acetonitrile) of the similar Os- and Ru-dendrimers $[Os\{(\mu\text{-}2,3\text{-}dpp)Ru(bpy)_2\}_3](PF_6)_8$, hereafter named Os-dend, and $[Ru\{(\mu\text{-}2,3\text{-}dpp)Ru(bpy)_2\}_3](PF_6)_8$, hereafter named Ru-dend (see Fig. 3.2.1-1). In these systems, particularly in Os-dend, a new charge-transfer effect is observed upon increasing concentration, pointing towards aggregation induced energy-transfer. The branched and polymorph nature of the Os/Ru-dend together with the low scattering cross-section at such low concentrations make the system particularly difficult for parametric modelling of the SAXS data. First, a formalism will be derived that allows estimating the aggregation number from PDDF.

3.2.2 Derivation - aggregation number estimated from the PDDF

The following aims at estimating how many of the molecules present in solution are in an aggregated state. This estimation is based on the assumption that only monomers and dimers of Os-dend or Ru-dend with equal electron density difference Δρ are in solution. Hence, the measured scattering intensity is the sum of both monomer and dimer scattering, such that

$$I_{exp}(q) = \Delta\rho^2\left[c_M {V_M}^2 \, |F_M(q)|^2 + c_D {V_D}^2 \, |F_D(q)|^2\right] \tag{3.2.2-1}$$

given c_M and c_D, V_M and V_D as well as $|F_M(q)|^2$ and $|F_D(q)|^2$ represent the number density, single particle volume as well as the normalized form-factor of the corresponding species, respectively.[34] Similarly, the PDDF $P(r)$ of the experimental scattering curve is written as[34]

$$P_{\text{exp}}(r) = \Delta\rho^2[c_M \, P_M^0(r) + c_D \, P_D^0(r) \,] \tag{3.2.2-2}$$

where the form-factor $|F(q)|^2$ is related to the normalized monomer and dimer PDDF $P_M^0(r)$ and $P_D^0(r)$, respectively, via the inverse Fourier transform, according to[34]

$$P_i^0(r) = \frac{V_i^2}{2\pi^2}\int_0^\infty |F_i(q)|^2 \, qr \, \sin qr \, dq. \tag{3.2.2-3}$$

Thus, the PDDF of a single species i is denoted as $P_i^0(r)$, where $i = M$ for monomers and $i = D$ for dimers. As the form-factor is defined as $|F_i(0)|^2 = 1$, it is known that[34]

$$\int_0^\infty P_i^0(r) \, dr = \frac{V_i^2}{4\pi}. \tag{3.2.2-4}$$

The monomer and dimer PDDFs are now entangled by looking at their relative contributions at a given pair distance r. In the case of the monomer, where $D_{M,max}$ is the maximum dimension found in a single molecule, equation 3.2.2-4 results in

$$\int_0^{\infty} P_M^0(r)\, dr = \int_0^{D_{M,max}} P_M^0(r)\, dr = \frac{V_M^2}{4\pi}. \tag{3.2.2-5}$$

Therefore, all PDDF contributions found for $r > D_{M,max}$ must be caused by the dimeric species. In extension to equation 3.2.2-5, the dimer PDDF $P_D^0(r)$ consists of single molecular contributions $P_M^0(r)$, as well as intermolecular contributions $P_{int}^0(r)$. Assuming preservation of the scattering density leading to $V_D = 2 * V_M$, this results in

$$\begin{aligned}\int_0^{\infty} P_D^0(r)\, dr = \; & 2 * \int_0^{D_{M,max}} P_M^0(r)\, dr + \int_0^{D_{D,max}} P_{int}^0(r)\, dr = \frac{V_D^2}{4\pi} \\ & = \frac{4V_M^2}{4\pi},\end{aligned} \tag{3.2.2-6}$$

hence the integral of the intermolecular contributions must yield

$$\int_0^{D_{D,max}} P_{int}^0(r)\, dr = 2 * \int_0^{D_{M,max}} P_M^0(r)\, dr = \frac{2V_M^2}{4\pi}. \tag{3.2.2-7}$$

Now looking at the ratio between the intermolecular ($0 < r < D_{D.max}$) and the monomeric contributions ($0 < r < D_{M.max}$) defined in equations 3.2.2-2, 5 and 7, the final deduction yields

$$\begin{aligned}\frac{\int_0^{D_{Dmax}} P_{\exp int}^{dimeric}(r)\, dr}{\int_0^{D_{M,max}} P_{exp}^{monomeric}(r)\, dr} & = \frac{c_D \int_0^{D_{D,max}} P_{int}^0(r)\, dr}{(c_M + 2 * c_D) \int_0^{D_{M,max}} P_M^0(r)\, dr} \\ & = \frac{c_D * 2\, V_M^2}{(c_M + 2 * c_D) * V_M^2} = \frac{2c_D}{c_M + 2c_D} = \varphi_D\end{aligned} \tag{3.2.2-8}$$

where φ_D is the number fraction of aggregated molecules. Therefore, φ_D can be obtained by numerical integration of the relative contributions in the experimentally fitted PDDF $P_{\exp}(r)$ by reframing equation 3.2.2-8, such that

$$\varphi_D = \frac{\int_0^{D_{D,max}} P_{exp}^{dimeric}(r)\, dr}{\int_0^{D_{M,max}} P_{exp}^{monomeric}(r)\, dr}. \tag{3.2.2-9}$$

As the intermolecular contributions cannot be distinguished from the monomeric contributions between $0 < r < D_{M.max}$, φ_D cannot be calculated exactly from the experimental $P_{\mathrm{exp}}(r)$. However, for most investigations an estimation of the lower limit of the aggregated number fraction is absolutely sufficient. Assuming all dimeric contributions at $r < D_{M,max}$ are neglected, we will systematically underestimate dimeric contributions, such that

$$\varphi_D = \frac{\int_0^{D_{M,max}} P_{exp}^{dimeric}(r)\,dr + \int_{D_{M,max}}^{D_{D,max}} P_{exp}^{dimeric}(r)\,dr}{\int_0^{D_{M,max}} P_{exp}^{monomeric}(r)\,dr} > \\ > \frac{\int_{D_{M,max}}^{D_{D,max}} P_{exp}^{dimeric}(r)\,dr}{\int_0^{D_{M,max}} P_{exp}^{monomeric}(r)\,dr} > \\ > \frac{\int_{D_{M,max}}^{D_{D,max}} P_{exp}^{dimeric}(r)\,dr}{\int_0^{D_{M,max}} P_{exp}^{monomeric}(r)\,dr + \int_0^{D_{M,max}} P_{exp}^{dimeric}(r)\,dr} = \varphi_D^{min}. \tag{3.2.2-10}$$

As the formalism above shows, one can now obtain the minimal number fraction of aggregated molecules φ_D^{min} by looking at the ratio of the integral of the experimental PDDFs between $0 < r < D_{M.max}$ and $D_{M.max} < r < D_{D.max}$. Of course, this implies that the choice of the integration boundaries is crucial for a meaningful estimate.

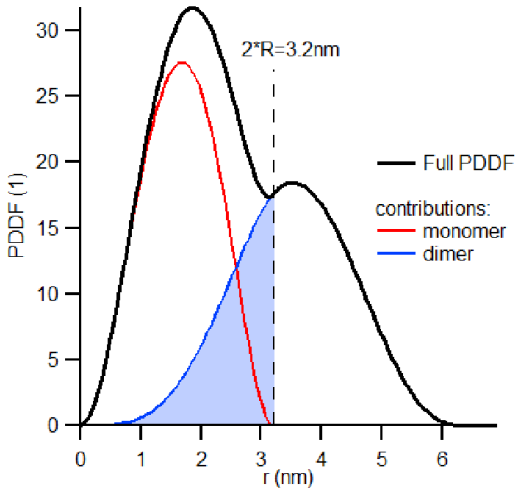

Fig. 3.2.2-1: Analytical pair distance distribution function (PDDF) of two contacting hard-spheres with a diameter of 3.2 nm. As the dimeric contributions for $r < D_{M,max}$ are neglected for the proposed estimation (see blue shaded region), the dimeric contributions will systematically be underestimated while the monomeric contributions will be overestimated.

In order to substantiate and visualize the proposed estimation of the aggregated number fraction, the relative monomeric and dimeric contributions are calculated analytically for the case of contacting hard-spheres of equal size.[198] As shown in Fig. 3.2.2-1, the proposed approach will not only underestimate the dimeric contributions but it will at the same time overestimate the monomeric contributions. As a result, the φ_D^{min} values will consistently underestimate the real condition by at least a factor of 2 and will thus provide a conservative estimate of the aggregated number fraction.

3.2.3 Application to experimental data

The scattering patterns together with the fitted PDDFs (using GIFT[206]) of Os- and Ru-dend are shown in Fig. 3.2.3-1a and b. Here, the "peaks" in the PDDF spectrum correspond to distances between high electron density clouds found with increased probability, which in this case correspond to heavy metal centers of Os-/Ru-dend. The peaks in the PDDF may hence be related to the dominant, metal-metal distances. A representation of a corresponding configuration is shown in Fig. 3.2.3-1c. Although such a model can only be taken with care (because several stereochemical and geometrical isomers are possible) some distances between two metal centers in such a dendrimer are independent of isomer structure: 1) the metal-metal distance between two metal centers only separated by a 2,3-dpp bridge (ca. 0.7 nm) and 2) the metal-metal distance between two metals having interposed a single $\{Ru(\mu\text{-}2,3\text{-}dpp)_3\}^{2+}$ unit, about 1.4 nm. Clearly, larger metal-metal distances, for example between metals belonging to different dendrimer branches (see example of one of them in Fig. 3.2.3-1c) are also present, but they are less relevant since their distances are less defined and the contributions to the PDDF would be much smaller.

A similar effect is observed in the PDDF of theoretically calculated scattering curves (using CRYSOL[54]) from models of a single possible conformation. As shown in Fig. 3.2.3-1b, only the two main metal-metal distances are evidenced, with the longer intra-dendrimer metal-metal distances probably being buried in the tail of the main peaks. A comparison between the experimental and theoretical PDDFs is quite instructive: for both, Os-dend and Ru-dend, the two "peaks" in the 0.6-1.8 nm range are present in experimental and theoretical data and can thus be considered as a conserved motif of the dendrimeric side arms in a relatively fixed conformation.

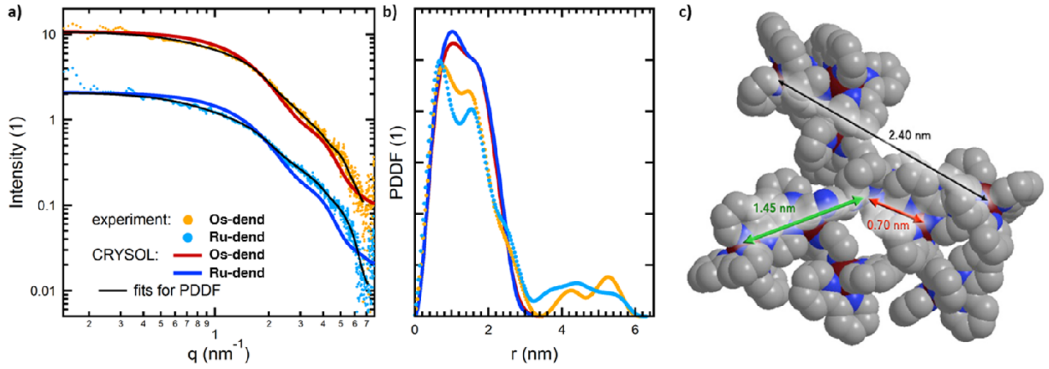

Fig. 3.2.3-1: SAXS investigation of Os-dend and Ru-dend. a) Experimental SAXS patterns together with PDDF fits and theoretical form-factor from a possible molecular conformation (see **c**). **b)** PDDFs corresponding to the fits shown in **a**. **c)** Conformation of Os-dend used to calculate the theoretical scattering pattern and PDDF shown in **a** and **b**. The colored arrows denote the mean distances found between the metal centers.

In regard of molecular aggregation, two effects are witnessed. For one, both compounds exhibit a sloped low-q behavior (q < 1 nm^{-1}), which is a characteristic feature of multimer formation between dispersed species (see deviation of the experimental pattern from the CRYSOL pattern in Fig. 3.2.3-1a at q≈1 nm^{-1}).[34] For the other, the PDDF of both compounds (see Fig. 3.2.3-1b) presents "peaks" at distance > 3 nm (and also the ca. 2.5 nm shoulder) that are absent in the computed PDDF of isolated dendrimers. In analogue to the theoretical example of contacting hard-spheres (see Fig. 3.2.2-1), these oscillations are assigned to inter-dendrimer metal-metal interactions resulting from dendrimer-dendrimer aggregation. Taking 3.2 nm as the border between the monomeric and dimeric contributions results in the integration regions $0 < r < 3.2\ nm$ and $3.2 < r < 6.3\ nm$ for the estimation of aggregation number. The results are found in Table 3.2.3-1, yielding a minimal aggregation number of 11.8 and 14.6% for Os-dend and Ru-dend, respectively. As already mentioned further above, this approximation underestimates the real volume-fraction by at least a factor of 2. It can hence be concluded that approx. 25-30% of the molecules are in an aggregated state.

Table 3.2.3-1: Results of the estimation of the aggregation number. The integration boundaries $D_{M,max}$ and $D_{D,max}$ were chosen to be 3.2 and 6.3 nm, respectively, as obtained from the PDDF fits. The minimum aggregated monomer number fraction φ_D^{min} was calculated according to equation 3.2.2-10.

	$\int_0^{D_{M,max}} P_{exp}(r)\,dr$, *(1)*	$\int_{D_{M,max}}^{D_{D,max}} P_{exp}(r)\,dr$, *(1)*	φ_D^{min}, *(%)*
Os-dend	1.772	0.209	**11.79**
Ru-dend	1.769	0.259	**14.64**

3.2.4 Summary & concluding remarks

In summary, the above work presents a fast and easy pathway towards estimating the lower limit of the aggregation number for colloidal solutions by determining integral values of the PDDF. This approach only relies on the fitting of the PDDF to the experimental pattern and does not require the formulation and construction of a parametric model. The formalism is used on the system of low-concentrated Ru and Os dendrimeric compounds, where the recorded scattering patterns are close to the resolution limit of SAXS. From the estimation, it can experimentally be confirmed that approx. 25-30% of the molecules form aggregated species, most probably dimers. The newly observed charge-transfer effect witnessed under these conditions might therefore very well result from molecular aggregation, such that the close vicinity between dimeric molecules enables inter-molecular charge transfer.

3.3 Nanostructure of perylene-bisimides (PBI) in aqueous media

See Appendix A3 and A4 for adapted reprints of the original publications.

3.3.1 Introduction

As extensively discussed in section 2.2.1, the general hydrophobic nature of PBIs drives the formation of π-π-stacked superstructures in polar media, such as water. The characterization of such supermolecular PBI compounds is mainly based on changes in the optical properties, such as absorption, emission, quantum yield. etc.., paired with either computational results or reference literature. Experimental evidence of hypothesized models is rare. The goal was hence to obtain independent structural information of PBI superstructures, in order to test and extend current interpretations.

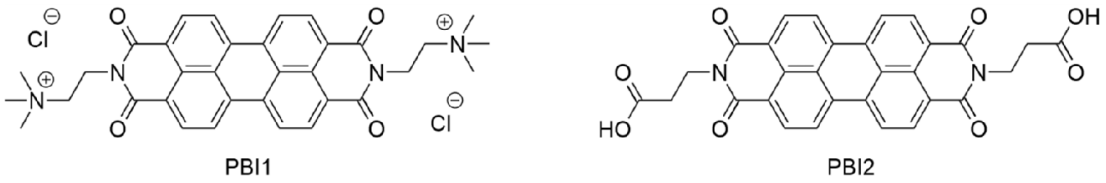

Fig. 3.3.1-1: Perylene bisimides used in this subsection.

The following subsections will focus on two structurally similar PBIs (see Fig. 3.3.1-1): i) N,N-bis(2-(trimethylammonium-cation)ethylene)-perylene-3,4,9,10-tetracarboxylic bisimide (PBI1) and ii) N,N'-bis(propanoic acid)-perylene-3,4,9,10-tetracarboxylic bisimide (PBI2). First, a survey on theoretical calculations applying to both compounds is given. Subsequently, the nanostructure of the cationic PBI1 and in aqueous solutions is compared with optical observations. A special focus is then set on the gelated state of PBI2, induced by pH shock: a detailed structural model was constructed from which valuable insight on long-range charge transfer in such gels can be made.

3.3.2 Theoretical considerations

The compounds PBI1 and PBI2 only differ in their tail-functionalized ligand: as this functionalization occurs symmetrical at the N nodes, the perylene core should remain flat. Crystal structures from single-crystals grown in aqueous media of both compounds confirm

this hypothesis (see Fig. 3.3.1-2), showing π-π-stacked columns that cross-link via their tail-functionalized ligands.

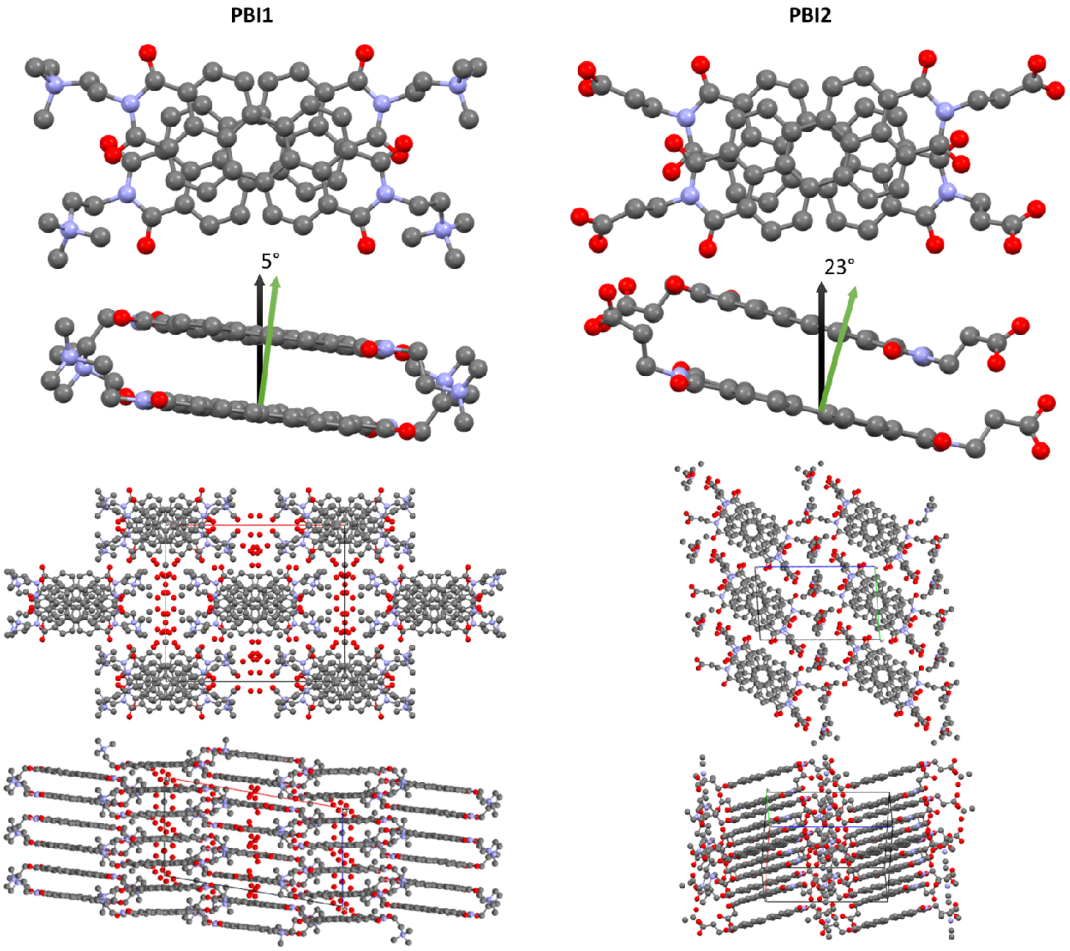

Fig. 3.3.2-1: PBI dimers from the crystal structures of PBI1 and PBI2 (hydrogens omitted for clarity). The black arrows indicate the column-axis, whereas the green arrows indicate the π-π-stacking direction.

As, both compounds were grown from aqueous solutions (PBI1 from pure water, PBI2 from pH 10 triethylamine (TEA)), intra-columnar hydrogen bonding between the columnar stacked PBIs is observed. In case of PBI2, partial protonation followed by hydrogen-bonding between the tail-functionalized carboxylic groups occurs, causing a longitudinal shift of the PBIs and hence a 23° tilt between the π-π-stacking direction and the column axis (see green and black arrow in Fig. 3.3.2-1). In case of PBI1, the interaction between the tail-functionalized trimethylammonium-cation and the imide carbonyl is much weaker (shielded by Cl^- counter-ions), such that the tilting angle decreases to 5°.

In order to understand the effect of the intra-columnar tilt on the optical properties, time-dependent density-functional theory (TD-DFT) calculations of exemplary PBI dimers and a reference PBI monomer were made (neglecting the tail-functionalized ligands). Here, the crystal structures were used to construct dimers with 0° and 25° tilt (see Fig. 3.3.2-2 for PBEh-3c geometry optimized structures) of which the corresponding absorption spectra were calculated (ωB97X – TD-DFT). As shown in Fig. 3.3.2-2 right, the untilted stacking (blue trace) is in agreement with general H-type stacking theory[116,207] (note the blue-shift compared to the monomeric case (black trace)). Further, a partially allowed J-band transition at higher wavelengths (caused by rotational displacement between the two perylenes[116]) is found. In case of the tilted stacking, an overall broadening and red-shift of the spectrum is observed. This shift, together with the increased rotational displacement from β = 31° to 39°, enhances the now stronger J-band. At this point, it should be noted that these TD-DFT calculations do not reproduce the vibronic structure of the aggregation compounds, such that only the lowest lying transitions are determined.

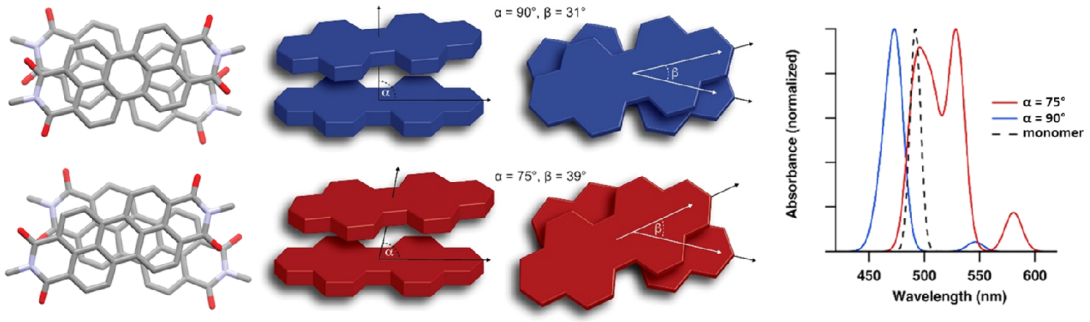

Fig. 3.3.2-2: Time dependent DFT calculations of two exemplary PBI dimers. Left: Molecular representations of the two geometry optimized dimers. Middle: Respective illustrative models, showing the detailed dimeric arrangement and the corresponding tilting angles. Right: Theoretical absorption spectra of the geometry optimized dimers, showing the commonly observed blue-shift and red-shift for the untilted (blue) and the longitudinally displaced (red) arrangement, respectively.

3.3.3 In-solution structure – a concentration series

The first focus towards understanding the in-solution nanostructure of both PBIs was set on the quasi-parallel π-π-stacking PBI1. The low-concentration regime (1-50 µM) was investigated by UV/Vis absorption and emission measurements, as shown in Fig. 3.3.3-1. All recorded absorption spectra exhibit two peaks at 537 nm and 501 nm, corresponding to the

0→0 and the 0→1 transition.[1] The ratio of the peak absorbance of the lowest two energy transitions $A^{0\rightarrow0}/A^{0\rightarrow1}$ can be used to interpret the level of aggregation: in case of individual molecules with normal Franck-Condon progression, this ratio should be around 1.6,[208,209] whereas for aggregated (dimeric) species typical values are <0.7.[209,210] Even at the lowest measured concentration of 1 µM the $A^{0\rightarrow0}/A^{0\rightarrow1}$ ratio is 0.95, indicating a first sign of π-π-stacked aggregation (see inset in Fig. 3.3.3-1a). At higher concentrations, this ratio further decreases, approaching a minimum around 0.60. At this state, the spectrum is overall blue-shifted, hence indicating parallel H-type aggregation. Similarly, at low-concentrations the emission intensity gradually increases with concentration until approx. 10 µM (quantum yield of 7%), at which point the emission remains constant (see inset in Fig. 3.3.3-1b).

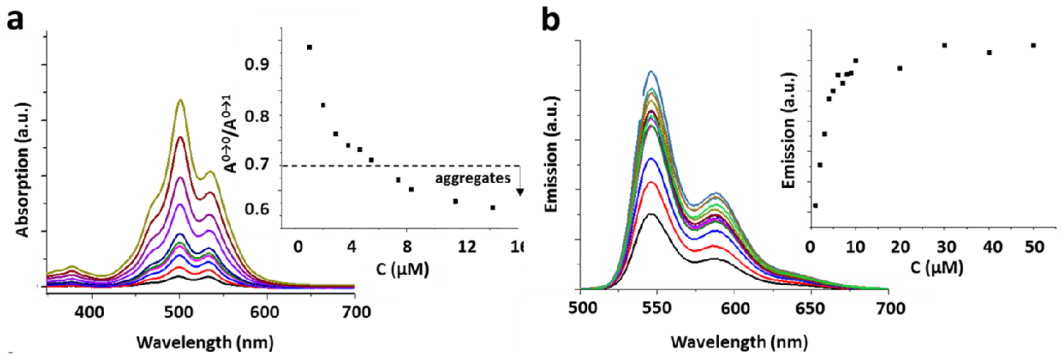

Fig. 3.3.3-1: Aggregation dynamics of PBI1 in the low-concentration regime. a) Absorption spectra of PBI1 measured from 1 µM to 14 µM. The 537 nm/501 nm ratio dependence on PBI1 concentration is shown in the inset. **b)** Corresponding fluorescence spectra measured in the rage of 1-50 µM. Similar to above, a clear correspondence between the PBI1 concentration and the emission intensity at 545 nm is seen in the inset. Adapted from *M.Burian, et.al.*[211]

More direct insight on the structural aspects is gained from SAXS at the methodological lowest possible concentration of 0.6 mM. As seen in Fig. 3.3.3-2a, the scattering pattern of PBI1 shows a distinct increase in the low-q regime ($q<0.5$ nm^{-1}), characteristic of large-scale aggregate scattering.[34] However, the mid- and higher-q regime ($q>1$ nm^{-1}) are dominated by the form-factor scattering of a modeled PBI1 dimer (see inset Fig. 3.3.3-2a). Full-pattern refinement (see black trace in Fig. 3.3.3-2a) was possible using a parametric model, consisting

[1] It should be noted that this notation of the absorption bands can be confusing in regard to the singlet state transitions. E.g., $S^0\rightarrow S^1$ denotes the transition from the singlet ground- to the singlet excited state, which is here corresponds to the 0→0 band. The transition from the singlet ground- to the first energetically slightly-higher, vibronically allowed excited state (see dashed lines in Fig. 2.2.1-2) here corresponds to the 0→1 band.[114,235,236]

of a -4 sloped Porod contribution[34] and the theoretical form-factor of the H-type stacked PBI dimer (calculated using CRYSOL[54]). See section 5.3.1 for fitting details.

Upon increase of the PBI1 concentration to 20 mM, the scattering pattern drastically changes (see Fig. 3.3.3-2b). Especially in the mid-q regime a strong deviation of the previous curve is observed: the dimeric PBI1 form-factor scattering is not present any more. The previous model function was adjusted to now include the contribution of a core-shell cylinder: also in this case, full-pattern refinement is possible where best agreement is found for a cylinder of 4 nm height and 2 nm diameter. Comparison of these results with the characteristic dimensions of a single PBI1 molecule strongly suggests the formation of a π-π-stacked conformation, as sketched in the inset of Fig. 3.3.3-2b. Wide-angle X-ray scattering (WAXS) measurements confirm this hypothesis: a strong diffraction peak corresponding to the π-π-stacking d-spacing of 0.34 nm with a coherent domain size of 3.9 nm (peak FWHM of 1.35 nm^{-1}) is visible.

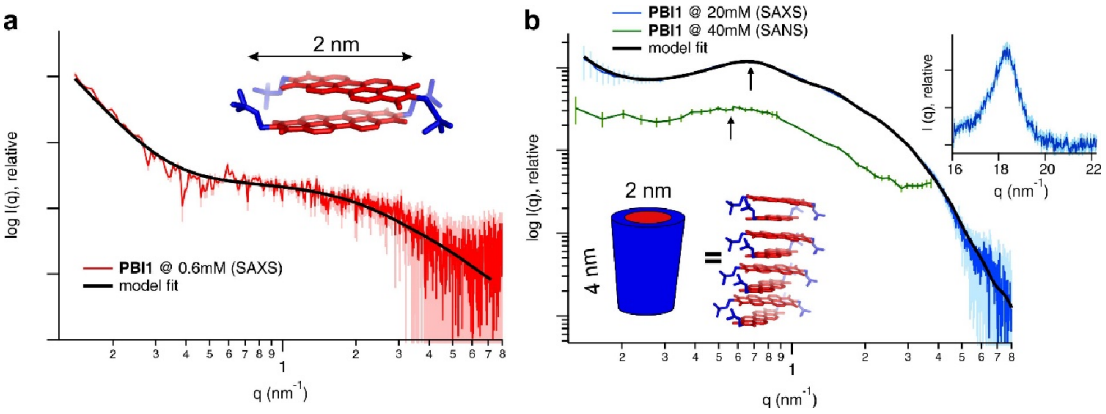

Fig. 3.3.3-2: Aggregation dynamics of PBI1 in the higher-concentration regime. a) SAXS pattern of PBI1 at 0.6 mM (red) as well as a corresponding model fit (black) utilizing the form-factor scattering of the PBI1 dimer shown in the inset. **b)** SAXS (blue) and SANS (green) patterns of PBI1 at 20 mM and 40 mM, respectively. The fitted model curve yields best agreement for a core-shell cylinder of π-π-stacked molecules as confirmed by the WAXS data (see π-π-stacking peak in the inset). The black arrows indicate the position of the first structure-factor peak relating to the mean distance between the cylindrical aggregates. Adapted from *M.Burian, et.al.*[211]

The concentration increase of PBI1 from 0.6 to 20 mM not only affects the form-factor scattering, but also causes a significant structure-factor contribution (described by a Sticky-hard-sphere model[212]), which describes the interactive forces between the cylindrical aggregates. E.g., the first broad peak at approx. 0.65 nm^{-1} relates to the mean next-neighbor distance between the cylinders, whereas the fitting-results determined this distance to be about 4.0 nm (see black arrow in Fig. 3.3.3-2b). Comparison of this value with the cylindrical dimensions above suggest that the length of the π-π-stacked nano-crystals dominates the mean

interparticle distance. Additional neutron scattering experiments (SANS) of PBI1 at an increased concentration of 40 mM are consistent with this hypothesis: as the concentration is increased, the nano-crystals are most likely to grow along the π-π-stacking direction, resulting in an increased cylinder length. This further increases the mean interparticle distance such that the first structure factor peak shifts to lower q values (see black arrows in Fig. 3.3.3-2b). See section 5.3.1 for fitting details.

In conclusion, PBI1 forms cylindrical π-π-stacks of crystalline nature in aqueous solution. Single-molecule interactions in the low-concentration regime (<50 μM) define the optical properties of the system while higher concentrations (>0.6 mM) cause the formation of nano-crystalline colloids.

3.3.4 Hydrogelation of PBI – a multiscale model

With the insights gained from the PBI1 system, the next focus was set on the carboxylic acid functionalized PBI2. As already known from the crystal structure, deprotonation of PBI2 tends to induce a tilted J-type π-π-stacked arrangement due to intra-columnar hydrogen bonding. A detailed view of this effect may be seen in Fig. 3.3.4-1a. To recall, the initial precursor solution ([PBI2] = 8.8 mM) was prepared under basic conditions (pH 10, TEA) in order to increase solubility. As a side-effect, the basic condition induces partial deprotonation of the carboxylic tails, which hydrogen-bond with a protonated counterpart.

From this observation, it would be expected that J-type stacking is the structural motif of PBI2 in its solution state. Interestingly, this fact is not observed: UV/Vis absorption spectra show a strong suppression of the $A^{0\rightarrow0}$ band at 550 nm, which is linked to an untilted H-type stacking (see blue trace in Fig. 3.3.4-1b). This behavior implies that the carboxylic groups are either fully protonated or deprotonated, such that hydrogen-bonding is omitted. Indeed, upon full protonation induced by a pH shock (addition of 4 M HCl) a new absorption peak appears at 588 nm (see black arrow and red trace in Fig. 3.3.4-b) – a phenomenon linked to J-type stacking. Hence, the de/protonation allows for tuneability of the π-π-stacking type.

The change in optical absorption is accompanied by a gelation process: 10 minutes after addition of the acid, a hydrogel capable of holding its own weight has formed. In order to investigate the underlying structural transition, SAXS measurements were made before and after the addition of the acid. In both cases, the full pattern could be fitted using parametric

models (see Fig. 3.3.4-1c and experimental section 5.3.2). In the precursor state, PBI2 forms H-type, π-π-stacked tetramers, as derived from the form-factor scattering. In the gelated state, two major differences in the scattering pattern occur: i) in the low-q regime ($q<2$ nm^{-1}) a Porod slope of -1.7 suggests the formation of a ribbon-like nanostructure and ii) in the higher-q regime ($q>2$ nm^{-1}) diffraction peaks reveal a crystalline nature of the nanostructure (see black peaks in Fig. 3.3.4-1c). CryoTEM images confirm these findings: ribbon-like structures are found as the main building-blocks of the hydro-gel (see Fig. 3.3.4-1d).

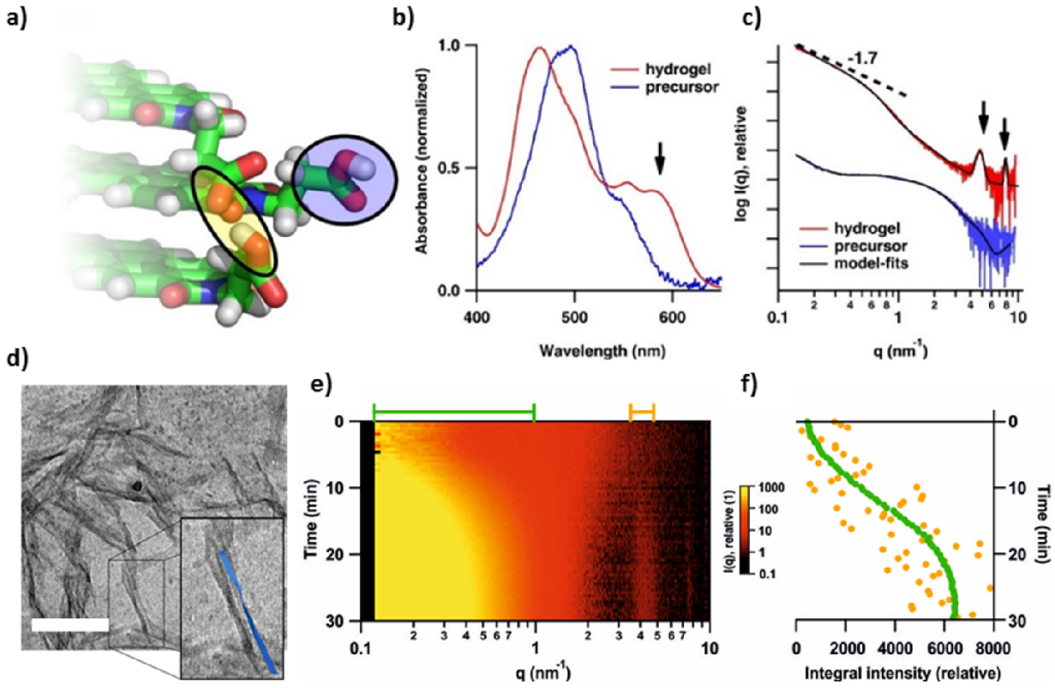

Fig. 3.3.4-1: Hydrogel formation of PBI2. a) Zoom-in of the PBI2 crystal-structure, showing the intra-columnar hydrogen-bonding between partially deprotonated carboxylic tail-groups. **b)** UV/Vis absorption of PBI2 before (blue) and after (red) the addition of 4M HCl. The black arrow denotes the peak, linked to J-Type stacking. **c)** SAXS patterns of PBI2 before (blue) and after (red) the addition of 4M HCl. The dashed line denotes the Porod-slope of $q^{-1.7}$, characteristic of for ribbon-like nanostructures. The black peaks indicate positions of the Bragg-reflections suggesting a crystalline nature of the nano-ribbons. **d)** CryoTEM image of the hydrogel. The white bar denotes 200 nm. **e)** Results of the *in-situ* SAXS experiments. The green and red brackets denote the interagl regions shown in **f**. **f)** Integral intensity calculated in different q-regimes. The behavior of the low-q (green) and Bragg-peak (orange) regions is similar, hence suggesting that the nano-ribbons are crystalline in nature. The time-scale was normalized to the onset of hydrogelation.

In order to see if crystalline-nature suggested by the diffraction peaks indeed corresponds to the witnessed nano-ribbons, *in-situ* SAXS measurements were made. Here, the PBI2 precursor solution was placed in a 1.5 mm capillary and the 4M HCl acid was added on top. The scattering patterns were then collected approx. 5 mm from the interface, where hydrogelation initiated approx. 40 min after acidification. As shown in Fig. 3.3.4-1e, the low-q intensity

increase (green region) as well as the appearance of the first diffraction peak (orange region) is witnessed. Comparison of the integral intensities over these regions (see Fig. 3.3.4-1f and section 5.3.2 for details) reveals that both features present the same reaction dynamic. Hence, the formation of the nano-ribbons (linked to the low-q regime) is directly connected to the "crystallinity" of the sample (linked to the Bragg reflections). From this, it can be concluded that the nano-ribbons are in fact crystalline in morphology.

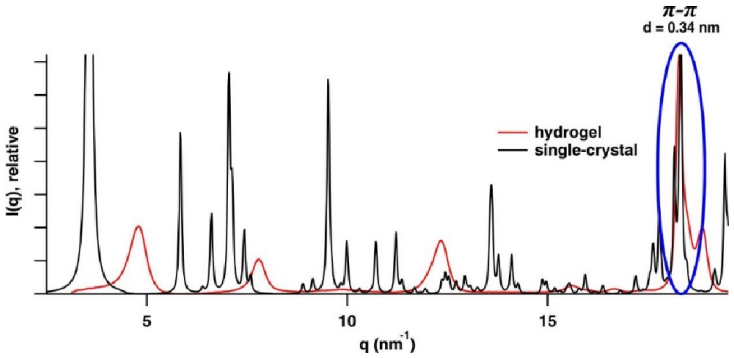

Fig. 3.3.4-2: XRD comparison of hydrogel and single-crystal. A detailed overlay of the wide angle scattering pattern of the hydrogel (red) and corresponding scattering pattern of single-crystal data (black) immediately identifies only one consistent structural feature: the strong peak at 18.28 nm^{-1} (blue circle) is indicative of the π-π-stacking distance between perylene cores within a single PBI1 column. In the angular regime between 2 < q <19 nm^{-1} no other similarities between the two scattering patterns are apparent.

In order to derive the detailed inter-molecular structure within the crystalline nano-ribbons, X-ray diffraction (XRD) measurements were conducted. Comparison of the hydrogel-pattern with the single-crystalline pattern (see Fig. 3.3.4-2) immediately shows that only the π-π-stacked nature is conserved in the hydrogel, while none of the other diffraction peaks may be linked. However, from the presence of the identical π-π-stacking peak in the hydrogel scattering, it can be concluded that the nano-crystalline columns prevail as building-blocks in the hydrogel. Indeed, all but the latter two reflections can be indexed using a two-dimensional oblique (P1) lattice with a = 2.188 nm, b = 1.367 nm, and γ = 36.14°, as shown in Fig. 3.3.4-3a, which relate to mean distances between these π-π-stacked columns. Using the π-π-stacked columnar motif of the single-crystal structure as building-block, the columnar cross-section only fits inside the hydrogel unit cell if both long axis are aligned parallel (Fig. 3.3.4-3b). The full structural arrangement then becomes apparent by multiplying the unit cell using its oblique dimensions. The resulting model compared to the single-crystalline structure is shown in Fig. Fig. 3.3.4-3b, revealing a similar structural motif in both cases: the columns appear to cross-link preferentially between the now protonated carboxylic groups. Yet, the distance

along this direction is identical, leaving polar channels for water to penetrate. In lateral direction, the oblique unit cell angle decreases from 54.78° to 36.14°, resulting in a linear alignment of neighboring imide groups (see inset in Fig. 3.3.4-3b). A cross-section of one a full nano-ribbon based on this model can be found in Fig. 3.3.4-3c.

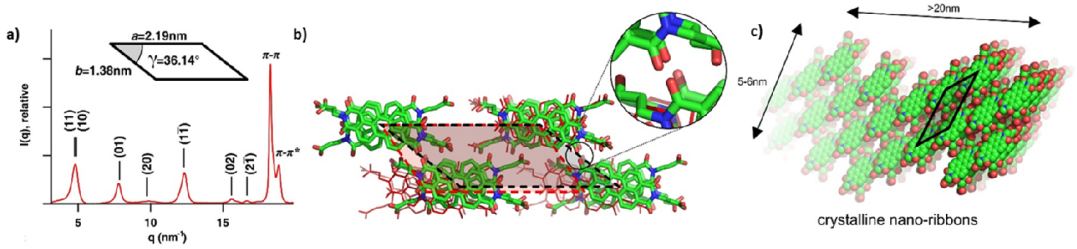

Fig. 3.3.4-3: Inter-molecular architecture of the PBI hydrogel. a) XRD pattern of the hydrogel: the sharp peaks correspond to the oblique unit cell (black inset) of π-π-stacked PBI2. **b)** Cross-sectional view of the unit cell within the hydrogel (black) compared to the single-crystalline motif (red). The magnification shows the now preferred alignment between the PBI1 carbonyl groups. **c)** Representation of the unit-cell (black) within the crystalline nano-ribbons that form during gelation process.

Infrared spectra confirm this arrangement: the peaks related to both the carboxylic and amidic C=O distances red-shift due to increasing peripheral interaction, such as hydrogen bonding (see Fig. 3.3.4-4a). This suggests hydrogen bonding between these moieties instead of electrostatic repulsion between the carbonyl oxygen atoms. Further confirmation of this model is found by CO_2 absorption measurements: imide-functionalized organic molecules are known to bind CO_2 at the carbonyl positions, forming semicarbonates.[213–215] This phenomenon is directly seen in the redox properties of the pigments and can therefore be probed by cyclic voltammetry (CV).[214,215] A CV of the precursor in under N_2 flux deaerated aqueous solution shows two reduction processes centered around –0.3 and –0.7 V vs. Ag/AgCl, which correlate to the reduction of the carbonyl moieties (see Fig. 3.3.4-4b). This redox activity disappears after purging the solution for 10 min with CO_2, which indicates the formation of the related semi-carbonate. The latter is not electrochemically active in the potential window between 0.2 and –0.8 V. The same measurements obtained of the hydrogel yield a strikingly different result (see Fig. 3.3.4-4c). The voltammograms are unaffected by the presence of CO_2 and show both under N_2 and CO_2 atmosphere a reversible redox couple centered on -0.3 V. This indicates that the imide groups are blocked by the close, intermolecular arrangement within the crystalline nano-ribbons, such that CO_2 cannot access the absorbing atomic sites.

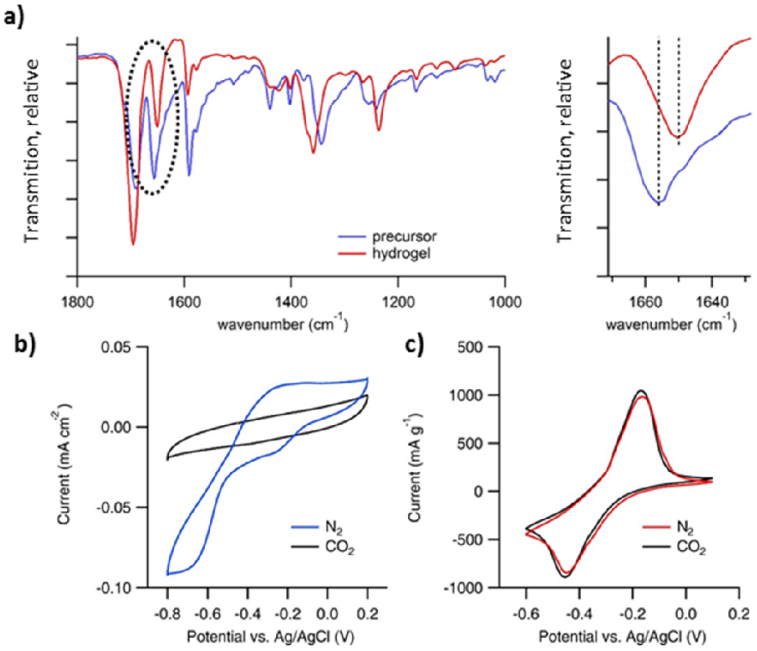

Fig. 3.3.4-3: Confirmation of the XRD-based model. a) AR-FTIR measurements of PBI2 before (blue) and after (red) the gelation process. The black dotted circle marks the region for the zoom-in shown on the right, focusing on the C=O carbonyl absorption peak. The red-shift occurring upon gelation is indicative of an increase in the peripheral interaction due to the close-packed nature of PBI2 within the crystalline nano-ribbons. **b)** Cyclic voltammograms of the PBI2 precursor solution when N2 purged (blue) and after 10 min purging with CO2 (black) at a glassy carbon working electrode. **c)** Cyclic voltammograms of the immobilized hydrogel under N2 (red) and CO2 atmosphere (black). All measurements were recorded at 50 mV s^{-1}.

Summarizing the findings above, the hydrogel consists PBI2 nano-ribbons with high crystalline order (see Fig. 3.3.4-3c). A crucial side effect of this crystallinity is that the nano-ribbons are encapsulated by the carboxylic chains. These chains cross-link via hydrogen bonds and are therefore responsible for the structural cohesion between nano-ribbons.

3.3.5 Long-range charge transfer – a structure/function correlation

The crystalline nature of the nano-ribbons is particularly important for long-range charge transfer as it enables charge-mobility along the π-π stacked columns.[209] However, this mechanism is only one-dimensional. Bulk-conductivity over all three dimensions therefore requires *lateral* charge transfer, that is between the π-π-stacked columns and further between the crystalline nano-ribbons. Since both, the π-π stacked columns as well as the crystalline nano-ribbons, are inter-connected via hydrogen-bonding, charge-transfer between two entities must occur via bridging sites. If this hypothesis is correct, absorbing protic media should be able to activate the hydrogen-bridging sites and therefore allow long-range charge-transfer.

In order to test this hypothesis, simple gas-sensing devices were fabricated by drop-casting of PBI2 hydrogel between two Au electrodes on a glass-substrate. The electrode spacing of 300 µm is unlikely to be bridged by a single hydrogel ribbon and thus this setup measures overall bulk-conduction including inter-backbone conduction. SEM and grazing incidence SAXS (GISAXS) measurements confirm that the hydrogel-characteristic nano-ribbons as well as the intermolecular motif are stable after drying (see Fig. 3.3.5-1)

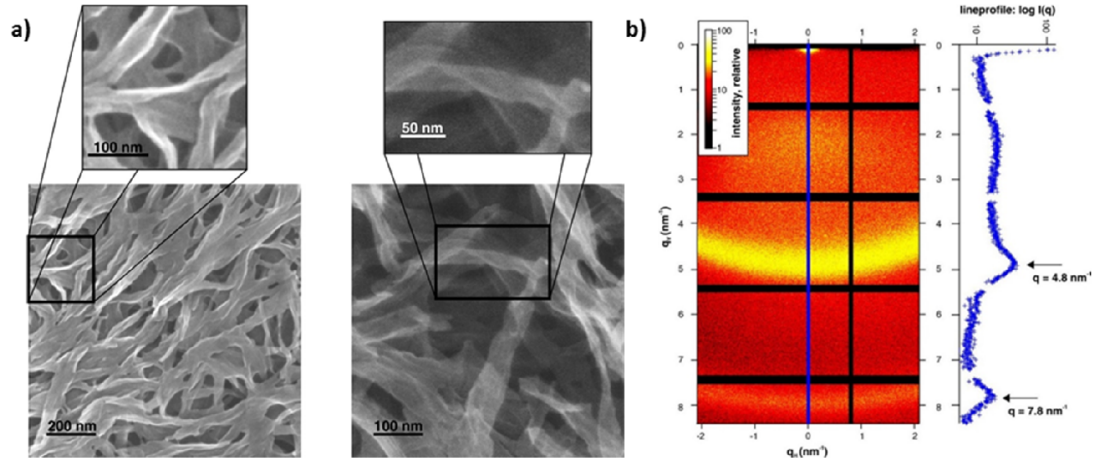

Fig. 3.3.5-1: Structural investigation of the PBI2 hydrogel in its dried state. a) Scanning electron microscopy (SEM) images of the dried hydrogel, confirming the presence of the nano-ribbons. **b)** Grazing incidence SAXS (GISAXS) image of the dried hydrogel, showing two diffuse diffraction rings. A vertical cut at q_H=0 nm^{-1} identifies the corresponding peak centers at 4.8 and 7.8 nm^{-1}, which is identical to the diffraction peaks found in the undried hydrogel (see Fig. 3.3.4-3a).

The gas-sensing devices were tested using a custom "gas-pulse" setup, which allowed deposition of H_2O vapor pulses as short as 100 ms. An illustration of the sample-geometry is shown in Fig. 3.3.5-2. Prior to the measurement, the sample was flushed for 10 min using N_2. In the dry state, the current through the hydrogel is as low as 2 pA at a bias of 2 V. When the sample was repeatedly exposed to 300 ms pulses, the current increased by nearly five orders of magnitude to 93.3 ± 3.3 nA (see Fig. 3.3.5-2a). Probing the sample with even shorter pulses of 100 ms led to a sharp rise in current within 10s of milliseconds over two orders of magnitude, followed by complete re-equilibration within 2 seconds.

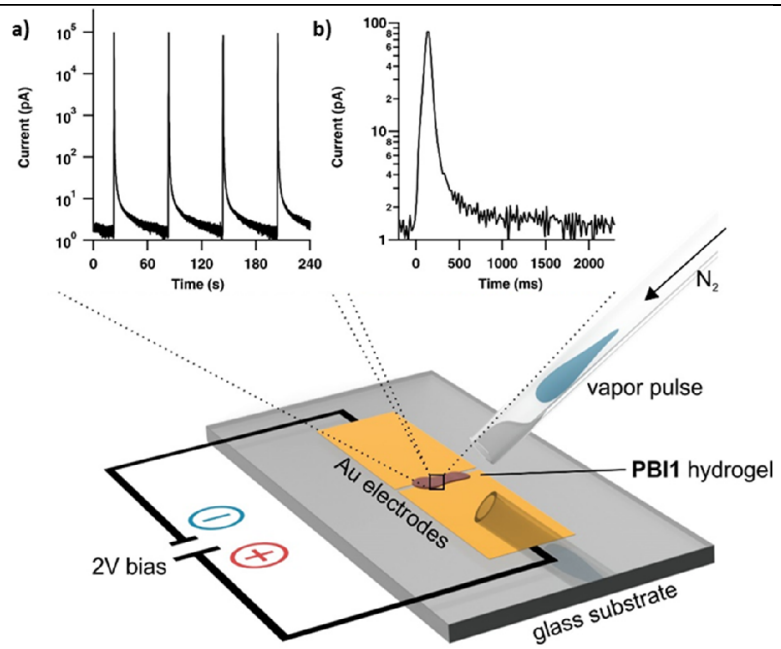

Fig. 3.3.5-2: Electric response of the dried hydrogel to H_2O vapor – a Schematic representation of the experimental setup. a) Electrical response after deposition of 300 ms pulses of saturated H_2O vapor, showing an increase of conductivity over 5 orders of magnitude. **b)** Time-resolved electrical response of a single 100 ms pulse of saturated H_2O.

This fast electrical response is attributed to the solvent-induced activation of the lateral inter-columnar charge transfer. Therefore, the previously determined carboxylic groups between the π-π-stacked columns are not only responsible for the structural cohesion, but also act as conduction bridges between nano-ribbons: water forms temporary hydrogen bridges between the nano-ribbons, allowing for charge transfer between them. Upon flushing the sample with N_2, the intercalated water is removed such that conduction between the nano-ribbons is suppressed. Hence, the detailed structural motif of PBI2 within the crystalline nano-ribbons determines the long-range charge-transfer capability of such dried hydrogels.

3.3.6 Summary & concluding remarks

In summary, the above work represents a structural cornerstone for the use of PBIs in aqueous solution. The use of x-ray and neutron scattering techniques, complemented with electron-beam imaging and optical absorption measurements allowed the formulation of a multi-length-scale structural model of PBI1 and PBI2. In both cases, strong hydrophobic nature of the planar perylene-cores drives the formation of π-π-stacked organic nano-cylinders. In case of PBI1, a clear dependence of the cylinder height on the molecular concentration is observed. In case of

PBI2, acidification forms a hydrogel consisting of nano-crystalline volume. Here, the carboxylic tail-groups are identified as structural and functional key positions, as pH dependent de/protonation causes intra- and inter-columnar hydrogen-bonding: the first induces an H- to J-type transition and therefore changes the system's optical properties, the second is responsible for the structural stability of the gel and enables long-range charge-transfer by forming temporary bridging sites between the nano-ribbons.

3.4 Nanostructure of Ru_4POM based water oxidation systems

See Appendix A5 and A6 for adapted reprints of the original publications.

3.4.1 Introduction

The inorganic Ru_4POM molecule is a promising water-splitting agent, where the catalytic reaction can be initiated by means of a reactive oxidizing agent. While oxidative salts, such as Ce(IV), would be sufficient to commence the reaction, it is much more appealing to use solar light as a driving force, hence pairing Ru_4POM with compatible photosensitizers. In such heteromolecular systems, the electrostatic nature of the anionic catalyst and cationic photosensitizer is thought to form charge-equilibrated, structural assemblies. Derived from transient absorption experiments, the occurrence of such supramolecular aggregates has a remarkable impact in the overall efficiency of the light activated cycle. In particular, Ru_4dend/Ru_4POM aggregation in 1:1 stoichiometry, is responsible for fast, reductive quenching of Ru_4dend triplet excited state by Ru_4POM, occurring in a hundred ps timescale [12b], and initiating the cascade of electron transfer events that ultimately lead to O_2 production with a quantum yield of 0.30 [12]. The first goal was hence set to investigate and understand the intermolecular nanostructure of existing Ru_4POM based water-splitting systems, using either $Ru(bpy)_3^{2+}$, Ru_4dend and PBI1 as photosensitizers.

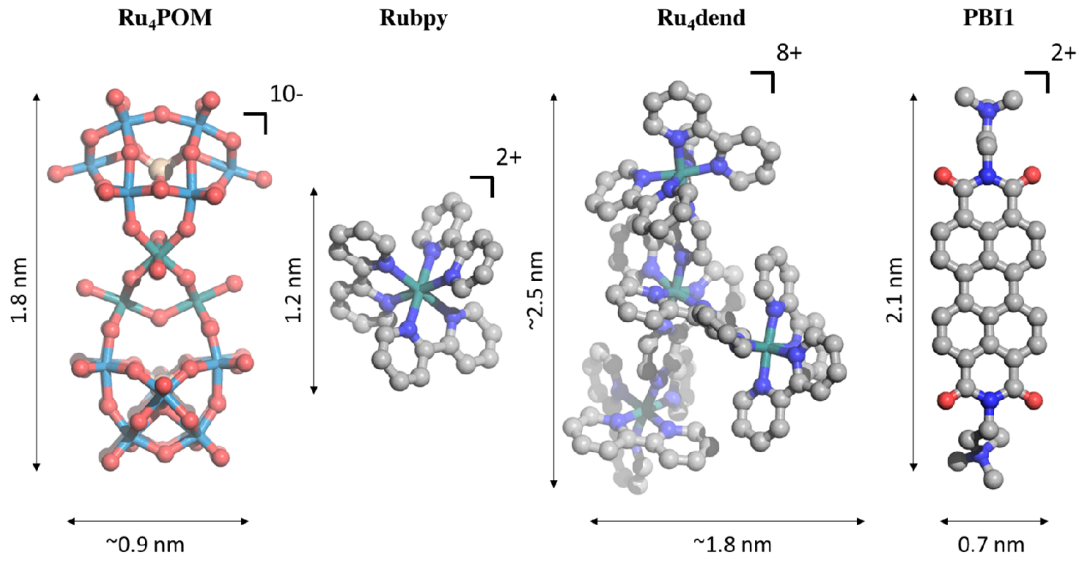

Fig. 3.4.1-1: Molecular building-blocks, and their relative charges and dimensions, used in this subsection.

The following subsections will focus on the determination of the nanostructure of hetero-molecular, Ru_4POM based water-oxidation systems. First, the known water-splitting systems Ru_4POM/Rubpy and Ru_4POM/Ru_4dend are investigated by means of TEM and SAXS, from which first insights on the disordered nature of such systems are gained. In a subsequent study, a new system involving the metal-free PBI1 as photosensitizer is studied, where the inter-molecular structure, particularly the corolla-like motif, presents a striking resemblance to the natural photosystem II.

3.4.2 Nanostructure of Ru_4POM/Ru(bpy) and Ru_4POM/Ru_4dend

Upon mixing of the constituents Ru_4POM/Rubpy (1:4) and Ru_4POM/Ru_4dend (1:1) in water, no particle formation or sedimentation was observed by eye. Nevertheless, association of Ru_4POM with Ru_4dend and Rubpy in 1:1 and 1:4 ratios, respectively, was suggested by means of conductometric titrations[16], and can be justified on the basis of the charge-balance provided by the cationic photosensitizer with respect to the Ru_4POM polyanion (see Fig. 3.4.1-1). The first attempt to derive information on the intermolecular structure of both systems was hence to obtain TEM images of the dried solution. As shown in Fig. 3.4.2-1, sub-micrometer sized aggregates with a disordered, rather random morphology are observed. In both cases, the disordered nature leaves pores in the order of < 50 nm, which allow solvent accessibility.

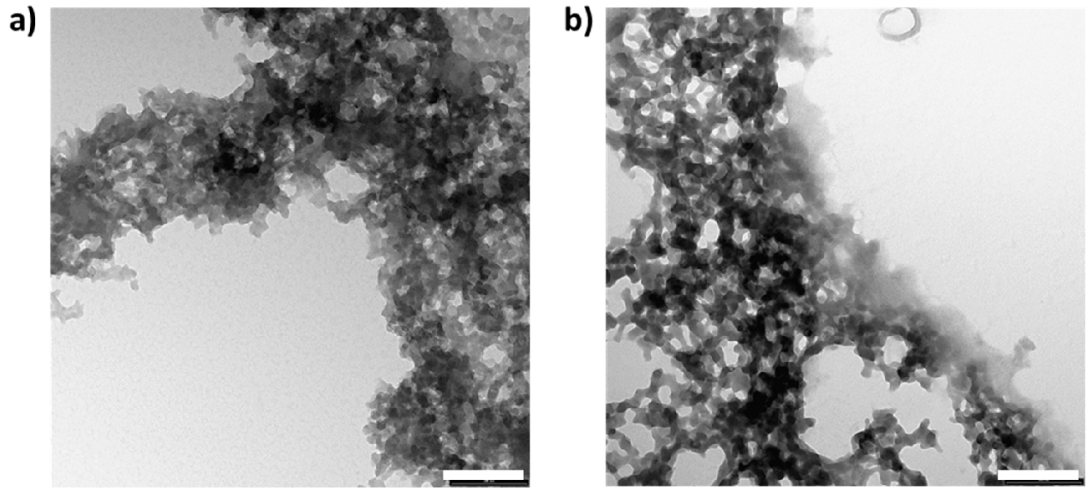

Fig. 3.4.2-1: TEM images of a) Ru_4POM/Rubpy (1:4) and b) Ru_4POM/Ru_4dend (1:1). The scale bar denotes 200 nm.

Such seemingly-disordered molecular systems are ideal candidates for SAXS as it gives information on the mean-intermolecular scale. In the X-ray scattering experiment, the

scattering intensity correlates quadratically with the electron density of an atom. In the context of such inorganic/organic hybrid systems, this means that the C- and N-components of the molecules are seemingly transparent compared to the heavy Ru and W atoms (see section 2.1.2 for details). This concept should be kept in mind in order to better understand the following interpretation.

The scattering from both systems is shown in Fig. 3.4.2-2. The first clear observation is the strong intensity-increase in the low-q regime, which is characteristic for aggregate-scattering. The slopes of the power-law scattering in the low-q regime of -2.98 (Ru_4POM/Ru_4dend) and -4.02 ($Ru_4POM/Rubpy$) suggest a more porous nanostructure in the case of Ru_4POM/Ru_4dend compared to $Ru_4POM/Rubpy$ (see dashed lines in Fig. 3.4.2-2). It should, at this point, be emphasized that the SAXS-sensitive *porosity* size-regime is within the order of 1 nm – Porod-slope derived information is only qualitative and mainly shows deviations from a homogenous, defect-free electron-density distribution. Hence, Ru_4POM/Ru_4dend appears to consist of a more defected packing than $Ru_4POM/Rubpy$. An explanation for the increased porosity might be the larger size of Ru_4dend with respect to Rubpy (see Fig. 3.4.1-1): the dendrimeric branches act as ‘‘spacers” between interacting Ru_4POM molecules, whereas in the case of the quasi-spherical and significantly smaller Rubpy, a more compact packing can be envisioned.

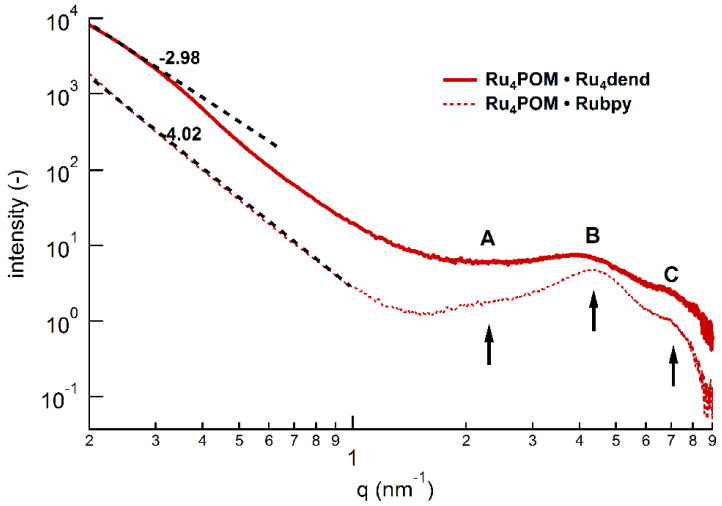

Fig. 3.4.2-2: SAXS patterns of $Ru_4POM/Rubpy$ (1:4) and Ru_4POM/Ru_4dend (1:1). The black-dotted lines represent the Porod fits in the low-q regime that reveal a more porous structure in the case of Ru_4POM/Ru_4dend. The black arrows indicate the correlation peaks (**A, B, C**) resulting from inter-molecular mean distances (see Table 3.4.2-1 for the exact d-spacings).

Table 3.4.2-1: Mean intermolecular d-spacings obtained from the correlation peaks. The values were obtained by full pattern refinement of three Gaussian peaks on a Porod slope of q^{-3}, where the d-spacings are calculated form the peak-positions via $d = 2\pi/q$. The errors (standard deviations) are specified in brackets.

	A, (nm)	**B,** (nm)	**C,** (nm)
Ru4POM/Rubpy (1:4)	2.56 (0.48)	1.47 (0.03)	0.95 (0.10)
Ru4POM/Ru4dend (1:1)	*3.06 (0.20)*	*1.64 (0.09)*	*0.97 (0.06)*
Ru4POM/Ru4dend (0.5:1)	2.89 (0.27)	1.57 (0.10)	0.91 (0.12)

Interestingly, both curves exhibit rather broad correlation peaks in the mid to high-q regime that correspond to intermolecular distances in the aggregate. Given the fact, that the scattering intensity is dominated by the heavy-atom content, the observed correlation peaks most likely represent mean distances between Ru4POM molecules inside the aggregates. The broad nature of the peaks immediately implies that the molecular arrangements are disordered in the sense that no coherent long range order exists, hence the terminology *mean* intermolecular-distance is used hereafter. The positions of the correlation peaks **A, B** and **C** fall in a similar region, for both Ru4POM/Ru4dend and the Ru4POM/Rubpy nano-hybrids (Fig. 3.4.2-2), implying an analogous structural motifs within both aggregates. A detailed look at the d-spacing values in Table 3.4.2-1 shows that both **A** and **B** peaks are found at higher values in the case of Ru4POM/Ru4dend, thus supporting the notion that the bulky tetraruthenium dendrimer increases the mean distance between the Ru4POM scatterers.

In order to better understand the coordination behavior, SAXS patterns were collected at a different mixing ratio of Ru4POM/Ru4dend = 0.5:1 (see Figure 3.4.2-3). Here, the low-q regime remains unaffected, pointing to the same meso-porous morphology as in the equimolar mixed sample. However, the intensities of correlation peaks **A** and **B** are reduced by approx. 25%, confirming the hypothesis that these scattering features correspond to a Ru4POM/Ru4dend conformation. Peak **C** is only slightly affected, suggesting that it is not directly related to the Ru4POM concentration.

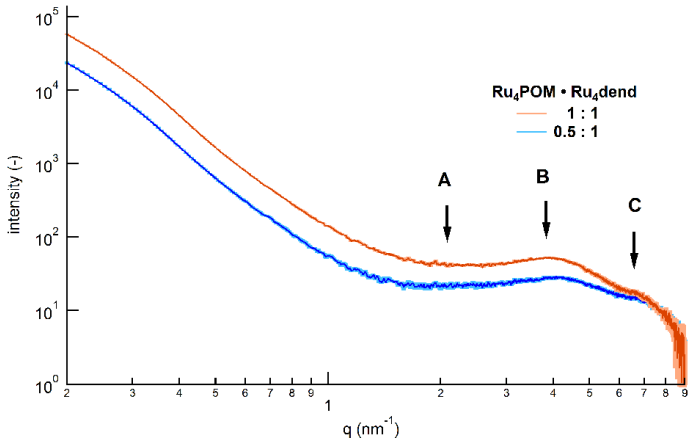

Fig. 3.4.2-3: SAXS patterns of Ru4POM/Ru4dend mixed in ratios 1:1 and 0.5:1. The correlation peaks are indicated by black arrows.

Before putting these observations into a molecular context, one has to consider that for the case of Ru4dend and Rubpy (even though less pronounced) a range of possible geometrical conformations may be found in the solute state. [143,168] Further, it has to be considered that the observed Porod slope of q^{-3} in the low-q regime is connected to a random, isotropic morphology (e.g. plate-like or fiber-like arrangement would have a slope of q^{-2} or q^{-1}, respectively). Hence, there exist no anisotropic alignment effects induced by the molecular arrangement. These observations together with the broad nature of the peaks are a clear indication that no long range order (larger than 2-3 nm) between the molecules exists (so only the first coordination shell appears to be similar). Accordingly, the observed correlation peaks in the scattering data have to be the result from a three-dimensionally disordered system, representing the spherically-averaged mean distance between the molecular components. Given the above considerations and comparing the approximate dimensions of the intra-molecular motifs of Ru4dend and Rubpy with the exact size of Ru4POM (see Fig. 3.4.1-1) shows the assignment of peaks **A** and **B** to a Ru4POM - Ru4POM arrangement with full or partial intercalation of the sensitizer, respectively.

3.4.3 Nanostructure of Ru4POM/PBI1

The available excitation-generated oxidation potential in the transient state of the photosensitizer is the thermodynamic initiator of the oxygen evolution energy cascade in hetero-molecular light-harvesting systems. In quantitative terms, Rubpy and Ru4dend, molecules that have successfully been paired with Ru4POM, exhibit a transient one-electron

reduction potential of 0.84 and 1.30 V vs SCE.[16,143,216] In the photo-generated transient-state, the metal free PBI1 exhibits an even stronger $PBI1^{*/2+}$ to $PBI1^{1+}$ reduction potential of 2.00 V vs SCE,[217,218] making it an attractive candidate as electron-scavenger. Based on these comparisons, a water-oxidizing system involving PBI1, Ru_4POM and persulfate as photo-sensitizer, molecular catalyst and sacrificial electron acceptor, respectively, was constructed.

Considering the respective charges of $PBI1^{2+}$ and Ru_4POM^{10-}, an equilibrated stoichiometry of Ru_4POM/PBI of 1 to 5 is suggested. Indeed, absorption titrations show a decrease of the PBI1 absorption maximum (at 500 nm) upon addition of Ru_4POM until the pivot point at Ru_4POM/PBI of 0.2 to 1 (equiv. to 1 to 5) (see Fig. 3.4.3-1a). At this mixing ratio, sedimentation of dark flakes is seen by eye after several hours, suggesting the formation of large-scale aggregates.

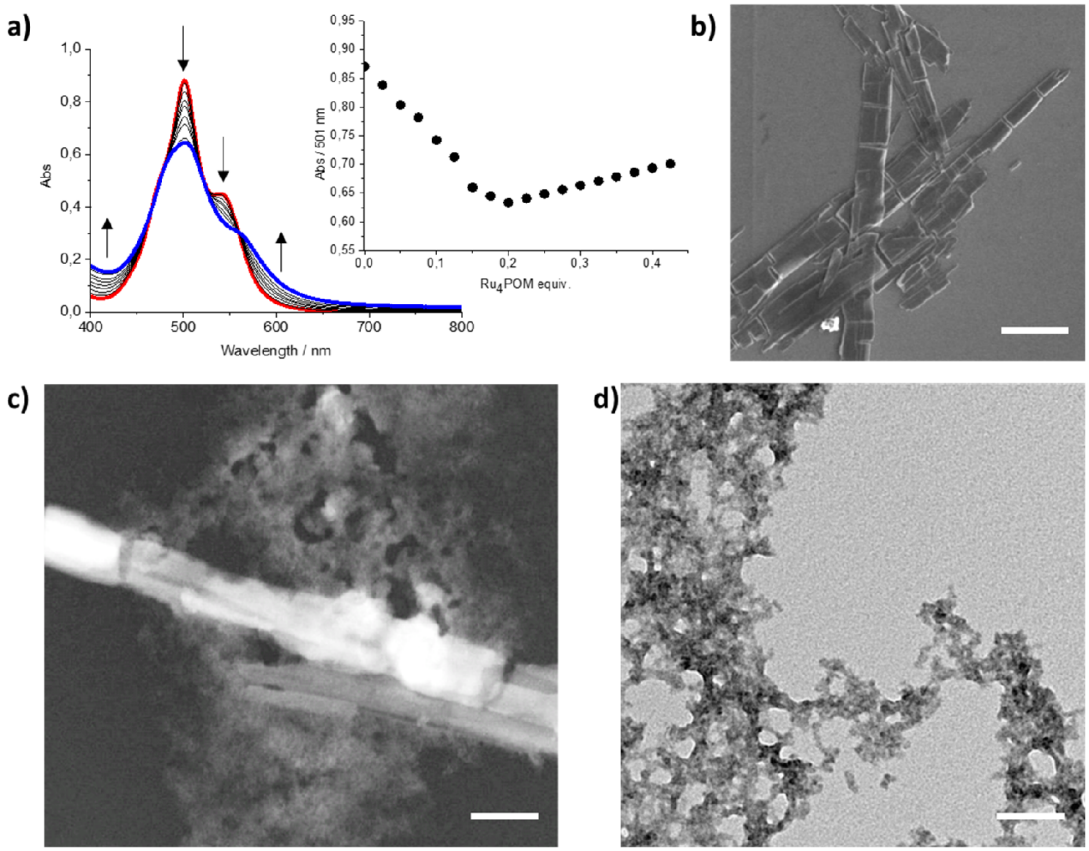

Fig. 3.4.3-1: Initial analysis of Ru_4POM/PBI1 (@pH 7, 20 mM PBS). a) UV/Vis titration of PBI (red) with increasing Ru_4POM concentration (blue line represents Ru_4POM/PBI=0.5:1). The inset shows the absorption at 501 nm as a function of Ru_4POM equivalents – a turning point at Ru_4POM/PBI=0.2:1 is observed. **b)** SEM image of the dried PBI1 precursor solution (the scale bar denotes 2 µm). **c)** SEM of the dried Ru_4POM/PBI = 0.13:1 solution, showing how Ru_4POM increasingly exfoliates the PBI1 crystals (the scale bar denotes 1 µm). **d)** TEM images Ru_4POM/PBI = 0.2:1 solution (the scale bar denotes 100 nm).

In order to investigate the morphology of Ru_4POM/PBI aggregates, SEM images of the dried solution were made (see Fig. 3.4.3-1b and c). Compared to the sheet/needle like structures witnessed in PBI1 (see Fig. 3.4.3-1b), addition of Ru_4POM destroys the highly ordered meso-structures: SEM images a conservatively mixed solution of Ru_4POM/PBI = 0.13:1 = 1:8 (see Fig. 3.4.3-1c) clearly shows exfoliation of the remaining preexisting PBI1 aggregates by Ru_4POM. More detailed TEM images (see Fig. 3.4.3-1d) show a highly porous nano-morphology, of which no further information on the intermolecular structure can be deduced.

Similar to the case of Ru_4POM/Rubpy and Ru_4POM/Ru_4dend, SAXS measurements of the hybrid system were performed to deduce structural information on the molecular level. As shown in Fig. 3.4.3-2, addition of Ru_4POM to the PBI1 precursor causes a strong increase in the low-q regime. In contrary to previous cases, a Porod slope of $q^{-1.9}$ is observed, suggesting the formation of 2D, plate-like nanostructures and hence anisotropic molecular alignment. A corresponding Guinier fit in this region estimates a plate-thickness of approx. 8.2 nm. Further addition of the persulfate sacrificial electron acceptor causes no change in the scattering pattern, implying structural stability of the nanostructure.

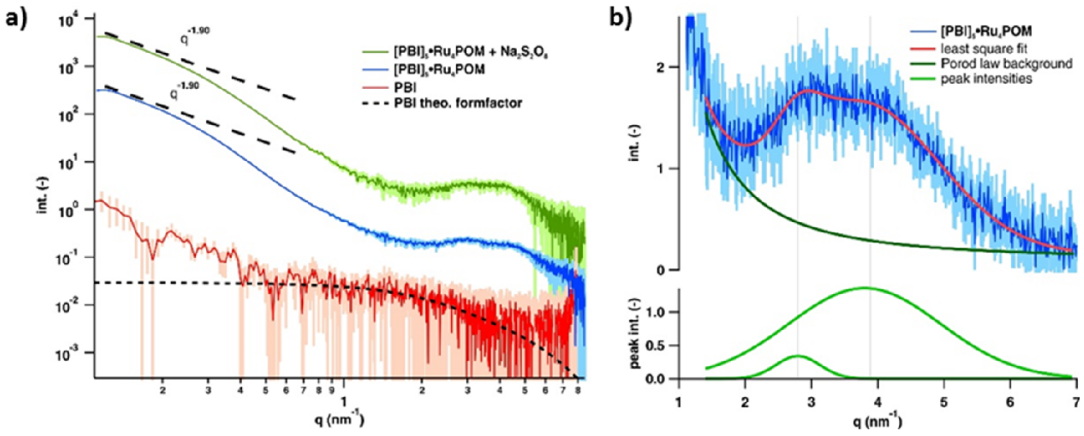

Fig. 3.4.3-2: SAXS analysis of Ru_4POM/PBI1 (@ph 7, 20 mM PBS). a) SAXS pattern of PBI1 (red), Ru4POM/PBI1 (blue) and Ru4POM/PBI1 + persulfate (green). **b)** Detailed peak-fitting results of Ru4POM/PBI1.

In addition to the low-q intensity increase, two broad correlation peaks are witnessed in the $2 < q < 7$ nm^{-1} regime. A detailed peak fit (see Fig. 3.4.3-1b) links these peaks to molecular d-spacings of 2.3 ± 0.3 nm and 1.7 ± 0.6 nm. Given that the peak widths are strikingly different in their respective widths, a property that directly correlates with the dimensions of the scattering entities, it can be assumed that the underlying structural dimensions are not connected.

Before drawing further conclusions from the scattering patterns, a few considerations have to be made. For one, similar to the cases of Ru_4POM paired with Rubpy and Ru_4dend, recorded intensity is dominated by the scattering of Ru_4POM, making PBI1 quasi transparent. Yet, and in sharp contrast to the previous systems, the exact dimensions of PBI1 are known, which allows deduction of a more detailed structural model. For the other, the strong electrostatic interactions between the anionic Ru_4POM and the cationic PBI1 strongly suggest the formation of a charge-equilibrated, super-molecular building-block, consisting of a central Ru_4POM^{10-} molecule encapsulated by five $PBI1^{2+}$ molecules.

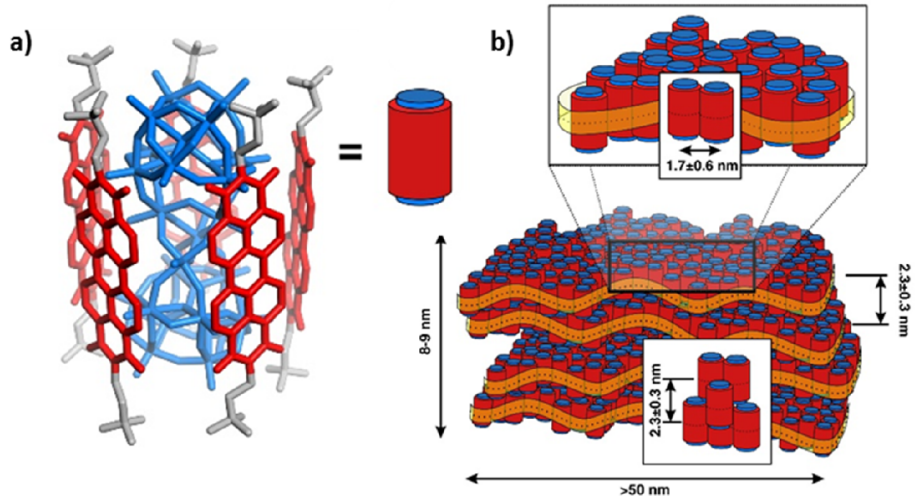

Fig. 3.4.3-3: SAXS based models of the Ru_4POM/PBI1 photosynthetic aggregates. a) Figurative representation of the Ru_4POM/PBI1 building-block [Ru_4POM = blue framework; PBI1 = red (aromatic body) and grey (alkylammonium tails) framework], shown as a core-shell cylindrical amphiphile [cartoon: PBI1 shell = red cylinder, Ru_4POM = blue cylinder]. **b)** Multi-scale model representation of the cylinders packing into stacked nano-lamellae, where the mean molecular out-of-plane distance corresponds to 2.3± 0.3 nm, causing the first correlation peak in the scattering data. The building-blocks are not necessarily confined into each lamella. The zoom-in shows a single lamellar plane, built from the parallel alignment of the cylinders with a mean in-plane distance of 1.7± 0.6 nm.

Comparing the molecular structures of Ru_4POM and PBI1 (see Fig. 3.4.1-1 and Fig. 3.4.3-3a) immediately yields that a d-spacing of 1.7 ± 0.6 nm can only be achieved by a Ru_4POM - Ru_4POM coordination with intercalation of a π-π-stacked PBI1 doublet (assuming a π-π-stacking distance of 0.3 nm) or possibly a single PBI1 molecule. However, the broad peak width related to this structural feature suggests a high degree of disorder (the size of the coherent scattering volume is approx. $2\pi/FWHM = 2.1\,nm$, where FWHM is the peak's full width half-maximum). As a consequence of this arrangement, an axial, parallel alignment of Ru_4POM and PBI1 can be expected (see Fig. 3.4.3-3b). Based on the quasi-cylindrical

geometry of Ru_4POM it is very likely that the observed 2D morphology of the nano-sheets is determined by this anisotropic alignment. The second correlation peak, corresponding to a d-spacing of 2.3 ± 0.3 nm, must therefore relate to the mean distance between lamellar layers of the parallel aligned Ru_4POM-PBI1-(PBI1)-Ru_4POM occurrences (see Fig. 3.4.3-3b). Interestingly, the size of the coherent scattering volume of this peak corresponds to approx. 8 nm, which is in agreement with the previously determined plate thickness.

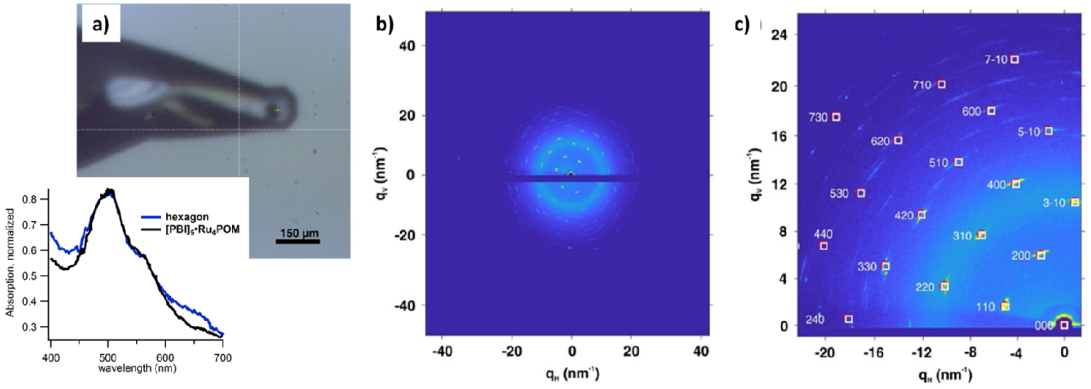

Fig. 3.4.3-4: XRD study of crystalized Ru_4POM/PBI1 hexagons. a) Microscopic image of the crystallized hexagon mounted on the goniometer tip (see yellow cross for position of the X-ray beam). The inset shows the UV/VIS spectrum of isolated hexagons compared to the solution measurement. **b)** X-ray diffraction pattern of the hexagon shown in **a,** aligned with the hexagonal cross-section perpendicular to the X-ray beam. **c)** Low-angle **z**oom-in of the x-ray pattern together with the indexed lattice peaks.

After several months of resting of the Ru_4POM/PBI1 solution, isolated crystals sediment, confirmed by their UV/Vis absorption fingerprint (see inset in Fig. 3.4.3-4a). These crystallites are hexagonal in shape, hence named *hexagons*, suggesting a high-degree of order. Yet, the hexagons are opaque, indicating no single-crystallinity (see Fig. 3.4.3-4a). Indeed, X-ray diffraction patterns of a single crystallite aligned with its hexagonal cross-section perpendicular to the X-ray beam shows a distinct diffraction pattern (see Fig. 3.4.3-4b). Manual indexing with subsequent least-square optimization[219] links the main reflections to a C2 (strained hexagonal) cell with approx. a = 1.5 nm and b = 2.0 nm (see Fig. 3.4.3-4c). Depending on the selected diffraction peak, a mosaicity of 10-15° is determined. Weaker other reflections are therefore likely the result of misaligned neighboring lattice planes where only the respective peak-tails are recorded. Hence, the hexagons consist of misaligned, single-crystalline domains, most-likely corresponding to strained-hexagonal arrangement of $Ru_4POM{\cdot}PBI1_5$ building-blocks.

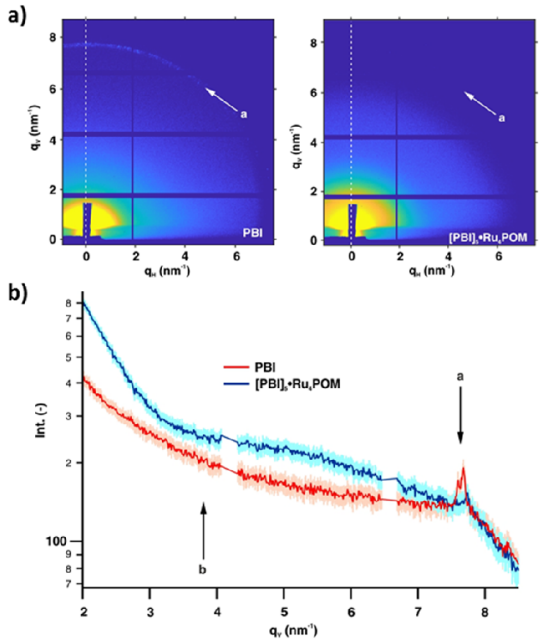

Fig. 3.4.3-5: GISAXS study of Ru4POM/PBI1 on WO3 electrodes. a) GISAXS images of PBI1 (left) and Ru4POM/PBI1 (right) measured at an incidence angle of 0.6°. The white arrows indicate the position of a PBI1 crystalline-phase-peak. **b)** GISAXS intensities along vertical cuts at q_H=0 nm^{-1} (see white dotted lines in **a**), where a distinct PBI inherent scattering peak (peak a) is registered, which is strongly reduced in the presence of Ru4POM. A broader correlation peak (peak b) arises corresponding to the Ru4POM–Ru4POM scattering centers.

In order to avoid the use of the sacrificial electron acceptor persulfate, the Ru4POM/PBI1 may also be transferred onto electrodes. Here, nanostructured WO3 was used as photo-anode. Upon functionalization of the electrodes with PBI1 alone, a distinct diffraction streak is seen in the out-of-plane direction (see peak a in Fig. 3.4.3-5) – a scattering feature indicating a crystalline degree of molecular order. Upon addition of Ru4POM, this scattering peak is strongly suppressed, indicating a Ru4POM induced molecular arrangement. In addition, a broad correlation peak, most likely corresponding to the Ru4POM–Ru4POM scattering centers, arises (see peak b in Fig. 3.4.3-5b). These results are coherent with the solution state of Ru4POM/PBI1: Ru4POM induces an exfoliation process of the preexisting PBI1 nano-crystallites and drives the formation of a hetero-molecular coordinated nanostructure.

3.4.4 Summary & concluding remarks

In summary, the above work represents the first structural investigation of hetero-molecular solar-light driven water-oxidation systems. In all three investigated systems, so Ru4POM paired with Rubpy, Ru4dend or PBI1, the formation of molecular-structured nano-aggregates

is observed. Interestingly, the geometry of the photosensitizer determines not only the dimensionality of the corresponding aggregates (3D and random in the case of Rubpy and Ru_4dend while 2D lamellae-like in the case of PBI1) but also the mean inter-molecular distances and hence the nano-porosity. In particular the last aspect deems to be critical in respect to accessibility of the catalytic reaction sites, such that a more porous packing enables better solvent diffusion through the nano-aggregates. Indeed, the more porous Ru_4POM/Ru_4dend system performs at significantly higher quantum yields (approx. 2 fold better) compared to the related Ru_4POM/Rubpy reference system.[16,18] In the case of Ru_4POM/PBI1, a structurally defined building block, the core-shell arrangement of a central Ru_4POM encapsulated by five PBI1 molecules, with a striking similarity to the natural oxygen evolving photosystem II, can be identified.

4 Conclusion

This work is the first attempt to study the inter-molecular nanostructure of organic/inorganic photosystems. The investigative technique critical in this respect is small angle X-ray scattering (SAXS), which allowed unprecedented insight in the selected photosystems under working conditions: in aqueous solution-state. Yet, prior to the experiments, methodological developments were inevitable. Given the initially clearly defined objectives, the following accomplishments were made.

First, a fitting-algorithm for the evaluation of SAXS data from elongated, fiber-like structures was successfully developed and implemented. The algorithm reconstructs the 3D structural-motif by means of optimizing a dummy atom (DA) configuration and simultaneously fitting the corresponding scattering pattern. A *projection scheme*, which projects the infinite nature of fiber-like systems onto a single structural building-block motif, was critical. A series of reconstructions from model and experimental data confirm applicability of the corresponding program. Future efforts will be directed towards including evaluation tasks prior to the fitting process, such that e.g. determination of the stacking-distance and estimation of a fiber-cross-section is done autonomously without user interaction.

Second, a simple mathematical approximation for the model-free evaluation of scattering data from weakly interacting systems was made. This specific task arose from the nature of dendrimer compounds, which possess a multitude of conformations in solution, such that parametric models fail to adequately describe the scattering pattern. Here, the pair distance distribution function (PDDF) is used to quantitatively estimate the aggregation number of such systems by simple comparison of integral values. This straight-forward approach yields a quick method to determine critical information from branched molecular systems, without the need of advanced modelling techniques.

Third, the nanostructure of a series of amphiphilic perylene-bisimides (PBI) in aqueous solution was characterized. In an initial investigation, the formation of π-π-stacked multimers is observed, where the number of PBIs involved in each stack may be controlled by adjusting the concentration. Subsequently, the formation of a PBI hydrogel by pH shock was studied: fast acidification of the solvent induces the formation of crystalline PBI nano-ribbons which act as a structural and electronic backbone of the hydrogel. This crystalline nature is critical

not only for the mechanical properties of the gel, but also for long-range conductivity via inter-backbone charge transfer at H-bond activated binding sites. In the future, the focus is set on the charge-transfer interface: foreseen transient-absorption coupled with transient-scattering experiments will allow us to study how excitons and charge-separated states undergo inter-backbone transfer.

Fourth, the nanostructure of Ru_4POM paired with known photosensitizers was studied. An initial investigation on the two reference cases Ru_4POM /Ru-bipyridine and Ru_4POM /Ru-dendrimer showed the formation of disordered, porous nano-aggregates, where the photosensitizers intercalate between neighboring Ru_4POMs. Interestingly, the latter system of Ru_4POM /Ru-dendrimer exhibits higher porosity such that increased solvent accessibility might be the cause for the significantly higher energy-conversion quantum yield. A further study was then focused on the new water-oxidation system Ru_4POM /PBI. Here, SAXS data revealed the formation of paracrystalline 2D nano-lamellae. The structural building block, consisting of a centered Ru_4POM encapsulated by approx. 5 PBI molecules, was found in the solution state and when immobilized on electrochemical devices. Most interestingly, this structural motif shows a striking resemblance to the natural photosystem II and might therefore be seen as the first artificial and structural analogue. Also in this case, pump-probe scattering experiments are foreseen in the future, which will capture structural transitions of the catalytic water-splitting process on the molecular level.

The findings resulting from this work are of diverse interest for the surrounding scientific communities. For one, the methodological advancements, particularly the possibility to reconstruct the structural motif of elongated structures from solution scattering data, will find appeal in many areas, including inter-molecular chemistry, biochemistry and pharmaceutical research. Software dissemination is commencing and so far the corresponding program SasHel has found positive resonance in the community. For the other, the success of using SAXS to study the nanostructure of hybrid inorganic/organic photoactive systems has sparked new ideas in the collaborative framework: next efforts will be directed towards i) controlling the intermolecular motif with the ultimate goal to build ordered frameworks with tunable accessibility of the catalytic reaction sites and ii) forming an antenna-like hierarchical network such that a single molecular reaction center is fueled by multiple light-absorbing antenna units. This will allow to reach the full catalytic potential of similar water-splitting systems while at the same-time minimizing the use of precious noble-metal compounds.

5 Experimental

5.1 Materials

All materials used in this thesis were synthesized by collaborating partners, which are accredited respectively. The reactants were purchased from Sigma-Aldrich or Arcos and were used without further purification/alteration.

PBI1 was synthesized by F. Rigodanza and Z. Syrgiannis (University of Trieste, Italy) according to the literature.[93,220] In detail, 100 milligrams of perylene-3,4,9,10-tetracarboxylic bisanhydride were suspended in dry DMF (5 mL) with 2 equiv. of N,N-dimethyl ethylene diamine in a pressure-tight microwave tube. The suspension was sonicated for a few minutes before heating under microwave irradiation at 50W for 10 min. Five cycles. The maximum temperature was set at 200 °C. After cooling, the color of the medium turned dark red and the mixture appeared more homogeneous. Fifty milliliters of 1 M NaOH were added to the starting material and stirred for 20 min. The precipitate was filtered and washed thoroughly with water until pH neutralization and dried in vacuum. For the methylation of the tertiary amines, the precursor diamine (0.25 gr, 0.46 mmol) and MeI (40 mmol) were solubilized in toluene (20 mL) and the mixture was refluxed for 5 h. The solution was cooled to r.t. and the precipitate was filtered and washed with Et_2O (2 × 30 mL). The resulting solid was dried in vacuum to afford the iodine salt of 1 (0.32 gr, 98%) as a dark red powder.[220] The chemicals were purchased from Acros and used without any further purification. The PBI1 was dissolved in deionized water in different concentrations. [220]

PBI1-Br$_2$ was synthesized by F. Rigodanza and Z. Syrgiannis (University of Trieste, Italy) according to the literature.[93,220] In detail, 100 mg of bisbrominated perylene-3,4,9,10-tetracarboxylic bisanhydride were suspended in dry DMF (5 mL) with 2 equiv of the corresponding amine and 1 mL of acetic acid in a pressure-tight microwave tube. The suspension was sonicated for a few minutes before heating under microwave irradiation at 60W for 10 min. The maximum temperature was set at 200 °C. After cooling the color turned dark red and the mixture appeared more homogeneous. 50 mL of NaOH 1 M was added to the

starting material and stirred for 20 min. The precipitate was filtered, washed abundantly with water until pH neutralization, and dried in vacuum. [220]

PBI2 was synthesized by F. Rigodanza and Z. Syrgiannis (University of Trieste, Italy) according to the literature,[93] using the following protocol: 100 mg of perylene-3,4,9,10-tetracarboxylic bisanhydride were suspended in dry DMF (5 mL) with 2 equiv. of *β*-alanine in a pressure tight microwave tube. The suspension was sonicated for few minutes before heating under microwave irradiation at 60 W for 10 min. 10 cycles. Max T was set at 200 °C. After cooling, the color turned to dark red and the mixture appeared more homogenous. To the mixture, 50 mL of KOH 10% aq. solution was added and solution was stirred for 2h. The precipitate was filtered and washed abundantly with water until pH neutralization and dried using a vacuum pump.[93]

Rubpy was purchased from Sigma Aldrich as the dichloride, hexahydrate salt and used without further purification/alteration.

Ru$_4$dend was synthesized by F.Puntoriero (University of Messina, Italy) according to the literature.[143] In short, a mixture of [Ru(2,3-dpp)$_3$](PF$_6$)$_2$ (0.036 g, 0.032 mmol) and Ru(bpy),CI$_2$·H$_2$0 (0.057 g, 0.097 mmol) in anhydrous ethanol (1 5 mL) was refluxed for 48 h. To the cooled solution was added an excess of solid NH$_4$PF$_6$, and the resulting purple solid was recrystallized several times from acetonitrile/ethanol, washed with ethanol and diethyl ether, and dried in vacuo (70%).[143]

Ru-dend and Os-dend were synthesized by A.Arrigo and F.Puntoriero (University of Messina, Italy) according to the literature.[221] **Ru-dend:** To a solution of (Ru[(2,3-dpp)Ru(bpy)$_2$]$_2$Cl$_2$)(PF$_6$)$_4$ (0.116 g, 0.057 mmol) in 2:1 (v/v) methanol/water (4 mL) was added solid AgNO$_3$ (0.019 g, 0.1 12 mmol). After 2 h of stirring at room temperature [Ru(2,3-dpp)$_3$](PF$_6$), (0.0206 g, 0.019 mmol) and ethylene glycol (4 mL) were added, and the mixture was refluxed for 48 h. After removal of AgCl by repeated centrifugation, an excess of solid NH$_4$PF$_6$ was added to the mother liquor and the cyclamen solid thus obtained filtered out. The product was purified by size exclusion (chromatography) on Sephadex G-25 (acetonitrile eluant). From the eluate the product was recovered as a cyclamen powder by addition of ethanol and partial evaporation in vacuo.[221] **Os-dend:** The synthetic procedure was analogous to that used for Ru-dend: employed quantities, (Ru[(2,3-dpp)Ru(biq)$_2$]$_2$Cl$_2$)(PF$_6$)$_4$ (0.053 g,

0.022 mmol); 95% ethanol (3 mL); $AgNO_3$ (0.0073 g (0.044 mmol); $[Os(2,3\text{-dpp})_3](PF_6)_2$ (0.0085 g, 0.007 mmol); and ethylene glycol, 3 mL.[221]

Ru_4POM was synthesized by F.Rigodanza (University of Trieste, Italy) according to the literature.[185] In short, 262 mg (0.359 mmol) of $K_4Ru_2OCl_{10}$ were dissolved in 30 ml of deionized water; 1 g (0.336 mmol) of K_8 γ-$SiW_{10}O_{36}\cdot 12H_2O$ was then added. The dark brown solution has a pH = 6.2, and it is kept at 70°C for 1 h; after heating the pH is 1.8, and the solution is filtered. Excess of CsCl (4.4 g, 26.1 mmol) is added to precipitate the product as the Cs salt, which is then washed three times with 2-3 ml of cold water.[185]

5.2 Methods

CryoTEM images were recorded with a Gatan system mounted on a Tecnai12 electron microscope from FEI Company equipped with a LaB6 filament operating at 120 kV. Electron micrographs were recorded on a Gatan Bioscan CCD 1kx1k camera. The samples were prepared using manual preparation method: After applying the sample to the EM support grid (holey carbon film on copper grid) the excess has been carefully blotted away with a small piece of filter paper. Afterwards the TEM grids were plunged into liquid ethane as fast as possible to prevent the formation of ice-crystals. Finally the grids were stored in liquid nitrogen until they were investigated within the microscope.

DFT calculations of PBIs were preformed in collaboration with L.Đorđević (University of Trieste, Italy) according to the following: The geometries of the dimers were optimized by dispersion-corrected DFT according to Grimme's PBEh-3c[222] approach implemented in ORCA 4.0.1.[223] The UV/Vis spectra were calculated using the long-range corrected ωB97X[224] functional in ORCA 4.0.1. First, the models from experimental studies were used to aid the initial conformer search (using PM7 implemented in MOPAC).[225] In the next step, the dimers were optimized using the Grimme's PBEh-3c7 approach in ORCA 4.0.18, which has been reported to give good geometries for supramolecular complexes, including PBI dimers.[226] Finally, the 3-carboxyropyl chains were replaced with a methyl group and re-performed the calculations. This last step was necessary since, during rounds of DFT calculations, tightly bound dimers (with H-bond network, with one -COOH from a dimer accepting the H-OOC- and donating a H-bond with the O=C- from the other PBI) or rotationally displaced dimers in

case of all carboxy groups (the calculations had to ignore the solvated triethylammonium counter ions, which would require molecular dynamics calculations) yielded improbable geometries. The same DFT calculations were carried out using the CPCM solvation model (water) implemented in ORCA - no significant differences in geometries were found. For each dimer, the vertical excitation energies was then calculated using the long range corrected ωB97X9,[227] density functional, with the 6-31G** basis-set.[228] This functional was used to correctly describe the charge-transfer excitations, often not done in other density functionals.[226,229] The results from the TD-DFT calculations were then used to predict optical absorption spectra, which include a 0.7 eV rigid downward shift due to overestimated excitation energies for this range-separated functional.[226]

Electrochemical measurements were performed by means of cyclic voltammetry, employing a standard three-electrode setup in an air-tight glass cells with separate gas inlet and outlet through an oil-filled bubbler. In all cases, Pt and Ag/AgCl were used as counter and reference electrode, respectively. The voltammograms were recorded using an SP-150 potentiostat (Biologic, France) with a scan rate of 50 mV s^{-1}. In case of the PBI2 precursor measurements, 1 mL precursor solution was mixed with in 3 mL 0.1 M $NaSO_4$ and a 3 mm diameter glassy carbon was used as working electrode. In case of the PBI2 hydrogel, the working electrode was made by immobilizing 250 µl of the final hydrogel between two pieces of carbon paper (Freudenberg, H2315). 0.1M $NaSO_4$ was equally used as electrolyte. The cell was either purged with N_2 or CO_2.

GISAXS measurements were performed at the Austrian SAXS beamline of the electron storage ring ELETTRA[230] using a photon energy of 8 keV. The beamline setup was adjusted to a sample to detector distance corresponding to the accessible q-range. A secondary vertical beamstop was used for detector safety, resulting in an anisotropic accessible q-range. All images were recorded using the Pilatus 1M detector (DECTRIS Ltd., Baden-Daettwil, Switzerland) with multiple exposures of at least 10 seconds each per sample to check for radiation damage. Reference patterns to calibrate the q-scale were collected of silver-behenate (d-spacings of 5.838 nm). The incidence angle was estimated from the position of the Yoneda peak. The image calibration and the calculation of the vertical slices were conducted using the NIKA2D software package.[231] All presented data were corrected for fluctuations of the primary intensity.

IR Spectra were measured on Bruker ALPHA spectrometer in ATR mode by simple drop-casting of the solutions.

SAXS measurements were performed at the Austrian SAXS beamline of the electron storage ring ELETTRA using a photon energy of 8 keV.[230] The beamline setup was adjusted to a sample to detector distance corresponding to the accessible q-range. All images were recorded using the Pilatus 1M detector (Dectris, Switzerland). For each sample, multiple exposures of at least 10 seconds per sample were made in order to check for radiation damage. Reference patterns to calibrate the q-scale were collected of silver-behenate (*d*-spacings of 5.838 nm). All solution-scattering measurements were done using a 1.5 mm quartz flow cell capillary. The radial averaging and the image calibration were conducted using the FIT2D software.[232] All presented data was corrected for fluctuations of the primary intensity and the corresponding background has been subtracted from each solution scattering pattern.

SEM images were taken on a Tescan MIRA 3 microscope operated with 30 kV electron beam energy. Polished and acetone cleaned Si wafers were used as substrates. The samples were dried for 30 minutes under pure N_2 conditions to remove all water.

Single Crystal XRD was performed at the X-ray diffraction beamline (XRD1) of the Elettra Synchrotron, Trieste (Italy). Crystals were dipped in NHV oil (Jena Bioscience GmbH) and mounted on the goniometer head with a nylon loop. Complete datasets were collected at 100 K (nitrogen stream supplied through an Oxford Cryostream 700 - Oxford Cryosystems Ltd., Oxford, United Kingdom) through the rotating crystal method. Complete datasets may have been obtained merging different data collections done on the same crystal, mounted with different orientations. Data were acquired using a monochromatic wavelength as specified in Table 5.4-1 on a Pilatus 2M hybrid-pixel area detector (DECTRIS Ltd., Baden-Daettwil, Switzerland). The diffraction data were indexed and integrated using XDS. Semi-empirical absorption corrections and scaling were performed on datasets, exploiting multiple measures of symmetry-related reflections, using SADABS program. The structures were solved by the dual space algorithm implemented in the SHELXT code. Fourier analysis and refinement were performed by the full-matrix least-squares methods based on F^2 implemented in SHELXL-2014. Thermal motion and geometric restrains on bond lengths, angles (DFIX, DANG, FLAT and SIMU) have been used for disordered fragments (triethylammine molecule and a carboxylic lateral group). Hydrogen atoms were included at calculated positions with isotropic $U_{factors} = 1.2 \cdot U_{eq}$ or $U_{factors} = 1.5 \cdot U_{eq}$ for methyl and hydroxyl groups (U_{eq} being the equivalent

isotropic thermal factor of the bonded non hydrogen atom). The Coot program was used for structure building.

UV/VIS Absorption measurements were carried out on an Agilent Cary60 spectrometer. High-concentration samples (>1mM) were placed between two mica-foils with 100 µm Kapton-foil spacer in between. Low-concentration samples (>1mM) were measured in Hellmanex quartz cuvettes with 1.5 or 10 mm optical path length.

Vapour response measurements were carried out using a custom-built humidity setup. Substrates were prepared by depositing 40 nm Au on 15 nm Cr electrodes onto glass (previously cleaned in piranha solution) under clean-room conditions. The effective distance between the electrodes was 300µm. After cleaning the substrates with isopropanol, 100 µl of the PBI2 gel were drop-casted between the electrodes and dried for 2 hours under N_2 atmosphere. During the measurement, samples were kept under continuous N_2 flow (2 L/min). Vapour pulses were generated using a function generator (Highland P400) controlling gas-flow valves to briefly redirect the N_2 flow into a container with saturated solvent vapour such that only small vapour pulses arrive directly at the sample. All measurements were conducted at both +2 and –2V to ensure repeatability and avoid possible mass-transport effects. The current was measured using a 4-probe setup directly placed on the Au electrodes (Agilent B1500 Semiconductor Device Analyser).

XRD measurements were performed at the X-ray diffraction beamline (XRD1) of the Elettra Synchrotron, Trieste (Italy) using a photon energy of 12.4 keV. The beamline setup, the sample to detector distance, was adjusted corresponding to the required resolution. All images were recorded using the Pilatus 2M detector (Dectris, Switzerland) with at least three exposures per sample to check for radiation damage. Reference patterns to calibrate the q-scale were collected of Lanthanum-hexaborid LaB6 NIST standard. The samples were mounted onto the goniometer head inside a nylon or kapton loop. For “powder-patterns, the sample was rotated by 360° during each exposure while maintaining 100 K (nitrogen stream supplied through an Oxford Cryostream 700 - Oxford Cryosystems Ltd., Oxford, United Kingdom).

5.3 SAXS Model functions

5.3.1 Fitting of PBI1

The scattering intensity $I_{calc}(q)$ for both theoretical models presented in subsection 3.3.3 was calculated according to

$$I_{calc}(q) = a * F(q) * S_{SHS}(q) + I_{Porod}(q) + BG \qquad (5.3.1\text{-}1)$$

where a denotes an intensity scalar, $F(q)$ denotes the form-factor scattering, $S_{SHS}(q)$ denotes the structure-factor contribution, $I_{Porod}(q)$ denotes the Porod-contribution resulting from *large scale* aggregates and BG denotes a constant background offset. In case of the dimeric scattering, the theoretical form-factor $F(q)$ was calculated numerically from the molecular dimer model shown in Fig. 3.3.3-2a using CRYSOL.[54] In case of the π-π-stacked PBI1 cylinder, a core-shell model as depicted in scheme Fig. 5.3.1-1 was used. If such a geometry is chosen, the form-factor scattering-intensity $F(q)$ can be calculated according to the literature[36] whereas the corresponding fitting parameters are explained graphically in Fig. 5.3.1-1.

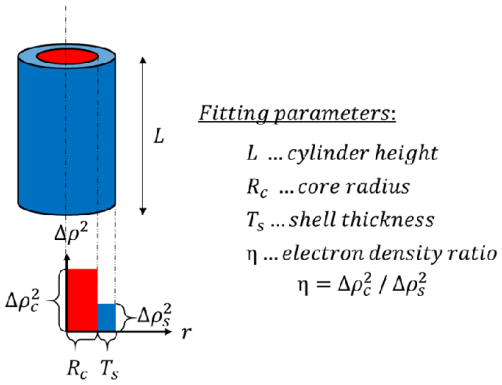

Fig. 5.3.1-1: Graphical illustration explaining the fitting parameters used for the calculation of the form-factor scattering of the π-π-stacked PBI1 cylinder.

In the case of the 20 mM PBI1 sample, *sticky-hard-sphere* potential was used to describe the interaction term between the π-π-stacked aggregates. A graphical overview of the underlying potential $U(r)$ between particles separated by a given distance r is depicted in scheme Fig. 5.3.1-2. The structure-factor $S_{SHS}(q)$ corresponding to this model can be calculated analytically according to the literature.[212,233]

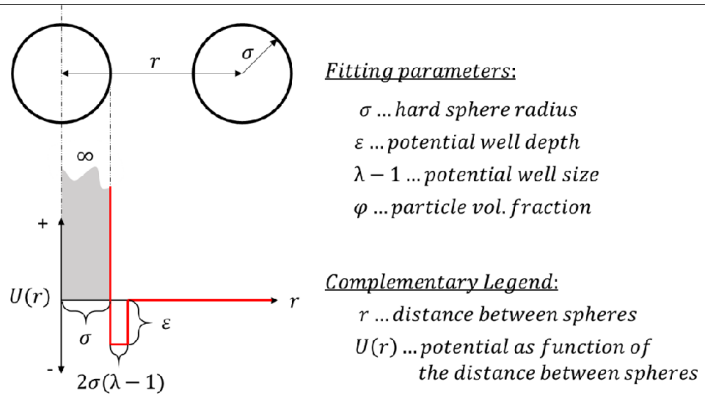

Fig. 5.3.1-2: Graphical illustration explaining the fitting parameters used for the calculation of the *sticky-hard-sphere* structure factor. The red line describes the potential $U(r)$ as a function between two particles separated by a given distance r.

The experimental scattering curves of both, the 0.6 and 20 mM, PBI1 samples present a low-q ($q < 0.5\ nm^{-1}$) increase, characteristic of large-scale aggregate formation beyond the resolution limit of SAXS.[34] Hence, a Porod contribution according to

$$I_{Porod}(q) = c_p * q^{-4} \tag{5.3.1-2}$$

was added to describe this intensity increase. In this formalism, only the absolute scalar c_p is optimized throughout the fitting process. All parameters were optimized by least-square fitting the corresponding models to the experimental scattering intensity. The final results as well as the weighted least-square value χ^2 as a measure for *goodness-of-fit* are shown in Tables 5.3.1-1 & 2.

Table 5.3.1-1: Fitting results corresponding to the model shown in Fig. 3.3.3-2, describing the SAXS pattern recorded from PBI1 at 0.6 mM.

Parameter	$\boldsymbol{a}$ [−]	$\boldsymbol{c_p}$ [−]	$\boldsymbol{BG}$ [−]	$\boldsymbol{\chi^2}$ [−]
Value	1.240 ± 0.013	0.035 ± 0.001	0.031 ± 0.001	1.302

Table 5.3.1-2: Fitting results corresponding to the model shown in Fig, 3.3.3-2, describing the SAXS pattern recorded from PBI1 at 20 mM. As there exists a correlation between the potential well size λ and its depth ε, λ was kept fixed at 1.1.

Parameter	$\boldsymbol{a}$ [−]	$\boldsymbol{L}$ $[nm]$	$\boldsymbol{R_C}$ $[nm]$	$\boldsymbol{T_S}[nm]$	$\boldsymbol{\eta}$ [−]	
Value	11.52 ± 0.02	3.88 ± 0.02	0.42 ± 0.01	0.58 ± 0.02	5.42 ±0.56	
Parameter	$\boldsymbol{\sigma}$ [−]	$\boldsymbol{\varphi}$[−]	$\boldsymbol{\varepsilon[k_BT]}$	$\boldsymbol{c_p}$ [−]	$\boldsymbol{BG}$ [−]	$\boldsymbol{\chi^2}$ [−]
Value	**4.04**	**0.007**	**25.5 7**	**0.05**	**0.011**	**1.021**
	± 0.01	**± 0.0003**	**± 0.18**	**± 0.002**	**± 0.002**	

5.3.2 Fitting of PBI2

The scattering intensities $I_{calc}(q)$ for the theoretical models were calculated according to two formalisms, which will be addressed separately. For the in-situ experiments capturing the transition from precursor to hydrogel, the integral intensity in a given regime $q_{min} < q < q_{max}$ was calculated calculate according to $I_{Int} = \int_{q_{min}}^{q_{max}} I(q)\, dq$.

In case of scattering from the precursor solution, first, the mean number of PBI1 molecules involved in the π-π-stacked aggregates was determeined: PBI1 molecules, previously determined from the single-crystal data, were stacked on top of each other with respective 45° degree twist. From these models, the theoretical scattering patterns were calculated using CRYSOL.[54] As seen in, Fig. 5.3.2-1, best agreement is found for the case of PBI1 stacked tetramers. However, it should be noted that in fact a distribution of linear aggregates will be present in solution – the tetrameric model in fact only represents the mean conformation. The scattering pattern of this tetrameric configuration is then used as the form-factor scattering $F(q)$ for the subsequent steps.

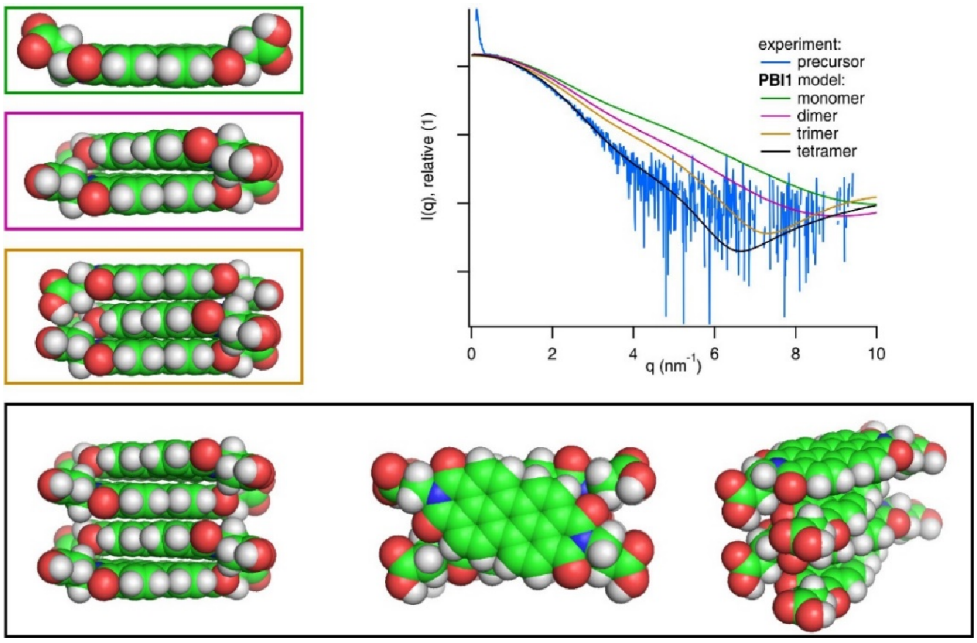

Fig. 5.3.2-1: Structural analysis of PBI1 in the precursor state from SAXS data. Consecutive models of H-type stacked PBI1 aggregates, i.e. monomer (green), dimer (violet), trimer (gold), tetramer (black) were built, from which the theoretical scattering patterns were calculated using CRYSOL.[54] The best agreement between experimental and model data is found for the case of tetramers.

In order to describe the experimental scattering pattern over the full q-range, a parametric model was constructed. This model assumes sticky-hard-sphere interaction (see Fig. 5.3.1-2) between the PBI1 tetramer building-blocks, resulting in a structure-factor contribution $S_{SHS}(q)$ in the scattering pattern.[212,233] Further, in order to describe the observed low-q ($q < 0.3\ nm^{-1}$) intensity increase characteristic of large-scale aggregate formation beyond the resolution limit of SAXS, a Porod contribution according to equation 5.3.1-2 is added to the model.[34] In the parametric formalism, only the absolute scalar c_{por} is optimized throughout the fitting process. In summary, the SAXS pattern of the precursor solution is fitted using the parametric model according to equation 5.3.1-1. The fitted scattering curve of the full-pattern refinement is found in Fig. 3.3.4-1c, whereas the results are represented in Table 5.3.2-1: the PBI1 tetramers show attractive interaction with a hard-sphere diameter of 4.1 nm.

Table 5.3.2-1: Fitting results of the full-pattern refinement of the SAXS data from PBI1 in the precursor state. As there exists a correlation between the potential well size λ and its depth ε, we kept λ fixed at 1.5.

Parameter	$\boldsymbol{a}$ [−]	$\boldsymbol{R_{HS}}$ [$\boldsymbol{nm}$]	$\boldsymbol{\varphi}$[%]	$\boldsymbol{\varepsilon}[\boldsymbol{k_BT}]$	$\boldsymbol{c_p}$ [−]	$\boldsymbol{BG}$ [−]
Value	95.55 ± 0.61	4.08 ± 0.57	0.21 ± 0.03	3.14 ± 0.08	0.17 ±0.04	0.02 ± 0.01

In case of scattering from the hydrogel, a second parametric model based on the chemically cross-linked hydrogel model by M.Shibayama, et.al.[234] was built. This model includes two separate terms: the first term describes the electron-density fluctuations between the compound rich and poor regions whereas the second term describes the domains in which correlated cross-linking occurs. In order to describe the two visible correlation peaks found in the experimental scattering curve we included two Gaussian peaks into the model. In summary, the SAXS pattern of the hydrogel is fitted using the parametric model according to,

$$I_{calc}(q) = a * I_{HG}(q) + I_{P1}(q) + I_{P2}(q) + BG \tag{5.3.2-1}$$

and

$$I_{HG}(q) = e^{-\frac{R_g^2 q^2}{3}} + \frac{I_L}{I_G}\frac{1}{\{1 + [(D+1)/3]\xi^2 q^2\}^{D/2}} \tag{5.3.2-2}$$

where a denotes an intensity scalar, $I_{HG}(q)$ denotes the scattering intensity according to the Shibayama model (see equation 5.3.2-2), $I_{P1}(q)$ and $I_{P2}(q)$ denote the first and second correlation peak, respectively and BG denotes a constant background offset. The fitted scattering curve of the full-pattern refinement is found in Fig. 3.3.4-1c, whereas the results are

represented in Table 5.3.2-2. The obtained dimensionality parameter $D = 3.29$ suggests hydrogen bonding in the system ($D > 2$)[24]. While the retrieved dimensions $\boldsymbol{R_G}$ and $\boldsymbol{\xi}$ are in agreement with general literature on hydrogels, they do not allow further conclusions on discrete shape/size of the hydrogel's intermediate building blocks. We hence performed a power-law fit of the low-q region ($0.12 < q < 0.22\ nm^{-1}$), whereas the retrieved slope of 1.78 suggests slightly-porous ($s_1 < 2$) plate-like structures.[34] A corresponding Guinier fit of the $I(q) \cdot q^2$ weighted scattering curve suggests an approximate plate-thickness of 5.3 nm. The two correlation peaks indicate crystalline order within the plate-like structures.

Table 5.3.2-2: Fitting results of the full-pattern refinement of the SAXS data from the PBI1 hydrogel. Please refer to literature[24] for detailed explanation of the Shibayama model parameters In short, R_G denotes the characteristic length of the polymer rich regions, I_L/I_G denotes the scaling factor between the two model terms, ξ denotes the domain size of the correlated regions and D denotes the fractal dimensionality ($D > 2$ for hydrogen-bonded gels). Each Gaussian peak is defined by its position in reciprocal space x_0, its width σ and its intensity i.

Parameter	$\boldsymbol{a}$ $[-]$	$\boldsymbol{R_G}$ $[\boldsymbol{nm}]$	$\boldsymbol{I_L/I_G}[-]$	$\boldsymbol{\xi}[\boldsymbol{nm}]$	$\boldsymbol{D}$ $[-]$
Value	869.98 ± 13.6	4.12 ± 0.43	51.43 ± 0.87	9.06 ± 1.2	3.29 ± 0.14

$\boldsymbol{x_{0,P1}}$ $[\boldsymbol{nm^{-1}}]$	$\boldsymbol{\sigma_{P1}}[\boldsymbol{nm^{-1}}]$	$\boldsymbol{i_{P1}}[-]$	$\boldsymbol{x_{0,P2}}$ $[\boldsymbol{nm^{-1}}]$	$\boldsymbol{\sigma_{P2}}[\boldsymbol{nm^{-1}}]$	$\boldsymbol{i_{P2}}[-]$	$\boldsymbol{BG}$ $[-]$
4.77 ± 0.09	0.27 ± 0.02	1.14 ± 0.05	7.81 ± 0.81	0.12 ± 0.02	0.32 ± 0.01	0.01 ± 0.003

5.4 Crystal structures

PBI1 and PBI1-Br crystallized in two different monoclinic unit cells, with one and two crystallographically independent PDI molecules in the asymmetric units (ASUs) respectively (see Fig. 5.4-1). PBI2 crystallized in a triclinic unit cell containing one and half crystallographically independent PDI molecules, showing different protonation states (see Fig. 5.4-1). Crystal packing views (see Fig. 5.4-2, 3 and 4) for the three compounds show that PBI1 and PBI1-Br are similar, despite the spacing and relative angle among stacked PBI neighbors changes significantly. This effect is related to the presence of bulky bromine substituents in PBI-Br, which are responsible also for a significant distortion of PDI planarity.

Each PBI molecule stacks (with two crystallographically not equivalent molecules) to form molecular pillars with characteristic π-π orientations and similar average distance among PBI planes among the three crystal forms (~3.2 Å – with average six membered ring centroids distances of ~3.5 Å).

Intrinsic resolution limit of the data doesn't allow hydrogens to be directly located in electron density maps for all the models, however clear hydrogen bond contacts can be recognized between crystallographic, not equivalent, PBI2 moieties. The PBI molecules lying on crystallographic inversion center have two protonated carboxylate groups that links two lateral PBI2 moieties, partially protonated. This hydrogen bond pattern keeps tightly linked neighbor columns and is terminated on lateral moieties by ionic couples formed with triethylamine (TEA) counterions. Furthermore, each partially protonated PBI2 molecule is involved in intra-pillar H-bond contacts forming sandwiches where a fully protonated PBI is enclosed in a cage of molecules with only one uncharged carboxylate group. The two PBI2 protonation variants have superimposable PBI scaffolds but different carboxylate arrangements. For PBI1 and PBI1-Br the positively charged amino sidechains are not protonated, show disordered conformations and are surrounded by chlorine counterions which are disordered as well.

Crystal packing show no voids, with layers of TEA parallel to ab unit cell face evenly spaced by 17.7 Å (corresponding to crystallographic axis c cell length). In between TEA layers, PBI2 pillars form a closed pack arrangement held together by hydrophobic interactions (see Fig. 5.4-2, 3 and 4). Similar hydrophobic contacts are present also in PBI and PBI-Br, where channels parallel to crystallographic c axis are present and they are filled by poorly ordered water molecules.

For further details, see the Table 5.4-1 for crystallographic data as well as Figs. 5.4.1-4 of graphical representations.

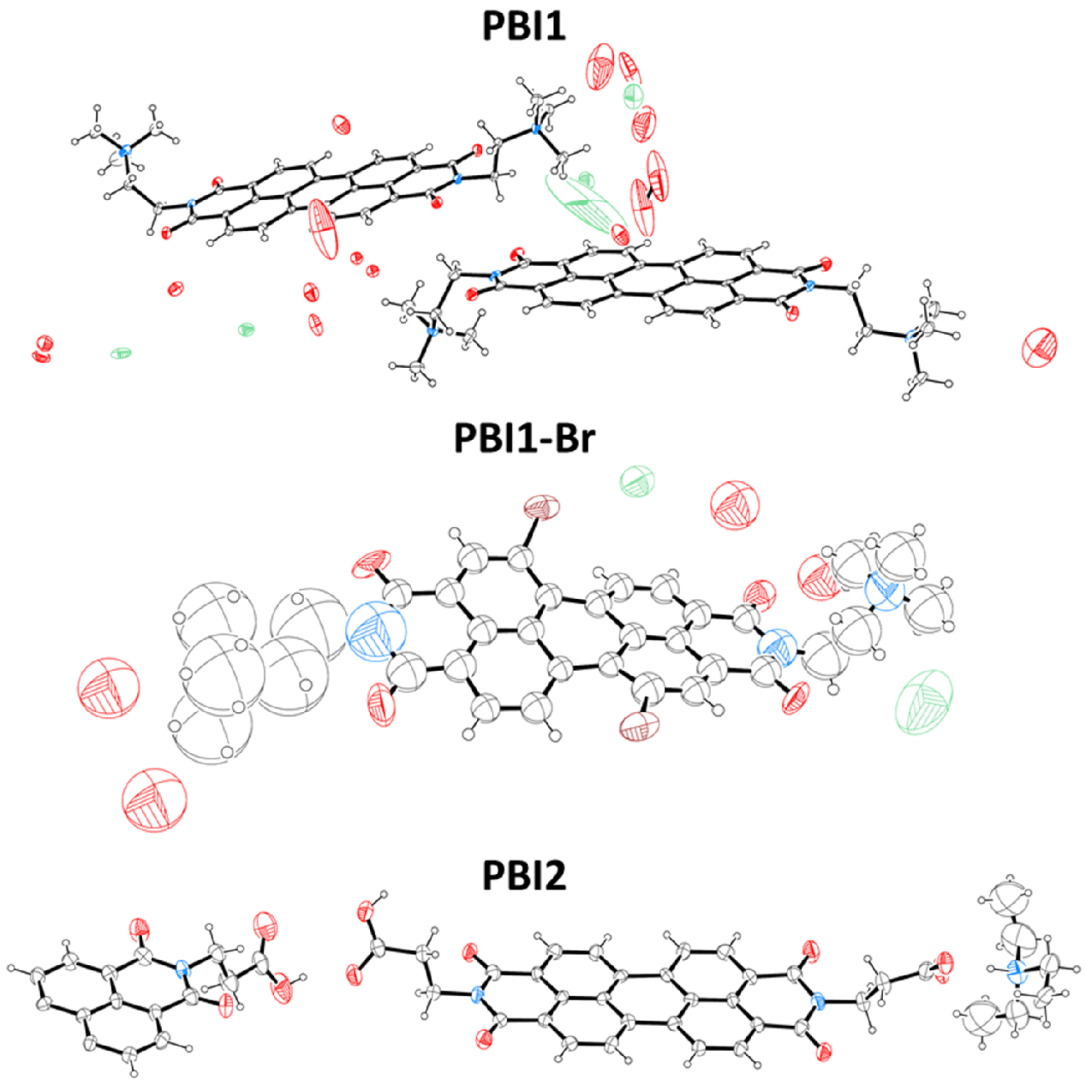

Fig. 5.4-1: Ellipsoid representation of PBI1, PBI1-Br and PBI2 crystal ASU contents (50% probability). Disordered conformations omitted for clarity.

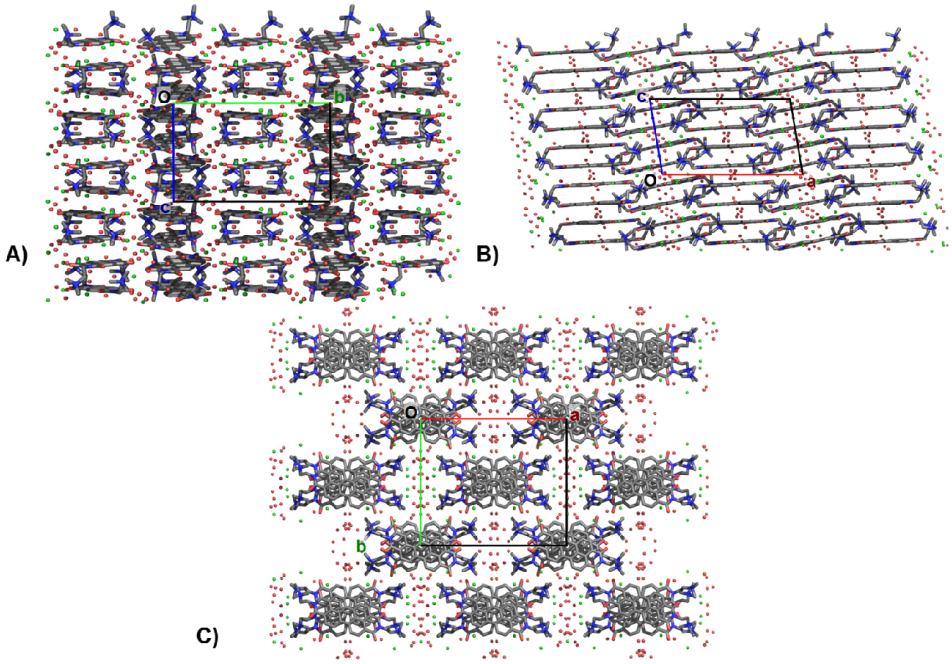

Fig. 5.4-2: Crystal packing views along *a*, *b* and *c* unit cell axes, of the PBI1 crystal form. Counterions are represented with green sticks or spheres. Disordered conformations and hydrogens omitted for clarity.

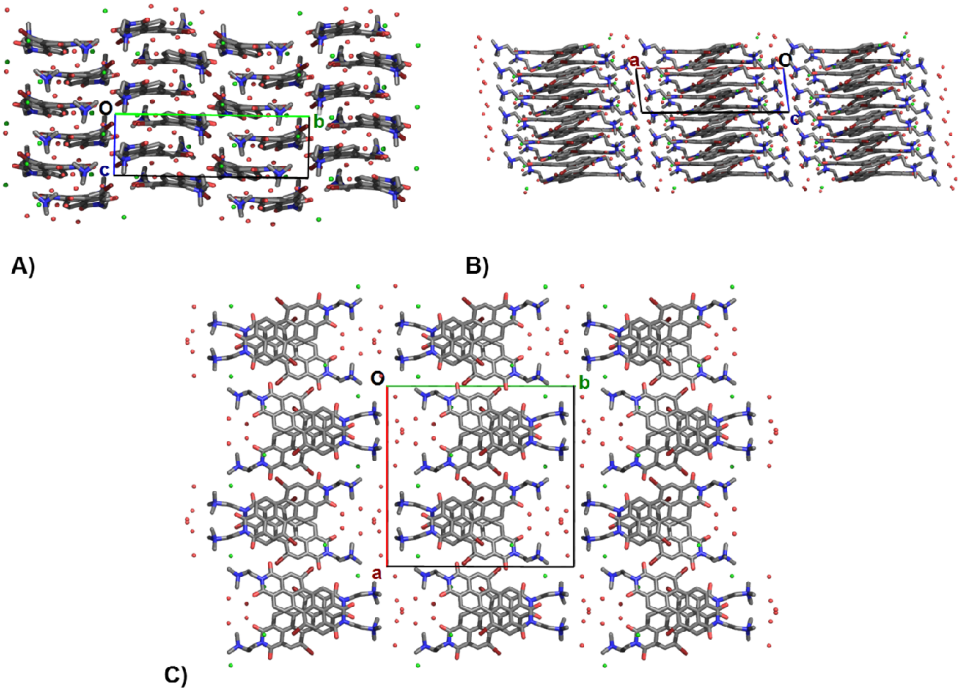

Fig. 5.4-3: Crystal packing views along *a*, *b* and *c* unit cell axes, of the PBI1-Br crystal form. Counterions are represented with green sticks or spheres. Disordered conformations and hydrogens omitted for clarity.

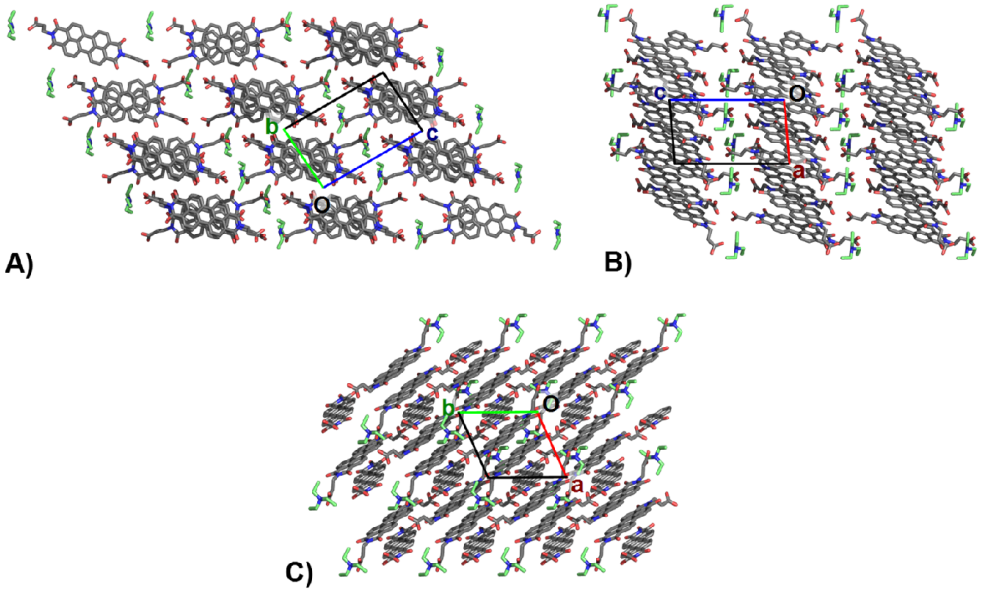

Fig. 5.4-4: Crystal packing views along *a*, *b* and *c* unit cell axes, of the PBI2 crystal form. Counterions are represented with green sticks or spheres. Disordered conformations and hydrogens omitted for clarity.

Table 5.4-1: Crystallographic data and refinement details for compounds PBI1, PBI1-Br and PBI2

	PBI1	PBI1-Br	PBI2
Chemical Formula	$C_{34}H_{34}Cl_2N_4O_{10}$	$C_{34}H_{32}Br_2Cl_2N_4O_7$	$C_{51}H_{42}N_4O_{12}$
Formula weight	719.97 g/mol	839.35 g/mol	902.88 g/mol
Temperature	100(2) K	100(2) K	100(2) K
Wavelength	0.700 Å	0.700 Å	0.700 Å
Crystal system	Monoclinic	Monoclinic	Triclinic
Space Group	P 2/c	P 21/c	P -1
Unit cell dimensions	a = 24.455(5) Å	a = 23.037(5) Å	a = 10.856(2) Å
	b = 20.998(4) Å	b = 22.144(4) Å	b = 11.859(2) Å
	c = 13.325(3) Å	c = 7.057(1) Å	c = 17.712(4) Å
	α = 90°	α = 90°	α = 92.06(3)°
	β = 99.89(3)°	β = 96.31(3)°	β = 93.78(3)°
	γ = 90°	γ = 90°	γ = 114.52(3)°
Volume	6741(2) $Å^3$	3578.2(12) $Å^3$	2065.1(8) $Å^3$
Z	8	4	2
Density (calculated)	1.419 $g \cdot cm^{-3}$	1.558 $g \cdot cm^{-3}$	1.452 $g \cdot cm^{-3}$
Absorption coefficient	0.187 mm^{-1}	2.375 mm^{-1}	0.100 mm^{-1}
F(000)	3003	1696	944
Crystal size	0.12 x 0.06 x 0.03 mm^3	0.1 x 0.03 x 0.02 mm^3	0.08 x 0.01 x 0.01 mm^3
Crystal habit	Dark red thin needles	Dark red thin needles	Dark brown needles
Theta range for data collection	1.27° to 27.40°	0.88° to 16.26°	1.14° to 21.86°
Index ranges	$-32 \le h \le 31$, $-23 \le k \le 27$, $-17 \le l \le 10$	$-18 \le h \le 18$, $-17 \le k \le 17$, $-5 \le l \le 5$	$-11 \le h \le 11$, $-12 \le k \le 12$, $-18 \le l \le 18$
Reflections collected	24018	9013	15497
Independent reflections	14480, 7818data with $I>2\sigma(I)$	1917, 1042 data with $I>2\sigma(I)$	5096, 2370 data with $I>2\sigma(I)$
Data multiplicity (max resltn)	3.33 (3.14)	4.58 (4.68)	2.98 (2.86)
$I/\sigma(I)$ (max resltn)	4.59 (1.37)	4.86 (1.94)	3.90 (1.59)
R_{merge} (max resltn)	0.148 (0.559)	0.202 (0.533)	0.134 (0.471)
Data completeness (max resltn)	96% (97%)	99% (98%)	98% (97%)
Refinement method	Full-matrix least-Squares on F^2	Full-matrix least-Squares on F^2	Full-matrix least-Squares on F^2
Data / restraints / parameters	14480/0/656	1917/229/309	5096/43/552

Table 5.4-1 – cont.: Crystallographic data and refinement details for compounds PBI1, PBI1-Br and PBI2

	PBI1	PBI1-Br	PBI2
Goodness-of-fit on F^2	1.026	1.086	1.020
Δ/σ_{max}	0.002	0.142	0.002
Final R indices [I>2σ(I)]	R_1 = 0.1299, wR_2 = 0.3085	R_1 = 0.1221, wR_2 = 0.2661	R_1 = 0.0977, wR_2 = 0.2587
R indices (all data)	R_1 = 0.2057, wR_2 = 0.3655	R_1 = 0.2054, wR_2 = 0.3143	R_1 = 0.1919, wR_2 = 0.3263
Largest diff. peak and hole	0.860 and -0.605 eÅ^{-3}	0.811 and -0.780 eÅ^{-3}	0.690 and -0.336 eÅ^{-3}
R.M.S. deviation from mean	0.131 eÅ^{-3}	0.152 eÅ^{-3}	0.073 eÅ^{-3}

$R_1 = \Sigma \, ||Fo|-|Fc|| \, / \, \Sigma \, |Fo|$, $wR_2 = \{\Sigma \, [w(Fo^2 - Fc^2)^2] \, / \, \Sigma \, [w(Fo^2)^2]\}^{½}$

6 Bibliography

1. Ort, D. R. *et al.* Redesigning photosynthesis to sustainably meet global food and bioenergy demand. *Proc. Natl. Acad. Sci.* **112,** 8529–8536 (2015).

2. Blankenship, R. E. *et al.* Comparing photosynthetic and photovoleteaic ifficiencies and recognizing the potential for improvemenet. *Science* **332,** 805–809 (2011).

3. Larcher, D. & Tarascon, J. M. Towards greener and more sustainable batteries for electrical energy storage. *Nature Chemistry* **7,** 19–29 (2015).

4. Lin, M. T., Occhialini, A., Andralojc, P. J., Parry, M. A. J. & Hanson, M. R. A faster Rubisco with potential to increase photosynthesis in crops. *Nature* **513,** 547–550 (2014).

5. Bryant, D. A. & Canniffe, D. P. How nature designs light-harvesting antenna systems: design principles and functional realization in chlorophototrophic prokaryotes Tutorial How nature designs light-harvesting antenna systems: design principles and functional realization in chlorophototrophic prokaryotes. *J. Phys. B At. Mol. Opt. Phys. J. Phys. B At. Mol. Opt. Phys. J. Phys. B At. Mol. Opt. Phys. J. Phys. B At. Mol. Opt. Phys* **51,** (2018).

6. Umena, Y., Kawakami, K., Shen, J.-R. & Kamiya, N. Crystal structure of oxygen-evolving photosystem II at a resolution of 1.9 Å. *Nature* **473,** 55–60 (2011).

7. McKone, J. R., Lewis, N. S. & Gray, H. B. Will solar-driven water-splitting devices see the light of day? *Chemistry of Materials* **26,** 407–414 (2014).

8. Benniston, A. C. & Harriman, A. Artificial photosynthesis. *Materials Today* **11,** 26–34 (2008).

9. Hashimoto, H., Sugai, Y., Uragami, C., Gardiner, A. T. & Cogdell, R. J. Natural and artificial light-harvesting systems utilizing the functions of carotenoids. *Journal of Photochemistry and Photobiology C: Photochemistry Reviews* **25,** 46–70 (2015).

10. Tian, Z., Yu, J., Wu, C., Szymanski, C. & McNeill, J. Amplified energy transfer in conjugated polymer nanoparticle tags and sensors. *Nanoscale* **2,** 1999 (2010).

11. Yeo, H., Tanaka, K. & Chujo, Y. Effective Light-Harvesting Antennae Based on BODIPY-Tethered Cardo Polyfluorenes via Rapid Energy Transferring and Low Concentration Quenching. *Macromolecules* **46,** 2599–2605 (2013).

12. Thomas, S. W., Joly, G. D. & Swager, T. M. Chemical sensors based on amplifying fluorescent conjugated polymers. *Chemical Reviews* **107,** 1339–1386 (2007).

13. Yang, J., Yoon, M.-C., Yoo, H., Kim, P. & Kim, D. Excitation energy transfer in multiporphyrin arrays with cyclic architectures: towards artificial light-harvesting antenna complexes. *Chem. Soc. Rev.* **41,** 4808 (2012).

14. Son, H. J. *et al.* Light-harvesting and ultrafast energy migration in porphyrin-based metal-organic frameworks. *J. Am. Chem. Soc.* **135,** 862–869 (2013).

15. Natali, M. *et al.* Photoinduced water oxidation by a tetraruthenium polyoxometalate catalyst: Ion-pairing and primary processes with Ru(bpy)32+ photosensitizer. *Inorg. Chem.* **51,** 7324–7331 (2012).

16. Natali, M. *et al.* Working the Other Way Around: Photocatalytic Water Oxidation Triggered by Reductive Quenching of the Photoexcited Chromophore. *J. Phys. Chem. C* **119,** 2371–2379 (2015).

17. Sartorel, A. *et al.* Water oxidation at a tetraruthenate core stabilized by polyoxometalate ligands: Experimental and computational evidence to trace the competent intermediates. *J. Am. Chem. Soc.* **131,** 16051–16053 (2009).

18. Orlandi, M. *et al.* Ruthenium polyoxometalate water splitting catalyst: very fast hole scavenging from photogenerated oxidants. *Chem. Commun. (Camb).* **46,** 3152–3154 (2010).

19. Zhou, H. *et al.* Highly active catalyst derived from a 3D foam of Fe(PO3)2/Ni2P for extremely efficient water oxidation. *Proc. Natl. Acad. Sci. U. S. A.* **114,** 5607–5611 (2017).

20. Blasco-Ahicart, M., Soriano-López, J., Carbó, J. J., Poblet, J. M. & Galan-Mascaros, J. R. Polyoxometalate electrocatalysts based on earth-abundant metals for efficient water oxidation in acidic media. *Nat. Chem.* **10,** 24–30 (2017).

21. Huynh, M., Ozel, T., Liu, C., Lau, E. C. & Nocera, D. G. Design of template-stabilized active and earth-abundant oxygen evolution catalysts in acid. *Chem. Sci.* **8,** 4779–4794 (2017).

22. Zhao, Z. *et al.* Bifunctional metal phosphide FeMnP films from single source metal organic chemical vapor deposition for efficient overall water splitting. *Nano Energy* **39,** 444–453 (2017).

23. Garcia-Esparza, A. T. *et al.* An Oxygen-Insensitive Hydrogen Evolution Catalyst Coated by a Molybdenum-Based Layer for Overall Water Splitting. *Angew. Chemie* **129,** 5874–5878 (2017).

24. Dasgupta, S. *et al.* Tetrametallic molecular catalysts for photochemical water oxidation. *Chem. Soc. Rev. Chem. Soc. Rev* **4261,** 306–12 (2013).

25. Geletii, Y. V. *et al.* An all-inorganic, stable, and highly active tetraruthenium homogeneous catalyst for water oxidation. *Angew. Chemie - Int. Ed.* **47,** 3896–3899 (2008).

26. Otero, R., Vázquez de Parga, A. L. & Gallego, J. M. Electronic, structural and chemical effects of charge-transfer at organic/inorganic interfaces. *Surf. Sci. Rep.* **72,** 105–145 (2017).

27. Yang, W. *et al.* Aggregation-induced emission and intermolecular charge transfer effect in triphenylamine fluorophores containing diphenylhydrazone structures. *Phys. Chem. Chem. Phys.* **18,** 28052–28060 (2016).

28. Arrigo, A. *et al.* Aggregation-Induced Energy Transfer in a Decanuclear Os(II)/Ru(II) Polypyridine Light-Harvesting Antenna Dendrimer. *Chem* **3,** 494–508 (2017).

29. Hutchison, G. R., Ratner, M. A. & Marks, T. J. Intermolecular charge transfer between heterocyclic oligomers. Effects of heteroatom and molecular packing on hopping transport in organic semiconductors. *J. Am. Chem. Soc.* **127,** 16866–16881 (2005).

30. Rodríguez-Fernández, J. *et al.* Tuning Intermolecular Charge Transfer in Donor–Acceptor Two-Dimensional Crystals on Metal Surfaces. *J. Phys. Chem. C* **121,** 23505–23510 (2017).

31. Graham, K. R. *et al.* The Roles of Structural Order and Intermolecular Interactions in Determining Ionization Energies and Charge-Transfer State Energies in Organic Semiconductors. *Adv. Energy Mater.* **6,** 1601211 (2016).

32. Geletii, Y. V. *et al.* Homogeneous light-driven water oxidation catalyzed by a tetraruthenium complex with all inorganic ligands. *J. Am. Chem. Soc.* **131,** 7522–7523 (2009).

33. Als-Nielsen, J. & McMorrow, D. *Elements of Modern X-ray Physics: Second Edition*. *Elements of Modern X-ray Physics: Second Edition* (John Wiley & Sons, Inc., 2011). doi:10.1002/9781119998365

34. Glatter, O. & Kratky, O. *Small Angle X-ray Scattering*. (Academic Press, 1982). doi:10.1002/actp.1985.010360520

35. Feigin, L. A. & Svergun, D. I. *Structure Analysis by Small-Angle X-Ray and Neutron Scattering. Current Opinion in Structural Biology* (Plenum Press, 1987). doi:10.1007/978-1-4757-6624-0

36. Pedersen, J. S. Analysis of small-angle scattering data from colloids and polymer solutions: modeling and least-squares fitting. *Adv. Colloid Interface Sci.* **70,** 171–210 (1997).

37. Sztucki, M., Di Cola, E. & Narayanan, T. Instrumental developments for anomalous small-angle X-ray scattering from soft matter systems. *J. Appl. Cryst.* **43,** 1479–1487 (2010).

38. Guinier, A. & Fournet, G. *Small angle scattering of X-rays.* (John Wiley & Sons, Inc., 1955). doi:10.1002/pol.1956.120199326

39. Debye, P. Zerstreuung von Röntgenstrahlen. *Ann. Phys.* **351,** 809–823 (1915).

40. Skov Pedersen, J. in *Neutrons, X-Rays and Light* (ed. P.Lindner, T. Z.) 391–420 (Elsevier Science B.V., 2002).

41. Strobl, G. R. & Schneider, M. Direct evaluation of the electron density correlation function of partially crystalline polymers. *J. Polym. Sci. Polym. Phys. Ed.* **18,** 1343–1359 (1980).

42. Goderis, B. Use of SAXS and Linear Correlation Functions for the Determination of the Crystallinity and Morphology of SemiCrystalline Polymers. Application to Linear Polyethylene. *J. Polym. Sci. Part B Polym. Phys.* **37,** 1715–1738 (1999).

43. Ingham, B., Li, H., Allen, E. L. & Toney, M. F. SAXSMorph: A program for generating representative morphologies for two-phase materials from small-angle X-ray and neutron scattering data. *J. Appl. Cryst.* **44,** 221–224 (2011).

44. Brunner-Popela, J. & Glatter, O. Small-Angle Scattering of Interacting Particles. I. Basic Principles of a Global Evaluation Technique. *J. Appl. Cryst.* **30,** 431–442 (1997).

45. Weyerich, B., Brunner-Popela, J. & Glatter, O. Small-angle scattering of interacting particles. II. Generalized indirect Fourier transformation under consideration of the effective structure factor for polydisperse systems. *J. Appl. Cryst.* **32,** 197–209 (1999).

46. Glatter, O. Determination of particle-size distribution functions from small-angle scattering data by means of the indirect transformation method. *J. Appl. Cryst.* **13,** 7–11 (1980).

47. Svergun, D. I. Determination of the Regularization Parameter in Indirect- Transform Methods Using Perceptual Criteria. *J. Appl. Cryst.* **25,** 495–503 (1992).

48. Svergun, D. I. Restoring Low Resolution Structure of Biological Macromolecules from Solution Scattering Using Simulated Annealing. *Biophys. J.* **76,** 2879–2886 (1999).

49. Franke, D. & Svergun, D. I. DAMMIF , a program for rapid ab-initio shape determination in small-angle scattering. *J. Appl. Cryst.* **42,** 342–346 (2009).

50. Koutsioubas, A., Jaksch, S. & Pérez, J. DENFERT version 2: extension of ab initio structural modelling of hydrated biomolecules to the case of small-angle neutron scattering data. *J. Appl. Cryst.* **49,** 690–695 (2016).

51. Chacón, P., Morán, F., Díaz, J. F., Pantos, E. & Andreu, J. M. Low-Resolution Structures of Proteins in Solution Retrieved from X-Ray Scattering with a Genetic Algorithm. *Biophys. J.* **74,** 2760–2775 (1998).

52. Burian, M. *et al.* Considerations on the model-free shape retrieval of inorganic nanocrystals from small-angle scattering data. *J. Appl. Cryst.* **48,** 857–868 (2015).

53. Stuhrmann, H. B. Interpretation of small-angle scattering functions of dilute solutions and gases. A Representation of the Structures Related to a One-Particle-Scattering Function. *Acta Crystallogr. Sect. A* **26,** 297–306 (1970).

54. Svergun, D., Barberato, C. & Koch, M. H. J. CRYSOL – a Program to Evaluate X-ray Solution Scattering of Biological Macromolecules from Atomic Coordinates. *J. Appl. Cryst* **28,** 768–773 (1995).

55. Grudinin, S., Garkavenko, M., Kazennov, A. & IUCr. *Pepsi-SAXS* : an adaptive method for rapid and accurate computation of small-angle X-ray scattering profiles. *Acta Crystallogr. Sect. D Struct. Biol.* **73,** 449–464 (2017).

56. Pringle, O. A. & Schmidt, P. W. Small-Angle X-ray Scattering from Helical Maeromolecules*. *J. Appl. Cryst.* **4,** 290–293 (1970).

57. Kardos, M. Deutsches Reichspatent DE 276357. (1913).

58. Huang, C., Barlow, S. & Marder, S. R. Perylene-3,4,9,10-tetracarboxylic acid diimides: Synthesis, physical properties, and use in organic electronics. *Journal of Organic Chemistry* **76,** 2386–2407 (2011).

59. Zollinger, H. *Color chemistry : syntheses, properties, and applications of organic dyes and pigments*. (Verlag Helvetica Chimica Acta, 1991).

60. Herbst, W. & Hunger, K. *Industrial Organic Pigments: Production, Properties, Applications*. (Wiley-VCH, 2006). doi:10.1002/3527602429

61. Würthner, F. Perylene bisimide dyes as versatile building blocks for functional supramolecular architectures. *Chem. Commun.* 1564–1579 (2004). doi:10.1039/B401630K

62. Kircher, T. & Löhmannsröben, H.-G. Photoinduced charge recombination reactions of a perylene dye in acetonitrile. *Phys. Chem. Chem. Phys.* **1,** 3987–3992 (1999).

63. Langhals, H., Karolin, J. & Johansson, L. B.-Å. Spectroscopic properties of new and convenient standards for measuring fluorescence quantum yields. *J. Chem. Soc. Faraday Trans.* **94,** 2919–2922 (1998).

64. Struijk, C. W. *et al.* Liquid crystalline perylene diimides: Architecture and charge carrier mobilities. *J. Am. Chem. Soc.* **122,** 11057–11066 (2000).

65. Dimitrakopoulos, C. D. & Malenfant, P. R. L. Organic Thin Film Transistors for Large Area Electronics. *Adv. Mater.* **14,** 99–117 (2002).

66. van Herrikhuyzen, J., Syamakumari, A., Schenning, A. P. H. J. & Meijer, E. W. Synthesis of n-Type Perylene Bisimide Derivatives and Their Orthogonal Self-Assembly with p-Type Oligo(p -phenylene vinylene)s. *J. Am. Chem. Soc.* **126,** 10021–10027 (2004).

67. Di Donato, E. *et al.* n-Type Charge Transport and Mobility of Fluorinated Perylene Bisimide Semiconductors. *J. Phys. Chem. B* **114,** 5327–5334 (2010).

68. Hüttner, S., Sommer, M. & Thelakkat, M. N-type organic field effect transistors from perylene bisimide block copolymers and homopolymers. *Appl. Phys. Lett.* **92,** 93302 (2008).

69. Zhang, W. *et al.* Reaction of tetrachlorinated perylene bisimide in a strong base to form an asymmetric compound with charge transfer optical properties. *Chem. Commun.* **49,** 11560 (2013).

70. Beckers, E. H. A., Jonkheijm, P., Schenning, A. P. H. J., Meskers, S. C. J. & Janssen, R. A. J. Charge transfer in supramolecular coaggregates of oligo(p-phenylene vinylene) and perylene bisimide in water. *ChemPhysChem* **6,** 2029–2031 (2005).

71. Santos, E. R. dos *et al.* Photoinduced Energy and Electron-Transfer Reactions by Polypyridine Ruthenium(II) Complexes Containing a Derivatized Perylene Diimide. *J. Phys. Chem. C* **120,** 22831–22843 (2016).

72. Hippius, C. *et al.* Energy Transfer in Calixarene-Based Cofacial-Positioned Perylene Bisimide Arrays Energy Transfer in Calixarene-Based Cofacial-Positioned Perylene Bisimide Arrays. *J. Am. Chem. Soc.* **128,** 3870–3871 (2006).

73. Pandey, A. K. & Nunzi, J.-M. Upconversion injection in rubrene/perylene-diimide-heterostructure electroluminescent diodes. *Appl. Phys. Lett.* **90,** 263508 (2007).

74. Ramos, A. M., Rispens, M. T., Van Duren, J. K. J., Hummelen, J. C. & Janssen, R. A. J. Photoinduced electron transfer and photovoltaic devices of a conjugated polymer with pendant fullerenes [4]. *Journal of the American Chemical Society* **123,** 6714–6715 (2001).

75. Kozma, E., Mróz, W. & Galeotti, F. A polystyrene bearing perylene diimide pendants with enhanced solid state emission for white hybrid light-emitting diodes. *Dye. Pigment.* **114,** 138–143 (2015).

76. Dobrawa, R. & Würthner, F. Photoluminescent supramolecular polymers: metal-ion directed polymerization of terpyridine-functionalized perylene bisimide dyes. doi:10.1039/b205478g

77. Kamm, V. *et al.* Polythiophene:perylene diimide solar cells - The impact of alkyl-substitution on the photovoltaic performance. *Adv. Energy Mater.* **1,** 297–302 (2011).

78. Liang, N. *et al.* Perylene Diimide Trimers Based Bulk Heterojunction Organic Solar Cells with Efficiency over 7%. *Adv. Energy Mater.* **6,** 1600060 (2016).

79. Zhu, N. *et al.* Layer-by-Layer-Processed Ternary Organic Solar Cells Using Perylene Bisimide as a Morphology-

Inducing Component. *ACS Appl. Mater. Interfaces* **9,** 17265–17270 (2017).

80. Nian, L. *et al.* Perylene Bisimide as a Promising Zinc Oxide Surface Modifier: Enhanced Interfacial Combination for Highly Efficient Inverted Polymer Solar Cells. *ACS Appl. Mater. Interfaces* **7,** 25821–25827 (2015).

81. Bisri, S. Z., Piliego, C., Yarema, M., Heiss, W. & Loi, M. A. Low driving voltage and high mobility ambipolar field-effect transistors with PbS colloidal nanocrystals. *Adv. Mater.* **25,** 4309–4314 (2013).

82. Schmidt, R. *et al.* High-Performance Air-Stable n-Channel Organic Thin Film Transistors Based on Halogenated Perylene Bisimide Semiconductors. *J. Am. Chem. Soc.* **131,** 6215–6228 (2009).

83. Liu, Y., Wang, K.-R., Guo, D.-S. & Jiang, B.-P. Supramolecular Assembly of Perylene Bisimide with β -Cyclodextrin Grafts as a Solid-State Fluorescence Sensor for Vapor Detection. *Adv. Funct. Mater.* **19,** 2230–2235 (2009).

84. Zhang, X., Rehm, S., Safont-Sempere, M. M. & Würthner, F. Vesicular perylene dye nanocapsules as supramolecular fluorescent pH sensor systems. *Nat. Chem.* **1,** 623–629 (2009).

85. Ruan, Y.-B., Li, A.-F., Zhao, J.-S., Shen, J.-S. & Jiang, Y.-B. Specific Hg2+-mediated perylene bisimide aggregation for highly sensitive detection of cysteine. *Chem. Commun.* **46,** 4938 (2010).

86. Peng, H. *et al.* An Ultrasensitive Fluorescent Sensing Nanofilm for Organic Amines Based on Cholesterol-Modified Perylene Bisimide. *Chem. - An Asian J.* **7,** 1576–1582 (2012).

87. Seybold, G. & Wagenblast, G. New perylene and violanthrone dyestuffs for fluorescent collectors. *Dye. Pigment.* **11,** 303–317 (1989).

88. Langhals, H. Cyclic carboxylic imide structures as structure elements of high stability. Novel developments in perylene dye chemistry. *Heterocycles* **40,** 477–500 (1995).

89. Herbst, W., Hunger, K., Wilker, G., Ohleier, H. & Winter, R. *Industrial Organic Pigments: Production, Properties, Applications: Third, Completely Revised Edition*. *Industrial Organic Pigments: Production, Properties, Applications: Third, Completely Revised Edition* (Wiley-VCH, 2005). doi:10.1002/3527602429

90. Würthner, F. *et al.* Perylene Bisimide Dye Assemblies as Archetype Functional Supramolecular Materials. *Chem. Rev.* **116,** 962–1052 (2016).

91. Rademacher, A., Märkle, S. & Langhals, H. Lösliche Perylen-Fluoreszenzfarbstoffe mit hoher Photostabilität. *Chem. Ber.* **115,** 2927–2934 (1982).

92. Wescott, L. D. & Mattern, D. L. Donor-σ-Acceptor Molecules Incorporating a Nonadecyl-Swallowtailed Perylenediimide Acceptor. *J. Org. Chem.* **68,** 10058–10066 (2003).

93. Rigodanza, F., Tenori, E., Bonasera, A., Syrgiannis, Z. & Prato, M. Fast and Efficient Microwave-Assisted Synthesis of Perylenebisimides. *European J. Org. Chem.* **2015,** 5060–5063 (2015).

94. Würthner, F., Sautter, A. & Schilling, J. Synthesis of diazadibenzoperylenes and characterization of their structural, optical, redox, and coordination properties. *J. Org. Chem.* **67,** 3037–3044 (2002).

95. George, C., Strekowski, R. S., Kleffmann, J., Stemmler, K. & Ammann, M. Photoenhanced uptake of gaseous NO2 on solid organic compounds: a photochemical source of HONO? *Faraday Discuss.* **130,** 195 (2005).

96. Feng, X. *et al.* Towards high charge-carrier mobilities by rational design of the shape and periphery of discotics. *Nat. Mater.* **8,** 421–426 (2009).

97. Würthner, F., Bauer, C., Stepanenko, V. & Yagai, S. A Black Perylene Bisimide Super Gelator with an Unexpected J-Type Absorption Band. *Adv. Mater.* **20,** 1695–1698 (2008).

98. Yagai, S., Seki, T., Karatsu, T., Kitamura, A. & Würthner, F. Transformation from H- to J-Aggregated Perylene Bisimide Dyes by Complexation with Cyanurates. *Angew. Chemie Int. Ed.* **47,** 3367–3371 (2008).

99. Heek, T. *et al.* Highly fluorescent water-soluble polyglycerol-dendronized perylene bisimide dyes. *Chem. Commun.* **46,**

1884 (2010).

100. Rehm, S., Stepanenko, V., Zhang, X., Rehm, T. H. & Würthner, F. Spermine-functionalized pen lene bisimide dyes-highly fluorescent bola-amphiphiles in water. *Chem. - A Eur. J.* **16,** 3372–3382 (2010).

101. Ford, W. E. & Kamat, P. V. Photochemistry of 3,4,9,10-perylenetetracarboxylic dianhydride dyes. 3. Singlet and triplet excited-state properties of the bis(2,5-di-tert-butylphenyl)imide derivative. *J. Phys. Chem.* **91,** 6373–6380 (1987).

102. Mizuguchi, J. Polymorph of N,N′-di-n-butylperylene-3,4:9,10-bis(dicarboximide) and their electronic structure. *Dye. Pigment.* **70,** 226–231 (2006).

103. Carmen Ruiz Delgado, M., Kim, E. G., Da Silva Filho, D. A. & Bredas, J. L. Tuning the charge-transport parameters of perylene diimide single crystals via end and/or core functionalization: A density functional theory investigation. *J. Am. Chem. Soc.* **132,** 3375–3387 (2010).

104. Pan, F., Gao, F., Liang, W. & Zhao, Y. Nature of low-lying excited states in H-aggregated perylene bisimide dyes: Results of TD-LRC-DFT and the mixed exciton model. *J. Phys. Chem. B* **113,** 14581–14587 (2009).

105. Hippius, C., Van Stokkum, I. H. M., Zangrando, E., Williams, R. M. & Würthner, F. Excited state interactions in calix[4]arene-perylene bisimide dye conjugates: Global and target analysis of supramolecular building blocks. *J. Phys. Chem. C* **111,** 13988–13996 (2007).

106. Walsh, J. J. *et al.* Controlling Visible Light Driven Photoconductivity in Self-Assembled Perylene Bisimide Structures. *J. Phys. Chem. C* **120,** 18479–18486 (2016).

107. Beckers, E. H. A. *et al.* Charge separation and recombination in photoexcited oligo(p-phenylene vinylene): Perylene bisimide arrays close to the marcus inverted region. *J. Phys. Chem. A* **108,** 6933–6937 (2004).

108. Chen, Z., Baumeister, U., Tschierske, C. & Würthner, F. Effect of core twisting on self-assembly and optical properties of perylene bisimide dyes in solution and columnar liquid crystalline phases. *Chem. - A Eur. J.* **13,** 450–465 (2007).

109. Bialas, D. *et al.* Exciton-Vibrational Couplings in Homo- and Heterodimer Stacks of Perylene Bisimide Dyes within Cyclophanes: Studies on Absorption Properties and Theoretical Analysis. *Chem. - A Eur. J.* **22,** 15011–15018 (2016).

110. Osswald, P. & Würthner, F. Effects of bay substituents on the racemization barriers of perylene bisimides: Resolution of atropo-enantiomers. *J. Am. Chem. Soc.* **129,** 14319–14326 (2007).

111. Schenning, A. P. H. J. *et al.* Photoinduced electron transfer in hydrogen-bonded oligo(p-phenylene vinylene)-perylene bisimide chiral assemblies. *J. Am. Chem. Soc.* **124,** 10252–10253 (2002).

112. Kaiser, T. E., Wang, H., Stepanenko, V. & Würthner, F. Supramolecular construction of fluorescent J-aggregates based on hydrogen-bonded perylene dyes. *Angew. Chemie - Int. Ed.* **46,** 5541–5544 (2007).

113. Görl, D., Zhang, X. & Würthner, F. Molecular assemblies of perylene bisimide dyes in water. *Angewandte Chemie International Edition* **51,** 6328–6348 (2012).

114. Chen, Z. *et al.* Photoluminescence and conductivity of self-assembled π-π stacks of perylene bisimide dyes. *Chem. - A Eur. J.* **13,** 436–449 (2007).

115. Ghosh, S., Li, X. Q., Stepanenko, V. & Würthner, F. Control of H- and J-type π stacking by peripheral alkyl chains and self-sorting phenomena in perylene bisimide homo- and heteroaggregates. *Chem. - A Eur. J.* **14,** 11343–11357 (2008).

116. Kasha, M., Rawls, H. R. & Ashraf El-Bayoumi, M. The exciton model in molecular spectroscopy. *Pure Appl. Chem.* **11,** 371–392 (1965).

117. McRae, E. G. & Kasha, M. Enhancement of Phosphorescence Ability upon Aggregation of Dye Molecules. *J. Chem. Phys.* **28,** 721–722 (1958).

118. Würthner, F., Kaiser, T. E. & Saha-Möller, C. R. J-Aggregates: From Serendipitous Discovery to Supramolecular Engineering of Functional Dye Materials. *Angew. Chemie Int. Ed.* **50,** 3376–3410 (2011).

119. Liess, A. *et al.* Exciton Coupling of Merocyanine Dyes from H- to J-type in the Solid State by Crystal Engineering. *Nano Lett.* **17,** 1719–1726 (2017).

120. Balakrishnan, K. *et al.* Effect of Side-Chain Substituents on Self-Assembly of Perylene Diimide Molecules: Morphology Control. *J. Am. Chem. Soc.* **128,** 7390–7398 (2006).

121. Ye, Y. *et al.* Controllable Self-Assembly of Amphiphilic Zwitterionic PBI Towards Tunable Surface Wettability of the Nanostructures. *Chem. - An Asian J.* **12,** 1020–1024 (2017).

122. Würthner, F., Sautter, A., Schmid, D. & Weber, P. J. A. Fluorescent and Electroactive Cyclic Assemblies from Perylene Tetracarboxylic Acid Bisimide Ligands and Metal Phosphane Triflates. *Chemistry (Easton).* **7,** 894–902 (2001).

123. van der Weegen, R. *et al.* Small sized perylene-bisimide assemblies controlled by both cooperative and anti-cooperative assembly processes. *Chem. Commun.* **49,** 5532 (2013).

124. Sugiyasu, K., Kawano, S.-I., Fujita, N. & Shinkai, S. Self-Sorting Organogels with p−n Heterojunction Points. *Chem. Mater.* **20,** 2863–2865 (2008).

125. Li, X.-Q. *et al.* Functional organogels from highly efficient organogelator based on perylene bisimide semiconductor. *Chem. Commun.* **0,** 3871–3873 (2006).

126. Datar, A., Balakrishnan, K. & Zang, L. One-dimensional self-assembly of a water soluble perylene diimide molecule by pH triggered hydrogelation. *Chem. Commun.* **49,** 6894 (2013).

127. Görl, D., Soberats, B., Herbst, S., Stepanenko, V. & Würthner, F. Perylene bisimide hydrogels and lyotropic liquid crystals with temperature-responsive color change. *Chem. Sci.* **7,** 6786–6790 (2016).

128. Lin, X. *et al.* Water-induced helical supramolecular polymerization and gel formation of an alkylene-tethered perylene bisimide dyad. *Chem. Commun.* **53,** 168–171 (2017).

129. Sung, J., Kim, P., Fimmel, B., Würthner, F. & Kim, D. Direct observation of ultrafast coherent exciton dynamics in helical π-stacks of self-assembled perylene bisimides. *Nat. Commun.* **6,** 8646 (2015).

130. Chen, Z. *et al.* Near-IR Absorbing J-Aggregate of an Amphiphilic BF_2 -Azadipyrromethene Dye by Kinetic Cooperative Self-Assembly. *Angew. Chemie Int. Ed.* **56,** 5729–5733 (2017).

131. Assali, M. *et al.* Glyconanosomes: Disk-shaped nanomaterials for the water solubilization and delivery of hydrophobic molecules. *ACS Nano* **7,** 2145–2153 (2013).

132. Wang, K. R., Guo, D. S., Jiang, B. P., Sun, Z. H. & Liu, Y. Molecular aggregation behavior of perylene-bridged bis(ß-cyclodextrin) and its electronic interactions upon selective binding with aromatic guests. *J. Phys. Chem. B* **114,** 101–106 (2010).

133. Ustinov, A. V., Dubnyakova, V. V. & Korshun, V. A. A convenient 'click chemistry' approach to perylene diimide–oligonucleotide conjugates. *Tetrahedron* **64,** 1467–1473 (2008).

134. Görl, D., Zhang, X., Stepanenko, V. & Würthner, F. Supramolecular block copolymers by kinetically controlled co-self-assembly of planar and core-twisted perylene bisimides. *Nat. Commun.* **6,** 7009 (2015).

135. Bai, S. *et al.* Differential Self-Assembly and Tunable Emission of Aromatic Peptide *Bola* -Amphiphiles Containing Perylene Bisimide in Polar Solvents Including Water. *Langmuir* **30,** 7576–7584 (2014).

136. Kalyanasundaram, K. Photophysics, photochemistry and solar energy conversion with tris(bipyridyl)ruthenium(II) and its analogues. *Coord. Chem. Rev.* **46,** 159–244 (1982).

137. Campagna, S., Puntoriero, F., Nastasi, F., Bergamini, G. & Balzani, V. Photochemistry and photophysics of coordination compounds: Ruthenium. *Top. Curr. Chem.* **280,** 117–214 (2007).

138. Serroni, S. *et al.* Dendrimers based on ruthenium(II) and osmium(II) polypyridine complexes and the approach of using complexes as ligands and complexes as metals. *Chem. Soc. Rev.* **30,** 367–375 (2001).

139. Balzani, V. *et al.* Dendrimers based on photoactive metal complexes. Recent advances. *Coordination Chemistry Reviews* **219–221,** 545–572 (2001).

140. Launay, J. P., Fraysse, S. & Coudret, C. Incorporation of a Photochromic Moiety in a Mixed-Valent Complex: Switching 'On' and 'Off' an Intervalence Electron Transfer. *Mol. Cryst. Liq. Cryst. Sci. Technol. Sect. A. Mol. Cryst. Liq. Cryst.* **344,** 125–132 (2000).

141. Kuang, D. *et al.* High molar extinction coefficient heteroleptic ruthenium complexes for thin film dye-sensitized solar cells. *J. Am. Chem. Soc.* **128,** 4146–4154 (2006).

142. Biener, J. *et al.* Macroscopic 3D nanographene with dynamically tunable bulk properties. *Adv. Mater.* **24,** 5083–5087 (2012).

143. Denti, G. *et al.* Luminescent and Redox-Reactive Building Blocks for the Design of Photochemical Molecular Devices: Mono-, Di-, Tri-, and Tetranuclear Ruthenium(II) Polypyridine Complexes. *Inorg. Chem.* **29,** 4750–4758 (1990).

144. Rudmann, H., Shimada, S. & Rubner, M. F. Solid-state light-emitting devices based on the tris-chelated ruthenium(II) complex. 4. High-efficiency light-emitting devices based on derivatives of the tris(2,2′-bipyridyl) ruthenium(II) complex. *J. Am. Chem. Soc.* **124,** 4918–4921 (2002).

145. Argazzi, R., Bignozzi, C. A., Heimer, T. A., Castellano, F. N. & Meyer, G. J. Enhanced Spectral Sensitivity from Ruthenium(II) Polypyridyl Based Photovoltaic Devices. *Inorg. Chem.* **33,** 5741–5749 (1994).

146. Hager, G. D. & Crosby, G. A. Charge-Transfer Exited States of Ruthenium(II) Complexes. I. Quantum Yield and Decay Measurements. *J. Am. Chem. Soc.* **97,** 7031–7037 (1975).

147. Demas, J. N. & Crosby, G. A. Quantum Efficiencies on Transition Metal Complexes. II.: Charge-Transfer Luminescence. *J. Am. Chem. Soc.* **93,** 2841–2847 (1971).

148. Bradley, P. G., Kress, N., Hornberger, B. A., Dallinger, R. F. & Woodruff, W. H. Vibrational Spectroscopy of the Electronically Excited State. 5. Time-Resolved Resonance Raman Study of Tris(bipyridine)ruthenium(II) and Related Complexes. Definitive Evidence for the 'Localized' MLCT State. *J. Am. Chem. Soc.* **103,** 7441–7446 (1981).

149. Yeh, A. T. Ultrafast Electron Localization Dynamics Following Photo-Induced Charge Transfer. *Science* **289,** 935–938 (2000).

150. Benkö, G., Kallioinen, J., Korppi-Tommola, J. E. I., Yartsev, A. P. & Sundström, V. Photoinduced ultrafast dye-to-semiconductor electron injection from nonthermalized and thermalized donor states. *J. Am. Chem. Soc.* **124,** 489–493 (2002).

151. Lin, C. T., Böttcher, W., Chou, M., Creutz, C. & Sutin, N. Mechanism of the Quenching of the Emission of Substituted Polypyridineruthenium(II) Complexes by Iron(III), Chromium(III), and Europium(III) Ions. *J. Am. Chem. Soc.* **98,** 6536–6544 (1976).

152. Damrauer, N. H. *et al.* Femtosecond dynamics of excited-state evolution in [Ru(bpy)3]2+. *Science* **275,** 54–57 (1997).

153. Broomhead, J. A., Young, C. G. & Hood, P. in *Inorganic Syntheses: Reagents for Transition Metal Complex and Organometallic Syntheses* 338–340 (John Wiley & Sons, Inc., 2007). doi:10.1002/9780470132593.ch86

154. Sullivan, B. P., Salmon, D. J. & Meyer, T. J. Mixed Phosphine 2,2'-Bipyridine Complexes of Ruthenium. *Inorg. Chem.* **17,** 3334–3341 (1978).

155. Zhou, M., Robertson, G. P. & Roovers, J. Comparative Study of Ruthenium(II) Tris(bipyridine) Derivatives for Electrochemiluminescence Application. doi:10.1021/ic0510112

156. Schubert, U. S. & Eschbaumer, C. Macromolecules containing bipyridine and terpyridine metal complexes: Towards metallosupramolecular polymers. *Angewandte Chemie - International Edition* **41,** 2892–2926 (2002).

157. Van Houten, J. & Watts, R. J. The Effect of Ligand and Solvent Deuteration on the Excited State Properties of the Tris(2,2′-bipyridyl)ruthenium(II) Ion in Aqueous Solution. Evidence for Electron Transfer to Solvent. *Journal of the*

American Chemical Society **97,** 3843–3844 (1975).

158. Baudin, H. B. *et al.* Ultrafast energy transfer in binuclear ruthenium-osmium complexes as models for light-harvesting antennas. *J. Phys. Chem. A* **106,** 4312–4319 (2002).

159. Paul Rillema, D., Allen, G., Meyer, T. J. & Conrad, D. Redox Properties of Ruthenium(II) Tris Chelate Complexes Containing the Ligands 2,2′-Bipyrazine, 2,2′-Bipyridine, and 2,2/-Bipyrimidine. *Inorg. Chem.* **22,** 1617–1622 (1983).

160. Hauser, A. & Krausz, E. The excited-state absorption of Ru(bpy)2+3 reexamined. *Chem. Phys. Lett.* **138,** 355–360 (1987).

161. Juris, A., Campagna, S., Balzani, V., Gremaud, G. & Zelewsky, A. von. Absorption Spectra, Luminescence Properties, and Electrochemical Behavior of Tris-Heteroleptic Ruthenium(II) Polypyridine Complexes. *Inorg. Chem.* **27,** 3652–3655 (1988).

162. Fukuzumi, S., Jung, J., Yamada, Y., Kojima, T. & Nam, W. Homogeneous and Heterogeneous Photocatalytic Water Oxidation by Persulfate. *Chem. - An Asian J.* **11,** 1138–1150 (2016).

163. Marcaccio, M. *et al.* Electrochemistry of multicomponent systems. Redox series comprising up to 26 reversible reduction processes in polynuclear ruthenium(II) bipyridine- type complexes. *J. Am. Chem. Soc.* **121,** 10081–10091 (1999).

164. Josefsson, I., Eriksson, S. K., Rensmo, H. & Odelius, M. Solvation structure around ruthenium(II) tris(bipyridine) in lithium halide solutions. *Struct. Dyn.* **3,** 23607 (2016).

165. Dong, W., Shu-Feng, S., Liao, D.-Z., Jiang, Z.-H. & Yan, S.-P. Syntheses and Crystal Structures of Two Ion Pair Complexes, $[Ru(bpy)_3]_2[Fe(CN)_6]I \cdot 7H_2O$ and $[Ru(bpy)_3]$- $[Fe(CN)_5NO]CH_3OH \cdot H_2O$. *J. Coord. Chem.* **56,** 531–538 (2003).

166. Otsuka, T. *et al.* Crystal Structure and Energy Transfer in Double-Complex Salts Composed of Tris(2,2‘-bipyridine)ruthenium(II) or Tris(2,2‘-bipyridine)osmium(II) and Hexacyanochromate(III). *Inorg. Chem.* **38,** 1340–1347 (1999).

167. Gallhuber, E., Hensler, G. & Yersin, H. Magnetic-field effects in the low-temperature polarized emission and absorption spectra of single-crystal tris(2,2’-bipyridine)ruthenium(2+) bis(hexafluorophosphate) ([Ru(bpy)3](PF6)2). *J. Am. Chem. Soc.* **109,** 4818–4822 (1987).

168. Campagna, S. *et al.* Aggregation in Fluid Solution of Dendritic Supermolecules made of Ruthenium(II)- and Osmium(II)-Polypyridine Building Blocks. *J. Am. Chem. Soc.* **117,** 1754–1758 (1995).

169. Rhule, J. T., Hill, C. L., Judd, D. A. & Schinazi, R. F. Polyoxometalates in Medicine. *Chem. Rev.* **98,** 327–358 (1998).

170. Wang, S. S. & Yang, G. Y. Recent Advances in Polyoxometalate-Catalyzed Reactions. *Chemical Reviews* **115,** 4893–4962 (2015).

171. Pope, M. T. & Müller, A. Polyoxometalate Chemistry: An Old Field with New Dimensions in Several Disciplines. *Angew. Chemie Int. Ed. English* **30,** 34–48 (1991).

172. Gumerova, N. I. & Rompel, A. Synthesis, structures and applications of electron-rich polyoxometalates. *Nat. Rev. Chem.* **2,** 112 (2018).

173. Song, Y.-F. & Tsunashima, R. Recent advances on polyoxometalate-based molecular and composite materialsw. *Chem. Soc. Rev. Chem. Soc. Rev* **41221,** 306–12 (2012).

174. Hutin, M., Rosnes, M. H., Long, D. L. & Cronin, L. in *Comprehensive Inorganic Chemistry II (Second Edition): From Elements to Applications* **2,** 241–269 (2013).

175. Judd, D. A. *et al.* Polyoxometalate HIV-1 protease inhibitors. A new mode of protease inhibition. *J. Am. Chem. Soc.* **123,** 886–897 (2001).

176. Absillis, G., Cartuyvels, E., Van Deun, R. & Parac-Vogt, T. N. Hydrolytic cleavage of an RNA-model phosphodiester

catalyzed by a highly negatively charged polyoxomolybdate [M0 7O 24] 6 Cluster. *J. Am. Chem. Soc.* **130,** 17400–17408 (2008).

177. Muñiz, J. *et al.* First principles study on the electronic structure properties of Keggin polyoxometalates on Carbon substrates for solid-state devices. *Theor. Chem. Acc.* **136,** 26 (2017).

178. Busche, C. *et al.* Design and fabrication of memory devices based on nanoscale polyoxometalate clusters. *Nature* **515,** 545–549 (2014).

179. Douvas, A. M. *et al.* Polyoxometalate-based layered structures for charge transport control in molecular devices. *ACS Nano* **2,** 733–742 (2008).

180. Huang, Z. *et al.* Efficient Light-Driven Carbon-Free Cobalt-Based Molecular Catalyst for Water Oxidation. *J. Am. Chem. Soc.* **133,** 2068–2071 (2011).

181. al., A. S. et. Water Oxidation at a Tetraruthenate Core. *J. Am. Chem. Soc.* **131,** 16051–16053 (2009).

182. Toma, F. M. *et al.* Efficient water oxidation at carbon nanotube–polyoxometalate electrocatalytic interfaces. *Nat. Chem.* **2,** 826–831 (2010).

183. Li, M., Wang, W. & Yin, P. A General Approach to Access Morphologies of Polyoxometalate in Solutions Using SAXS: An Ab Initio Modeling Protocol. *Chem. - A Eur. J.* (2018). doi:10.1002/chem.201800344

184. Yin, P. *et al.* X-ray and Neutron Scattering Study of the Formation of Core–Shell-Type Polyoxometalates. *J. Am. Chem. Soc.* **138,** 2638–2643 (2016).

185. Sartorel, A. *et al.* Polyoxometalate embedding of a tetraruthenium(IV)-oxo-core by template-directed metalation of [γ-SiW10O36] 8-: A totally inorganic oxygen-evolving catalyst. *J. Am. Chem. Soc.* **130,** 5006–5007 (2008).

186. Osman, J. R., Crayston, J. A. & Richens, D. T. Structure of Tetrameric Aqua Ruthenium(IV): an Investigation by Ruthenium K Edge EXAFS. *Inorg. Chem.* **37,** 1665–1668 (1998).

187. Heerman, L., Van Nijen, H. & D'Olieslager, W. Electrochemical oxidation of ruthenium(IV) at platinum rotating disk electrodes: preparation and characterization of a tetrameric ruthenium(4.25) species. *Inorg. Chem.* **27,** 4320–4323 (1988).

188. Piccinin, S. *et al.* Water oxidation surface mechanisms replicated by a totally inorganic tetraruthenium-oxo molecular complex. *Proc. Natl. Acad. Sci. U. S. A.* **110,** 4917–4922 (2013).

189. Anwar, N. *et al.* Surface Immobilization of a Tetra-Ruthenium Substituted Polyoxometalate Water Oxidation Catalyst Through the Employment of Conducting Polypyrrole and the Layer-by-Layer (LBL) Technique. *ACS Appl. Mater. Interfaces* **6,** 8022–8031 (2014).

190. Quintana, M. *et al.* Knitting the catalytic pattern of artificial photosynthesis to a hybrid graphene nanotexture. *ACS Nano* **7,** 811–817 (2013).

191. Renger, G. Mechanism of light induced water splitting in Photosystem II of oxygen evolving photosynthetic organisms. *Biochim. Biophys. Acta - Bioenerg.* **1817,** 1164–1176 (2012).

192. Puntoriero, F. *et al.* Photo-induced water oxidation with tetra-nuclear ruthenium sensitizer and catalyst: A unique 4 × 4 ruthenium interplay triggering high efficiency with low-energy visible light. *Chem. Commun.* **46,** 4725 (2010).

193. Glatter, O. Evaluation of small-angle scattering data from lamellar and cylindrical particles by the indirect transformation method. *J. Appl. Cryst.* **13,** 577–584 (1980).

194. Schmidt, P. W. Small Angle X-ray Scattering from Helical Filaments*. *J. Appl. Cryst.* **3,** 257–264 (1970).

195. Hamley, I. W. Form Factor of Helical Ribbons. *Macromolecules* **41,** 8948–8950 (2008).

196. Teixeira, C. V. *et al.* Form factor of an N-layered helical tape and its application to nanotube formation of hexa-peri-hexabenzocoronene-based molecules. *J. Appl. Cryst.* **43,** 850–857 (2010).

197. Volkov, V. V & Svergun, D. I. Uniqueness of ab initio shape determination in small-angle scattering. *J. Appl. Cryst.* **36,** 860–864 (2003).

198. Glatter, O. Computation of Distance Distribution Functions and Scattering Functions for Small Angle Scattering Experiments. *Acta Phys. Austriaca* **52,** 243–256 (1980).

199. Svergun, D. I., Petoukhov, M. V & Koch, M. H. Determination of domain structure of proteins from X-ray solution scattering. *Biophys. J.* **80,** 2946–2953 (2001).

200. Koutsioubas, A. & Pérez, J. Incorporation of a hydration layer in the `dummy atom' ab initio structural modelling of biological macromolecules. *J. Appl. Cryst.* **46,** 1884–1888 (2013).

201. Taleb, N. N. & Douady, R. Mathematical definition, mapping, and detection of (anti)fragility. *Quant. Financ.* **13,** 1677–1689 (2013).

202. Kawaguchi, T. Radii of gyration and scattering functions of a torus and its derivatives. *J. Appl. Cryst.* **34,** 580–584 (2001).

203. Schneidman-Duhovny, D., Hammel, M., Tainer, J. A. & Sali, A. FoXS, FoXSDock and MultiFoXS: Single-state and multi-state structural modeling of proteins and their complexes based on SAXS profiles. *Nucleic Acids Res.* **44,** W424–W429 (2016).

204. Kornmueller, K. *et al.* Tracking morphologies at the nanoscale: Self-assembly of an amphiphilic designer peptide into a double helix superstructure. *Nano Res.* **8,** 1822–1833 (2015).

205. Kozin, M. B. & Svergun, D. I. Automated matching of high- and low-resolution structural models. *J. Appl. Cryst.* **34,** 33–41 (2001).

206. Bergmann, A., Fritz, G. & Glatter, O. Solving the generalized indirect Fourier transformation (GIFT) by Boltzmann simplex simulated annealing (BSSA). *J. Appl. Cryst.* **33,** 1212–1216 (2000).

207. Chen, Z., Baumeister, U., Tschierske, C. & Würthner, F. No Title. *Chem. - A Eur. J.* **13,** 450–465 (2007).

208. Wang, W. *et al.* Dynamic π−π Stacked Molecular Assemblies Emit from Green to Red Colors. *Nano Lett.* **3,** 455–458 (2003).

209. Fink, R. F. *et al.* Exciton Trapping in π-Conjugated Materials: A Quantum-Chemistry-Based Protocol Applied to Perylene Bisimide Dye Aggregates. *J. Am. Chem. Soc.* **130,** 12858–12859 (2008).

210. Wang, W., Wan, W., Zhou, H. H., Niu, S. & Li, A. D. Q. Alternating DNA and π-conjugated sequences. Thermophilic foldable polymers. *J. Am. Chem. Soc.* **125,** 5248–5249 (2003).

211. Burian, M. *et al.* Structural and optical properties of a perylene bisimide in aqueous media. *Chem. Phys. Lett.* **683,** 454–458 (2017).

212. Pontoni, D., Finet, S., Narayanan, T. & Rennie, A. R. Interactions and kinetic arrest in an adhesive hard-sphere colloidal system. *J. Chem. Phys.* **119,** 6157–6165 (2003).

213. Singh, P. *et al.* Electrochemical Capture and Release of Carbon Dioxide Using a Disulfide–Thiocarbonate Redox Cycle. *J. Am. Chem. Soc.* **139,** 1033–1036 (2017).

214. Apaydin, D. H. *et al.* Electrochemical Capture and Release of CO_2 in Aqueous Electrolytes Using an Organic Semiconductor Electrode. *ACS Appl. Mater. Interfaces* **9,** 12919–12923 (2017).

215. Apaydin, D. H., G??owacki, E. D., Portenkirchner, E. & Sariciftci, N. S. Direct electrochemical capture and release of carbon dioxide using an industrial organic pigment: Quinacridone. *Angew. Chemie - Int. Ed.* **53,** 6819–6822 (2014).

216. White, H. S., Becker, W. G. & Bard, A. J. Photochemistry of the tris(2,2'-bipyridine)ruthenium(II)-peroxydisulfate system in aqueous and mixed acetonitrile-water solutions. Evidence for a long-lived photoexcited ion pair. *J. Phys. Chem.* **88,** 1840–1846 (1984).

217. Supur, M. & Fukuzumi, S. Tuning the photodriven electron transport within the columnar perylenediimide stacks by changing the π-extent of the electron donors. *Phys. Chem. Chem. Phys.* **15,** 2539 (2013).

218. Supur, M. & Fukuzumi, S. Photodriven electron transport within the columnar perylenediimide nanostructures self-assembled with sulfonated porphyrins in water. *J. Phys. Chem. C* **116,** 23274–23282 (2012).

219. Klinger, M. More features, more tools, more CrysTBox. *J. Appl. Cryst.* **50,** 1226–1234 (2017).

220. Tenori, E. *et al.* Perylene Derivatives As Useful SERRS Reporters, Including Multiplexing Analysis. *ACS Appl. Mater. Interfaces* **7,** 28042–28048 (2015).

221. Denti, G., Campagna, S., Serroni, S., Ciano, M. & Balzani, V. Decanuclear Homo-and Heterometallic Polypyridine Complexes: Syntheses, Absorption Spectra, Luminescence, Electrochemical Oxidation, and Intercomponent Energy Transfer. *J. Am. Chem. Soc.* **114,** 2944–2950 (1992).

222. Grimme, S., Brandenburg, J. G., Bannwarth, C. & Hansen, A. Consistent structures and interactions by density functional theory with small atomic orbital basis sets. *J. Chem. Phys.* **143,** 54107 (2015).

223. Neese, F. The ORCA program system. *Wiley Interdiscip. Rev. Comput. Mol. Sci.* **2,** 73–78 (2012).

224. Chai, J. Da & Head-Gordon, M. Systematic optimization of long-range corrected hybrid density functionals. *J. Chem. Phys.* **128,** 84106 (2008).

225. James J. P. Stewart. Stewart Computational Chemistry, Colorado Springs. (2012).

226. Draper, E. R. *et al.* pH-Directed Aggregation to Control Photoconductivity in Self-Assembled Perylene Bisimides. *Chem* **2,** 716–731 (2017).

227. Hariharan, P. C. & Pople, J. A. The influence of polarization functions on molecular orbital hydrogenation energies. *Theor. Chim. Acta* **28,** 213–222 (1973).

228. Hehre, W. J., Ditchfield, R. & Pople, J. A. Self—Consistent Molecular Orbital Methods. XII. Further Extensions of Gaussian—Type Basis Sets for Use in Molecular Orbital Studies of Organic Molecules. *J. Chem. Phys.* **56,** 2257–2261 (1972).

229. Walter, C., Krämer, V. & Engels, B. On the applicability of time-dependent density functional theory (TDDFT) and semiempirical methods to the computation of excited-state potential energy surfaces of perylene-based dye-aggregates. *Int. J. Quantum Chem.* **117,** e25337 (2017).

230. Amenitsch, H. *et al.* First performance assessment of the small-angle X-ray scattering beamline at ELETTRA. *J. Synchrotron Radiat.* **5,** 506–508 (1998).

231. Ilavsky, J. Nika : software for two-dimensional data reduction. *J. Appl. Cryst.* **45,** 324–328 (2012).

232. Hammersley, A. P. *et al.* Calibration and correction of distortions in two-dimensional detector systems [a]. *Rev. Sci. Instrum.* **66,** 2729–2733 (1995).

233. Shtykova, E. V. *et al.* Structure and Properties of Iron Oxide Nanoparticles Encapsulated by Phospholipids with Poly(ethylene glycol) Tails. *J. Phys. Chem. C* **111,** 18078–18086 (2007).

234. Shibayama, M., Tanaka, T. & Han, C. C. Small angle neutron scattering study on poly(N-isopropyl acrylamide) gels near their volume-phase transition temperature. *J. Chem. Phys.* **97,** 6829–6841 (1992).

235. Gvishi, R., Reisfeld, R. & Burshtein, Z. Spectroscopy and laser action of the 'red perylimide dye' in various solvents. *Chem. Phys. Lett.* **213,** 338–344 (1993).

236. Sadrai, M. *et al.* Lasing action in a family of perylene derivatives: singlet absorption and emission spectra, triplet absorption and oxygen quenching constants, and molecular mechanics and semiempirical molecular orbital calculations. *J. Phys. Chem.* **96,** 7988–7996 (1992).

7 List of publications

Related to this work – see Appendix A for reprints:

Bonchio, M., Syrgiannis, Z., **Burian, M.,** Pizzolato, E., Dirian, K., Rigodanza, F., Volpato, G.A., La Ganga,G., Marino, N., Demitri, N., Berardi, S., Amenitsch, H., Guldi, D.M., Caramori, S., Bignozzi, C.A., Sartorel, A. & Prato, M., *Artificial Quantasomes: Hierarchical Organization of Perylene-Bisimides and Polyoxometalates for Photo-assisted Water Oxidation.* - Submitted (2018).

Burian, M. & Amenitsch, H., *Dummy atom modelling of stacked and helical nanostructures from solution scattering data.* IUCrJ 5 (2018).

Burian, M., Rigodanza, F., Demitri, N., Đorđević, L., Marchesan, S., Steinhartova, T., Letofsky-Papst, I., Khalakhan, I., Mourad, E., Freunberger, S.A., Amenitsch, H., Prato, M. & Syrgiannis, Z. *Inter-backbone charge transfer as prerequisite for long-range conductivity in perylene bisimide hydrogels.* Submitted (2018).

Arrigo, A., Puntoriero, F., La Ganga, G., Campagna, S., **Burian, M.,** Bernstorff, S. & Amenitsch, H. *Aggregation-Induced Energy Transfer in a Decanuclear Os(II)/Ru(II) Polypyridine Light-Harvesting Antenna Dendrimer*. Chem 3, 494–508 (2017).

Burian, M., Rigodanza, F., Amenitsch, H., Almásy, L., Khalakhan, I., Syrgiannis, Z. & Prato, M. *Structural and optical properties of a perylene bisimide in aqueous media. Chemical Physics Letter* 683, 454–458 (2017).

Burian, M., Syrgiannis, Z., La Ganga, G., Puntoriero, F., Natali, M., Scandola, F., Campagna, S., Prato, M., Bonchio, M., Amenitsch, H. & Sartorel, A. *Ruthenium based photosensitizer/catalyst supramolecular architectures in light driven water oxidation. Inorganica Chimica Acta* 454, 171–175 (2017).

Others:

Burian, M., Karner, C., Yarema, M., Heiss, W., Amenitsch, H., Dellago, C., & Lechner, R.T., Shape induced orientation phase within 3D nanocrystal *solids*. Adv. Mater. - Accepted (2018).

Dirian, K., Bauroth, S., Roth, A., Syrgiannis, Z., Rigodanza, F., **Burian, M.,** Amenitsch, H., Sharapa, D. I., Prato, M., Clark, T. & Guldi, D. M. *A water-soluble, bay-functionalized perylenediimide derivative – correlating aggregation and excited state dynamics.* Nanoscale 10, 2317–2326 (2018).

Sytnyk, M., Yakunin, S., Schöfberger, W., Lechner, R. T., **Burian, M.**, Ludescher, L., Killilea, N. A., Yousefiamin, A., Kriegner, D., Stangl, J., Groiss, H. & Heiss, W. *Quasi-epitaxial Metal-Halide Perovskite Ligand Shells on PbS Nanocrystals.* ACS Nano 11, 1246–1256 (2017).

Prehal, C., Koczwara, C., Jäckel, N., Schreiber, A., **Burian, M.,** Amenitsch, H., Hartmann, M. A., Presser, V. & Paris, O. *Quantification of ion confinement and desolvation in nanoporous carbon supercapacitors with modelling and in situ X-ray scattering.* Nature Energy 2, (2017).

Appendix A:
publications related to this work

A1: Dummy atom modelling of stacked and helical nanostructures from solution scattering data

Max Burian and Heinz Amenitsch*

Institute of Inorganic Chemistry, Graz University of Technology, Stremayrgasse 9/IV, 8010 Graz, Austria.

* correspondence: amenitsch@elettra.eu

Published in *IUCrJ* 5 (2018).

The availability of dummy atom modelling programs to determine the shape of monodisperse, globular particles from small angle solution scattering data has led to outstanding scientific advances. However, no such existing procedure allows modelling of stacked, seemingly-endless structures, such as e.g. helical systems. In this work, we present a bead-modelling algorithm that reconstructs the structural motif of rod-like systems. The algorithm is based on a projection scheme: by exploiting the recurrent nature of stacked systems, such as helices, the full structure is reduced to a single building-block motif. This building-block is fitted by allowing random dummy atom movements without an underlying grid. We verify the proposed method using a variety of analytical models and present examples of successful shape reconstruction from experimental datasets. To expose the algorithm to the scientific community, it is implemented in a graphical computer program that encourages user interaction during the fitting process and also includes an option for shape reconstruction of globular particles.

1 Introduction

Small angle x-ray scattering (SAXS) is an established technique to study structural aspects, such as size and shape, of molecular systems in solution. (Li *et al.*, 2016) As this structural information is not directly apparent from the recorded scattering intensity, one requires a fitting process that generally relies on an underlying mathematical model (Pedersen, 1997). While a variety of such analytic models is available in literature (Pedersen, 1997), each of them is bound to a given shape. The fitting process of an experimental dataset therefore requires previous knowledge of the sample such that the appropriate model can be chosen.

Dummy atom (DA) modelling, so describing the particle shape as a variable bead assembly, bypasses this issue as the fitting process is not anymore constrained to a single geometry (Chacón *et al.*, 1998; Walther *et al.*, 2000; Svergun *et al.*, 2001; Franke & Svergun, 2009; Koutsioubas *et al.*, 2016). Consequently, no *a-priori* knowledge regarding the solute's shape is necessary. This advancement has aided to make SAXS an attractive technique to characterize stable molecules in solution, far outside the scattering experts' community (Yang, 2014).

But, single molecules in solution are not always stable. In fact, it is in their nature to interact and aggregate, often resulting in highly organized hierarchical systems stretching over several orders of magnitude (Palmer & Stupp, 2008; Wasielewski, 2009; Busseron *et al.*, 2013; Praetorius & Dietz, 2017). Helical and chiral superstructures are a common, yet spectacular class of such systems: e.g., the length of the human-genome DNA double-helix exceeds several centimeters (Venter *et al.*, 2001) while the forces that cause the characteristic helical motif act on the molecular, nanometer, level (Dobbs, 2007). Amyloid fibrillation, that is the aggregation of proteins into insoluble often helical fibrils, has been linked to critical diseases such as Type 2 diabetes or Alzheimer (Dobson, 2003; von Bergen *et al.*, 2000) as well as to unwanted drug degradation (Morozova-Roche & Malisauskas, 2007; Vestergaard *et al.*, 2007). Consequently, a comprehensive understanding of these systems requires structural characterization at the (supra-)molecular scale. Small angle x-ray diffraction of aligned fibers (e.g. the famous studies on the structure of DNA (Wilkins *et al.*, 1953; Watson & Crick, 1953)), is a powerful technique for this purpose. However, the evaluation of solution scattering data from randomly oriented helical structures faces two challenges: 1) only a few analytical models are available, from which structural information, such as pitch and twist, can be retrieved (Schmidt, 1970; Pringle & Schmidt, 1970; Hamley, 2008; Teixeira *et al.*, 2010) and 2) the endless nature of helices does not allow DA modelling using current programs (Volkov & Svergun, 2003; Gingras *et al.*, 2008).

In this work, we present a bead-modelling algorithm to determine the structural motif of monodisperse, in 1D highly-elongated systems in solution from SAXS data. We use symmetrical boundary conditions to project the seemingly infinite nature of e.g. helical systems onto a single building-block unit, represented by dummy atoms (DA). This building-block is altered by random DA movements while simultaneously fitting the corresponding scattering curve against the experimental one. The proposed method is verified using

simulated data-sets of various one-dimensional structures and we subsequently applied it to experimentally obtained SAXS data. The full algorithm is implemented in a computer program (SasHel), which also includes an option for globular geometries. The reduction of the system's complexity by symmetric projection as well as the fast code implementation result in a toolkit that allows a full shape retrieval from scattering data in the order of 3-90 minutes on standard work stations (see Appendix A1), depending on the level of detail.

2 Projection scheme

Dummy atom modelling is based on the idea that a given particle shape is represented by an assembly of N small beads of equal scattering length density, also called dummy atoms (DA). According to the Debye formula (Debye, 1915), the scattering intensity of this assembly can then be calculated from the bead assembly as

$$I(q) = f_{DA}(q)^2 \sum_{i=1}^{N} \sum_{j=1}^{N} \frac{\sin(q r_{ij})}{q r_{ij}} \qquad (1)$$

where the norm of the scattering vector is denoted as $q = 4\pi \sin(\theta)/\lambda$ (2θ is the scattering angle and λ is the radiation wavelength) and $f_{DA}(q)$ represents the DA form factor (in this work given by a Gaussian sphere approximation (Koutsioubas & Pérez, 2013; Svergun *et al.*, 1995; Grudinin *et al.*, 2017; Fraser *et al.*, 1978) – a DA diameter of 0.2 nm was used for all reconstructions). As this formalism considers the distances between all possible DA pairs $r_{ij} = |\boldsymbol{r_j} - \boldsymbol{r_i}|$ inside the assembly, its mathematical complexity is $\mathcal{O}(N^2)$. Hence, the computational effort increases drastically for large N. Adequate modelling of seemingly infinite, rod-like geometries requires very large numbers of DAs ($N > 10.000$), making the Debye formula appear inadequate in its standard notation.

Rod-like structures, such as e.g. helical structures, often possess a certain structural motif, a building block, which recurs along the elongation direction. Hence, only this building block is of interest for shape reconstruction. We define a building block of N_{BB} dummy atoms with its elongation direction parallel to the $\boldsymbol{z}$-axis (see Figure 1). The full rod-like structure is then reproduced by duplicating the building block *M* times along the $\boldsymbol{z}$-direction, with a stacking distance corresponding to the building block's height H_{BB} (see Figure 1). The evaluation of this stacked model by means of the Debye formula (equation (1)) now includes redundant

terms, as distinct motifs inside the structure are now recurrent. For instance, the single building block motif would be evaluated at each repetition along ***z***, such that the same computation is performed a total of *M* times. It is therefore sufficient to calculate the scattering intensity of the building block only once and scale it by the number of stacks. The same principle applies to inter-building block contributions: as e.g., the motif of neighboring building-blocks can be found $(M-1)$ times in the full structure we can evaluate this motif once and, again, multiply it by the corresponding scalar.

In mathematical terms, the Debye formula can be adjusted to neglect these redundancies, resulting in

$$I(q) = f_{DA}(q)^2 \left[M \sum_{i=1}^{N_{BB}} \sum_{j=1}^{N_{BB}} \frac{\sin(q|\boldsymbol{r_j} - \boldsymbol{r_i}|)}{q|\boldsymbol{r_j} - \boldsymbol{r_i}|} + 2 \sum_{k=1}^{M-1} (M-k) \sum_{i=1}^{N_{BB}} \sum_{j=1}^{N_{BB}} \frac{\sin(q|(\boldsymbol{r_j} + k \cdot H_{BB}\boldsymbol{e_z}) - \boldsymbol{r_i}|)}{q|(\boldsymbol{r_j} + k \cdot H_{BB}\boldsymbol{e_z}) - \boldsymbol{r_i}|} \right] \quad (2)$$

where $\boldsymbol{e_z}$ denotes the unit vector along the z axis (elongation/stacking direction). This formalism reduces the calculation of the scattering intensity to the sum of structural motifs found inside of the stacked model (see scheme in Figure 1). It further bypasses the demand of a DA model representing the full structure as we solely evaluate projections of the building block instead of all stacked duplicates; hence the term *projection scheme*. Its benefit, compared to the standard Debye formula, is a reduction of the mathematical complexity from $\mathcal{O}((M \cdot N_{BB})^2)$ to $\mathcal{O}(M \cdot N_{BB}^2)$. In the case of the example shown in Figure 1 ($N_{BB} = 400, M = 15$), this increases the calculation speed by approx. 7 fold.

The notion of reducing a given model to its *structural motifs* raises a critical point regarding the required number of stacks *M* necessary to represent a *seemingly endless* structure. This number defines the length of the entire projected model *L*, simply via $L = M \cdot H_{BB}$. According to scattering theory, rod-like structures present a characteristic q^{-1} power-law behavior in the intermediate Porod regime (Glatter & Kratky, 1982), whereas the transition from this Porod regime (q^{-1}) to the adjacent lower-angular Guinier regime $((q^{-0})$ occurs at a specific scattering vector q_1 depending on the length of the rod, which can be estimated with $q_1 = \sqrt{18}/L$ in the simplified framework of the Hammouda-model (Hammouda, 2010). Thus, if the experimental data presents a q^{-1} power-law even at the smallest accessible scattering

angle q_{min}, the length of the structure must be larger than $L > \sqrt{18}/q_{min}$. Similarly, we use this relation to determine the minimal number of required stacks, according to $M > 2 + \sqrt{18}/(H_{BB} \cdot q_{\min})$ (additional term of $+2$ to avoid truncation effects).

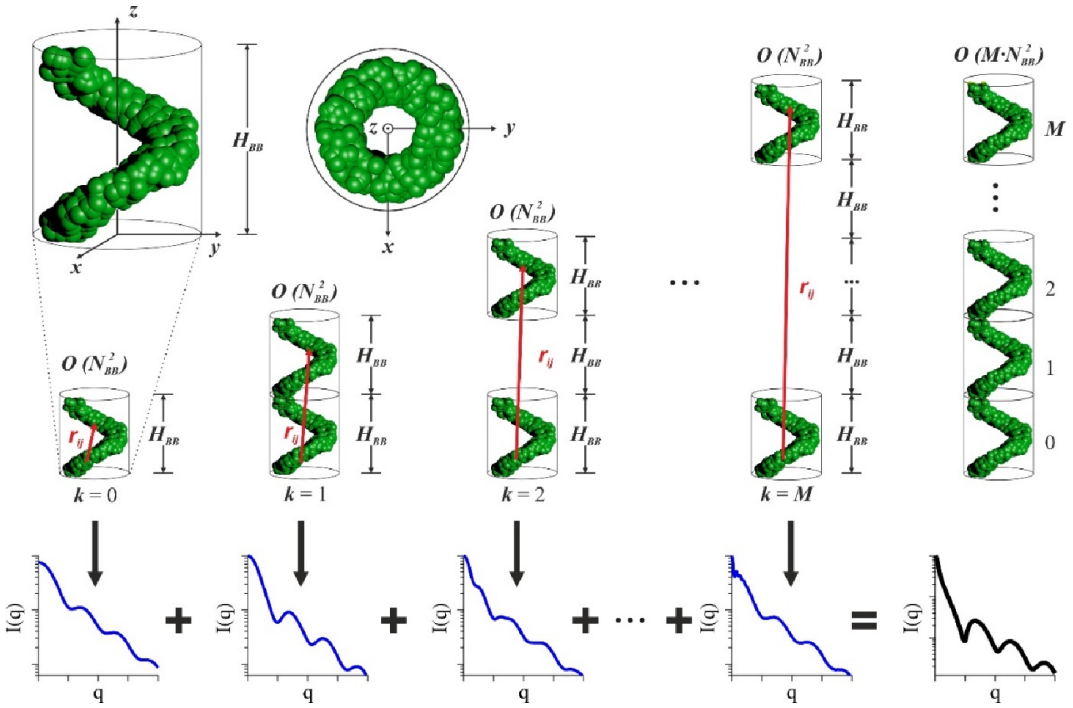

Fig. 1: Projection-scheme, visualized using the example of a single-strand helix. For such seemingly-endless geometries, there exists a building-block (see upper left corner) that is recurrent along the z-axis (see full helix on the right). For a full body consisting of $\boldsymbol{M}$ stacked building-blocks, one finds distinct structural motifs, such as e.g. the building-block itself, neighboring building-blocks, single-spaced building-blocks, up to $(M-1)$-spaced building-blocks. The scattering intensity of the full geometry can hence be calculated by summing up the contributions of these structural motifs, scaled by their recurrence. This bypasses the demand of an actual DA model representing the full structure as we solely evaluate projections of the building block instead of actual stacked duplicates, hence the term *projection scheme.*

3 Determination of the stacking distance

The *projection scheme* is a faster alternative to calculate the scattering intensity of a stacked structure compared to the standard Debye formula. As it is apparent from equation (2), the formalism requires an additional input parameter: the stacking distance between the building-blocks H_{BB}. In the following, we present a pathway to determine this using the pair distance distribution function (PDDF).

The PDDF corresponds to the surface-weighted probability to find two points separated by a distance r inside a particle, see (Glatter & Kratky, 1982). It is thus a histogram of all distances that appear inside a given particle, weighted by the corresponding electron densities. In case of DA assemblies the PDDF can be also interpreted as the volume weighted pair correlation function p(r).

An analytically available example of this definition yields the case of stacked spheres using the algorithm based on (Glatter, 1980) from which a series of conclusions can be drawn (see Supporting Figure S1 for a system of 10 stacked spheres). Evidently, as the system contains of 10 spheres the corresponding PDDF presents 10 peaks. The first peak (see blue trace in Supporting Figure S1) relates to the mean shape of all involved spheres – it is hence an *intra*-building-block PDDF. The following nine peaks (see red traces in Supporting Figure S1) are caused by the repetitive nature of the system as for each possible sphere-to-sphere distance a new peak is found – they are hence *inter*-building-block PDDFs. These *inter*-building-block PDDFs, in particular the distance between them, therefore hold information on the stacking distance between the building-blocks.

In order to determine the stacking-distance of a structure from a given PDDF, it would be intuitive to measure the peak distances. However, the exact peak shapes and therefore positions are distorted due to: 1) the linear high-r decay in the PDDF (see dashed line in Supporting Figure S1) and 2) the overlap of neighboring peak-contributions (Glatter, 1980; Feigin & Svergun, 1987). A direct measurement of the peak positions in the PDDF might therefore result in misdetermination of the stacking-distance. A stable approach to circumvent this issue is to calculate the *derivative* of the PDDF (dPDDF). This numerically fast and easy operation suppresses the mentioned decay distortion (see dPDDF in Supporting Figure S1). The resulting dPDDF can then be fitted by an e.g. damped sinusoidal function in which the

period is directly related to the mean stacking distance (see Supporting Figure S1 and Supporting Information section S1).

A more complex example illustrating the named distortion effects is the case of a torus (ring with circular cross section) (Kawaguchi, 2001). Such a torus presents two characteristic dimensions: the ring-center diameter and the ring-thickness. As a result, the PDDF of such a *single* torus exhibits two distinct peaks correlating to these structural features[2] (see Supporting Figure S2). Considering now the case of *multiple* stacked rings (Kornmueller *et al.*, 2015), for each ring that is added on top of the other(s) we find a new peak in the corresponding PDDF (see Supporting Figures S2 & S3). However, in this case, the radial size of the tori (diameter of 20 nm) was selected larger than the stacking distance between them (7 nm), resulting in an increased distortion of the *inter*-building block peak positions (see distortion phenomenon 2 above as well as Supporting Figure S2). As shown in Supporting Figure S2, the determination of the stacking-distance by fitting of the dPDDF yields a stable result.

We employ this approach to determine the stacking distance from all repetitive structures presented in this work. The advantage of this choice is that we avoid the use of a complementary characterization technique, as the underlying PDDF can be determined from a given dataset using a variety of available software packages. For the interested reader, a more detailed discussion on limitations and possible causes of misdetermination can be found in the Supporting Information sections S1.2 and S1.3 as well as Supporting Figures S1-6.

4 Fitting algorithm

According to the presented *projection scheme*, we reduce a *seemingly infinite* structure to a building-block motif together with two boundary conditions: the stacking-distance H_{BB} and the number of necessary stacks M. As these two values are directly determined from either the PDDF or the scattering data, the *modeling* occurs within the single building-block volume. We thus represent the building-block motif by a dummy atom configuration X such that the scattering intensity $I_{calc}(q_m)$ can be calculated using equation (2). To find a configuration that best fits the experimental scattering intensity $I_{exp}(q_m)$ the relation

[2] The model scattering data, including an artificial error band, was calculated according to Appendix A.

$$\chi^2 = \frac{1}{N_{exp}} \sum_{m}^{N_{exp}} \left(\frac{I_{exp}(q_m) - I_{calc}(q_m)}{\sigma_{\exp}(q_m)} \right)^2 \qquad (3)$$

is to be minimized, where $\sigma_{\exp}(q_m)$ denotes the experimental error and N_{exp} the number of datapoints.

In DA modelling, the principle idea behind this minimization procedure is straightforward: a given initial configuration is gradually altered until best agreement between the corresponding scattering curves is found. Here, we randomly fill an initial building-block volume with DAs that are set free at the start of the fitting procedure (500-1500 DAs per building block are suggested, depending on the experimental resolution – see Supporting Information section S2). We then employ a metaheuristic fitting procedure (Boussaïd *et al.*, 2013; Gogna & Tayal, 2013) with an antifragile implementation (Taleb & Douady, 2013), similar to Simulated Annealing (Kirkpatrick *et al.*, 1983): the algorithm improves the χ^2 by randomly moving single DAs. In contrast to current DA modelling programs, the DAs do not move on an underlying grid. As the magnitude of the movement is scaled by a temperature factor, we force the system to eventually freeze in a given condition and the algorithm to converge.

DA modelling faces the general problem of uniqueness: as models consist of $>10^3$ DAs, the information content given by the scattering data is highly overdetermined by a given configuration. Fitting of the scattering data without restraints can therefore lead to physically unfeasible results, in particular in regard of model homogeneity and compactness. Current algorithms control and optimize these two properties during the fitting process by means of a *looseness penalty* regularization term as a quantitative measure of the DAs' local vicinity: by counting and maximizing the number of contacting neighbors of each DA, a compact and homogeneous configuration is achieved (Svergun, 1999; Franke & Svergun, 2009; Koutsioubas *et al.*, 2016). We adapt this proven technique to our grid-free algorithm in two manners. For one, we introduce the d_{N12} parameter, denoting the distance between a given DA and its 12 (close-packed-limit) next neighbors. Similar to the *looseness penalty,* the d_{N12} quantifies the local vicinity of each DA, acting as a homogeneity classifier for the algorithm to decide if a given DA position is accepted or not. For the other, we apply the idea of a regularization term and introduce a *radial compactness* parameter $RC(X)$ in the minimization procedure, keeping DA close to the (radial) center of mass of the configuration.

As the choice of a grid-free DA algorithm is a departure from current implementations, we face challenges for which no readily available solutions exist so far. In particular, we must introduce new concepts to a) obtain a hard-contact limit for neighboring DAs, b) allow model scalability over different length-scales and c) generate a random movement depending on the current annealing temperature. In the following subsections we discuss these topics in more detail, starting with the introduction of the scaling parameter D_X as well as the random movement generator and then moving to the mathematical definitions of d_{N12} and $RC(X)$ regarding homogeneity and compactness. A general overview of these concepts and its parameters is given in Table 1. At the end of this section, we further address the topic of model uniqueness and repeatability and give a conclusive overview of the algorithm's implementation in the program SasHel.

Table 1: Main concepts of the proposed grid-free fitting algorithm, the corresponding mathematical parameters, their function and their implementation in comparison to current solutions in fixed-grid DA modelling programs. For details on current fixed-grid methods see (Svergun, 1999; Franke & Svergun, 2009; Koutsioubas & Pérez, 2013)

Concept	Fixed-grid methods	Parameter	Function	Implementation
Scalability	Grid size	D_X	Scaling parameter	d_{N12}, $RC(X)$, random movement generator
Homogeneity	Fixed grid / looseness penalty	d_{N12}	Avoid DA clustering / disconnected DAs	Movement classifier / forced reconfiguration
Compactness	Looseness penalty / limited search volume	$RC(X)$ / $D_{X,crit}$	Keep DAs close to (radial) center of mass / avoid model explosion	Regularization term / forced reconfiguration

4.1 Scalability – scaling parameter D_X

Allowing DAs to move randomly without an underlying grid bears an advantage in regard of the model volume and therefore radial size. In a fixed grid system, the final DA density is predefined by the grid-resolution (which is further defined by the real-space resolution provided by the scattering pattern). An e.g. growing model will therefore require an increasing amount of DAs ($N_{DA} \sim r^2$for radial growth) resulting in a significant higher computational overhead. An e.g. shrinking model on the other hand will suffer in spatial resolution. Our grid free approach does not present such limitations: as the number of DAs per building-block is kept constant (depending on the experimental resolution), the algorithm on its own adapts to

a change in DA density while at the same time maintaining relative model resolution and computational resources (see Supporting Information section S2.2 for a discussion on model resolution). This in particular benefits users that have wrongfully chosen the radial size of the starting configuration as the algorithm adapts according to the scattering curve without computational draw-backs. We realize this adaptive potential of our algorithm using an estimated diameter D_X of a given configuration X, which acts as a scaling parameter throughout the algorithm.

We quantitatively track the growing or shrinking of the DA configuration X throughout the fitting process via the radius of gyration $R_{G,X}$. For elongated cases, we assume a cylindrical reference geometry, such that we estimate D_X after every DA movement according to

$$D_X = 2\sqrt{2} * R_{G,X} = 2\sqrt{2} \cdot \sqrt{\frac{1}{N_{BB}} \sum_{i=1}^{N_{BB}} x_i^2 + y_i^2} \qquad (4)$$

Along the z-axis we introduce a continuity condition (see the limited building-block height in Figure 1) such that DAs leaving the building block in the vertical direction are re-projected back inside the building-block volume.

4.2 Random movement generator

As we pursue the concept of grid-free, random DA movements to find an optimal configuration, we require a random movement generator that depends on a series of parameters, including: i) the dimension of the current DA configuration (H_{BB} and D_X), ii) the current temperature T of the fitting process ($1 > T > 0$) and iii) the helical chirality of the sample (helical field bias γ). In every numerical iteration throughout the fitting process, a chosen DA is moved along the unit axes $\boldsymbol{e_x}, \boldsymbol{e_y}$ and $\boldsymbol{e_z}$ by the random vector $\boldsymbol{r_{rand}}(T)$, whereas

$$\boldsymbol{r_{rand}}(T) = \begin{pmatrix} D_X\, T \cdot \left[Rand_x + \gamma\, T \cos\left(\frac{2\pi\, z_i}{H_{BB}}\right) \right] \boldsymbol{e_x} \\ D_X\, T \cdot \left[Rand_y + \gamma\, T \sin\left(\frac{2\pi\, z_i}{H_{BB}}\right) \right] \boldsymbol{e_y} \\ \frac{H_{BB}\, T}{10} \cdot Rand_z\, \boldsymbol{e_z} \end{pmatrix} \qquad (5)$$

Here, a random number generator $Rand$ returns any value between $-1 < Rand_{x,y,z} < 1$ every time when called. In order to adjust the random movement by the size of the current configuration, the radial and longitudal contributions are scaled by the current diameter D_X or the building-block height H_{BB}, respectively (movement along the $\mathbf{z}$ direction is scaled down to ensure axial homogeneity). Further, each movement along either $\boldsymbol{x}, \boldsymbol{y}$ or $\boldsymbol{z}$ direction is scaled by the current temperature T. In case of radial movement along the $\boldsymbol{x}$ or $\boldsymbol{y}$ direction we added a helical bias term (depending on the DA's current $\boldsymbol{e_z}$ position z_i – the building-block motif extents from $z = 0$ to $z = H_{BB}$). This bias term is scaled by the helical field bias γ (user defined with values in the order of $0 < \gamma < 1$, default 0.3) as well as by the current temperature T, such that it favors counter-clockwise solutions (motivated by the first structural model of DNA (Watson & Crick, 1953)). It is important to note that mathematically, the helical bias term correlates quadratically with the current temperature T. Therefore its contribution is only significant in the early stage of the fitting process (see Supporting Figure S11 on its influence on the reconstruction), such that using its default value of 0.3 it does not influence the modelling of non helical systems (see Supporting Figure S15) but facilitates the reconstruction of high aspect helical motives.

In case of fitting of globular structures ($M = 1$), the random movement vector $\boldsymbol{r_{rand}}(T)$ is significantly simplified according to

$$\boldsymbol{r_{rand}}(T) = \begin{pmatrix} D_X\, T\, Rand_x\, \boldsymbol{e_x} \\ D_X\, T\, Rand_y\, \boldsymbol{e_y} \\ D_X\, T\, Rand_z\, \boldsymbol{e_z} \end{pmatrix} \qquad (6)$$

whereas the current diameter D_X is now evaluated over all three directions, such that equation 4 now also includes the contribution of the DAs' current $\boldsymbol{z}$ positions z_i^2.

4.3 Homogeneity - d_{N12} parameter

The random nature of DA movements causes a side-effect in regard of the uniqueness of the fitted model: as there exist infinite possibilities to describe a given structure by randomly filling it with point scatterers, the terminology of a unique model is not reasonable in this context. However, certain criteria related to the homogeneity of the DA configuration make a fitted DA reconstruction, in a physical sense, very unlikely. These scenarios are: 1) high-density DA clusters and 2) single disconnected DAs far away from the remaining configuration.

We optimize the homogeneity throughout the fitting process in analogue to the known *looseness-parameter* in fixed-grid systems (Svergun, 1999; Franke & Svergun, 2009; Koutsioubas & Pérez, 2013): by evaluating the local vicinity around each DA. In these fixed-grid implementations, the distance between neighboring DA is known such that only the number of contacts needs to be counted. In our, grid-free, case we use the same principle in an inverted manner: we assume an ideal close-packed condition with 12 neighbors and calculate their mean distance to the center DA, resulting in the d_{N12} parameter. In the extreme case of a DA within a high-density cluster (scenario 1), d_{N12} will be very small. On the other hand, for a single, free-floating DA that is far away from the core DA assembly (scenario 2), d_{N12} will be very large. The magnitude of d_{N12} is hence inverse proportional to the DA density around a given DA. Equally, the average d_{N12} over the full DA configuration $\langle d_{N12,X} \rangle$ denotes an inverse measure of the mean DA density of the configuration.

We use the d_{N12} parameter for a twofold purpose. In order to avoid szenario 1, we do not allow DAs to come closer than $0.1 \cdot \langle d_{N12,X} \rangle$. This acts as a hard-contact limit such that we circumvent DA clustering and therefore unfeasible singularities throughout the fitting process. In order to avoid szenario 2, we repeatedly force DAs with $d_{N12} > 2 \cdot \langle d_{N12,X} \rangle$ that are outside the mean radial distance $\langle |\boldsymbol{r}| \rangle_X$ to move towards the center of mass of closest fraction of DAs. This avoids free-floating of single DA and therefore forces DAs to remain in a compact configuration. A detailed description on how the d_{N12} parameter is implemented in the fitting algorithm can be found in Supporting Information section S3 and Supporting Figure S27.

4.4 Compactness – radial compactness $RC(X)$

In order to prevent unphysical *disassembly* of the DA configuration during the fitting procedure, we retain DAs close to the radial center of mass (RCOM) of a given configuration. We achieve this by tracking the DA distances from the radial center of mass and weighting it according to a radial-symmetric error-function. As a result, we obtain the radial compactness parameter $RC(X)$ according to

$$RC(X) = \frac{1}{N_{BB}} \sum_{i=1}^{N_{BB}} 0.5 \cdot \left[1 + \mathrm{erf}\left(-0.5 - \left(1 - \frac{2r_i^{com}}{D_x}\right)\frac{\pi}{2}\right)\right] \qquad (7)$$

where r_i^{com} represents the radial distance between the RCOM of X and the i^{th} DA (in case of globular geometries, r_i^{com} represents the distance between the center of mass X and the i^{th} DA). This formalism (based on the solution of the Poisson equation for Gaussian distributed electrostatic charges (Schlick, 2010)) exhibits an asymptotic behavior $(0 < RC(X) < 1)$, which is briefly described in the following. For a very compact structure, such as e.g. a cylinder with a smooth surface or an infinitely thin cylindrical shell, $RC(X)$ will be approx. 0.06 or 0.24, respectively. Each single atom moving further away from D_X will cause $RC(X)$ to increase towards 1. To still allow the building block to grow or shrink in its radial direction throughout the fitting process, the diameter of X and hence the scaling parameter D_X in the calculation of $RC(X)$, is recalculated after every DA movement.

We account for this radial compactness throughout the fitting process by using $RC(X)$ scaled by the compactness weight β as a regularization term. Thus, the algorithm in fact minimizes the functional

$$f(X) = \chi^2 + |\beta| \cdot RC(X) \qquad (8)$$

instead of only χ^2 alone.

As an ultimate radial boundary, similar to the search volume diameter in DAMMIN, we apply a critical diameter $D_{X,crit} = 2 \cdot D_X$ such that single DAs moving far away from the RCOM are repeatedly forced into a more compact configuration (see Supporting Information section S3 and Supporting Figure section S27 for a detailed description on how the radial compactness is implemented in the algorithm).

4.5 Model resolution and uniqueness

The most obvious, visual side-effect of using random movements is related to the outer surface of the fitted model. E.g., if DAs can only move on an artificial grid, the fitted configuration of a globular particle will present a surface smoothness according to the lattice planes of the grid. As already discussed above, allowing random DA movements results in infinite possibilities to represent a given particle volume and thus also its surface. Consequently, the surface of a random movement fitted configuration will be significantly rougher than a corresponding fixed-grid model. However, this increased surface roughness is just a visual symptom of the information content provided by the scattering curve as we discuss in the following.

In absolute terms, it can be expected to end up with a fitted configuration that presents structural features on the surface *and* within its volume below the resolution limit of the experimental data ($d_{min} = \pi/q_{max}$ where q_{max} is the upper angular range of the experimental data). This implies that e.g. thin helical tapes require a large accessible angular range in order to be resolved properly. If this is not the case, the retrieved model is at high risk of being over interpreted. On a less obvious note, a low angular resolution can further lead to artefacts *within* the configuration that might not be seen by a common surface representation (we address this topic in more detail in the Supporting Information section S2).

A common technique to avoid misinterpretation of such artefacts is to test the reproducibility of the reconstruction (Volkov & Svergun, 2003). This approach bears a series of advantages. First, the overall stability and reliability of the reconstruction from a given dataset is assessed. Second, a consecutive averaging process of all reconstructions projects DAs onto an artificial, occupancy-weighted grid, which provides a straight-forward procedure to determine DA validity and volume inhomogeneity. Third, this occupancy map helps to identify structural artefacts in single reconstructions caused by insufficient information content of the scattering data, thus avoiding over interpretation. Fourth, the reconstruction of an arbitrary shape from scattering data is a (highly) underdetermined problem such that it is not guaranteed to obtain a unique result from a given fitting algorithm. Performing a reproducibility analysis whenever reconstructing the structural motif from experimental scattering data, in particular when information content and validity of the data are questionable, is hence highly recommended. In quantitative terms, the reproducibility of a reconstruction may be judged by the mean normalized spatial discrepency <NSD> of parallel reconstructions, which represents an measure of dissimilarity (<NSD> = 0 for identical models) of the independent runs.(Volkov

& Svergun, 2003) In the following section, we present reference values for a series of model geometries.

4.6 Implementation

We implemented the fitting algorithm in the computer program SasHel: a Qt graphical user interface (GUI) written in C++ that allows user interaction. When starting a fitting procedure, the program generates a random cylindrical starting-configuration according to a user-defined diameter, the building block stacking distance and number of DAs per building-block. Once started, the fitting algorithm undergoes N_k iterations: starting from a temperature T_0 the system cools down as defined by the quenching coefficient q_T $(0 < q_T < 1)$ such that the current temperature at a given iteration k is $T_k = T_0 \cdot q_T^k$ (we recommend the default values $N_k = 100$, $T_0 = 1$ and $q_T = 0.99$ as an initial set of parameters for convergence). In each k-iteration, all DAs are randomly moved using the random movement generator (see section 4.2.) under the restraints explained in section 4.3, such that a movement is only accepted if: a) the new DA position complies with the hard contact limit $0.1 \cdot \langle d_{N12,X} \rangle$ (if not, up to 100 new movements are considered) and b) an improvement of the functional $f(X)$ is found (see equation 8). After each k-iteration the sequence of DA is randomly mixed to avoid sequential biasing of the algorithm.

Throughout the fitting procedure, we pursue the concept of antifragility (Taleb & Douady, 2013), a concept applicable to metaheuristic optimization (Boussaïd *et al.*, 2013; Gogna & Tayal, 2013): the converging system is repeatedly forced out of its local minimum such that a global minima is more likely to be found. These non-optimal moves are forced onto the configuration without consideration of the damage caused to the model, making the algorithm less prone to distortion of the solution space by regularization terms. A summary of the full algorithm, including an exemplary implementation in pseudo code, can be found in Supporting Information section S3 and Supporting Figure S27.

The program SasHel further includes a “parallel mode” that runs a unique reconstruction on each available CPU core such that the model validity and reproducibility can easily be tested using e.g. DAMAVER (Volkov & Svergun, 2003).

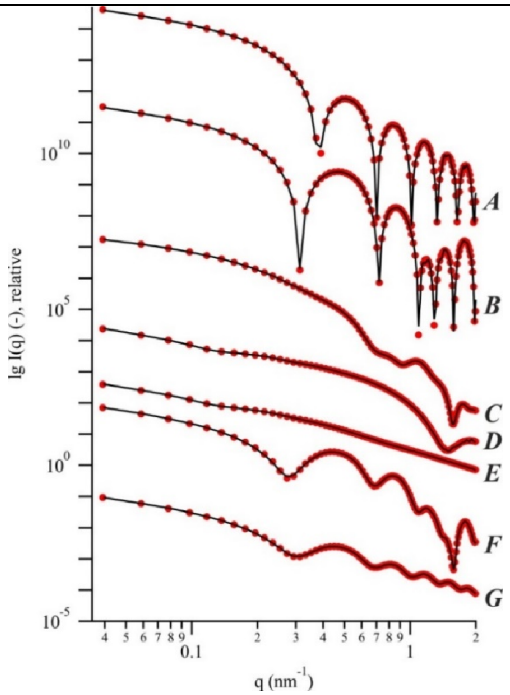

Fig. 2: Scattering curves computed from seemingly endless model geometries *A*-*G* shown in Figure 3 (red circles - see Appendix A for model details) and fits from the reconstruction (black lines). For better visualization, the scattering patterns are shifted vertically and error bars are omitted (see Supporting Figure S14 for a high-q magnification f).

5 Model examples

To test the implemented algorithm, we simulated a number of scattering intensities from seemingly-endless bodies (see Appendix A for detailed dimensions). All reconstructions were performed using the default fitting parameters as follows: starting temperature $T_0 = 1$, quenching coefficient $q_T = 0.99$, number of iterations $N_k = 200$, helical bias parameter $\gamma = 0.3$, compactness weight $\beta = 1$, DA formfactor diameter $D_{DA} = 0.2\,nm$ and number of stacked building blocks $M = 10$). The dimensions of the initial random configuration, including the stacking-distance of the building blocks, were determined from the relative dPDDFs (see Supporting Figure S12 and S13). For all reconstructions, we used 500-800 DAs per building-block, resulting in computation times for each run between 20-60 minutes on a standard workstation, respectively.

The scattering intensities of the theoretical models are shown in Figure 2 along with the fits from the reconstructions. For all used geometries, we find agreement between the theoretical and fitted scattering intensities (the χ^2 value of all fits is below the threshold of 0.1). Yet,

cases ***A-D*** show slight oscillations in the higher q-regime $1 < q < 2nm^{-1}$ (see Supporting Figure S14), which is a resonance effect caused by the stacking nature of identical building-blocks (see Supporting Information section S2.3).

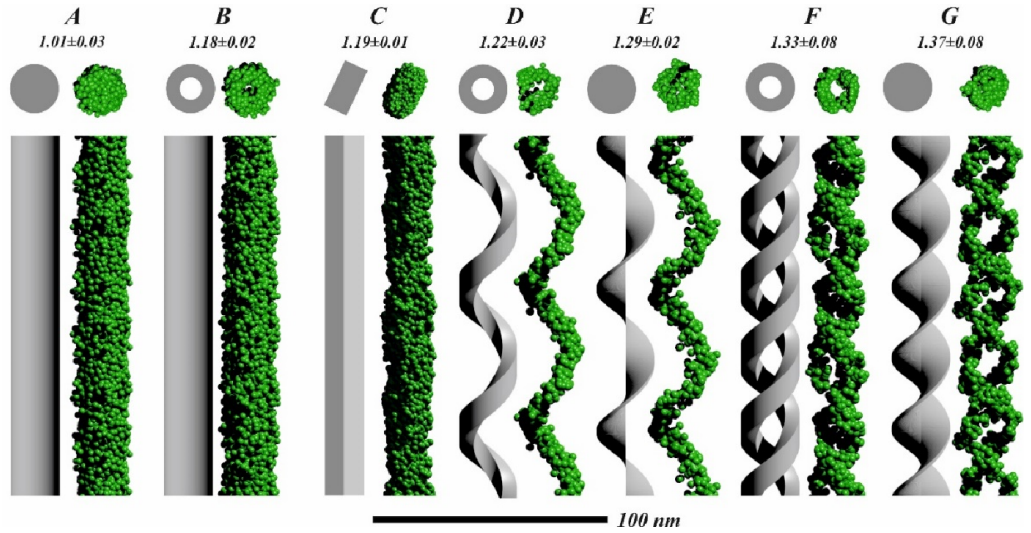

Fig. 3: Theoretical and reconstructed 3D models of the used seemingly-endless geometries. The numbers below the labels denote the mean normalized spatial discrepancy (<NSD>), obtained from eight independent reconstructions (random artificial cylinder: <NSD> = 1.03 ± 0.01, random artificial single-strand helix: <NSD> = 1.06 ± 0.01). The PDDFs and dPDDFs used to determine the stacking-distance between the building-block can be found in Supporting Figures S12 & S13. See Figure 2 for the corresponding scattering intensities as well as Supporting Figure S15 for point representations, as denoted by the letters ***A-G***.

Figure 3 presents the corresponding 3D models and reconstructions (see Supporting Figure S15 for point representations). Models ***A*** and ***B*** show a circular cross-section in agreement with the model, while in the case the cylindrical shell, the empty core is present. Further, the rectangular cross section of model ***C*** is visible in the reconstructed model. However, the sharp corners are not fully resolved, which is most likely the effect of insufficient resolution from the scattering data ($d_{res} \approx 1.6$ nm compared to the rectangular cross section: $a\ x\ b = 4\ x\ 20$ nm). In the cases ***D-G***, the helical fingerprints (single or double-strand nature) are well resolved in the reconstructed models. ***D*** and ***E*** as well as ***F*** and ***G*** present noticeable differences in their cross-sections, helping to distinguish between helical filament (empty core) and helical tape (filled core). Further, variations in the thickness of the helical strands can be observed. The overall agreement of model and reconstruction of the main features demonstrates the functionality of the algorithm for similar, seemingly-endless bodies.

In order to evaluate the stability and reproducibility of the reconstruction algorithm, eight independent runs for each model geometry were analyzed using DAMAVER according to the

literature (Volkov & Svergun, 2003). Accordingly, we obtain the mean normalized spatial discrepancy (<NSD>) as a measure of similarity between the independent reconstructions of each model (<NSD> = 0 for identical configurations). As shown in Figure 3, the <NSD> of ***A-G*** gradually increases from $1.01 - 1.37$ with model complexity. On absolute scale, these <NSD> values are higher compared to literature (Volkov & Svergun, 2003), where stable reconstructions were linked to a <NSD> of $0.4 - 0.7$. The reason for this difference is found in the grid-free nature of our approach: NSD values for grid-free programs such as e.g. GASBOR are generally higher (Svergun *et al.*, 2001). To validate our findings, we constructed eight randomly filled, artificial cylinders and single-strand helices ($N_{DA} = 700$), yielding a <NSD> of 1.03 ± 0.01 and 1.06 ± 0.01, respectively. These values, in context with the <NSD> of the above reconstructions, provide a reference for grid-free models where a <NSD> between 1 and 1.4 is observed.

It is also possible to run the fitting algorithm using only $M = 1$ stacks, which corresponds to the case of the building block alone. Thus, the same program can also be used to fit globular particles. We tested this option similar to above by simulating a number of scattering intensities from globular bodies (see Appendix A for detailed dimensions). For all reconstructions, we used the same default fitting parameters as mentioned previously. The dimensions of the initial random configurations were determined from the maximum dimension found in the relative PDDFs (see Supporting Figure S12). However, we increased the number of DAs to 800-1200 DAs, now resulting in computation times between 5-10 minutes per run on a standard workstation, respectively.

The scattering intensities of the theoretical models along with the fits from the reconstructions are shown in Figure 4a. For all used geometries, we find agreement between the theoretical and fitted scattering intensities (the χ^2 value of all fits is below the threshold of 0.1). Evidently, the oscillations previously found for the repeating motive in the higher angular regime (see Figure 2) are not present. The 3D models and reconstructions corresponding to the scattering patterns are shown in Figure 4b (see Supporting Figure S16 for point representations). Also in this case, the fitted morphologies clearly represent the according models, including the hollow geometries ***I*** and ***L***. <NSD> values of eight independent reconstructions of each geometry are within the range of $0.96 - 1.28$, as denoted in Figure 4b (in relative terms, the <NSD> of eight randomly filled artificial spheres and cubes ($N_{BB} = 1500$) was 1.04 ± 0.01 and 1.06 ± 0.01, respectively). These findings validate the use of the algorithm also for globular bodies.

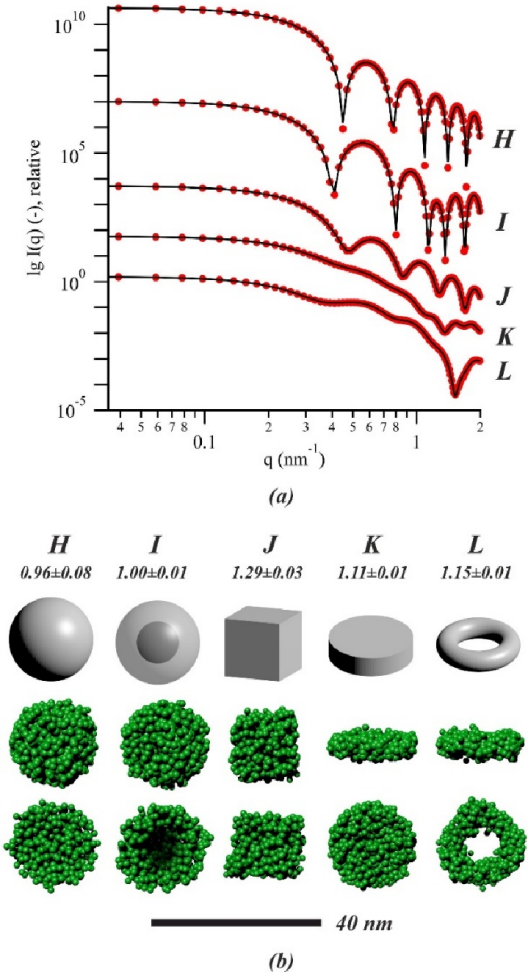

Fig. 4: (a) Scattering curves computed from globular model geometries (red circles – see Appendix A for model details) and fits from the reconstruction (black lines). For better visualization, the scattering patterns are shifted vertically and error bars are omitted. The PDDFs of all models can be found in Supporting Figure S12. **(b)** Theoretical and reconstructed 3D models of the used globular geometries (see Supporting Figure S16 for point representations of the reconstructions). The numbers below the labels denote the mean normalized spatial discrepancy (<NSD>), obtained from eight independent reconstructions (random artificial sphere: <NSD> = 1.04 ± 0.01, random artificial cube: <NSD> = 1.06 ± 0.01).

6 Experimental examples

As final example, we applied the described reconstruction procedure to experimental data of a self-assembled peptide double-strand-helix (Kornmueller *et al.*, 2015). Prior to the fitting process, we determined a building-block stack-spacing of 53 nm from the corresponding PDDF (see inset Figure 5 and Supporting Figure S13). The scattering data was then fitted using 800 DAs over the angular range $0.08 < q < 2.14$ nm^{-1}, resulting in a real-space resolution of approx. π/q_{max} = 1.5 nm, whereas the default fitting parameters according to section 4 were used.

As shown in Figure 5a, we again find agreement between the experimental and fitted scattering curves (χ^2=0.08). The corresponding real-space reconstruction (Figure 5b) presents two independent tapes within the building block (see Supporting Figure S17a for point representations). However, the two tapes do not appear to be symmetric along the z-direction, suggesting a displacement angle of $\varphi \neq 180°$ between them. The cross-section of the helical-tapes presents a rather rough surface that does not allow more detailed interpretation, as typical for such random-movement DA models. Nevertheless, a comparison of the reconstruction with the model according to the previously published dimensions (Kornmueller *et al.*, 2015) is in good agreement (see red model in Figure 5c). A movie of the rotating helices can be found in the electronic Supporting Information. To obtain a measure of uniqueness of the final model, we repeated the fitting procedure to end up with 16 independent reconstructions. The average of all 16 models (Volkov & Svergun, 2003), as shown in Supporting Figure S18a, is consistent with the single reconstruction. In agreement with the reference values shown in Figure 3, the <NSD> was found to be 1.27 ± 0.02, hence confirming the reproducibility of the reconstruction.

In analogue to above, we further applied the reconstruction procedure to experimental data of the globular protein alcohol dehydrogenase 1 (ADH) in PBS at pH 7.5. The data set was taken from the SASBDB database[3] (Valentini *et al.*, 2015), corresponding to the identifier *SASDA52*. Again, we first determined the size of the initial random configuration ($d = 9$ nm) from the PDDF, as seen in Figure 5 right. We then fitted the scattering data over the angular range $0.13 < q < 6\ \mathrm{nm}^{-1}$, corresponding to a real-space resolution of approx. 0.5 nm. The default fitting parameters ($M = 1$) according to section 4 were used, yet this time, the number of DAs was increased to 1500, due to the outstanding angular range.

[3] Date of download: Dec. 12th, 2016

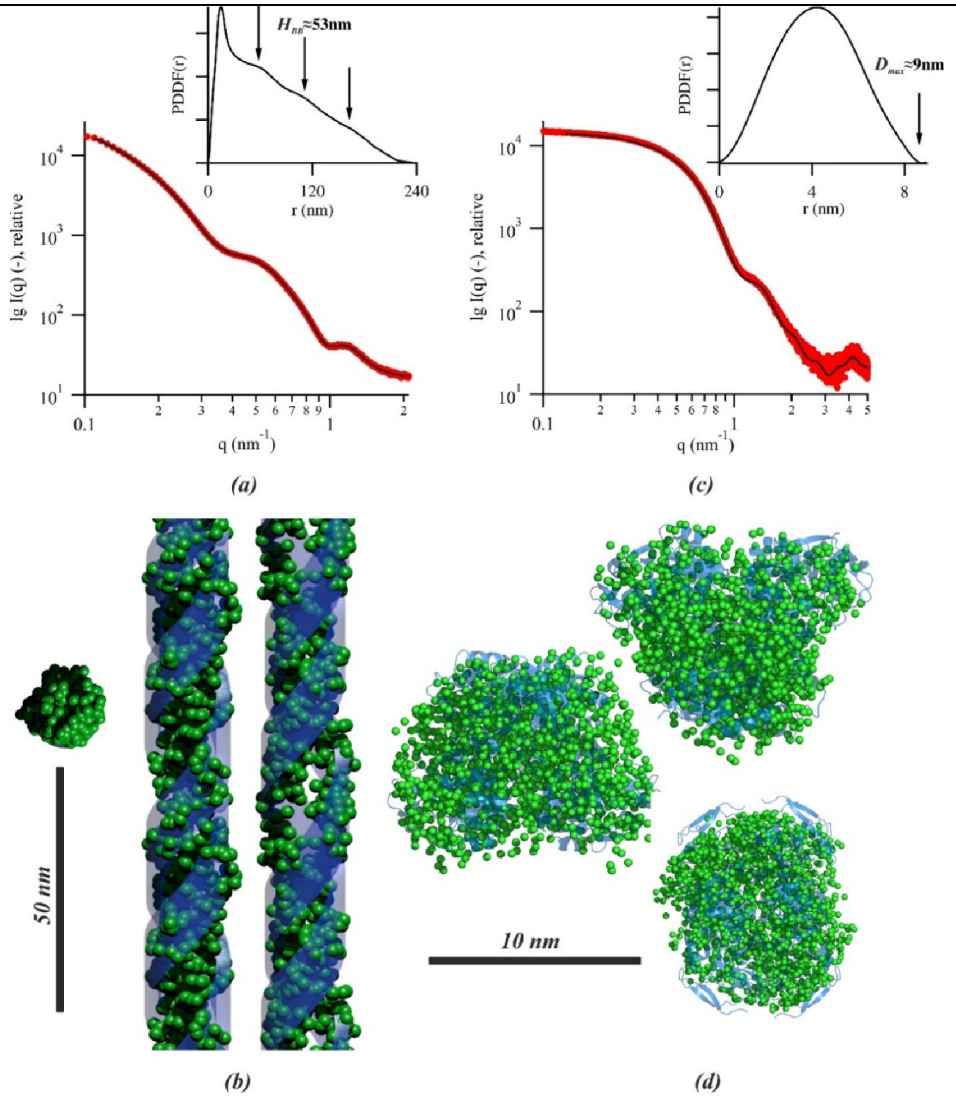

Fig. 5: Verification of the reconstruction algorithm using experimental scattering data. (a) Experimental scattering data (error bars omitted for clarity) and fitted curve from the reconstruction of the self-assembled peptide double-helix. The corresponding pair distance distribution function (PDDFs) is shown in the inset whereas the dPDDF used to determine the stacking-distance can be found in Supporting Figure S13. **(b)** Orthogonal views of the model reconstructed from the scattering pattern in **(a)** (green), compared to previously published structure (blue). **(c)** Experimental data, fitted curve and PDDF for alcohol dehydrogenase 1 (ADH). **(d)** Orthogonal views of the model reconstructed from the scattering pattern in **(c)** (green), compared to the crystal structure model (blue). See Supporting Figure S17 for point representations of the reconstructions shown in **(b)** and **(d)** as well as Supporting Figure S18 for numerical stability analysis of both reconstructions.

Also in this case, the experimental data is fully fitted throughout the reconstruction procedure (χ^2=0.24 - see Figure 5c). Interestingly, the corresponding real-space model (Figure 5d) presents a characteristic triangular cross-section that is recurrent from different perspectives (see Supporting Figure S17b for point representations). We thus compared the reconstruction to the ADH crystal structure found in the literature (Raj *et al.*, 2014), whereas an overlay of

both models can be seen in Figure 5 bottom. Undoubtedly, the reconstructed model is qualitatively in agreement with the molecular structure – quantitatively we find a NSD between crystal structure and reconstruction of 0.93. Also in this case, we performed a total of 16 independent reconstructions (<NSD> of 1.20 ± 0.02), whereas the averaged representation is consistent with molecular structure (see Supporting Figure S18b).

This, in congruence with the upper example, demonstrates the applicability of the proposed fitting algorithm for real-space reconstruction of seemingly-infinite and globular geometries from experimental small angle scattering data.

7 Conclusions

In conclusion, we present a new method for the reconstruction of the structural motif of seemingly-endless rod-like systems, such as helices. In this regard, the following points were critical:

(i) We optimized the numerical complexity of the Debye formula for the unique case of a recurrent symmetry along the elongation direction, resulting in the proposed *projection scheme*.

(ii) Based on this *projection scheme*, we developed a metaheuristic fitting algorithm: Instead of minimizing a variety of structural penalties (Franke & Svergun, 2009), the system is repeatedly forced out of the current numerical equilibrium by forcing DA to move, regardless of the caused damage.

(iii) The algorithm is implemented in a multi-platform compatible graphical computer program SasHel, which allows live tracking of the fitting progress in real and reciprocal space and encourages user interaction.

We demonstrate the functionality and reliability of the presented method using a variety of analytical and experimental examples. These showcases provide a comprehensive reference for future users. We further address and discuss the risks of wrongfully chosen fitting parameters as well as insufficient data quality: we illustrate a series of negative examples to discuss which reconstructed features might be true or not (see Supporting Information section S2 as well as Supporting Figures S7-11, S19-26). SasHel, the computer program corresponding to this work, also includes an option for shape reconstruction of globular particles. This, in congruence with its originally intended use, makes the program applicable

over a wide range of SAXS-based structural studies, expanding the scope of currently available dummy atom modelling software.

The program SasHel is freely available for academic use. The most current version can be obtained upon publication from http://www.tugraz.at or upon request from the authors.

Acknowledgement

We thank K. Kornmüller and R. Prassl for providing us the experimental scattering data of the self-assembled peptide-double-helix. We further thank M. DeMarco for the first core implementation of the algorithm and consultation throughout the program development as well as M. Kriechbaum for revision of the manuscript. This project has received funding from the EU-H2020 research and innovation program under grant agreement No 654360 NFFA-Europe.

References

von Bergen, M., Friedhoff, P., Biernat, J., Heberle, J., Mandelkow, E. M. & Mandelkow, E. (2000). *Proc. Natl. Acad. Sci. U. S. A.* **97**, 5129–5134.

Bergmann, A., Fritz, G. & Glatter, O. (2000). *J. Appl. Cryst.* **33**, 1212–1216.

Boussaïd, I., Lepagnot, J. & Siarry, P. (2013). *Inf. Sci. (Ny).* **237**, 82–117.

Busseron, E., Ruff, Y., Moulin, E. & Giuseppone, N. (2013). *Nanoscale*. **5**, 7098.

Chacón, P., Morán, F., Díaz, J. F., Pantos, E. & Andreu, J. M. (1998). *Biophys. J.* **74**, 2760–2775.

Damaschun, G., Müller, J. J. & Pürschel, H. V. (1968). *Monatshefte Für Chemie*. **99**, 2343–2348.

Debye, P. (1915). *Ann. Phys.* **351**, 809–823.

Dobbs, M. B. (2007). *Clin. Orthop. Relat. Res.* **462**, 2.

Dobson, C. M. (2003). *Nature*. **426**, 884–890.

Feigin, L. A. & Svergun, D. I. (1987). Structure Analysis by Small-Angle X-Ray and Neutron Scattering. New York: Plenum Press.

Franke, D. & Svergun, D. I. (2009). *J. Appl. Cryst.* **42**, 342–346.

Fraser, R. D. B., Macrae, T. P. & Suzuki, E. (1978). *J. Appl. Cryst*. **11**, 693–694.

Gingras, A. R., Bate, N., Goult, B. T., Hazelwood, L., Canestrelli, I., Grossmann, J. G., Liu, H., Putz, N. S. M., Roberts, G. C. K., Volkmann, N., Hanein, D., Barsukov, I. L. & Critchley, D. R. (2008). *EMBO J.* **27**, 458–469.

Glatter, O. (1980). *Acta Phys. Austriaca*. **52**, 243–256.

Glatter, O. & Kratky, O. (1982). Small Angle X-ray Scattering London: Academic Press.

Gogna, A. & Tayal, A. (2013). *J. Exp. Theor. Artif. Intell.* **25**, 503–526.

Grudinin, S., Garkavenko, M., Kazennov, A. & IUCr (2017). *Acta Crystallogr. Sect. D Struct. Biol.* **73**, 449–464.

Guinier, A. & Fournet, G. (1955). Small angle scattering of X-rays. New York: John Wiley & Sons, Inc.

Hamley, I. W. (2008). *Macromolecules*. **41**, 8948–8950.

Hammouda, B. (2010). *J. Appl. Cryst.* **43**, 1474–1478.

Kawaguchi, T. (2001). *J. Appl. Cryst.* **34**, 580–584.

Kirkpatrick, S., Gelatt, C. D. & Vecchi, M. P. (1983). *Science*. **220**, 671–680.

Konarev, P. V. & Svergun, D. I. (2015). *IUCrJ*. **2**, 352–360.

Kornmueller, K., Letofsky-Papst, I., Gradauer, K., Mikl, C., Cacho-Nerin, F., Leypold, M., Keller, W., Leitinger, G., Amenitsch, H. & Prassl, R. (2015). *Nano Res.* **8**, 1822–1833.

Koutsioubas, A., Jaksch, S. & Pérez, J. (2016). *J. Appl. Cryst.* **49**, 690–695.

Koutsioubas, A. & Pérez, J. (2013). *J. Appl. Cryst.* **46**, 1884–1888.

Li, T., Senesi, A. J. & Lee, B. (2016). *Chem. Rev.* **116**, 11128–11180.

Morozova-Roche, L. & Malisauskas, M. (2007). *Curr. Med. Chem.* **14**, 1221–1230.

Palmer, L. C. & Stupp, S. I. (2008). *Acc. Chem. Res.* **41**, 1674–1684.

Pedersen, J. S. (1997). *Adv. Colloid Interface Sci.* **70**, 171–210.

Praetorius, F. & Dietz, H. (2017). *Science*. **355**, eaam5488.

Pringle, O. A. & Schmidt, P. W. (1970). *J. Appl. Cryst.* **4**, 290–293.

Raj, S. B., Ramaswamy, S. & Plapp, B. V. (2014). *Biochemistry*. **53**, 5791–5803.

Schlick, T. (2010). Molecular Modeling and Simulation: An Interdisciplinary Guide New York, NY: Springer New York.

Schmidt, P. W. (1970). *J. Appl. Cryst.* **3**, 257–264.

Shannon, C. E. & Weaver, W. (1949). The Mathematical Theory of Communication Urbana: University of Illinois Press.

Svergun, D., Barberato, C. & Koch, M. H. J. (1995). *J. Appl. Cryst*. **28**, 768–773.

Svergun, D. I. (1999). *Biophys. J.* **76**, 2879–2886.

Svergun, D. I., Petoukhov, M. V & Koch, M. H. (2001). *Biophys. J.* **80**, 2946–2953.

Taleb, N. N. & Douady, R. (2013). *Quant. Financ.* **13**, 1677–1689.

Taupin, D. & Luzatti, V. (1982). *J. Appl. Cryst*. **15**, 289–300.

Teixeira, C. V., Amenitsch, H., Fukushima, T., Hill, J. P., Jin, W., Aida, T., Hotokka, M. & Lindén, M. (2010). *J. Appl. Cryst.* **43**, 850–857.

Valentini, E., Kikhney, A. G., Previtali, G., Jeffries, C. M. & Svergun, D. I. (2015). *Nucleic Acids Res.* **43**, D357-63.

Venter, J. C., Adams, M. D., Myers, E. W. & Al., E. (2001). *Science*. **291**, 1304–1351.

Vestergaard, B., Groenning, M., Roessle, M., Kastrup, J. S., de Weert, M. van, Flink, J. M., Frokjaer, S., Gajhede, M. & Svergun, D. I. (2007). *PLoS Biol.* **5**, e134.

Volkov, V. V & Svergun, D. I. (2003). *J. Appl. Cryst.* **36**, 860–864.

Walther, D., Cohen, F. E. & Doniach, S. (2000). *J. Appl. Cryst.* **33**, 350–363.

Wasielewski, M. R. (2009). *Acc. Chem. Res.* **42**, 1910–1921.

Watson, J. D. & Crick, F. H. C. (1953). *Nature*. **171**, 737–738.

Wilkins, M. H. F., Stokes, A. R. & Wilson, H. R. (1953). *Nature*. **171**, 738–740.

Yang, S. (2014). *Adv. Mater.* **26**, 7902–7910.

Appendix A1: Model calculations

All scattering patterns shown throughout this work were calculated according to the literature, whereas the exact dimensions and references are shown in Table 2. The error-band of each

dataset was estimated according to $\sigma(q) = 0.2\ [cm^{-\frac{1}{2}}] \cdot \sqrt{I(q)}$ (see Supporting Information section S2 and Supporting Figures S19-23 for test-cases with noisy data). For models ***A-L*** we used a total of 124 data-points in the angular range $0.01 < q < 2\ \mathrm{nm}^{-1}$. In case of the seemingly endless geometries, we further ensured that the stacking-distance H_{BB} is resolvable in the lower angular limit ($H_{BB} < \pi/q_{min}$). All PDDFs throughout this work were calculated using the GIFT software package (Bergmann *et al.*, 2000).

All reconstructions were performed on a "standard work station" from Hewlett-Packard, using an Intel Core i7 4800MQ processor with 4 cores, each operating @ 2.7 GHz.

Table 2: Detailed dimensions of the models shown in Figures 3 and 4 – explanation of the model variables can be found in the corresponding references. [1] (Feigin & Svergun, 1987); [2] (Pringle & Schmidt, 1970); [3] (Guinier & Fournet, 1955); [4] (Kawaguchi, 2001)

	Model											
Parameter	**A**	**B**	**C**	**D**	**E**	**F**	**G**	**H**	**I**	**J**	**K**	**L**
Reference	[1]	[1]	[1]	[2]	[2]	[2]	[2]	[1]	[1]	[1]	[3]	[4]
R_o **(nm)**	10	10	-	10	10	10	10	10	10	-	10	10
R_i **(nm)**	0	5	-	5	0	5	0	-	5	-	-	5
a; b (nm)	-	.	8; 20	-	-	-	-	-	-	15	-	-
L = c (nm)	1000	1000	1000	1000	1000	1000	1000	-	-	15	5	-
P (nm)	-	-	-	50	50	50	50	-	-	-	-	-
ω **(°)**	-	-	-	45	6	45	6	-	-	-	-	-
φ **(°)**	-	-	-	-	-	180	180	-	-	-	-	-

A2: Aggregation-induced energy transfer in a decanuclear, mixed-metal Os(II)/Ru(II) polypyridine light-harvesting antenna dendrimer

Antonino Arrigo,[1] Fausto Puntoriero,[1] Giuseppina La Ganga,[1] Sebastiano Campagna,[1,*] **Max Burian**,[2] Sigrid Bernstorff[3] and Heinz Amenitsch[2,*]

[1]Dipartimento di Scienze Chimiche, Biologiche, Farmaceutiche ed Ambientali, Università di Messina, and Centro Interuniversitario per la conversione dell'energia solare (SOLARCHEM), via F. Stagno d'Alcontres 31, 98166 Messina, Italy. campagna@unime.it

[2]Institute of Inorganic Chemistry, Graz University of Technology, Stremayergasse 9/V, 8010 Graz, Austria

[3]Elettra-Sincrotrone Trieste, Strada Statale 14, Km 163.5, 34149 Basovizza (TS), Italy. amenitsch@elettra.eu

Published in *Chem* 3, 494–508 (2017).

Self-assembly of light-harvesting antenna (multichromophoric) systems is a typical feature of natural photosynthetic organisms, aimed to maximize light absorption and solar energy conversion. Inspired by this concept, self-assembly strategies for integrating light harvesting units are highly desired objectives in supramolecular chemistry. Here we demonstrate that self-assembly of light-harvesting dendrimers based on Ru(II) and Os(II) polypyridine complexes leads to aggregation-induced energy transfer. This phenomenon is proposed to be due to inter-dendrimer electronic interactions involving electronic energy donors and acceptors of different dendrimers and suggests that the title dendrimer shows features reminescent of the energy migration patterns occurring among LH1 and LH2 assemblies of natural systems. Even in consideration of the reported use of similar dendrimers for photochemical water oxidation, the aggregation-induced energy transfer here reported, as well as the self-assembly of the light-harvesting dendrimers itself, can be useful for designing new integrated systems for solar fuels production.

Light-harvesting antenna systems are expected to be essential elements of artificial photosynthesis systems, as well as they are for natural photosynthetic organisms.[1-7] For example, in the *Rhodopseudomonas Acidophila* bacteria, light is absorbed by bacteriochlorophylls (BChl) molecules, that are arranged into the so-called LH2 and LH1

multicomponent arrays.[2,4] The outer antenna LH2 is made of nine coplanar BChl chromophores arranged in a ring conformation, and by 18 BChl units overimposed to the same ring and arranged as the wheels of a turbine (see Figure 1). The inner antenna LH1 is made of 36 BChl units, similarly arranged to the 18 BChl of the above mentioned LH2, but of course identifying a larger "wheel" of chromophores. Although the various BChl units are basically identical one another, their excited-state energy is different, as a consequence of their position within the supramolecular structure and therefore of their environment, and a driving force for energy migration is generated, with light absorbed by the LH2 chromophores being transferred within various LH2 and finally conveyed to LH1 on a ps timescale. From LH1, light energy is ultimately funnelled to the reaction center (RC), which is immersed within the central space of the LH1 ring (**Figure 1**).[1,4,5] The light energy trapped - in the form of electronic energy - in RC produces charge separation, providing the redox energy for the successive reactions leading to the (photo-powered) synthesis of high-energy content chemicals (fuels).

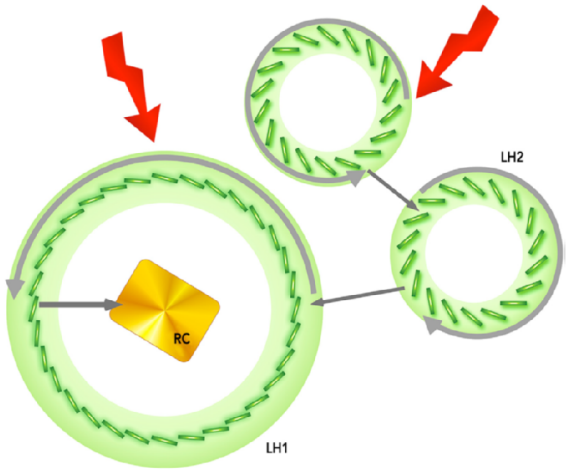

Fig. 1: Representation of the natural photosynthetic systems LH1 and LH2 and of the energy migration patterns occurring within the overall assembly. RC is the reaction center, in which charge separation takes place. The green rectangles within each light-harvesting multicomponent assembly is a single BChl chromophore. In LH2 the coplanar nine BChl units are omitted.

To summarize, in natural antennae the multichromophoric subunits (i.e., LH1 and LH2), which are supramolecular assemblies in their turn, are arranged in larger architectures so that energy migration takes place first (on shorter timescales) *within* each "single" multichomophoric subunit (*intra-assembly* energy migration) and finally (on a slightly longer timescale) *between* different multicomponent subunits (*inter-assemblies* energy migration).

Synthetic, (multichromophoric) light-harvesting antenna assemblies have been designed and extensively investigated in the last three decades.[8-14] Among such systems, light-harvesting dendrimers play an important role.[15-20] In many cases, quite efficient photoinduced energy migration has been proved in dendrimers, even by means of pump-probe femtosecond spectroscopy. Some of us contributed to the field, designing one of the early developed families of light-harvesting dendrimers, in which the chromophore subunits are mostly Ru(II) and Os(II) polypyridine complexes:[21-24] Sub-picosecond energy transfer between nearby chromophoric units in the presence of suitable energy gradients was occurring in such species.[25-27]

Inter-dendrimer energy transfer processes in self-assembled multidendrimer systems have never been reported, although in light-harvesting dendrimers different energy transfer patterns, called *inter-wheel* and *intra-wheel* energy transfer, have been described, in which energy transfer takes place between chromophores belonging to the same branch (*intra-wheel*) or different branches (*inter-wheel*) of the dendrimers.[28] Similarly, intra-dendrimer energy transfer processes that become active upon aggregation are also unknown. Indeed, inter-dendrimer energy transfer would be a quite interesting process, as it would resemble the energy migration processes occurring *among various* LH2 subunits – or LH2 and LH1 subunits - of the natural photosynthetic edifices, possibly following intra-dendrimer energy transfer, that would be analogous to energy migration processes *within single* LH2 or LH1 edifices. To identify synthetic systems in which concentration-controlled energy transfer can occur among multichromophoric subunits, could inspire the design of more efficient light-harvesting systems for solar energy conversion or light-powered molecular machines in general.

Here we report for the first time that an energy transfer process which is not active in isolated dendrimers becomes efficient in solution in self-assembled multi-dendrimer systems, that is the phenomenon of *aggregation-induced energy transfer*; this information is obtained by investigating the energy transfer process occurring in a decanuclear, second generation, mixed-metal dendrimer. The investigated compound, **1** (**Figure 2**), has general formula $[Os\{(\mu\text{-}2,3\text{-dpp})Ru[(\mu\text{-}2,3\text{-dpp})Ru(bpy)_2]_2\}_3](PF_6)_{20}$ (bpy = 2,2'-bipyridine; 2,3-dpp = 2,3-bis(2'-pyridyl)pyrazine).[21] For such a decanuclear dendrimer, energy transfer from the triplet metal-to-ligand charge-transfer (MLCT) state(s) involving the peripheral chromophoric building block(s) $\{(\mu\text{-}2,3\text{-dpp})Ru(bpy)\}^{2+}$ to the lower-lying, triplet MLCT state of the central chromophoric unit $\{Os(\mu\text{-}2,3\text{-dpp})_3\}^{2+}$, is known to be inefficient in dilute acetonitrile

solution, due to the presence of the interposed $\{Ru(\mu\text{-}2,3\text{-}dpp)_3\}^{2+}$ chromophore(s), having higher-energy MLCT states and therefore representing an energy barrier to the process (see **Figure 3**, bottom, extreme left).[21,29] However, here we demonstrate that on increasing concentration, complete Ru-to-Os energy transfer takes place in **1**. This process, inhibited within a single, isolated dendrimer species, is attributed to an inter-dendrimer interaction promoted by concentration-induced aggregation, as also evidenced by small angle X-ray scattering (SAXS) experiments, together with luminescence and transient absorption spectroscopy results.

Results and Discussion

From extensive investigations performed on dendrimers based on Ru(II) and Os(II) polypyridine complexes and containing bis(pyridyl)pyrazine (dpp) as bridging ligands, it is known that:[29-31]

(i) multimetallic Ru(II)/Os(II) polypyridine dendrimers like the ones shown in **Figure 2A** exhibit a large absorption in the visible region, due to several spin-allowed and forbidden MLCT transitions localized in the various subunits of their structure (see the absorption spectrum of **1**, **Figure 2C**). In fact, each metal-based subunit brings its own absorption properties within the dendrimer arrays;[29]

(ii) down-hill energy transfer processes between nearby subunits occur from nonequilibrated excited states, in fs regimes. Such ultrafast processes also involve singlet states, and not only triplet states as it is the usual case for transition (heavy) metal compounds;[25-27]

(iii) when the donor and acceptor chromophoric subunits are spatially separated by other metal-based unit(s), whose lowest-energy excited state is higher in energy of both donor and acceptor units, these interposed units behave as an insulating interface and energy transfer does not take place.

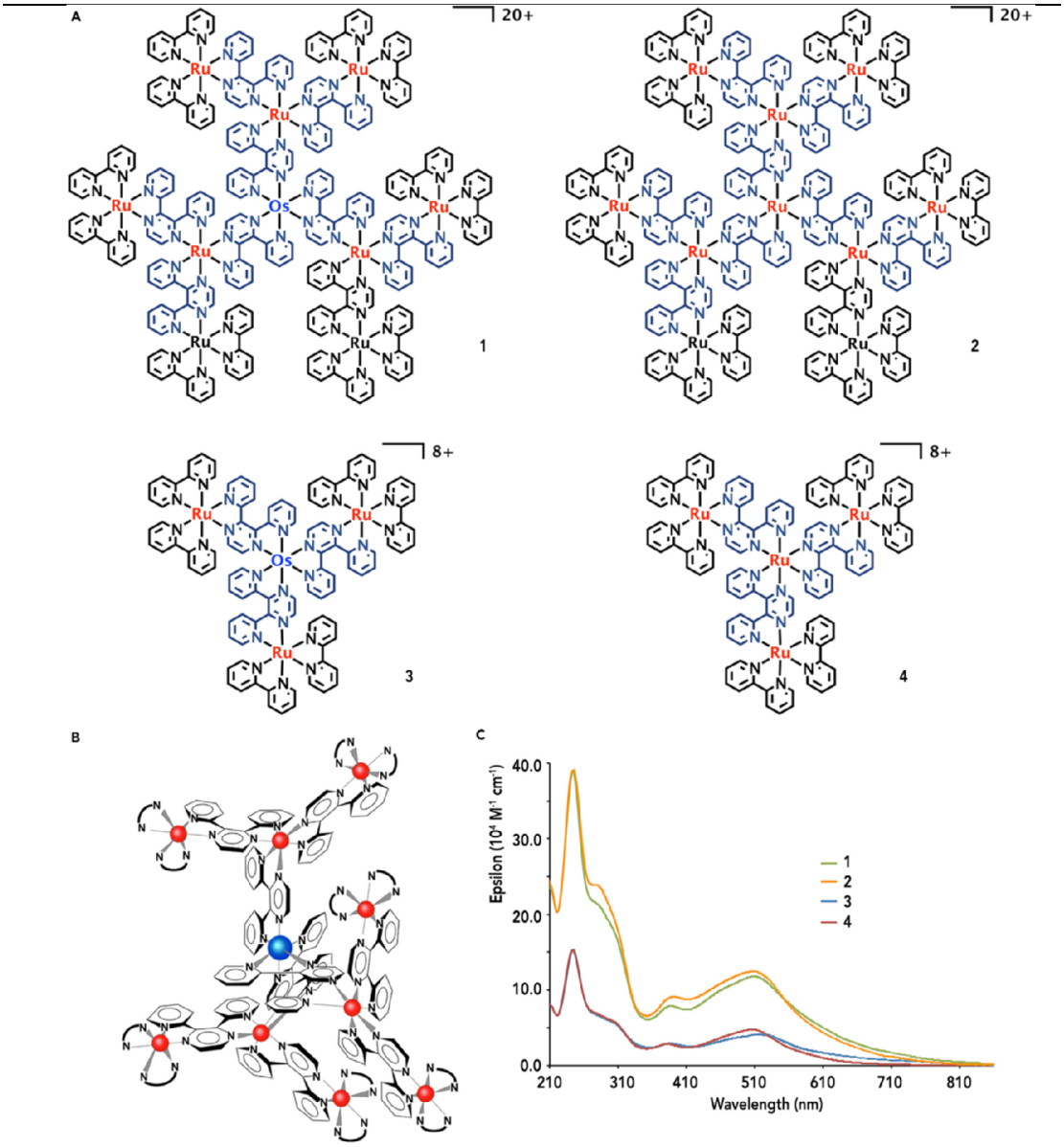

Fig. 2: Structural formulae of the metal dendrimers discussed in this work (A). Counter ions (hexafluorophosphate anions) are omitted. Panel **B** shows a different representation of **1** (N-N stands for bpy; charge omitted). Panel **C** shows the absorption spectra of **1-4** (concentration: 4 x 10^{-6} M) in acetonitrile.

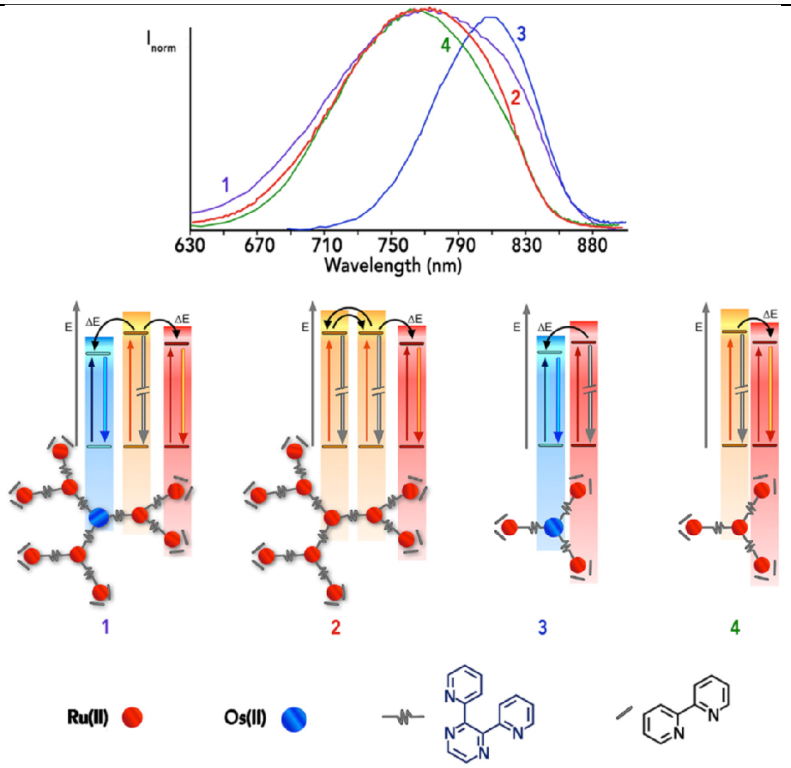

Fig. 3: Top: Emission spectra of 1-4 in acetonitrile at room temperature, color code in agreement with the colors of the numbered compounds reported below in this figure. Concentration is below 5 x 10^{-7} M for all the compounds. Excitation wavelength is 540 nm. Please note that the emission spectra to which we refer throughout all this paper and shown in the figures are uncorrected ones, preferred to corrected ones for better direct, internal comparison, so avoiding any possible origin of errors due to spectral correction; corrected emission spectra values are reported in **Supplemental Information** and in the original references. Bottom: Representation of the components Ru(II), Os(II), dpp, and bpy and schematization of compounds **1-4**, with the lower-energy excited state levels involving different subunits evidenced, together with the down-hill (or isoergonic) energy transfer processes between subunits. More details are given in the **Supplemental Information**. Charges of compounds are omitted (formal charge is 20+ for **1** and **2** and 8+ for **3** and **4**; counter-ions are PF_6^- anions). In **1** (extreme left), through-bond energy transfer from the peripheral units to the core, although thermodynamically allowed, has to overcome an energy barrier constituted by the intermediate, higher-energy subunits. Direct through-space peripheral-to-core energy transfer is inefficient.

Compound **1** is a paradigmatic example of the above points (ii) and (iii): while the first generation dendrimer $[Os\{(\mu\text{-}2,3\text{-}dpp)Ru(bpy)_2\}_3](PF_6)_8$ (**3**; **Figure 2A**) exhibits an emission maximum at about 810 nm in acetonitrile fluid solution at room temperature (uncorrected spectrum; corrected emission maxima are reported in **Supplemental Information**, **Table S3**; see also caption of **Figure 3**), assigned to the ^{3}MLCT level centered on the $\{Os(\mu\text{-}2,3\text{-}dpp)_3\}^{2+}$ core, with the same quantum yield at any excitation wavelength[32] - so demonstrating quantitative energy transfer from the MLCT states involving the peripheral $\{(\mu\text{-}2,3\text{-}dpp)Ru(bpy)_2\}^{2+}$ subunits to the Os-based core - the emission spectrum of **1** in the same conditions is quite different (**Figure 3, top**), in spite of the essentially identical nature of the

peripheral (donor) and core (acceptor) building blocks that are present in **3** and **1**. In fact, emission of **1** in dilute solution shows an emission that is quite close to the typical emission of the peripheral $\{(\mu\text{-}2,3\text{-dpp})Ru(bpy)_2\}^{2+}$ subunits, peaking at about 765 nm (uncorrected), as exhibited, for example, by the first- and second-generation homometallic dendrimers $[Ru\{(\mu\text{-}2,3\text{-dpp})Ru(bpy)_2\}_3](PF_6)_8$ (**4**) and $[Ru\{(\mu\text{-}2,3\text{-dpp})Ru[(\mu\text{-}2,3\text{-dpp})Ru(bpy)_2]_2\}_3]$ $(PF_6)_{20}$ (**2**).[21,22] In these latter species the lowest-energy excited state is indeed the MLCT triplet state(s) involving the peripheral subunit(s), which collect all the light energy absorbed by the various chromophoric units of the multicomponent species by down-hill energy transfer processes on the femtosecond timescale (see schematic representation of energy transfer pathways in **2** and **4**, displayed in **Figure 3, bottom**).[25,27,31] The emission spectrum of **1**, dominated by the emission of the peripheral triplet Ru-based MLCT states, also shows a component at low energies, that is not present in **2** or **4**. This component is assigned to the emission from the ^{3}MLCT state of the Os(II)-based core, produced by direct absorption of such a subunit. As a matter of fact, energy transfer from the higher-lying MLCT states of the Ru-based peripheral subunit(s) to the lower-lying MLCT states of the Os-based core does not occur.[21,29]

However, the emission spectrum maximum of **1** shifts to lower energies (**Figure 4**) on increasing concentration, so that the emission spectrum of a 8×10^{-6} M acetonitrile solution of **1** is close to that of the first-generation mixed-metal tetranuclear dendrimer **3**, for which the emission is definitely contributed only by the Os-based MLCT state (**Figure 3**). Further increase in concentration does not cause any other significant change in the emission spectrum profile (in **Figure 4** data up to 3×10^{-5} M are shown). By plotting the emission maximum vs concentration, it appears that the emission of **1** becomes mainly core-based from being periphery-based on moving across a narrow concentration range, from about 6×10^{-7} M to 6×10^{-6} M (**Figure 4**). Noteworthy, this is roughly the same range of concentration that promotes self-aggregation of **1**, as well as of **2**, in acetonitrile, as demonstrated some years ago by dynamic light scattering and conductivity analysis,[33] although consequences of the aggregation process on the photophysical properties were not studied at that time. Apparently, self-assembly of **1** in solution makes the periphery-to-core energy transfer feasible. The process is fully reversible: on concentrating and diluting the solution of **1** in acetonitrile, the emission spectrum is moved from higher to lower energies and backward indefinitely (see **Supplemental Information, Figure S1**), indicating that self-assembly, and as a consequence

the activation/de-activation of the energy-transfer process, is reversible and can be fully controlled. It can be recalled that closely-related heptanuclear Ru(II) dendrimers have been demonstrated to form organized patterns on graphite substrates,[34] and that other multimetallic Ru(II) complexes have also been verified to aggregate,[35] but in none of those cases photophysical consequences were reported or even predicted.

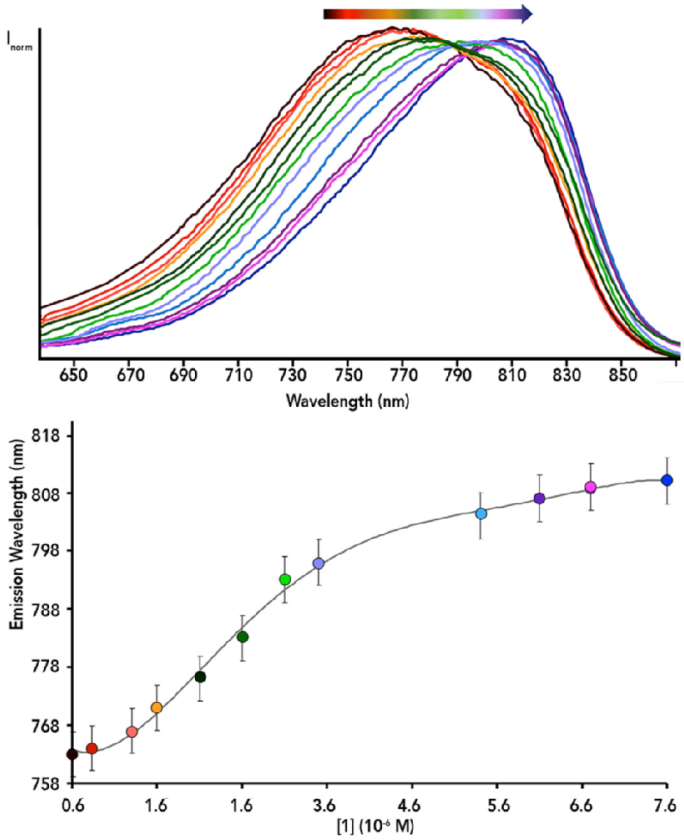

Fig. 4: Top: emission spectra of 1 in acetonitrile on changing concentration, showing the red shift of the emission maximum on increasing concentration (color code of concentration as in the bottom panel). The emission maxima changes with concentration are evidenced by the drawing in the bottom panel. The emission spectra does not change significantly outside the concentration value range reported in Figure. Please note that the emission spectrum of the highest–cencentrated solution of **1** exhibits the same maximum of the emission spectrum of **3** (see **Figure 3**). The spectra are uncorrected for PMT response, and compared with uncorrected spectra, recorded in the same conditions. Corrected spectra for diluted and concentrated solutions of **1** are shown in the **Supplemental Information**.

To further investigate the systems, we performed small-angle X-ray scattering (SAXS) experiments. **Figure 5a** shows the experimental data obtained from concentrated samples (2.8 x 10^{-5} M) of **1** and **2** in acetonitrile together with fits of the corresponding pair distance distribution functions (PDDF). In this type of experiment, the "peaks" in the PDDF spectrum correspond to distances between high electron density clouds found with increased probability.

In our case, such high electron density clouds correspond to metal centers, so the peaks in the PDDF spectrum are the dominant, metal-metal distances. **Figure 5b** shows a representation of **1**: although such a representation can only be taken with care, because several stereochemical and geometrical isomers of **1** are possible,[21,29] some distances between two metal centers in such a dendrimer are independent of isomer structure, and they are the metal-metal distance between two metal centers only separated by a 2,3-dpp bridge (ca. 0.7 nm) and the metal-metal distance between two metals having interposed a single $\{Ru(\mu\text{-}2,3\text{-}dpp)_3\}^{2+}$ unit, about 1.4 nm. Clearly, larger metal-metal distances in **1** and **2** are also present, for example between metals belonging to different dendrimer branches (one of them is shown in **Figure 5b**), but they are less relevant since their distances are less defined and the contributions to the PDDF would be much smaller. This effect is observed in the PDDF of theoretically calculated scattering curves (using CRYSOL[36]) from models of a single possible conformation of **1** and **2**, shown in **Figure 5a** (right panel): as expected, only the two main metal-metal distances are evidenced, with the longer intra-dendrimer metal-metal distances probably being buried in the tail of the main peaks. A comparison between the experimental and theoretical PDDF (**Figure 5a**) is quite instructive: for both **1** and **2**, the two "peaks" in the 0.6-1.8 nm range are present in both experimental and theoretical data and can thus be considered as a conserved motif of the dendrimeric side arms in a relatively fixed conformation. The "peaks" at distance > 3 nm (and also the ca. 2.5 nm shoulder) are absent in the computed PDDF of isolated dendrimers and are hence assigned to inter-dendrimer metal-metal interactions and can be considered a further proof for dendrimer-dendrimer aggregation. A more basic but equally convincing confirmation is found directly in the scattering data: **1** and **2** both exhibit a sloped low-q behaviour ($q < 1$ nm^{-1}), which is a characteristic feature of multimer formation between dispersed species.[37] A quantitative evaluation of the relative monomeric and dimeric contributions to the PDDF of the experimental data estimates that for both **1** and **2** *at least* 20% of the molecules are in an aggregated state at the concentration used for the SAXS experiments (see details in **Supplemental Information**, including **Figs. S2-S5**). Please note, anyway, that 20% is just a low limit for aggregation, directly derived from SAXS results: photophysical results strongly indicate that aggregation percentage is much higher, probably quantitative at 10^{-5} M acetonitrile solution.

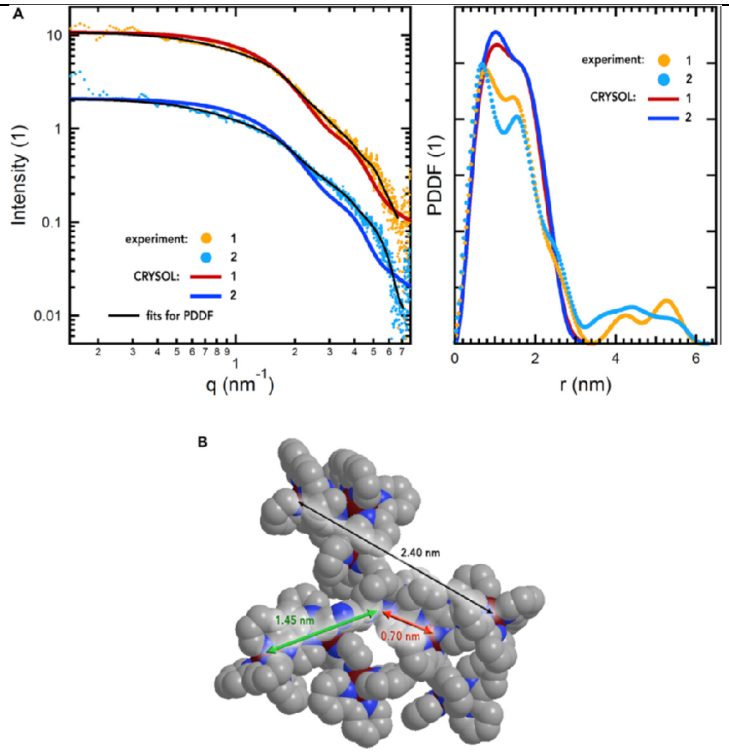

Fig. 5: (a) SAXS experimental and calculated (by CRYSOL) data from concentrated samples (2.8 x 10^{-5} M) of **1** and **2** in acetonitrile, together with fits of the corresponding pair distance distribution functions (PDDF). (b) Distances between metal centers in **1** (green: distance between two metal centers connected by a dpp bridging ligand (e.g., Os(II) →intermediate Ru(II) centers); red: distance between two metal centers having an interposed {(dpp)Ru(dpp)} unit (e.g., Os(II) →peripheral Ru(II) centers); black: distance between two peripheral Ru(II) centers belonging to different dendrimer branches).

However, whereas aggregation is here experimentally well documented, as well as the change in luminescence properties upon aggregation, to safely state that energy transfer is the reason for the emission spectrum change occurring in **1** upon self-aggregation requires that other options are excluded. For example, self-aggregation might quench the peripheral Ru-based emission by some other process (triplet-triplet annihilation, for example), leaving only the Os-core emission – already present in **1** thanks to the light directly absorbed by the Os-based central unit – visible. To verify this possibility, we studied the emission properties of **2**,[21] the all-ruthenium decanuclear compound analogous to **1**, as a function of concentration: indeed a slight shift of the emission spectrum also occurs for **2** in the same concentration range studied for **1** (see **Supplemental Information, Figure S7**). Such a shift, however, is much smaller than that obtained for **1**, and can be interpreted as a perturbation of the peripheral Ru-based MLCT emissive state upon interaction with other dendrimer supermolecules in the aggregated assemblies (more details in the **Supplemental Information**). In this case, anyway, the

localization of the emissive state remains the same (i.e., the ^{3}MLCT state involving the peripheral $\{(\mu\text{-}2,3\text{-dpp})Ru(bpy)\}^{2+}$ subunit(s)). Most importantly, this experiment demonstrates that the peripheral Ru-based emission is not quenched by self-aggregation process when the Os subunit is not present (i.e. triplet-triplet annihilation does not occur), so the disappearance of the Ru-based emission in **1** on increasing concentration must be due to the presence of the Os-based chromophore.

As a further proof of energy transfer, we had to verify that the light energy absorbed by the peripheral Ru-based chromophores in concentrated **1** solution effectively contributes to Os-based emission, that is the Os-based emission is sensitized in **1** on increasing concentration. Unfortunately, we could not rely on straightforward excitation spectroscopy, for several technical problems, including the absorption of the solutions to be used to be sure that aggregation is operative. So, we had to design indirect experiments to test sensitization: we used $[Os(bpy)_3]^{2+}$ (a well-behaved ^{3}MLCT emitter[38]) as a model compound, to introduce corrections and normalization factors. The procedure used is described in detail in the **Supplemental Information** (see: *Indirect method designed to prove energy transfer*). The results definitely indicate that the Os-based emission of **1** in concentrated solution is sensitized by light absorption of the Ru-based chromophores.

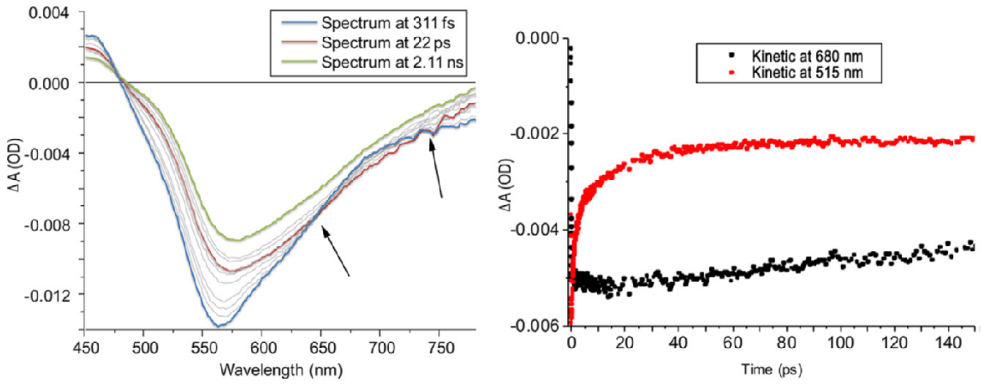

Fig. 6: Transient absorption spectra (left) and kinetics (right) of a 1.6 x 10^{-5} M acetonitrile solution of 1 (λ_{exc}: 400 nm, 100 fs pulse). In the left panel the arrows indicate the isosbestic points kept during the process occurring with a time constant of 18 ps. The kinetic of **1** at slower times (up to 3.2 ns) is shown in the Supplementary Information (**Figure S8**).

Pump-probe femtosecond transient absorption spectroscopy has been performed on **1**, at different concentrations (excitation wavelength, 400 nm). **Figure 6** shows the transient spectra and decays of a 1.6 x 10^{-5} M solution of **1**. The initial spectrum is similar to that of **4**, previously reported:[30,39] a bleaching, corresponding to the broad MLCT visible absorption, with a

minimum at about 560 nm, is present, together with a transient absorption at wavelengths shorter than 480 nm. The only relevant difference between the initial transient absorption spectra of **1** and **4** is that in **1** the bleach is more red-shifted, as expected because of the contribution of the MLCT bleach involving the directly, promptly-prepared excited Os(II) core, that absorbs at lower energies. The time-resolved transient spectra in **Figure 6** show that the initial bleach at 560 nm is fastly recovered in part, while a further bleach in the range 660-720 nm appears, evidencing a fast process with a time constant of 18 ps. During this process, an isosbestic point at about 655 nm is kept. The further bleach is assigned to an increased population of the triplet MLCT state involving the Os-based core, since the bleach at about 670-690 nm is a signature for Os-based MLCT state in **3**.[28,29] Therefore, we can safely assign the 18 ps process to energy transfer from the MLCT excited state(s) involving the Ru-based peripheral subunits to the MLCT triplet state of the Os core. After the above-described process, the transient spectrum undergoes some more changes with a time constant of 150 ps and finally decays very slowly with respect to the time limit of our fs pump-probe apparatus (3.3 ns), in agreement with the luminescence lifetime data of **1** in concentrated solution (multiexponential emission decay, due to several lifetimes close to one another, with average lifetime of about 100 ns, see **Supplemental Information**, *Additional information on excited-state properties*).

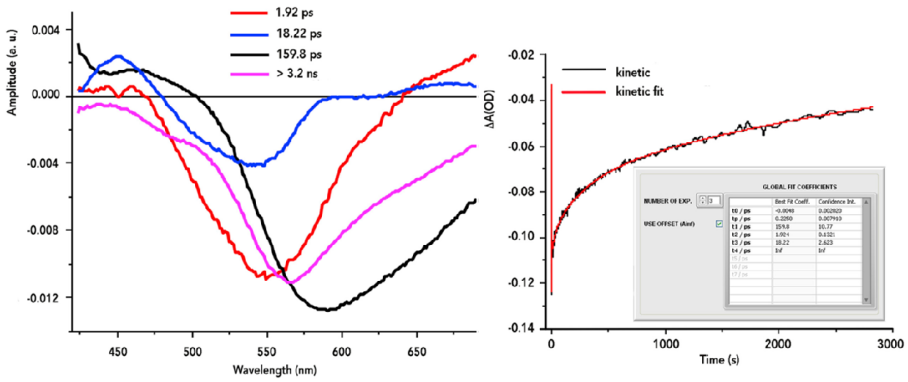

Fig. 7: Global decay fitting of a concentrated (1.6 x 10^{-5} M) acetonitrile solution of **1** (λ_{exc}: 400 nm, 100 fs pulse), and decay associated spectra, with their global fit coefficients.

To investigate in more detail the excited state properties of the concentrated solution of **1**, global decay analysis has been performed, whose results are shown in **Figure 7**. Four decay associated spectra are required to fit the global kinetic data, so indicating the presence of four main components contributing the transient absorption spectrum of **1**: (i) a short-lived component, characterized by a spectrum (associated lifetime, 1.9 ps) with a bleach peaking at 550 nm and exhibiting a transient absorption at wavelengths longer than 630 nm; (ii) a second

component (associated lifetime, 18.2 ps), with a spectrum exhibiting a similar bleach peak, but apparently a stronger transient absorption at wavelengths longer than 580 nm and another transient absorption at about 450 nm; (iii) a third component (associated lifetime, 159.8 ps), having a spectrum with a bleach strongly shifted towards the red (it peaks at about 580 nm, but with a larger component to longer wavelengths); (iv) a longer-lived component (associated lifetime, >3.2 ns), resembling the transient spectrum of **1** recorded with a delay of 2.1 ns, as showed in **Figure 6**. Intersystem crossing and down-hill energy transfer in this class of metallodendrimers occur in the sub-picosecond timescale,[25-27] so the 1.9 ps lifetime component cannot be due to such processes, that occurred on early times: it is rather assigned to vibrational cooling connected to some structural reorganization within the triplet states, supported by the assignment of vibrational cooling occurring in 4 ps in **3**.[27] The component (ii), whose bleaching red shifts on moving to longer-lived components, can be assigned to the ^{3}MLCT state involving the Ru-based peripheral subunits. The 18.2 ps lifetime of component (ii) corresponds to the decay of the Ru-based MLCT state, so confirming the kinetic of the Ru-to-Os energy transfer process discussed above. Component (iii) is assigned to a non-equilibrated Os-based triplet MLCT state, which decays to its thermally-equilibrated level (characterized by the spectrum of component (iv)) by a second vibrational cooling process: tentatively, we suggest that such a relatively slow process can involve solvent reorganization around the large dendrimer species. Relatively slow solvent reorganization processes have indeed been recently reported in metal polypyridine complexes (in particular, in Re(I) tricarbonyl species[40,41]), and have been attributed to some specific solvent-complex interactions: similar interactions are not expected here, but the dimension of second generation dendrimers like **1** as well as their three-branched. partially-hollowed structure (see **Figure 2B**) could be responsible for slowing down solvent reorganization processes.

Transient absorption spectrum of a 2.5 x 10^{-7} M acetonitrile solution of **1** behaves differently (**Supplemental Information, Figure S8**): the transient spectrum, otherwise qualitatively similar to that of the concentrated case, does not show any trace of the 18 ps process evidenced by the concentrated solution (in particular, the further bleach in the 660-720 nm range does not occur), but decays towards the ground state exhibiting a vibrational cooling process with a time constant of a hundred of ps, followed by a much slower process, corresponding to the decay of the relaxed emissive MLCT state.

To explain the aggregation-induced energy transfer occurring from the peripheral Ru-based MLCT state(s) to the core Os-based MLCT level in concentrated solutions of **1**, two hypotheses must to be taken into account: (i) intra-dendrimer and (ii) inter-dendrimer energy transfer pathways.

(i) *Intra-dendrimer energy transfer*, that is energy transfer from peripheral Ru-based unit(s) to the Os-based core *within a single dendrimer*, requires significant electronic changes at the level of the individual subunits upon aggregation, to make superexchange-assisted periphery-to-core energy transfer, inefficient in isolated dendrimers as indicated by the "dilute" situation, competitive with peripheral unit intrinsic decay in self-assembled aggregates. Actually, self-aggregation of **1** can affect the electronic properties of the various chromophores of the dendrimer structure, however the probability of intra-dendrimer Ru(peripheral)-to-Os(core) energy transfer via the interposed $\{Ru(\mu\text{-}2,3\text{-}dpp)_3\}^{2+}$ units is unlikely to be so strongly modified by self-aggregation to make the energy transfer process quantitative.

(ii) *Inter-dendrimer energy transfer*, involving energy migration *between different dendrimers*, requires interdigitated dendrimers. Thanks to the three-dimensional, partially-hollowed dendrimeric structures of **1**, typical of dendrimers in general,[17,42] interpenetration of branches of a dendrimer into another dendrimer, so that a (Ru-based) peripheral chromophore of a dendrimer can approach the (Os-based) chromophoric core of another dendrimer, is possible and could effectively switch on the energy transfer process: this sort of interdigitated multidendrimer assembly is also in someway supported by the solid state organization, recently visualized via X-ray crystal structure determination, of a related trinuclear Ru(II) polypyridine compound.[43] Moreover, electronic interactions between different dendrimer "supermolecules" upon aggregation, leading for example to excimer formation, is well documented,[20,44] though inter-dendrimer energy transfer has never been mentioned.

Although the possibility for intra-dendrimer energy transfer upon aggregation cannot be totally ruled out, on the basis of the relatively strong dendrimer-dendrimer electronic interactions reported for excimer formation and the interdigitated nature of the solid state structures of related multinuclear Ru(II) complexes, we propose that the energy transfer from Ru-based peripheral MLCT states to Os-based MLCT states promoted by self-aggregation in **1** is due to an *inter*-dendrimer mechanism.

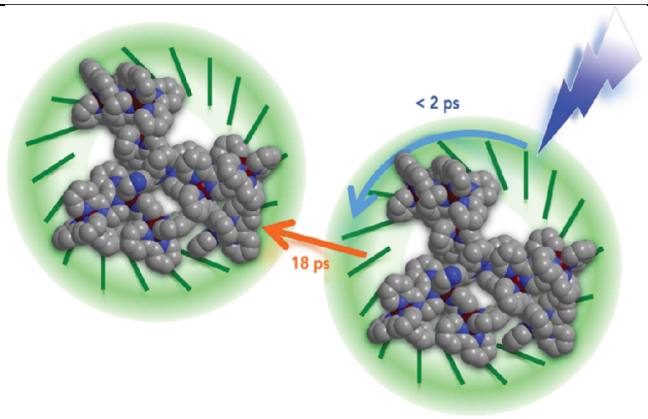

Fig. 8: Pictorial representation of the energy migration processes taking place in **1**, indicating the analogy with the (overimposed, schematized) LH2 assemblies. Intra-dendrimer energy transfer occurs with time constants lower than 1 ps (see refs. 29,30), and inter-dendrimer energy transfer takes place with a time constant of about 18 ps (see main text).

Conclusions

Electronic energy transfer from the Ru-based peripheral units to the Os-based, central chromophore in the second generation, mixed-metal decanuclear light-harvesting dendrimer **1** only takes place when concentration is larger than about 2 x 10^{-6} M in acetonitrile and becomes the main decay process of the peripheral chromophores for concentrations larger than 6 x 10^{-6} M. This concentration corresponds to the formation of organized assemblies of light-harvesting dendrimers, as clearly indicated by SAXS, which is here proved to be an extremely powerful technique to investigate both the inner structure of metal dendrimers and dendrimer-dendrimer aggregation at the molecular level. The Ru-to-Os energy transfer process is attributed to inter-dendrimer interactions, and although aggregation-induced intra-dendrimer energy transfer cannot be totally ruled out, we propose that its mechanism is energy transfer quenching of peripheral Ru(II)-based excited state of a dendrimer by the core Os(II)-based chromophore belonging to a different dendrimer supermolecule, within the interdigitated assemblies made of several **1** species. Time constant of such a process, as determined by pump-probe transient absorption spectroscopy, is 18 ps.

The proposed inter-dendrimer energy transfer process is in a someway reminescent of the energy migration processes occurring in the natural antenna LH1 and LH2: (i) subpicosecond down-hill or isoergonic energy transfer occurs within nearby chromophoric subunits of each **1** supermolecule, and this is similar to intra-assembly energy migration in LH1 and LH2; (ii)

on longer ps timescale, energy transfer can occur between different supermolecules, analogously to energy migration among different LH2 and from LH2 to LH1. **Figure 8** shows a pictorial representation of this analogy. Also in consideration of the role of this class of light-harvesting dendrimers in artificial photoinduced water oxidation processes,[45] the aggregation-induced energy transfer here reported, as well as the self-assembly process of the light-harvesting dendrimers, can give useful information for designing new integrated systems for solar fuels production.

References

1. Blakenship, R. E. Molecular mechanism of photosynthesis (Blackwell Science, Malden, 2002).
2. Cogdell, R. J., Howard, T. D., Isaacs, H. W., McLaskey, K. and Gardiner, A. T. (2002). Structural factors which control the position of the Q absorption band of bacteriochlorophyll *a* in purple bacteria antenna complexes. *Photosynth. Res.* **74**, 135-141.
3. Anna, J. M., Scholes, G. D., Van Grondelle, R. (2014). A little coherence in photosynthetic light harvesting. *BioScience* **64**, 14-25.
4. Cogdell, R. J., Isaacs, N. W., Freer, A. A., Arrelano, J., Howard, T. D., Papiz, M. Z., Hawthornthwaite-Lawless, A. M. and Prince, S. M. (1997). The structure and function of the LH2 (B800-850) complex from the purple photosynthetic bacterium *Rhodopseudomonas acidophila* strain 10050. Prog. Biophys. Mol. Biol. **68**, 1-27.
5. Pullerits, T. and Sundström, V. (1996).Photosynthetic light-harvesting pigment-protein complexes: toward understanding how and why. *Acc. Chem. Res*. **29**, 381-389.
6. Engel, G. S., Calhoun, T. R., Read, E. L., Ahn, T.-K., Mančal, T., Cheng, Y.-C., Blankenship, R. E. and Fleming, G. R. (2007). Evidence for wavelike energy transfer through quantum coherence in photosynthetic systems. *Nature* **44**, 782–786 .
7. Polivka, T. and Frank, H. A. (2010). Molecular factors controlling photosynthetic light harvesting by carotenoids. *Acc. Chem. Res.* **43**, 1125-1134.
8. Gust, D., Moore, T. A. and Moore, A. L. Solar Fuels via Artificial Photosynthesis. (2009). *Acc. Chem. Res.* **42**, 1890-1898
9. Wasielewski, M. R. (2009). Self-assembling strategies for integrating light harvesting and charge separation in artificial photosynthetic systems. *Acc. Chem. Res.* **42**, 1910-1921.
10. Choi, M.-S., Aida, T., Yamazaki, T. and Yamazaki, I. (2002). Dendritic multiporphyrin arrays as light-harvesting antennae: effects of generation number and morphology on intramolecular energy transfer. *Chem. Eur. J.* **8**, 2667-2678.
11. Yong, C.-K., Parkinson, P., Kondratuk, D. V., Chen, W.-H., Stannard, A., Summerfield, A., Sprafke, J. K., O'Sullivan, M. C., Beton, P. H., Anderson, H. L. and Herz, L. M. (2015). Ultrafast delocalization of excitation in synthetic light-harvesting nanorings. *Chem. Sci.* **6**, 181-189.
12. Imahori, H. (2004) Giant multiporphyrin arrays as artificial light-harvesting antennas. *J. Phys. Chem. B*, **108**, 6130-6143.

13. Kaloudi-Chantzea, A., Martinou, E., Seintis, K., Karakostas, N., Giastas, P., Pitterl, F., Oberacher, H., Fakis, M. and Pistolis, G. (2016). Formation of a highly-ordered rigid multichromophoric 3D supramolecular network by combining ionic and coordination-driven self-assembly. *Chem. Commun.* **52**, 3388-3391.

14. Sautter, A., Kaletas, B. K., Schmid, D. G., Dobrawa, R., Zimine, M., Jung, G., van Stokkum, I. H. M., De Cola, L., Williams, R. M. and Wurthner, F. (2005). Ultrafast energy-electron transfer cascade in a multichromophoric light-harvesting molecular square. *J. Am. Chem. Soc.* **127**, 6719-6729.

15. Balzani, V., Ceroni, P., Maestri, M. and Vicinelli, V. (2003). Light-harvesting dendrimers. *Curr. Opin. Chem. Biol.* **7**, 657-665.

16. Hofkens, J., Maus, M., Gensch, T., Vosch, T., Cotlet, M., Köhn, F., Herrman, A., Müllen, K. and De Schryver, F. C. (2000). Probing photophysical processes in individual multichromophoric dendrimers by single-molecule spectroscopy. *J. Am. Chem. Soc.* **122**, 9278-9288.

17. Campagna, S., Ceroni, P. and Puntoriero, F. Designing dendrimers (Wiley, New York, 2012).

18. Lee, H., Jeong, Y.-H., Kim, J.-H., Kim, I., Lee, E. and Jang, W.-D. (2015). Supramolecular coordination polymer formed from artificial light-harvesting dendrimer. *J. Am. Chem. Soc.* **137**, 12394-12399.

19. Adronov, A. and Fréchet, J. M. J. (2000). Light-harvesting dendrimers. *Chem. Commun.* 1701-1710.

20. Feng, F., Lee, S. H., Cho, S. W., Kömürlü, S., McCarley, T. D., Roitberg, A., Kleiman, V. D. and Schanze, K. S. (2012). Conjugated polyelectrolyte dendrimers: aggregation, photophysics, and amplified quanching. *Langmuir* **28**, 16679-16691.

21. Denti, G., Campagna, S., Serroni, S., Ciano, M. and Balzani, V. (1992). Decanuclear homo- and heterometallic polypyridine complexes: syntheses, absorption spectra, luminescence, electrochemical oxidation, and intercomponent energy transfer. *J. Am. Chem. Soc.* **114**, 2944-2950.

22. Campagna, S., Denti, G., Serroni, S., Juris, A., Venturi, M., Ricevuto, V. and Balzani, V. (1995). Dendrimers of nanometer size based on metal complexes: luminescent and redox-active polynuclear metal complexes containing up to twenty-two metal centers. *Chem. Eur. J.* **1**, 211-221.

23. Serroni, S., Juris, A., Venturi, M., Campagna, S., Resino Resino, I., Denti, G., Credi, A. and Balzani, V. (1997). Polynuclear metal complexes of nanometre size. A versatile synthetic strategy leading to a luminescent and redox-active dendrimer made of an Os(II)-based core and 21 Ru(II)-based units in the branches. *J. Mater. Chem.* **7**, 1227-1236.

24. Serroni, S., Campagna, S., Puntoriero, F., Di Pietro, C., Loiseau, F. and McClenaghan, N. D. (2001). Dendrimers based on ruthenium(II) and osmium(II) polypyridine complexes and the approach of using complexes as ligands and complexes as metals. *Chem. Soc. Rev.* **30**, 367-375.

25. Berglund Baudin, H., Davidsson, J., Serroni, S., Juris, A., Balzani, V., Campagna, S. and Hammarström, L. (2002). Ultrafast energy transfer in binuclear ruthenium-osmium complexes as models for light-harvesting antennas. *J. Phys. Chem. A*, **106**, 4312-4319.

26. Andersson, J., Puntoriero, F., Serroni, S., Yartsev, A., Pascher, T., Polivka, T., Campagna, S., S. and Sundström, V. (2004). New paradigm of transition metal polypyridine complex photochemistry. *Faraday Discuss.* **127**, 295-305.

27. Larsen, J., Puntoriero, F., Pascher, T., McClenaghan, N. D., Campagna, S., Åkesson, E. and Sundström, V. (2007). Extending light-harvesting of transition metal dendrimers. *ChemPhysChem*, **8**, 2643-2651.

28. Cho, S., Li, W.-S., Yoon, M.-C., Ahn, T. K., Jiang, D.-L., Kim, J., Aida, T., Kim, D. (2006). Relationship between incoherent excitation energy migration processes and molecular structures in zinc(II) porphyrin dendrimers. *Chem. Eur. J.* **12**, 7576-7584.

29. Balzani, V., Campagna, S., Denti, G., Juris, A., Serroni, S. and Venturi, M. (1998). Designing dendrimers based on transition-metal complexes. Light harvesting properties and predetermined redox patterns. *Acc. Chem. Res.*, **31**, 26-34.

30. Puntoriero, F., Serroni, S., Galletta, M., Juris, A., Licciardello, A., Chiorboli, C., Campagna, S. and Scandola, F. (2005). A new heptanuclear dendritic ruthenium(II) complex featuring photoinduced energy transfer across high-energy subunits. The overcome of a limitation in antenna metal dendrimers. *ChemPhysChem*, **6**, 129-138.

31. Arrigo, A., La Ganga, G., Nastasi, F., Serroni, S., Santoro, A., Santoni, M.-P., Galletta, M., Campagna, S. and Puntoriero, P. (2016). Artificial, molecular-based light-harvesting antenna systems made of metal dendrimers and multibodipy species. *C. R. Chimie*, doi:10.1016/j.crci.2016.02.011.

32. Campagna, S., Denti, G., Sabatino, L., Serroni, S., Ciano, M. and Balzani, V. (1989). A new hetero-tetrametallic complex of ruthenium and osmium: absorption spectrum, luminescence properties, and electrochemical behavior. *J. Chem. Soc., Chem. Commun.*, 1500-1501.

33. Campagna, S., Giannetto, A., Serroni, S., Denti, G., Trusso, S., Mallamace, F. and Micali, N. (1995). Aggregation in fluid solution of dendritic supermolecules made of ruthenium(II)- and osmium(II)-polypyridine building blocks. *J. Am. Chem. Soc.* **117**, 1754-1758.

34. Latterini, L., Poutois, G., Moucheron, C., Lazzaroni, R., Brédas, J.-L., Kirsch-De Mesmaeker and De Schryver, F. C. (2000). STM imaging of a heptanuclear ruthenium(II) dendrimer, mono-add layer on graphite. *Chem. Eur. J.* **6**, 1331-1336.

35. Newkome, G. R. and Moorefield, C. N. (2015). From 1 to 3 dendritic designs to fractal supramolecular constructs: understanding the pathway to the Siepinski gasket. *Chem. Soc. Rev.* **44**, 3954-3967.

36. Svergun, D., Barberato, C. and Koch, M. H. J. (1995). CRYSOL - a Program to Evaluate X-ray Solution Scattering of Biological Macromolecules from Atomic Coordinates. *J. Appl. Crystallogr.* **28**, 768-773.

37. Glatter, O. and Kratky, O. Small Angle X-ray Scattering. Academic Press, London (1982).

38. Kumaresan, D., Shankar, K., Vaidya, S. and Schmehl, R. H. (2007). Photochemistry and photophysics of coordination compounds: osmium. *Top. Curr. Chem.* **281**, 101-142.

39. Natali, M., Puntoriero, F., Chiorboli, C., La Ganga, G., Sartorel, A., Bonchio, M., Campagna, S. and Scandola, F. (2015). Working the other way around. Photocatalytic water oxidation triggered by reductive quenching of the photoexcited chromophore. *J. Phys. Chem. C* **119**, 2371-2379.

40. El Nahhas, A., Consani, C., Blanco-Rodriguez, A. M., Lancaster, K. M., Braem, O., Cannizzo, A., Towrie, M., Clark, I. P., Zalis, S., Chergui, M. and Vlcek, A. (2011). Ultrafast excited-state dynamics of rhenium(I) photosensitizers $[Re(Cl)(CO)_3(N,N)]$ and $[Re(imidazole)(CO)_3(N,N)]^+$: diimone effects. *Inorg. Chem.* **50**, 2932-2943.

41. Nastasi, F., Puntoriero, F., Natali, M., Mba, M., Maggini, M., Mussini, P., Panigati, M. and Campagna, S. (2015). Photoinduced intercomponent excited-state decays in a molecular dyad made of a dinuclear rhenium(I) chromophore and a fullerene electron acceptor unit. *Photochem. Photobiol. Sci.* **14**, 909-918.

42. Fréchet, J. M. J. and Tomalia, D. A. Dendrimers and other dendritic polymers (Wiley, Chichester, 2001).

43. Laramée-Milette, B., Lussier, F., Ciofini, I. and Hanan, G. S. (2015). A family of Ru(II) complexes built on a novel sexipyridine building block: synthesis, photophysical properties and the rare structural characterization of a triruthenium species. *Dalton Trans.* **44**, 11551-11561.

44. Lekha, P. K. and Prasad, E. (2010). Aggregation-controlled excimer emission from anthracene-containing polyamidoamine dendrimers. *Chem. Eur. J.* **16**, 3699-3706.

45. Puntoriero, F., La Ganga, G., Sartorel, A., Carraro, M., Scorrano, G., Bonchio, M. and Campagna, S. (2010). Photo-induced water oxidation with tetranuclear ruthenium sensitizer and catalyst: A unique 4x4 ruthenium interplay triggering high efficiency with low-energy visible light. *Chem. Commun.* **46**, 4725-4727.

A3: Structural and Optical Properties of a Perylene Bisimide in Aqueous Environment

Max Burian,[a] Francesco Rigodanza,[b] Heinz Amenitsch,[a] László Almásy,[c] Ivan Khalakhan,[d] Zois Syrgiannis,[b] Maurizio Prato[b,e,f]

[a] Institute of Inorganic Chemistry, Graz University of Technology, Stremayrgasse 9/V, Graz 8010, Austria, amenitsch@elettra.eu

[b] Department of Pharmaceutical Sciences University of Trieste, via L. Giorgieri 1 - 34127 Trieste, Italy

[c] Wigner Research Centre for Physics, HAS, H-1525, Budapest POB 49, Hungary

[d] Department of Surface and Plasma Science, Faculty of Mathematics and Physics, Charles University, V Holešovičkách 2, 180 00 Praha 8, Czech Republic

[e] Carbon Nanobiotechnology Laboratory, CIC biomaGUNE, Paseo de Miramón 182, 20009 Donostia-San Sebastian (Spain)

[f] Basque Fdn Sci, Ikerbasque, Bilbao 48013, Spain, prato@units.it

Published in *Chem. Phys. Lett.* 683, 454–458 (2017).

A water soluble, dicationic perylene bisimide derivative was synthesized and examined in aqueous solution and upon drying by means of absorption and emission spectroscopy, x-ray and neutron scattering techniques as well as electron microscopy. The presented results provide evidence for the existence of higher-ordered molecular-aggregates in solution, potentially utilizable in device fabrication as super-molecular building-blocks.

Introduction

During the last years the field of organic electronics evolved as one of the most active in chemistry and materials science [1,2]. On the one hand this development originated due to the prospects in high technology applications like organic field-effect transistors [3], organic light-emitting displays [4] and solar cells [5], on the other hand from the realization that a much larger range of π-conjugated molecules can be considered for applications in organic electronics than assumed in the earlier days of the field [2]. As a result, the creativity of chemists was stimulated to explore a broad variety of π-conjugated molecular scaffolds towards applications, especially in organic transistors or solar cell devices. The consequence

was an enormous expansion of available π-conjugated small molecules and polymers and a shift of the research field from physics towards chemistry.

These π-conjugated materials tend to aggregate into supramolecular architectures [6]. This effect is crucial and influence the photophysical properties of the final materials [7]. One of the most important changes is the effective transfer of electronic excitation energy coherently across many sites [8]. On the other hand, there have also been negative effects such as the quenching of the fluorescence emission [9]. Moreover, this aspect is not easily controllable eventually yielding unpredictable structures [10]. However, the beneficial properties that arise from the different packing behavior have been recognized in the field of organic electronics [7].

One of the most studied π-conjugated small molecules are perylene-based compounds and mainly perylene-bisimides, which are interesting candidates for several applications, including organic electronics. They are simple organic molecules possessing high molar extinction coefficients and good thermal and photochemical stability [11–14]. More importantly, perylene derivatives are already successfully utilized for gas-sensing [15,16], opto-electronics [17,18] and even hydrogen production [19]. Perylenes belong to the group of π-conjugated chromophores: their hydrophobic nature causes strong π-π interactions, making them apparently insoluble in aqueous media. However, what might seem to be a disadvantage can actually be exploited since supramolecular structures based on these type of aggregation forces have been shown to present enhanced optical and electronic properties [10,20,21].

More specifically, bis-(N,N-trimethylammonium-cation)ethylene)perylene-3,4,9,10-tetra-carboxylic bis-imide salts (PBIs) have the ability to form nanotubular structures [19], despite the strong cationic repulsion of the ammonium salts. In solution, these nanotubes can present an orientation, making PBIs part of the family of chromonic liquid crystal compounds [22,23]. Such chromonic liquid crystals are structurally characterized by a transition from isotropic to nematic phase and finally at higher concentrations to a hexagonal phase [24,25]. In this context, a selection of investigations have focused especially on the latter two phase transitions, whereas the structural analysis of these phenomena so far only took place in the solid state (deposition, crystallization) or at very high concentrations (crystalline conditions) [26–29]. On similar grounds, PBIs, together with anionic phosphate surfactants, cause self-alignment of the constituents, further resulting in supramolecular liquid-crystals in bulk [26,27]. While these investigations supply a comprehensive description of the final

compounds at both the meso- and nanoscale, no attention has so far been directed towards the formation of the liquid-crystalline building blocks at low-concentrations.

Herein, we address the structural nature of low-concentrated **PBI1** (Scheme 1) in aqueous media. We synthesized PBI1 and derivatives thereof via a facile, microwave-assisted route [30], whereas for this work Cl− was chosen as a charge-balancing counter-ion. Static absorption and emission spectroscopy measurements shine light onto the low concentration regime <50 μM, already suggesting the existence of π-π-stacked **PBI1** dimers. A series of X-ray and neutron scattering techniques provide evidence of dimer-growth into organic nanocrystals, which are thought to be the building-blocks for liquid-crystalline materials. Yet, the dried structure of **PBI1** reveals a strikingly different morphology compared to the solvent state, underlining the necessity of a thorough understanding of the compound behavior in aqueous media.

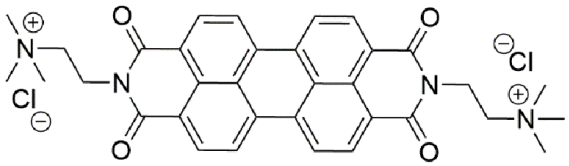

Scheme 1. N,N′-Bis(2-(trimethylammonium)ethylene)perylene-3,4,9,10-tetra-carboxylic acid bis-imide bis-chloride salt (**PBI1**).

2. Materials and methods

2.1. Synthesis of PBI1

PBI1 was synthesized according to the literature [30]. The chemicals were purchased from Acros and used without any further purifications.

2.2. Small angle neutron scattering (SANS)

Small-angle neutron scattering experiments were performed on the 'Yellow Submarine' instrument in Budapest Neutron Centre. The scattering vector q ranged from 0.1 to 3.7 nm^{-1}, by using two sample - detector distances of 1.2 and 5.2 m, and one wavelength of 0.5 nm. The samples were placed in Hellma Analytics quartz cuvettes tyoe 404-QX of the latest design, with flight path of 1 mm, and thermostated at 25 °C. The measured scattering curves were corrected for background scattering from the D_2O solvent, and put on absolute scale using water as secondary calibration standard. The data were processed by the BerSANS-PC software [31].

2.3. Small and wide angle X-ray scattering (SAXS & WAXS)

Small angle X-ray scattering (SAXS) experiments were performed at the Austrian SAXS beamline of Elettra synchrotron (Trieste, Italy) using 8 keV photon energy [32]. The liquid samples were filled in standard 1.5 mm quartz capillaries whereas 6–8 consecutive images were taken over time, to rule out possible radiation damage by comparison of the scattering pattern. The two-dimensional Pilatus1 M image detector (Dectris, Switzerland) was placed at a distance of approximately 90 cm to obtain an accessible q-range from 0.15 to 9.25 nm^{-1}. A reference measurement was made using silver-behenate as a standard for the calibration of the angular regime. Azimuthal integration of the 2D images was done using the Fit2D program [33]. The resulting integrated scattering curves were corrected for dark-current, normalized by sample transmission and subsequently the background was subtracted using the pure solvent-scattering. Theoretical form factors were calculated using the CRYSOL software [34]. Wide angle X-ray scattering (WAXS) data was recorded simultaneously with the corresponding SAXS measurement. In addition, a Pilatus100K image detector (Dectris, Switzerland) was placed vertically to cover scattering angles from 22° to 34°, resulting in an approximate q-range from 16 to 22 nm^{-1}. Further data treatment was done in analogue to the SAXS data.

2.4. Scanning electron microscopy (SEM)

Scanning electron microscopy images were obtained using a MIRA3 microscope (Tescan, Czech Republic) operating at an accelerating voltage of 30 kV. The liquid samples were dropped onto a Si wafer and spin-coated at 600 rpm for 120 s.

2.5. Absorption and emission measurements

Steady-state absorption spectroscopy studies have been performed at room temperature on a *Varian Cary 5000* UV–Vis–NIR double beam spectrophotometer; 10 mm path length Hellma Analytics 100 QS quartz cuvettes have been used.

Steady-state fluorescence spectra have been recorded on a *Varian Cary Eclipse Fluorescence* spectrophotometer; 10 mm path length *Hellma Analytics 117.100F QS* quartz cuvettes have been used.

3. Results and discussion

Amphiphilic **PBI1** carries two positive peripheral tetra-alkyl ammonium pendants at the central imide position (Scheme 1), with Cl^- as the counter anion. It is known from literature that PBIs tend to self-assemble into supramolecular architectures in protic media such as water [3]. A first indication of this phenomena is found in the absorption spectra of very low concentrated **PBI1** in aqueous solution.

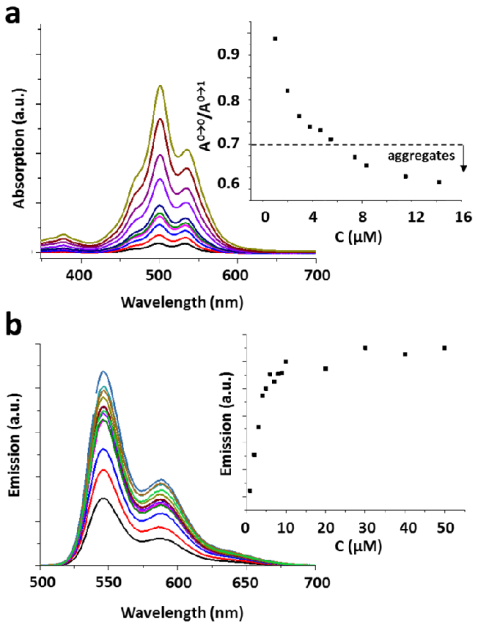

Figure 1. Absorption spectra measured for **PBI1** in deionized water, R.T., from 1 µM to 14 µM. The 537 nm/501 nm ratio dependence on **PBI1** concentration is shown in the inset. b) Corresponding fluorescence spectra measured for ranging from 1-50 µM. Similar to above, a clear correspondence between the **PBI1** concentration and the emission intensity at 545 nm is seen in the inset.

As depicted in Fig. 1a, the steady state absorption was performed in the concentration range between 1 µM to 14 µM. All recorded spectra exhibit two absorption peaks at 537 nm and 501 nm, corresponding to the 0 → 0 and the 0 → 1 transition. The ratio of the intensity of peak absorbance of the lowest two energy transitions $A^{0\to0}/A^{0\to1}$ can be used to interpret the level of aggregation of the perylene chromophores in solution. In the case of individual molecules with normal Franck-Condon progression, this ratio should be around 1.6 [35] whereas for aggregated species typical values are <0.7 [36,37]. The experimentally determined dependency of $A^{0\to0}/A^{0\to1}$ on the **PBI1** concentration is shown in the inset in Fig. 1a, whereas the relative intensities between the two peaks significantly change with increasing concentration. Even at the lowest measured concentration of 1 µM the peak ratio is 0.95, already indicating evidence of aggregation. This ratio further decreases with

increasing **PBI1** concentration, reaching a minimum at around 0.60. This general intensity reversal is attributed to the strong electron-phonon coupling in the aggregated structures and is characteristic for an H-type conformation (stacking direction is normal to the perylene-core plane) [38]. These results are in accordance with previous work and give us clues on the formation of aggregates in a parallel stacked H-type geometry [28,29].

In analogue, the emission spectrum of the **PBI1** is mirror image of the absorption spectrum (see Fig. 1b) [39,40]. In the case of DMF as a solvent, the fluorescence quantum yield is very high (near unity, Fig. S1). However, the emission yield is immediately quenched in the presence of water (7% for a solution of 10 µM, see Fig. S1). This effect is the second piece of evidence of the formation of supramolecular aggregates, at concentrations as low as 10 µM [10]. The emission quenching is further amplified at higher concentrations: as seen in Fig. 1b, the emission remains apparently constant when increasing the concentration from 10 to 50 µM, whereas a further increase to 0.1 and 1 mM actually causes a lowering of the emission intensity (see Fig. S2) [10].

To gain a more direct insight in the structural aspects, we performed small angle X-ray scattering (SAXS) measurements at the lowest possible concentration. As seen in Fig. 2a, the scattering pattern of **PBI1** at 0.6 mM shows a distinct increase in the low-q regime ($q < 0.5$ nm^{-1}), characteristic of large-scale aggregate scattering [41]. However, the mid- and higher-q regime ($q > 1$ nm^{-1}) are dominated by the form-factor scattering of a modeled **PBI1**dimer (see inset Fig. 2a). The full scattering-curve was hence fitted using a custom model (see black curve Fig. 2a), which includes both of the above scattering contributions (see Supporting Information for details).

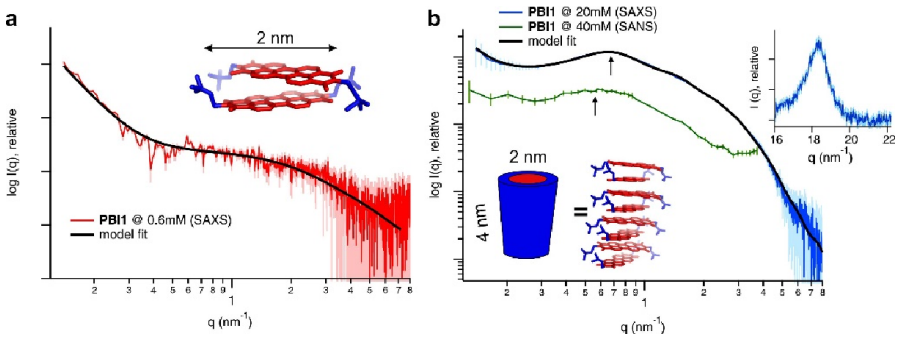

Figure 2. a) SAXS pattern of **PBI1** at 0.6 mM (red) as well as a corresponding model fit (black) utilizing the form-factor scattering of the **PBI1** dimer shown in the inset. b) SAXS (blue) and SANS (green) of **PBI1** at 20 mM and 40 mM, respectively. The fitted model curve yields best agreement for a core-shell cylinder of π-π-stacked molecules as confirmed by the WAXS data (see π-π-stacking peak in the inset). The black arrows indicate the position of the first structure-factor peak relating to the mean distance between the cylindrical aggregates.

Upon increase of **PBI1** concentration to 20 mM, the scattering pattern changes drastically (see Fig. 2b). Especially in the mid-q regime a strong deviation of the previous curve is observed, such that the dimeric **PBI1** form-factor scattering is not witness any more. We hence changed the previous model function to now include the contribution of a core-shell cylinder. Also in this case, the full pattern is fitted, whereas the best agreement is found for a cylinder of 4 nm height and 2 nm diameter. Comparison of these results with the characteristic dimensions of a single **PBI1** molecule strongly suggests the formation of a stacked conformation, as sketched in the inset of Fig. 2b (see Supporting Information for details).

To elucidate the intermolecular arrangement inside the cylinder, the simultaneously obtained WAXS measurements were further analyzed. As shown in the inset of Fig. 2b, a strong diffraction peak at 18.35 nm^{-1} (d-spacing of $d=2\pi/q = 0.34$ nm) is visible. This peak hence corresponds to the π-π-stacking distance of **PBI1**. Additionally, a coherent-domain size can be estimated from the peak width (FWHM = 1.35 nm^{-1}), such that the π-π-stacking extends over approx. 3.9 nm. This value is in agreement with the length of the cylinder axis previously determined from the SAXS data fit (see Fig. 2b), hence confirming the proposed model. Further, these results also imply that the cylindrical aggregates are crystalline such that they can be seen as nano-meter sized single-crystals.

However, the concentration increase of **PBI1** from 0.6 to 20 mM affects the SAXS data from more than one perspective: besides the discussed change in the form-factor scattering, a significant structure-factor contribution is observed (see Supporting Table 2). In the context of this investigation, the structure factor describes the interactive forces between the cylindrical aggregates. As an example, the first broad peak at approx. 0.65 nm^{-1} relates to the mean next-neighbor distance between the cylinders, whereas the fitting-results determined this distance to be about 4.0 nm (see black arrow in Fig. 2b). Comparison of this value with the cylindrical dimensions above suggest that the length of the π-π-stacked nano-crystals dominates the mean interparticle distance. Additional neutron scattering experiments (SANS) of **PBI1** at an increased concentration of 40 mM are consistent with this hypothesis: as the concentration increases, the nano-crystals are most likely growing along the π-π-stacking direction, resulting in an increased cylinder length. This further increases the mean interparticle distance such that the first structure-factor peak shifts to lower q-values (see black arrows in Fig. 2b). Therefore, further concentration increase will most-likely result in highly

elongated rod-like structures, similar to what found in liquid crystalline phases for the same compound [22].

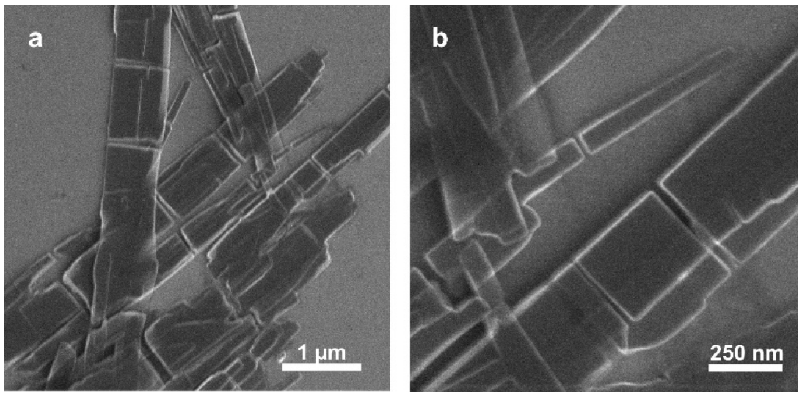

Figure 3. SEM images of **PBI1** nano-scaffolds after spin-coating a 0.6 mM aqueous solution. a) Contrary to the assumption that **PBI1** forms columnar 1D assemblies, the microscopic morphology appears to be of a more planar nature with sheet-like character. b) At such high-magnification, the **PBI1** aggregates present sharp edges, suggesting a higher-ordered, maybe even crystalline, molecular structure.

The tendency of **PBI1** to form highly ordered structures in aqueous solution is further confirmed by means of SEM. We selected a sample of 0.6 mM **PBI1**, as under these conditions no nano-crystals formed in solution. Yet, after spin-coating the sample on a Si wafer, the SEM images present micrometer-sized structures with sharp, well-defined edges as usually found for crystalline materials (see Fig. 3a and b). Surprisingly, the overall morphology of the structures does not appear to be columnar, as often reported for perylene-based materials [42,43] but more of planar, sheet-like nature. Hence, there exists a striking difference between the structural motive in-solution and the morphology in the dry state.

4. Conclusion

In this work, we address the structural nature of **PBI1** in aqueous solution, spanning over a concentration range from 1 µM to 40 mM. Under all the studied conditions, the hydrophobic π-π-interactions appear to be the dominant cause of molecular self-organization. Spectroscopic measurements suggest H-type aggregation, even at concentrations as low as 1 µM. SAXS data taken at 0.6 mM provides direct evidence of the presence of **PBI1** dimers, hence confirming the spectroscopic results. Upon further increasing the concentration, the **PBI1** dimers assemble along the π-π-stacking direction, forming highly ordered cylindrical nano-crystals. Complete drying of the solution causes the loss of the cylinder-like conformation, whereas a planar sheet-like morphology is observed. Hence, there exists a

significant difference between the solution and solid-state nature of the aggregated compounds. The presented findings are of special interest in the design and production of solution-processed materials, utilizing perylene compounds in aqueous light-harvesting systems and for the production of chromonic liquid crystals.

5. References

[1] I. Dincer, C. Acar, Int. J. Hydrogen Energy 40 (2015) 11094.

[2] P. Fornasiero, K.C. Christoforidis, ChemCatChem (2017).

[3] D. Baran, R.S. Ashraf, D.A. Hanifi, M. Abdelsamie, N. Gasparini, J.A. Rohr, S. Holliday, A. Wadsworth, S. Lockett, M. Neophytou, C.J.M. Emmott, J. Nelson, C.J. Brabec, A. Amassian, A. Salleo, T. Kirchartz, J.R. Durrant, I. McCulloch, Nat Mater advance online publication (2016).

[4] A.S. Weingarten, R.V. Kazantsev, L.C. Palmer, M. McClendon, A.R. Koltonow, P.S. SamuelAmanda, D.J. Kiebala, M.R. Wasielewski, S.I. Stupp, Nat Chem 6 (2014) 964.

[5] D. Görl, X. Zhang, F. Würthner, Angew. Chem. Int. Ed. 51 (2012) 6328.

[6] F. Wurthner, Chemical Communications (2004) 1564.

[7] C. Li, H. Wonneberger, Adv. Mater. 24 (2012) 613.

[8] C.D. Schmidt, A. Hirsch, Ideas in Chemistry and Molecular Sciences, Wiley-VCH Verlag GmbH & Co. KGaA, 2010, p. 283.

[9] D.M. Bassani, L. Jonusauskaite, A. Lavie-Cambot, N.D. McClenaghan, J.-L. Pozzo, D. Ray, G. Vives, Coordination Chemistry Reviews 254 (2010) 2429.

[10] S.W. Thomas, G.D. Joly, T.M. Swager, Chem. Rev. 107 (2007) 1339.

[11] X. Feng, L. Liu, S. Wang, D. Zhu, Chemical Society Reviews 39 (2010) 2411.

[12] E.-K. Fleischmann, R. Zentel, Angew. Chem. Int. Ed. 52 (2013) 8810.

[13] F.J.M. Hoeben, P. Jonkheijm, E.W. Meijer, A.P.H.J. Schenning, Chem. Rev. 105 (2005) 1491.

[14] S. Chen, P. Slattum, C. Wang, L. Zang, Chem. Rev. (2015).

[15] M.J. Ahrens, L.E. Sinks, B. Rybtchinski, W. Liu, B.A. Jones, J.M. Giaimo, A.V. Gusev, A.J. Goshe, D.M. Tiede, M.R. Wasielewski, J. Am. Chem. Soc. 126 (2004) 8284.

[16] S.-W. Tam-Chang, J. Helbley, I.K. Iverson, Langmuir 24 (2008) 2133.

[17] S.-W. Tam-Chang, I.K. Iverson, J. Helbley, Langmuir 20 (2004) 342.

[18] C.R. Weitzel, T.A. Everett, D.A. Higgins, Langmuir 25 (2008) 1188.

[19] Y. Huang, B. Quan, Z. Wei, G. Liu, L. Sun, J. Phys. Chem. C 113 (2009) 3929.

[20] J. Lydon, Journal of Materials Chemistry 20 (2010) 10071.

[21] S.-W. Tam-Chang, L. Huang, Chemical Communications (2008) 1957.

[22] A. Laiho, B.M. Smarsly, C.F.J. Faul, O. Ikkala, Adv. Funct. Mater. 18 (2008) 1890.

[23] Y. Huang, Y. Yan, B.M. Smarsly, Z. Wei, C.F.J. Faul, Journal of Materials Chemistry 19 (2009) 2356.

[24] E. Tenori, A. Colusso, Z. Syrgiannis, A. Bonasera, S. Osella, A. Ostric, R. Lazzaroni, M. Meneghetti, M. Prato, ACS Applied Materials & Interfaces 7 (2015) 28042.

[25] U. Keiderling, Appl. Phys. A 74 (2002) s1455.

[26] H. Amenitsch, M. Rappolt, M. Kriechbaum, H. Mio, P. Laggner, S. Bernstorff, Journal of Synchrotron Radiation 5 (1998) 506.

[27] A.P. Hammersley, S.O. Svensson, M. Hanfland, A.N. Fitch, D. Hausermann, High Pressure Research 14 (1996) 235.

[28] D. Svergun, C. Barberato, M.H.J. Koch, J. Appl. Crystallogr. 28 (1995) 768.

[29] W. Wang, J.J. Han, L.-Q. Wang, L.-S. Li, W.J. Shaw, A.D.Q. Li, Nano Letters 3 (2003) 455.

[30] W. Wang, W. Wan, H.-H. Zhou, S. Niu, A.D.Q. Li, J. Am. Chem. Soc. 125 (2003) 5248.

[31] S. Yagai, T. Seki, T. Karatsu, A. Kitamura, F. Würthner, Angew. Chem. Int. Ed. 47 (2008) 3367.

[32] T.A. Everett, D.A. Higgins, Langmuir 25 (2009) 13045.

[33] O. Glatter, J. Appl. Crystallogr. 10 (1977) 415.

[34] C. Huang, S. Barlow, S.R. Marder, J. Org. Chem. 76 (2011) 2386.

[35] K. Bag, P.K. Sukul, D. Chandra Santra, A. Roy, S. Malik, RSC Advances 6 (2016) 34027.

A4: Inter-backbone charge transfer as prerequisite for long-range conductivity in perylene bisimide hydrogels

Max Burian[†, $] , Francesco Rigodanza[‡, $], Nicola Demitri[§], Luka Đorđević[‡], Silvia Marchesan[⁋], Tereza Steinhartova[≠], Ilse Letofsky-Papst[ò], Ivan Khalakhan[¶], Eléonore Mourad[ǂ], Stefan A. Freunberger[ǂ], Heinz Amenitsch, [†, *] Maurizio Prato[‡, ┤, ≤,*] and Zois Syrgiannis[‡*]

[†] Institute of Inorganic Chemistry, Graz University of Technology, Stremayrgasse 9/IV, 8010 Graz, Austria, amenitsch@elettra.eu

[‡] Center of Excellence for Nanostructured Materials (CENMAT) and INSTM, unit of Trieste, Department of Chemical and Pharmaceutical Sciences, University of Trieste, via L. Giorgieri 1, 34127 Trieste, Italy, zsyrgiannis@units.it

[§] Elettra-Sincrotrone Trieste, Strada Statale 14, km 163.5 in AREA Science Park, 34149 Basovizza, Trieste, Italy.

[⁋] University of Trieste, Chemical and Pharmaceutical Sc. Dep., Via L. Giorgieri 1, 34127 Trieste, Italy

[≠] Istituto Officina dei Materiali, IOM – CNR, SS. 14 km 163.5 in Area Science Park, 34149 Basovizza, Italy; Department of Physics, University of Trieste, 34128 Trieste, Italy.

[ò] Institute for Electron Microscopy & Nanoanalysis and Center for Electron Microscopy, Graz University of Technology, NAWI Graz, Steyrergasse 17, 8010 Graz, Austria.

[¶] Department of Surface and Plasma Science, Faculty of Mathematics and Physics, Charles University, V Holešovičkách 2, 180 00 Praha 8, Czech Republic.

[ǂ] Institute for Chemistry and Technology of Materials, Graz University of Technology, Stremayrgasse 9, 8010 Graz, Austria.

[┤] Carbon Nanobiotechnology Laboratory CIC biomaGUNE, Paseo de Miramón 182 20009 Donostia-San Sebastian, Spain;

[≤] Basque Fdn Sci, Ikerbasque, Bilbao 48013, Spain, prato@units.it

Submitted in 2018.

Hydrogelation, the self-assembly of molecules into soft, water-loaded networks, bridges the structural gap between single molecules and functional materials. The potential of hydrogels, such as those based on perylene bisimides, lies in their chemical, physical, optical, and electronic properties, which are all governed by the inter- and supramolecular structure of the gel. However, these structural motifs and their precise role for long-range conductivity are unknown. Here, we present a comprehensive structural picture of a perylene bisimide hydrogel, suggesting that its long-range conductivity is limited by charge-transfer between electronic backbones. We reveal nano-crystalline ribbon-like structures as the electronic and structural backbone units between which charge transfer is mediated by polar solvent bridges.

We exemplify this effect with gas sensing, where exposure to polar vapor enhances conductivity by five orders of magnitude, emphasizing the crucial role of the interplay between structural motif and surrounding medium for the rational design of devices based on nano-crystalline hydrogels.

Organic semiconductors based on perylene bisimide (PBI) dyes have gained enormous attention due to their manifold potential applications. PBIs are robust organic molecules characterized by (i) a broad visible absorption cross-section, (ii) low cost of the sustainable metal-free raw materials, (iii) high thermal, photo, and oxidative stability, and (iv) versatile stereo-electronic properties of the photo-responsive core that can be easily fine-tuned.[1, 2] The aromatic π-conjugated PBI core is responsible not only for the molecule's optical properties, but also for its tendency to self-assemble through π-π-interactions,[3] leading to highly-ordered supramolecular aggregates that find application in water-splitting, organic field-effect transistors and sensors.[4-9] However, the molecular arrangement not only induces a structural motif, but also affects the molecular dipole-dipole alignments and therefore the electronic and optical properties.[10-13] According to this structure-function correlation, a clear and precise characterization of PBI-based materials at the molecular level is required for the successful design of future devices.

Due to its hydrophobic nature, the structure defining π-π-interaction is particularly robust in aqueous solvents – a principle that can be used to form water-based soft, molecular networks called hydrogels.[14, 15] Hydrogels find their full potential within their hierarchical nature: at the macroscopic level, hydrogels are highly porous materials that are easily loaded with e.g., colloidal nanocatalysts, and allow diffusion of educts and products from the reaction sites.[16-20] At the molecular level, PBI-based gels consist of π-π-stacked structures that are capable of charge-separation and transport.[21-24] While this molecular motif is thought to act as the electronic and structural backbone of the gel[23], the long-range charge-transfer mechanism between these backbone units, a prerequisite for application, is currently unknown.

Herein, we present a comprehensive structural framework of the pH-triggered hydrogel using single-crystal diffraction, mechanical, spectroscopic, scattering, imaging and computational techniques and we provide evidence for solvent-mediated inter-backbone charge transfer in PBI hydrogels. We reconstruct the underlying structural motif over a wide length-scale

ranging from crystalline ribbon-like nanostructures, which act as the electronic and structural backbone units, to their macroscopic arrangement. We find macroscopic conductivity of the dried gel only in the presence of a polar vapor, revealing the importance of inter-backbone hydrogen-bonding as charge-transfer bridges. We use this effect in gas-sensing devices that enhance electronic conductivity by five orders of magnitude within milliseconds in response to polar vapor concentration. The awareness of this inter-backbone charge-transfer mechanism is not only crucial to understand and design PBI-based hydrogels, but also to exploit the full potential of chemically related nano-crystalline hydrogel-based devices.

We synthesized the known from the literature N,N'-bis(propanoic acid)-perylene-3,4,9,10-tetracarboxylic bisimide (PBI1 - Figure 1a)[25] following a modified method with the use of a microwave-irradiation[26] (see Supporting Information for details) and then it is prepared a 8.8 mM PBI1 precursor in basic (pH 10) aqueous triethylamine (TEA) solution. To understand the molecular interactions of PBI1 under these conditions, we obtained crystallographic data of single crystals grown from the precursor (for details see single-crystal analysis in the Supporting Information). In its single-crystalline form, PBI1 forms typical π-π-stacked columns as shown in Figure 1b and Supporting Information, Figure S1. Within these columns, the molecules are both longitudinally and transversally shifted so that the stacking direction is tilted by 23° away from the direction perpendicular to the perylene plane (Figure 1b). The tilted axis is most likely caused by intra-columnar hydrogen-bonding between the carboxylic groups, resulting in sandwiched PBI1-trimers (yellow circle in Figure 1b and Supporting Information, Figure S1). This motif leaves two unused carboxylic acids per triplet, which offer binding moieties capable of cross-linking between longitudinal neighboring columns (blue circle in Figure 1b). In addition, the hydrophobic interaction between units of the perylene core causes transversal attraction between the stacks to minimize the core's exposure to the polar medium. This single-crystalline motif, in particular the columnar arrangement of PBI1, is the structural cornerstone for the following sections.

Acidifying the basic precursor solution of PBI1 with 4 M aq. HCl to pH 4 commences the gelation process.[25] After an aging period of approx. 4 min (the time depends on the volume of the precursor solution), the liquid precursor transforms into a gel-like substance that it is capable of holding its own weight in a glass vial (see Supporting Information, Figure S2a and Synthesis in the Supporting Information for further details). Oscillatory rheometry analysis of the gelation process (Supporting Information, Figure S2) supports the gel formation.

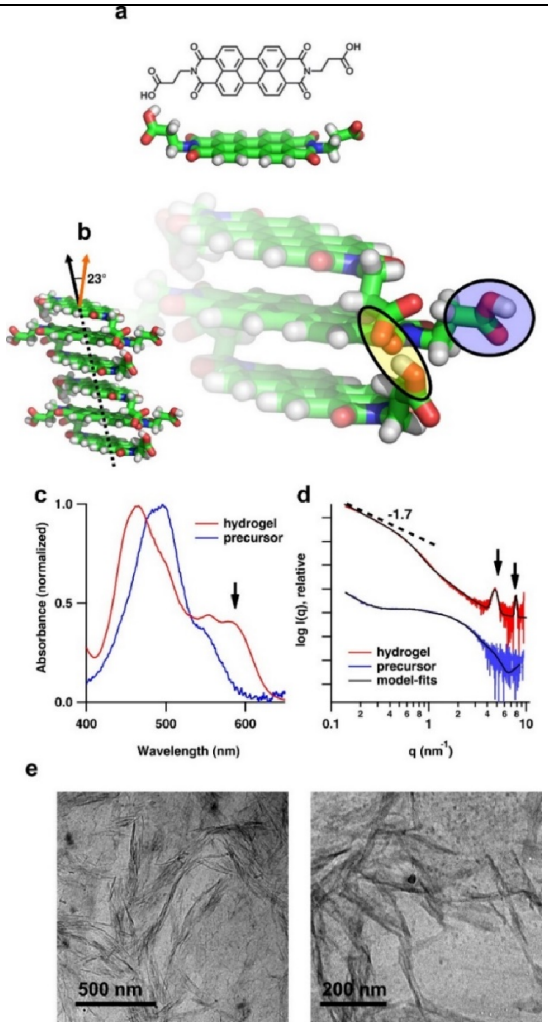

Figure 1. Structural characterization of PBI1 at the nanoscale. a, Representation and graphical model of the **PBI1** molecule. **b**, Molecular model of the π-π-stacked columns found in the crystal structure, illustrating the 23° difference between column axis (black arrow) and the direction perpendicular to the **PBI1** core (orange arrow). The magnified view highlights the intra-columnar hydrogen bonding between carboxylic groups within the characteristic **PBI1** triplet (yellow circle), leaving one sandwiched carboxylic group unbound (blue circle). **c,** UV/Vis absorption spectra of the **PBI1** precursor solution before addition of HCl (blue) and in the hydrogel (red) state. The black arrow indicates the absorption peak characteristic of the *J*-band for aggregation in the hydrogel. **d**, SAXS patterns corresponding to the UV/Vis absorption measurements in **c**, together with the full-pattern refined model-fits (black). The two black arrows indicate the positions of Bragg-peaks, characteristic for the nano-crystalline nature of the hydrogel. **e,** Two representative Cryo-TEM images of the hydrogel clearly reveal a ribbon-like nanostructure.

Gelation changes the sample color from dark red to dark brown (Supporting Information, Figure S2a). This color change suggests a structural reorientation and electronic states alteration, in accordance with the general structure-function relation in molecular photodyes, such as PBI1.[23] To understand this transition, we investigated the optical and structural nature of precursor and hydrogel by means of UV/Vis absorption, small angle-x-ray scattering

(SAXS) and cryogenic transmission electron microscopy (Cryo-TEM) (Figure 1c–e and Supporting Information, Figure S3-S7).

Generally, perylene bisimides exhibit a fine vibronic structure of the main electronic transitions. Yet, molecular aggregation induces strong exciton interactions between neighboring chromophores, which not only suppresses the monomeric fine structure but also leads to new absorption bands[27-29]. In case of the precursor solution, we observe the absorption maximum at 496 nm together with a weaker, red-shifted J-band at 554 nm (Figure 1c, blue trace and Supporting Information, Figure S3a for peak-fit). Such a spectrum results from H-type exciton coupling – a typical observation for perylene bisimides in solution, liquid-crystalline mesophases and spin-coated films of columnar π-π-stacks[27-29]. Gelation of the precursor causes a blue shift of the absorption maximum from 496 to 466 nm (Figure 1c, red trace and Supporting Information, Figure S3b for peak-fit).[30-32] We further observe the appearance of a new peak at 585 nm (see black arrow in Figure 1c) – a behaviour that has previously been linked to re-orientation or translation of π-π-interacting perylene bisimide cores[1, 33, 34]. Thus, UV/Vis suggests the gelation process to cause a change in the transition type, possibly related to a shift of the stacking direction away from the axis perpendicular the PBI1 molecular core or a change in the angle between the transition dipole moments of PBI1[1, 33, 34].

To obtain more direct information on the structural motif of the **PBI1** in the precursor, the transition during gelation, and the final gel, we performed SAXS measurements. The scattering data of the protonated precursor state (basic aqueous solution) shows a low–q transition to the Guinier regime (q^{-0}), which is characteristic for form-factor scattering of non-aggregated particles (Figure 1d). To model the pattern, we used a single **PBI1** molecule from the single-crystal structure to build a series of progressively stacked *H*-type arrays (more details about the modelling are given in the section SAXS model fitting in the Supporting Information). Best agreement between model and data was found for π-π-stacked tetramers (Supporting Information, Figure S5), and full pattern refinement suggests 4 nm mean distance between the tetramers (Figure 1d, black trace). It should, however, be noted that the tetrameric conformation only represents a *mean* observation, where in fact a series of other conformations, such as *e.g.* trimers, tetramers, decamers, etc., are present in solution[12]. Thus, the hydrophobic attraction of the perylene cores causes short column-like assemblies, in agreement with literature and the UV/Vis measurements.

We recorded the structural transition from precursor to hydrogel using *in-situ* SAXS measurements during the gelation process (Supporting Information, Figure S5a) and found two distinct phenomena. First, the strongly increasing scattering intensity in the low–q regime ($1 < q < 2$ nm^{-1}) signals a growing structural motif. Second, the two diffraction peaks that form in the mid–q regime ($4 < q < 5$ nm^{-1}) result from crystalline ordering. The comparison of the integral intensities of the two reciprocal space regions connects these named mechanisms (Supporting Information, Figure S5b). Analyzing the SAXS pattern of the hydrogel (Figure 1d, red trace) in more detail shows as the most striking difference to the precursor the transition in the low–q region: the power-law slope has increased from q^{-0} to $q^{-1.8}$. Such a behaviour characterizes the presence of a two-dimensional motif, such as, sheet- or ribbon-like structures with internal disorder and porosity (q^{-2} slope in the case of a solid sheet-like structure)[35]. The Guinier fit reveals an approximate sheet thickness of 5 nm (see SAXS model fitting in the Supporting Information for more details). Transmission electron microscopy (TEM) images taken under cryogenic conditions (Cryo-TEM) show a similar motif (Figure 1e and Supporting Information, Figure S6 for magnification), whereas the ribbon-like nanostructures act as the structural backbone through cross-linking between them. Atomic force microscopy (AFM) images of a drop-casted sample confirm a ribbon thickness of approx. 5 nm (Supporting Information, Figure S7).

The SAXS pattern of the final hydrogel shows two distinct peaks as indicated by the black arrows in Figure 1d, caused by a recurrent structural motif in the hydrogel. A corresponding wide-angle X-ray diffraction (XRD) pattern presents eight reflections (Figure 2a). As, beside the characteristic π-π-stacking peak, this pattern is significantly different from the single-crystal scattering (see Supporting Information, Figure S8), it suggests a different arrangement of the prevailing π-π-stacked columns in the hydrogel compared to the single-crystal. Indeed, all but the latter two reflections can be indexed using a two-dimensional oblique (P1) lattice[5] with a = 2.188 nm, b = 1.367 nm, and γ = 36.14° (see indexing in Figure 2a and for details see X-ray diffraction analysis in the Supporting Information).

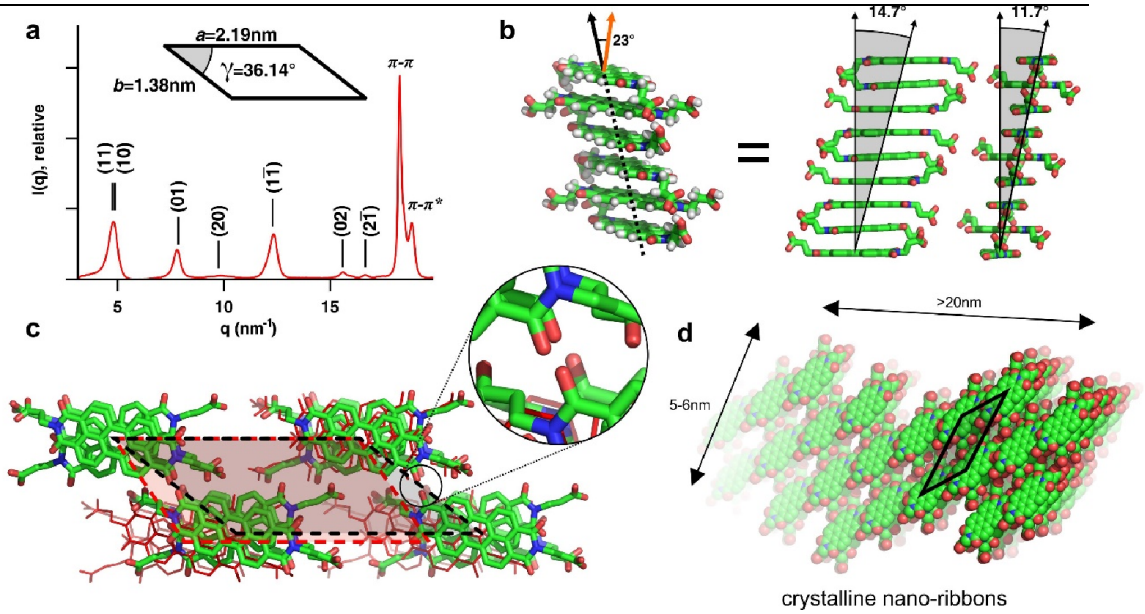

Figure 2. Molecular architecture within the PBI hydrogel. a, XRD pattern of the hydrogel. The sharp peaks correspond to the oblique unit cell (black inset) of π-π-stacked **PBI**. **b**, Overview as well as longitudinal and lateral view (left to right) of isolated π-π-stacked **PBI** columns. **c**, Top view of the unit cell within the hydrogel (black) compared to the single-crystalline motif (red). The magnified view shows the now preferred alignment between the **PBI1** carbonyl groups. **d**, Representation of the unit-cell (black) within the crystalline nano-ribbons that form during gelation process and act as structural backbone units of the hydrogel.

Single crystal- compared to hydrogel-scattering implies that only the intra-columnar *π*-*π*-stacked motif previously found in the single-crystal (see Figure 2b) is preserved in the gel state. Consequently, the oblique unit cell dimensions determined by XRD measurements relate to mean distances between these *π*-*π*-stacked columns. We take advantage of this circumstance and use a single molecular column from the crystallographic structure to build a structural model. By doing so, the columnar cross-section only fits inside the hydrogel unit cell if both long axis are aligned parallel (see Figure 2c). The full structural arrangement then becomes apparent by multiplying the unit cell using its oblique dimensions. The resulting model compared to the single-crystalline structure is shown in Figure 2c, revealing a similar structural motif in both cases: the columns appear to cross-link preferentially between the now protonated carboxylic groups. Yet, the distance along this direction is identical, leaving polar channels for water to penetrate. In lateral direction, the oblique unit cell angle decreases from 54.78° to 36.14°, resulting in a linear alignment of neighboring imide groups (see inset in Figure 2c). Infrared spectra confirm this arrangement: the peaks related to both the carboxylic and amidic C=O distances red-shift due to increasing peripheral interaction, such as hydrogen bonding (Supporting Information, Figure S9). This suggests hydrogen bonding between these

moieties instead of electrostatic repulsion between the carbonyl oxygen atoms. Hence, the hydrogel consists **PBI1** nano-ribbons with high crystalline order (see Figure 2d). A crucial side effect of this crystallinity is that the nano-ribbons are encapsulated by the carboxylic chains. These chains cross-link *via* hydrogen bonds and are therefore responsible for the structural cohesion between nano-ribbons.

To substantiate this proposition and to link scattering and spectroscopic data, we performed computational modelling based on the dimer approach – a method previously used to understand optical spectra of perylene-based aggregates[23]. We selected two characteristic structural motifs from which we constructed and optimized corresponding dimers, using the dispersion-corrected density functional theory (DFT) using Grimme's PBEh-3c approach[36] (Supporting Information, Figure S10 and S11 for possible conformations). These calculations verify the structural model, in particular the transition from perpendicular to a planar shifted π-π-stacking conformation of **PBI1** throughout the gelation process (see Supporting Information, DFT part, Figures S10 and S11).

To probe the accessibility of the imide groups and to derive additional information of the nano-ribbons' inner structure, we performed CO_2 absorption measurements. A variety of organic pigments, including imides, has been shown to absorb CO_2 at carbonyl positions to form semicarbonates[39-43]. This phenomenon is directly seen in the redox properties of the pigments and can therefore be probed by cyclic voltammetry (CV)[39-41, 43]. A CV of the precursor **PBI1** in by N_2 flux deaerated aqueous solution shows two reduction processes centered around –0.3 and –0.7 V vs. Ag/AgCl, which correlate to the reduction of the carbonyl moieties (Figure 4a). This redox activity disappears after purging the solution for 10 min with CO_2, which indicates the formation of the related semi-carbonate. The latter is not electrochemically active in the potential window between 0.2 and –0.8 V. The same measurements obtained of the hydrogel yield a strikingly different result (Figure 4b). The voltammograms are unaffected by the presence of CO_2 and show both under N_2 and CO_2 atmosphere a reversible redox couple centered around -0.3 V. This indicates that the imide groups are blocked by the close, intermolecular arrangement within the crystalline nano-ribbons, such that CO_2 cannot access the absorbing atomic sites. This effect emphasizes the importance of the structure-function interplay and further corroborates the molecular model of the hydrogel in Figure 2c and d.

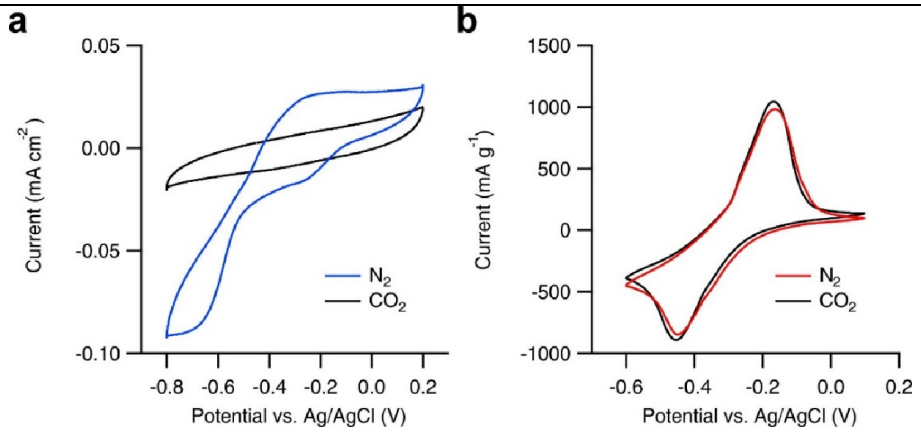

Figure 3. CO_2 absorption by the PBI1 and the hydrogel. a, Cyclic voltammograms of the **PBI1** precursor solution when N_2 purged (blue) and after 10 min purging with CO_2 (black) at a glassy carbon working electrode. **b**, Cyclic voltammograms of the immobilized hydrogel under N_2 (red) and CO_2 atmosphere (black). All measurements were recorded at 50 mV s^{-1}.

The crystalline nature of the nano-ribbons is of particular importance for long-range charge-transfer as it enables charge-mobility along the π-π stacked columns[44, 45]. However, this mechanism is only one-dimensional. Bulk-conductivity over all three dimensions therefore requires *lateral* charge transfer, that is between the π-π stacked columns and further between the crystalline nano-ribbons. Since both, the π-π stacked columns as well as the crystalline nano-ribbons, are inter-connected *via* hydrogen-bonding, charge-transfer between two entities must occur via bridging sites. If this hypothesis is correct, absorbing protic media should be able to activate the hydrogen-bridging sites and therefore allow long-range charge-transfer.

To investigate these *lateral* inter-columnar charge transfer mechanisms, we fabricated simple gas-sensing devices by drop-casting a **PBI1** hydrogel film between two Au electrodes on a glass substrate as detailed in the Methods. The electrode spacing of 300 µm is unlikely to be bridged by a single hydrogel ribbon and thus this setup measures overall bulk-conduction including inter-backbone conduction. SEM images and grazing incidence SAXS (GISAXS) measurements confirm that the hydrogel-characteristic nano-ribbons as well as the intermolecular motif remain intact after drying (Figure 5a and Supporting Information, Figure S12 and S13). In a dry state, the current through the hydrogel is as low as 2 pA at a bias of 2 V. When the sample was repeatedly exposed to 300 ms pulses of H_2O saturated air using a custom gas-flow setup (see illustration in Figure 5a), the current increased by nearly five orders of magnitude to 93.3 ± 3.3 nA (Figure 5b). We probed the response time to humidity changes

using 100 ms pulses, which led to a sharp rise in current within 10s of ms and re-equilibration to the dry conditions within two seconds (Figure 5c).

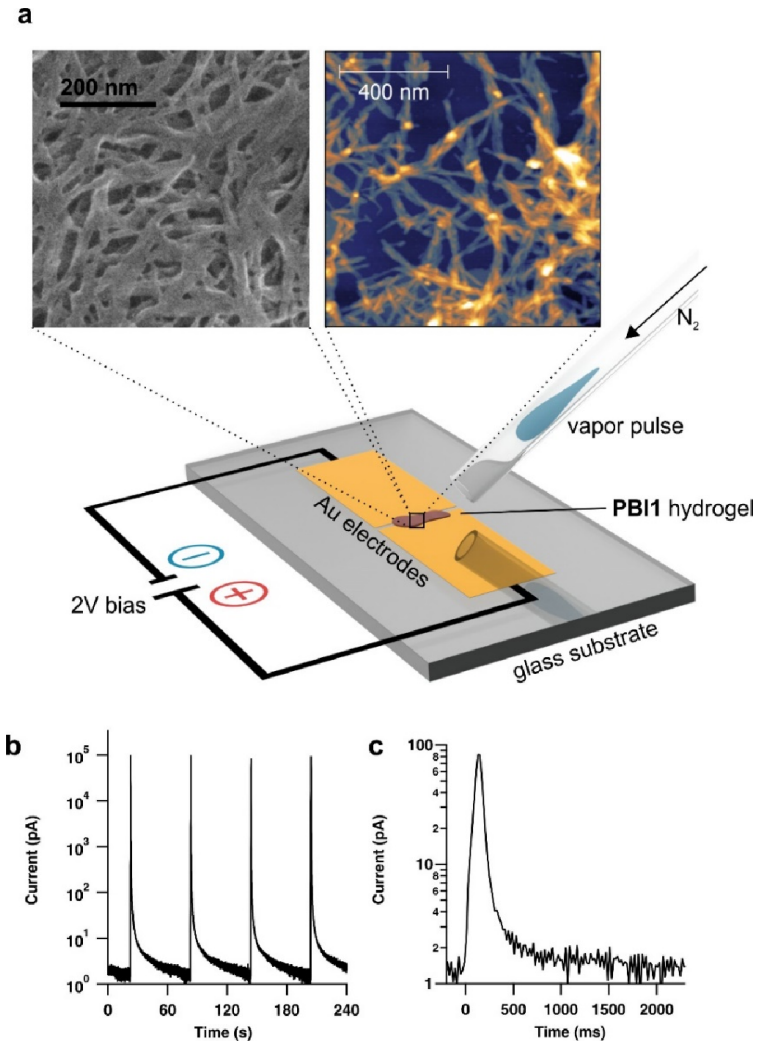

Figure 5. Electric response of the dried hydrogel to polar vapor. a, Schematic representation of the experimental setup together with AFM and SEM image of the dried hydrogel, confirming the ribbon-like nature of the hydrogel also in the dried state. **b**, Electrical response after deposition of 300 ms pulses of saturated H_2O vapor, showing an increase of conductivity over 5 orders of magnitude. **c**, Time-resolved electrical response of a single 100 ms pulse of saturated H_2O.

We attribute this behavior to the solvent-induced activation of the *lateral* inter-columnar charge transfer. We stipulate that the previously determined carboxylic groups are not only responsible for the structural cohesion, but also act as conduction bridges between nano-ribbons. Water forms temporary hydrogen bridges between the nano-ribbons, allowing for charge transfer between them. Upon flushing the sample with N_2, the intercalated water is removed such that conduction between the nano-ribbons is suppressed.

Synthetic routes and theoretical calculations of amphiphilic perylene imide hydrogels are known in literature[23, 25, 46]. Despite the large number of works that appeared in the field of perylene bisimide gels[47-49], only a few examples presented hydrogels[16, 21, 50, 51] and fewer provide experimental insights into the hydrogels' structure[5, 16, 52]. Specifically, the strong hydrophobic effect that can direct self-assembly in aqueous solutions has recently attracted interest. This effect has been only glanced at the gel-phase and it is of special interest in π-conjugated systems, because the structural changes accompanying the phase transition (from solution to gel) can be used to provoke optoelectronic changes[16, 23]. With the aim of elucidating the gap between the hydrogel structure and its properties, we have performed an in-depth study on **PBI1**, as a blueprint of π-conjugated molecules useful in optolectronic devices.

According to all the aforementioned techniques that we used, such as scattering, microscopic, electrochemical, and electrical methods, we could construct a comprehensive structural model based on a hierarchy of structure-directing motifs. First, π-π-stacking is without doubt the characteristic structural motif to form **PBI1** columns. Second, the protonated carboxylic groups of **PBI1** are responsible for longitudinal cross-linking between the π-π-stacked columns. Third, from the X-ray scattering data we find the symmetric imide groups to be responsible for the lateral *in-plane* attachment between the π-π-stacked columns (Figure 2c). We find confirmation for this structure in the CO_2 absorption measurements. While accessible in the precursor, the imide positions are structurally blocked in the hydrogel, such that CO_2 cannot access the carbonyl groups and cannot be absorbed. The X-ray scattering data provides further support for this arrangement of the π-π-stacked columns within the nano-ribbons, since other arrangements would result in different diffraction peaks for the unit-cell family.

This detailed structural picture allows to understand charge-transfer phenomena as a prominent feature of the hydrogel. We have shown that the nano-ribbon surface is mostly defined by dangling carboxylic groups looking to cross-link with neighboring sites. This cross-linking is responsible for the structural cohesion of the gel in aqueous media and provides mechanical deformability. The bonding sites are the only sites to give the structural vicinity for charge-hopping and they are very likely decisive for inter-ribbon charge-transfer. Hence, carboxylic groups of adjacent nano-ribbons form conduction bridges, responsible for the structural *and* electronic properties of the overall hydrogel. We probed the cross-linking by measuring how the dried hydrogel's conductivity responds to polar vapour. Short water vapour pulses directed onto the dry hydrogel activate conduction bridges between the nano-ribbons

as seen by a fast conductivity increase of almost five orders of magnitude. Upon re-drying of the gel with N_2 these bridges are broken up and long-range charge-transfer is impeded.

REFERENCES

1. Würthner, F.; Saha-Möller, C. R.; Fimmel, B.; Ogi, S.; Leowanawat, P.; Schmidt, D. Chem. Rev. 2016, 116, (3), 962-1052.
2. Huang, C.; Barlow, S.; Marder, S. R. J. Org. Chem. 2011, 76, (8), 2386-2407.
3. Chen, S.; Slattum, P.; Wang, C.; Zang, L. Chem. Rev. 2015.
4. Görl, D.; Zhang, X.; Würthner, F. Angew. Chem. Int. Ed. 2012, 51, (26), 6328-6348.
5. Weingarten, A. S.; Kazantsev, R. V.; Palmer, L. C.; McClendon, M.; Koltonow, A. R.; SamuelAmanda, P. S.; Kiebala, D. J.; Wasielewski, M. R.; Stupp, S. I. Nat Chem 2014, 6, (11), 964-970.
6. Wang, Q.; Li, Z.; Tao, D.-D.; Zhang, Q.; Zhang, P.; Guo, D.-P.; Jiang, Y.-B. Chem. Commun. 2016, 52, (88), 12929-12939.
7. Pfattner, R.; Pavlica, E.; Jaggi, M.; Liu, S.-X.; Decurtins, S.; Bratina, G.; Veciana, J.; Mas-Torrent, M.; Rovira, C. J. Mater. Chem. C 2013, 1, (25), 3985-3988.
8. Erten-Ela, S.; Turkmen, G. Renew. Energy 2011, 36, (6), 1821-1825.
9. Li, C.; Wonneberger, H. Adv. Mater. 2012, 24, (5), 613-636.
10. Hestand, N. J.; Spano, F. C. Acc. Chem. Res. 2017, 50, (2), 341-350.
11. Whitesides, G. M.; Boncheva, M. Proc. Natl. Acad. Sci. U.S.A. 2002, 99, (8), 4769-4774.
12. Chen, Z.; Stepanenko, V.; Dehm, V.; Prins, P.; Siebbeles, L. D. A.; Seibt, J.; Marquetand, P.; Engel, V.; Würthner, F. Chem. Eur. J. 2007, 13, (2), 436-449.
13. Ferlauto, L.; Liscio, F.; Orgiu, E.; Masciocchi, N.; Guagliardi, A.; Biscarini, F.; Samorì, P.; Milita, S. Adv. Funct. Mater. 2014, 24, (35), 5503-5510.
14. Voorhaar, L.; Hoogenboom, R. Chem. Soc. Rev. 2016, 45, (14), 4013-4031.
15. Du, X.; Zhou, J.; Shi, J.; Xu, B. Chem. Rev. 2015, 115, (24), 13165-13307.
16. Gorl, D.; Soberats, B.; Herbst, S.; Stepanenko, V.; Wurthner, F. Chem. Sci. 2016, 7, (11), 6786-6790.
17. Elisseeff, J. Nat Mater 2008, 7, (4), 271-273.
18. Shi, Y.; Peng, L.; Yu, G. Nanoscale 2015, 7, (30), 12796-12806.
19. Erbas, A.; Olvera de la Cruz, M. ACS Macro Lett. 2015, 4, (8), 857-861.
20. Draper, E. R.; Adams, D. J. Chem 3, (3), 390-410.
21. Kularatne, R. S.; Kim, H.; Ammanamanchi, M.; Hayenga, H. N.; Ware, T. H. Chem. Mater. 2016, 28, (23), 8489-8492.
22. Draper, E. R.; Walsh, J. J.; McDonald, T. O.; Zwijnenburg, M. A.; Cameron, P. J.; Cowan, A. J.; Adams, D. J. J. Mater. Chem. C 2014, 2, (28), 5570-5575.
23. Draper, E. R.; Greeves, B. J.; Barrow, M.; Schweins, R.; Zwijnenburg, M. A.; Adams, D. J. Chem 2017, 2, (5), 716-731.

24. Draper, E. R.; Schweins, R.; Akhtar, R.; Groves, P.; Chechik, V.; Zwijnenburg, M. A.; Adams, D. J. Chem. Mater. 2016, 28, (17), 6336-6341.

25. Datar, A.; Balakrishnan, K.; Zang, L. Chem. Commun. 2013, 49, (61), 6894-6896.

26. Rigodanza, F.; Tenori, E.; Bonasera, A.; Syrgiannis, Z.; Prato, M. Eur. J. Org. Chem. 2015, 2015, (23), 5060-5063.

27. Wurthner, F.; Chen, Z.; Dehm, V.; Stepanenko, V. Chem. Commun. 2006, (11), 1188-1190.

28. Würthner, F.; Thalacker, C.; Diele, S.; Tschierske, C. Chem. Eur. J. 2001, 7, (10), 2245-2253.

29. Hansen, M. R.; Schnitzler, T.; Pisula, W.; Graf, R.; Müllen, K.; Spiess, H. W. Angew. Chem. Int. Ed. 2009, 48, (25), 4621-4624.

30. Ghosh, S.; Li, X.-Q.; Stepanenko, V.; Würthner, F. Chem. Eur. J. 2008, 14, (36), 11343-11357.

31. Chen, Z.; Lohr, A.; Saha-Moller, C. R.; Wurthner, F. Chem. Soc. Rev. 2009, 38, (2), 564-584.

32. Lim, J. M.; Kim, P.; Yoon, M.-C.; Sung, J.; Dehm, V.; Chen, Z.; Wurthner, F.; Kim, D. Chem. Sci. 2013, 4, (1), 388-397.

33. Yagai, S.; Seki, T.; Karatsu, T.; Kitamura, A.; Würthner, F. Angew. Chem. Int. Ed. 2008, 47, (18), 3367-3371.

34. Würthner, F.; Scheblykin, I. G., J-AGGREGATES OF PERYLENE DYES. In J-Aggregates, WORLD SCIENTIFIC: 2012; pp 309-342.

35. Glatter, O.; Kratky, O., Small Angle X-ray Scattering. Academic Press: London, 1982.

36. Grimme, S.; Brandenburg, J. G.; Bannwarth, C.; Hansen, A. J. Chem. Phys. 2015, 143, (5), 054107.

37. Chai, J.-D.; Head-Gordon, M. J. Chem. Phys. 2008, 128, (8), 084106.

38. Kasha, M.; Rawls, H. R.; Ashraf El-Bayoumi, M., The exciton model in molecular spectroscopy. In Pure Appl. Chem., 1965; Vol. 11, p 371.

39. Weinberg, N. L.; Kentaro Hoffmann, A.; Reddy, T. B. Tetrahedron Lett. 1971, 12, (25), 2271-2274.

40. Apaydin, D. H.; Głowacki, E. D.; Portenkirchner, E.; Sariciftci, N. S. Angew. Chem. Int. Ed. 2014, 53, (26), 6819-6822.

41. Singh, P.; Rheinhardt, J. H.; Olson, J. Z.; Tarakeshwar, P.; Mujica, V.; Buttry, D. A. J. Am. Chem. Soc. 2017, 139, (3), 1033-1036.

42. Apaydin, D. H.; Gora, M.; Portenkirchner, E.; Oppelt, K. T.; Neugebauer, H.; Jakesova, M.; Głowacki, E. D.; Kunze-Liebhäuser, J.; Zagorska, M.; Mieczkowski, J.; Sariciftci, N. S. ACS Appl. Mater. Interfaces 2017, 9, (15), 12919-12923.

43. Rheinhardt, J. H.; Singh, P.; Tarakeshwar, P.; Buttry, D. A. ACS Energy Letters 2017, 2, (2), 454-461.

44. Wu, N.; Wang, C.; Slattum, P. M.; Zhang, Y.; Yang, X.; Zang, L. ACS Energy Lett. 2016, 1, (5), 906-912.

45. Fink, R. F.; Seibt, J.; Engel, V.; Renz, M.; Kaupp, M.; Lochbrunner, S.; Zhao, H.-M.; Pfister, J.; Würthner, F.; Engels, B. J. Am. Chem. Soc. 2008, 130, (39), 12858-12859.

46. Roy, S.; Kumar Maiti, D.; Panigrahi, S.; Basak, D.; Banerjee, A. RSC Advances 2012, 2, (29), 11053-11060.

47. Krieg, E.; Shirman, E.; Weissman, H.; Shimoni, E.; Wolf, S. G.; Pinkas, I.; Rybtchinski, B. J. Am. Chem. Soc. 2009, 131, (40), 14365-14373.

48. Roy, S.; Maiti, D. K.; Panigrahi, S.; Basak, D.; Banerjee, A. PCCP 2014, 16, (13), 6041-6049.

49. Wang, A.; Cui, L.; Debnath, S.; Dong, Q.; Yan, X.; Zhang, X.; Ulijn, R. V.; Bai, S. ACS Appl. Mater. Interfaces 2017, 9, (25), 21390-21396.

50. Weingarten, A. S.; Kazantsev, R. V.; Palmer, L. C.; Fairfield, D. J.; Koltonow, A. R.; Stupp, S. I. J. Am. Chem. Soc. 2015, 137, (48), 15241-15246.

51. Castilla, A. M.; Draper, E. R.; Nolan, M. C.; Brasnett, C.; Seddon, A.; Mears, L. L. E.; Cowieson, N.; Adams, D. J. Scientific Reports 2017, 7, (1), 8380.

52. Sukul, P. K.; Singh, P. K.; Maji, S. K.; Malik, S. Journal of Materials Chemistry B 2013, 1, (2), 153-156.

A5: Ruthenium based photosensitizer/catalyst supramolecular architectures in light driven water oxidation

Max Burian[a], Zois Syrgiannis[b,c], Giuseppina La Ganga[d], Fausto Puntoriero[d], Mirco Natali[e], Franco Scandola[e], Sebastiano Campagna[d,*], Maurizio Prato[c,f,g], Marcella Bonchio[b], Heinz Amenitsch[a,*] and Andrea Sartorel[b,*]

[a] Institute of Inorganic Chemistry, Graz University of Technology, Stremayrgasse 9/IV, Graz 8010, Austria,

[b] Department of Chemical Sciences University of Padova and Institute on Membrane Technology, Unit of Padova, via F. Marzolo 1, 35131, Padova, Italy.

[c] Department of Pharmaceutical Sciences University of Trieste, via L. Giorgieri 1 - 34127 Trieste, Italy.

[d] Department of Chemical, Biological, Pharmaceutical and Environmental Sciences, University of Messina and Centro Interuniversitario per la Conversione Chimica dell'Energia Solare, section of Messina, Via Sperone 31, 98166 Messina, Italy.

[e] Department of Chemical and Pharmaceutical Sciences University of Ferrara via Fossato di Mortara 17-19, 44121 Ferrara, Italy.

[f] Carbon Nanobiotechnology Laboratory, CIC biomaGUNE, Paseo de Miramón 182, 20009 Donostia-San Sebastian (Spain).

[g] Basque Fdn Sci, Ikerbasque, Bilbao 48013, Spain

Published in *Inorg.Chim.Act.* 454, 171-175 (2017).

Light driven water oxidation is a key step in artificial photosynthesis, aimed at splitting water into hydrogen and oxygen with sunlight. In such process, the interactions between a photosensitizer (PS) and a water oxidation catalyst (WOC) play a crucial role in the rates of photoinduced electron transfers, determining the overall quantum efficiency of the system. In this work, by means of Small Angle X-ray Scattering (SAXS) we investigate the nature of the aggregates between ruthenium polypyridine photosensitizers (Rubpy and Ru4dend) and a tetraruthenium polyoxometalate (Ru4POM) water oxidation catalyst. Aggregate scattering is confirmed by the strong intensity-increase in the low-q regime, whereas the power law-fit of this region show slopes between −3 and −4, suggesting globular and porous aggregates. Intermolecular PS/WOC distances lower than 3 nm support the observed fast photoinduced electron transfers (<120 ps), however the proximity of the two components in the hybrids is also responsible for fast charge recombination. Approaches for inhibiting such undesired process are discussed.

1. Introduction

Artificial photosynthesis yearns for splitting water into hydrogen and oxygen exploiting sunlight (Eq. (1)), and appears as a promising route towards the development of renewable and inexhaustible fuels [1]:

$$2H_2O + \text{sunlight} \rightarrow 2H_2 + O_2 \qquad (1)$$

The design and development of photosynthetic devices [2] may take inspiration from the natural process that foresees a suitable architecture of functional modules. In synergy, the final framework needs to be capable of light absorption, energy and electron transfer, charge separation, and catalytic routines where hydrogen and oxygen are concomitantly generated [3]. In order to overcome the complexity of such assemblies as well as the challenges of interfacing all different functionalities, optimization of the involved components is often carried on separately [4].

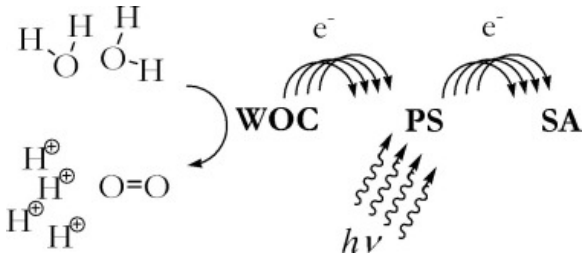

Scheme 1. Schematic representation of a three components system for light driven water oxidation, composed by a water oxidation catalyst (WOC), a photosensitizer (PS) and a sacrificial electron acceptor (SA).

In particular, light driven water oxidation, which has often been considered as the bottleneck of the entire process, takes advantage of a three components sacrificial system, composed by a water oxidation catalyst (WOC), a photosensitizer (PS), and a primary, sacrificial electron acceptor (SA), Scheme 1. Upon light absorption by the photosensitizer and generation of its excited state, an electron flow WOC→PS→SA is induced [5]; when this step is efficiently replicated several times, it ultimately leads to the formation of an oxidized form of the WOC, capable of oxidizing water to oxygen [6]. Typically, the persulfate dianion $S_2O_8^{2-}$ is employed as the SA, in virtue of its irreversible decomposition upon electron acceptance, which avoids unproductive, charge recombination events [5]. Concerning the photosensitizer PS, ruthenium polypyridine complexes have been widely considered due to their extended absorbance in the visible region, a suitable lifetime of the triplet manifold excited state as well as the high redox potential to feed the water oxidation process [5].

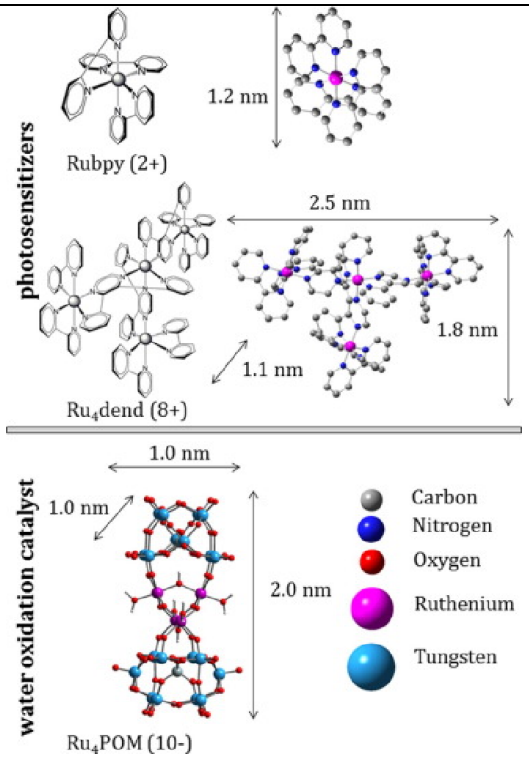

Fig. 1. Ruthenium polypyridine photosensitizers and tetraruthenium polyoxometalate water oxidation catalyst employed in this work. Some key dimensions of the three molecules are provided.

The forerunner of such coordination complexes is tris(2,2′-bipyridine)ruthenium(II), hereafter Rubpy (Fig. 1) [5,7], while the use of ruthenium based dendrimeric derivatives, such as $[Ru\{(\mu\text{-dpp})Ru(bpy)_2\}_3]^{8+}$ (dpp = 2,3-bis(2′-pyridyl)pyrazine), hereafter Ru_4dend (Fig. 1) [7–9], has provided significant advantages in terms of extended absorption in the visible spectra of solar light emission [9]. In particular, Rubpy and Ru_4dend photosensitizers have been combined with a tetraruthenium polyoxometalate $\{Ru_4(\mu\text{-}O)_4(\mu\text{-}OH)_2(H_2O)_4[\gamma\text{-}SiW_{10}O_{36}]\}^{10-}$(hereafter Ru_4POM, Fig. 1) as the water oxidation catalyst, reaching notable efficiency and unprecedented quantum yield towards oxygen generation, using persulfate as the sacrificial electron acceptor [10–12]. In both cases, the occurrence of supramolecular PS/WOC aggregates, formed by electrostatic based ion pairs between the cationic photosensitizers and the polyanionic WOC had a remarkable impact in the overall efficiency of the light activated cycle [11,12]. In particular, Ru_4dend/Ru_4POM aggregation in 1:1 stoichiometry, is responsible for fast, reductive quenching of Ru_4dend triplet excited state by Ru_4POM, occurring in a hundred ps timescale [12b], and initiating the cascade of electron transfer events that ultimately lead to O_2 production with a quantum yield of 0.30 [12].

In this work, we investigate the structural features of these electrostatic aggregates by means of Small Angle X-ray Scattering (SAXS), which is recognized as a state-of-the-art characterization technique for nano-assembly in solution [13]. From a single measurement this technique allows to gain insights on a wide structural range, starting from an estimate on the aggregates' size and morphology down to mean intermolecular distances within the assembly. The combination of SAXS evidence with Transmission Electron Microscopy (TEM) imaging, and elemental mapping techniques, has a definite potential regarding the characterization of competent photosynthetic nano-systems, formed in water by the supramolecular PS/WOC assembly. The final aim is to build effective structure–reactivity descriptors for the design of functional materials and photoelectrodes.

2. Experimental

2.1. Materials

Rubpy was purchased from Sigma–Aldrich as the dichloride, hexahydrate salt. Ru_4dend and Ru_4POM were synthesized according to the literature procedures [8c,14] and isolated as the PF_6^- and Na^+ salts, respectively.

2.2. Sample preparation

The Ru_4POM·Ru_4dend and Ru_4POM·Rubpy hybrid aggregates were obtained by simple mixing of precursors using ratios stated further below, by mixing stock solutions in 50/50 H_2O/tetrahydrofuran (THF) of Ru_4POM (1×10^{-4} M) and of Ru_4dend (1×10^{-4} M) or Rubpy (4×10^{-4} M). The actual mixing was performed ca 10 min before measurement. The mixed H_2O/THF was employed as the solvent due to a better dispersion of the aggregates with respect to pure aqueous media.

2.3. Small Angle X-ray Scattering (SAXS)

Small Angle X-ray Scattering experiments were performed at the Austrian SAXS beamline of Elettra synchrotron (Trieste, Italy) using 8 keV photon energy. The liquid samples were filled in standard 1.5 mm quartz capillaries whereas 6–8 consecutive images were taken over time, to rule out possible radiation damage by comparison of the scattering pattern. A two-dimensional image-plate detector (Mar300, Germany) was placed at a distance of approximately 90 cm to obtain an accessible q-range from 0.15 to 9.25 nm^{-1}. A reference

measurement was made using silver-behenate as a standard for the calibration of the angular regime. Azimuthal integration of the 2D images was done using the Fit2D program [15]. The resulting integrated scattering curves were corrected for dark-current, normalized by sample transmission and subsequently the background was subtracted using the pure solvent-scattering.

2.4. Transmission Electron Microscopy (TEM)

TEM images were acquired using a Philips EM 208 microscope, with accelerating voltage of 100 kV. Samples were prepared by drop casting of the mixed samples onto a carbon coated 200 mesh Ni grid (EM Sciences, Gibbstown, NJ) followed by solvent evaporation under vacuum.

2.5. Dynamic light scattering (DLS)

DLS experiments were performed with a Malvern Zetasizer Nano-S instrument, equipped with a quartz cuvette thermostated at 25 °C; laser wavelength 633 nm.

3. Results and discussion

3.1. SAXS

Synchrotron SAXS measurements were conducted on Ru_4POM·Ru_4dend hybridaggregates, prepared by mixing an equimolar amount of Ru_4dend and Ru_4POM precursors, as well as a comparative measurement of a 1:4 Ru_4POM:Rubpy mixture (association of Ru_4POM with Ru_4dend and Rubpy in 1:1 and 1:4 ratios, respectively, was observed by means of conductometric titrations [11a,12b], and can be justified on the basis of the charge-balance provided by the cationic photosensitizer with respect to the Ru_4POM polyanion, see Fig. 1). The scattering from both systems are shown in Fig. 2; the first clear observation is the strong intensity-increase in the low-q regime, which is characteristic for aggregate-scattering, as it is evident also from TEM images of the same mixtures as seen in Fig. 3.[4] The slopes of the Porod fits in the low-q regime of −2.98 (Ru_4POM·Ru_4dend) and −4.02 (Ru_4POM·Rubpy), suggest

[4] The presence of large aggregates is detected also with dynamic light scattering (DLS) experiments, although the low quality of the fitting of the correlation function, likely ascribable to non-monodisperse particles, does not allow a precise estimation of the size (see Fig. S3).

the presence of globular aggregates, that appear to be more porous in the case of $Ru_4POM{\cdot}Ru_4dend$ compared to $Ru_4POM{\cdot}Rubpy$, as indicated by the lower absolute value of the slope [16]. An explanation for the increased porosity might be the higher size of Ru_4dend with respect to Rubpy (see Fig. 1): the ruthenium dendrimer acts as a "spacer" between interacting molecules, whereas in the case of the quasi-spherical and significantly smaller Rubpy, a more compact packing can be envisioned.

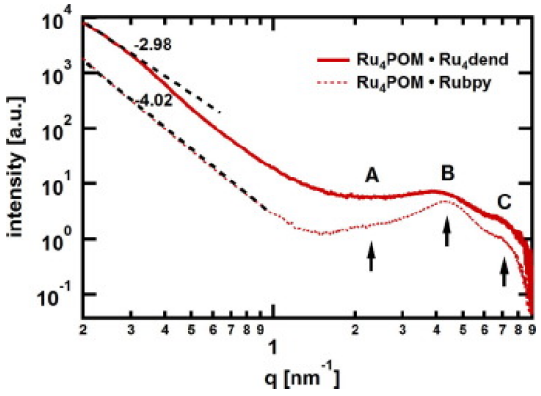

Fig. 2. SAXS data recorded for both $Ru_4POM{\cdot}Ru_4dend$ (1:1 ratio) and $Ru_4POM{\cdot}Rubpy$ (1:4 ratio) in H_2O/THF solution. The black-dotted lines represent the Porod fits in the low-*q* regime that reveal a more porous structure in the case of $Ru_4POM{\cdot}Ru_4dend$. The black arrows indicate the correlation peaks (**A**, **B**, **C**) resulting from inter-molecular mean distances (see Fig. S1), whereas the exact *d*-spacings of the reflections are found in Table 1. Error-bars are omitted for clarity.

More interestingly, both curves exhibit rather broad correlation peaks in the mid to high-*q*regime, that correspond to intermolecular distances in the aggregate (indeed, these peaks are not observed in the isolated solution of Ru_4POM, Ru_4dend, or Rubpy). To better understand these features, one should keep in mind that the recorded intensity in an X-ray scattering experiment is proportional to the square of the electron density difference in the sample. In the present case, the SAXS patterns will be then dominated by scattering from the heavy atoms (W atoms from the polyoxotungstate cage of Ru_4POM), which, as a side effect, makes the polypyridine groups comparably transparent to the X-rays. Therefore the observed correlation peaks most likely represent mean distances between Ru_4POM molecules inside the aggregates (see Table 1). In particular, the broad nature of the peaks immediately implies that the molecular arrangements are disordered in the sense that no coherent long range order exists, hence the terminology *mean* intermolecular-distance is used herein. It is, however, intriguing that the positions of the correlation peaks **A**, **B** and **C**fall in a similar region, for both $Ru_4POM{\cdot}Ru_4dend$ and the $Ru_4POM{\cdot}Rubpy$ nano-hybrids (Fig. 2), implying the occurrence of analogous structural motifs within both aggregates. A closer look at the *d*-spacing values

in Table 1 shows that both **A** and **B** peaks are found at higher values in the case of Ru_4POM·Ru_4dend, thus supporting the notion that the bulky tetraruthenium dendrimer increases the mean distance between the Ru_4POM scattering centres.

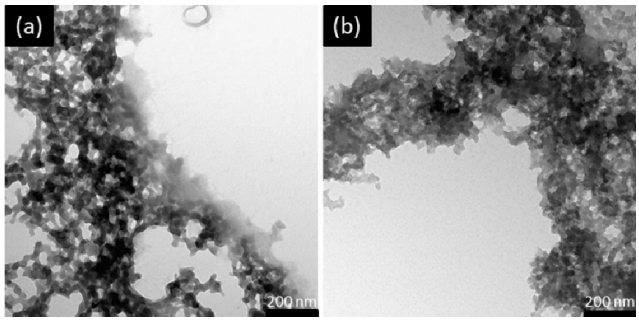

Fig. 3. TEM images of the aggregates (a) Ru4POM·Ru4dend and (b) Ru4POM·Rubpy. Scale bar: 200 nm.

To further investigate the nature of the correlation peaks and of the corresponding structural parameter (mean Ru_4POM distance) as a function of the Ru_4POM·Ru_4dend stoichiometry SAXS measurements were repeated at Ru_4POM:Ru_4dend = 0.5:1 ratio. In these conditions, due to strong electrostatic association, ca. 50% of the Ru_4dend is present in solution and the overall amount of Ru_4POM·Ru_4dend aggregates is halved, while their composition and nano-morphology are expected to be unchanged [12b]. Indeed, as seen in Fig. 4 (full scattering curves can be found in the Supporting information), the low-q aggregate scattering is very similar for both mixing ratios (Porod slope of −3.03 for Ru_4POM:Ru_4dend = 0.5:1), which implies that the nano-morphology of the aggregates is unchanged. This was further confirmed by comparable **A**, **B** and **C** d-spacings values (Table 1). In regard of the previously determined correlation peaks, two different behaviors can be observed as far as peak intensities are concerned: while peaks **A** and **B** decrease comparable to the low-q regime, peak **C** is only slightly lowered. To put these observations into context, it should be noted that the measured scattering intensity in such a X-ray scattering experiment directly correlates with the concentration of the aggregates, assuming all other parameters remain constant [16]. In this case, since the nano-morphology of the aggregates is identical, a reduction of the relative Ru_4POM concentration should hence scale down corresponding scattering features by the same amount. The data in Fig. 4 clearly show that this predicted behavior can actually be identified in the case of peaks **A** and **B**. On the other hand, the rather unexpected non-linear

behavior of peak **C** cannot as easily be connected to one of the nano-aggregate. An indisputable attribution of peak **C** will be therefore subject to further investigation.[5]

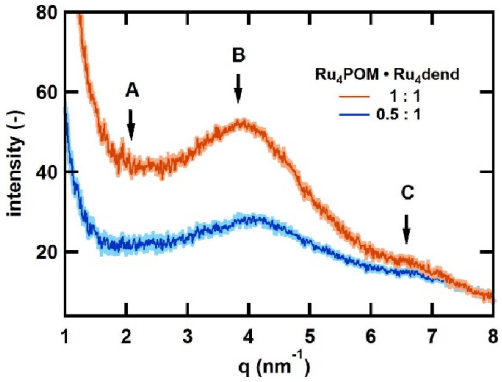

Fig. 4. SAXS data of Ru4POM:Ru4dend samples mixed 1:1 and 0.5:1 in H_2O/THF solution. The previously determined correlation peaks are marked by black arrows. For better comparability, the curves were normalized to the Ru4dend concentration in the final mixture. Error bars are represented by the light color background of the curves. As this data suggests, with decreasing Ru4POM concentration, peaks A and B are significantly decreased, while peak C appears to be invariant. (For interpretation of the references to colour in this figure legend, the reader is referred to the web version of this article.)

Table 1. Mean intermolecular *d*-spacings obtained from the correlation peaks as marked by the black arrows in Fig. 2. Errors are given in brackets. The corresponding fits can be found in Fig. S1 in the Supporting information.

	A, (nm)	**B,** (nm)	**C,** (nm)
Ru4POM/Rubpy (1:4)	2.56 (0.48)	1.47 (0.03)	0.95 (0.10)
Ru4POM/Ru4dend (1:1)	*3.06 (0.20)*	*1.64 (0.09)*	*0.97 (0.06)*
Ru4POM/Ru4dend (0.5:1)	2.89 (0.27)	1.57 (0.10)	0.91 (0.12)

3.2. Intermolecular arrangement

The obvious subsequent step towards elucidating the intermolecular features seen in the SAXS data is a comparison of the retrieved mean distances with dimensions from previously established theoretical models. Ru4POM has already been structurally characterized and described in literature [14]. An analogous characterization is missing for Ru4dend, mostly due to the existence of geometrical and stereo-isomers [8,17]; however the approximate dimensions of this latter species can be estimated, as shown in Fig. 1. Before focusing on the

[5] The seemingly constant scattering behavior of peak **C** under changing Ru4POM concentrations is unusual. While the present data doesn't allow a decisive assignment to a specific molecular arrangement, it might help to exclude possible conformations. The comparison of the corresponding mean molecular distance of 0.97 nm (retrieved from the peak position) with the structural dimensions of Ru4POM (see Fig. 1), together with the unaffected scattering intensity under changing conditions, makes an attribution of **C** to a Ru4POM–Ru4POM distance improbable.

information above about mean distances gained directly from the scattering data, an important consideration should be kept in mind: as seen by the −3 slope in the low-q regime of the SAXS measurements, the Ru4POM·Ru4dend aggregate morphology appears to be rather random and globular, implying that no preferred growth direction exists (slope values of −1 and −2 are instead expected for 1-D and 2-D aggregates, respectively) [16]. This also means that there is no molecular alignment or orientation relation since this would have anisotropic consequences on the underlying growth mechanism and therefore on the aggregate shape. All of the above observations together with the broad nature of the peaks are a clear indication that no long range order between the molecules exists. Accordingly, the observed correlation peaks in the scattering data have to be the result from a three-dimensionally disordered system, representing the spherically-averaged mean distance between the molecular components.

With this in mind the previous observations can now be put in a more global context. The molecular structure of Ru4POM represent a fairly rigid building block, where the atomic distances are well known from the solid-state crystallographic analysis. As a first SAXS model a double ellipsoid arrangement was postulated [18], which can be simplified as a cylindrical geometry with 1 nm of diameter and 2 nm in height. A comparison of these dimensions with the measured mean distances in the aggregate of 1.64 and 3.06 nm shows that their assignment to a Ru4POM–Ru4POM mean distance is plausible when assuming intercalation of Ru4dend molecules with different geometrical conformations.

3.3. Implication of Ru4POM·Ru4dend assembly on photoinduced electron transfer

The electrostatic association between Ru4POM and Ru4dend and the intimate distance between the two components in the aggregate (considering intercalation of one Ru4dend between two Ru4POM molecules, an estimate of the Ru4POM–Ru4dend distance is given by half values of the observed d-spacings, and therefore be in the 0.8–1.5 nm range) fully support the fast photoinduced, electron transfer leading to reductive quenching of the triplet metal-to-ligand charge-transfer (MLCT) excited state of Ru4dend by Ru4POM. Such a process is characterized by a relatively high driving force of $\Delta G = -0.58$ eV and takes place with a time constant of about 126 ps in phosphate buffer at pH 7 [12b,19]. Charge recombination is estimated to be even faster, as demonstrated by the non-accumulation of the charge-separated state in the ultrafast pump–probe spectroscopic experiments, and agrees with an even larger driving force (close to −1.1 eV) [12b]. This suggests that both forward and back electron transfer processes in the associated Ru4POM·Ru4dend systems are not slowed down by the nuclear barrier effects

usually occurring in restricted environments as a consequence of significant increase in reorganization energy [20]. Such result can be attributed to the "porous" nature of the Ru_4POM·Ru_4dend system discussed above, that would let enough mobility to the donor–acceptor pair to overcome problems due to the expected reorganization energy.

4. Conclusion

In this work we have investigated by means of Small Angle X-ray Scattering the nature of aggregates between ruthenium polypyridine photosensitizers Ru_4dend and Rubpy, and a tetraruthenium water oxidation catalyst Ru_4POM, that provide very efficient systems in light driven water oxidation with persulfate as electron acceptor [10–12]. Power law-fit in the low-q regime between −3 and −4 are diagnostic for globular, porous aggregates, that grow in a three dimensional, disordered network. Intermolecular PS/WOC distances lower than 3 nm are compatible with fast photoinduced electron transfers observed in a hundred of ps timescale [12b]; however the proximity of the two components in the aggregates promotes also very fast back electron transfer, that could be detrimental for the overall efficiency of the PS/WOC assembly when embedded onto a regenerative photoelectrode. This justifies the present, extensive efforts in the development of redox relays [21], aimed at decreasing charge recombination rates in photoactive assemblies. Moreover, parameters such as pore size and active surface area of the aggregates should be considered, since they could impact the overall photocatalytic performance of the device.

References

[1] (a) S. Berardi, S. Drouet, L. Francàs, C. Gimbert-Suriñach, M. Guttentag, C. Richmond, T. Stoll, A. Llobet, Chem. Soc. Rev. 43 (2014) 7501; (b) K.S. Joya, Y.F. Joya, K. Ocakoglu, R. van de Krol, Angew. Chem., Int. Ed. 52 (2013) 10426; (c) I. Yasuo, Coord. Chem. Rev. 257 (2013) 171.

[2] J.R. McKone, N.S. Lewis, H.B. Gray, Chem. Mater. 26 (2014) 407.

[3] N. Armaroli, V. Balzani, Angew. Chem., Int. Ed. 46 (2007) 52.

[4] J.H. Alstrum-Acevedo, M.K. Brennaman, T.J. Meyer, Inorg. Chem. 44 (2005) 6802.

[5] (a) A. Sartorel, M. Bonchio, S. Campagna, F. Scandola, Chem. Soc. Rev. 42 (2013) 2262; (b) F. Puntoriero, A. Sartorel, M. Orlandi, G. La Ganga, S. Serroni, M. Bonchio, F. Scandola, S. Campagna, Coord. Chem. Rev. 255 (2011) 2594.

[6] S. Piccinin, A. Sartorel, G. Aquilanti, A. Goldoni, M. Bonchio, S. Fabris, Proc. Acad. Natl. Sci. U.S.A. 110 (2013) 4917.

[7] (a) S. Serroni, S. Campagna, F. Puntoriero, C. Di Pietro, N.D. McClenaghan, F. Loiseau, Chem. Soc. Rev. 30 (2001) 367; (b) V. Balzani, A. Juris, Coord. Chem. Rev. 211 (2001) 97; (c) V. Balzani, P. Ceroni, A. Juris,

M. Venturi, S. Campagna, F. Puntoriero, S. Serroni, Coord. Chem. Rev. 219–221 (2001) 545; (d) F. Puntoriero, F. Nastasi, M. Cavazzini, S. Quici, S. Campagna, Coord. Chem. Rev. 251 (2007) 536.

[8] (a) W.R. Murphy, K.J. Brewer, G. Gettliffe, J.D. Petersen, Inorg. Chem. 28 (1989) 81; (b) S. Campagna, G. Denti, L. Sabatino, S. Serroni, M. Ciano, V. Balzani, J. Chem. Soc., Chem. Commun. (1989) 1500; (c) G. Denti, S. Campagna, L. Sabatino, S. Serroni, M. Ciano, V. Balzani, Inorg. Chem. 29 (1990) 4750.

[9] G. La Ganga, F. Nastasi, S. Campagna, F. Puntoriero, Dalton Trans. (2009) 9997.

[10] Y.V. Geletii, Z. Huang, Y. Hou, D.G. Musaev, T. Lan, C.L. Hill, J. Am. Chem. Soc. 131 (2009) 7522.

[11] (a) M. Natali, M. Orlandi, S. Berardi, S. Campagna, M. Bonchio, A. Sartorel, F. Scandola, Inorg. Chem. 51 (2012) 7324; (b) M. Orlandi, R. Argazzi, A. Sartorel, M. Carraro, G. Scorrano, M. Bonchio, F. Scandola, Chem. Commun. 46 (2010) 3152.

[12] (a) F. Puntoriero, G. La Ganga, A. Sartorel, M. Carraro, G. Scorrano, M. Bonchio, S. Campagna, Chem. Commun. 46 (2010) 4725; (b) M. Natali, F. Puntoriero, C. Chiorboli, G. La Ganga, A. Sartorel, M. Bonchio, S. Campagna, F. Scandola, J. Phys. Chem. C 119 (2015) 2371.

[13] (a) C.D. Putnam, M. Hammel, G.L. Hura, J.A. Tainer, Q. Rev. Biophys. 40 (2007) 191; (b) A.S. Weingarten, R. Kazantsev, L.C. Palmer, M. McClendon, A.R. Koltonow, A. P.S. Samuel, D.J. Kiebala, M.R. Wasielewski, S.I. Stupp, Nat. Chem. 6 (2014) 964; (c) M.R. Wasielewski, Acc. Chem. Res. 42 (2009) 1910; (d) B. Marmiroli, H. Amenitsch, Eur. Biophys. J. Biophys. Lett. 41 (2012) 851.

[14] A. Sartorel, M. Carraro, G. Scorrano, R. De Zorzi, S. Geremia, N.D. McDaniel, S. Bernhard, M. Bonchio, J. Am. Chem. Soc. 130 (2008) 5006.

[15] A.P. Hammersley, S.O. Svensson, M. Hanfland, A.N. Fitch, D. Hausermann, High Pressure Res. 14 (4–6) (1996) 235.

[16] O. Glatter, O. Kratky, Small Angle X-ray Scattering, Academic Press, London, 1982.

[17] (a) G. Denti, S. Campagna, S. Serroni, M. Ciano, V. Balzani, J. Am. Chem. Soc. 114 (1992) 2944; (b) S. Campagna, G. Denti, S. Serroni, A. Juris, M. Venturi, V. Ricevuto, V. Balzani, Chem. Eur. J. 1 (1995) 211.

[18] F.M. Toma, A. Sartorel, M. Iurlo, M. Carraro, P. Parisse, C. Maccato, S. Rapino, B. Rodriguez Gonzalez, H. Amenitsch, T. Da Ros, L. Casalis, A. Goldoni, M. Marcaccio, G. Scorrano, G. Scoles, F. Paolucci, M. Prato, M. Bonchio, Nat. Chem. 2 (2010) 826.

[19] Timescales in the order of ps are observed also for photoinduced electron transfers in covalently linked catalyst/sensitizer systems, see A. Montellano López, M. Natali, E. Pizzolato, C. Chiorboli, M. Bonchio, A. Sartorel, F. Scandola, Phys. Chem. Chem. Phys. 16 (2014) 12000.

[20] (a) G.L. Gaines, M.P. O'Neil, W.A. Svec, M.P. Niemczyk, M.R. Wasielewski, J. Am. Chem. Soc. 113 (1991) 719; (b) P.Y. Chen, T.J. Meyer, Chem. Rev. 98 (1998) 1439. In such studies, a destabilization of the charge separated state of about 0.6 eV on passing from room temperature fluid solution to 77 rigid matrix (where the matrix can be viewed as a restricted environment) is calculated. The destabilization of the charge separated state there justifies the inefficiency of electron transfer with mild driving forces. Similar effects can occur as a function of increased nuclear barrier to the electron transfer.

[21] J.D. Megiatto Jr., D.D. Méndez-Hernández, M.E. Tejeda-Ferrari, A.-L. Teillout, M. J. Llansola-Portolés, G. Kodis, O.G. Poluektov, T. Rajh, V. Mujica, T.L. Groy, D. Gust, T.A. Moore, A.L. Moore, Nat. Chem. 6 (2014) 423.

A6: Artificial Quantasomes: Hierarchical Organization of Perylene-Bisimides and Polyoxometalates for Photo-assisted Water Oxidation

Marcella Bonchio,[a] Zois Syrgiannis,[a,b] **Max Burian**,[c] Erica Pizzolato,[a,b] Konstantin Dirian,[d] Francesco Rigodanza,[a] Giulia Alice Volpato,[b] Giuseppina La Ganga,[e] Nadia Marino,[b] Nicola Demitri,[f] Serena Berardi,[g] Heinz Amenitsch,[c] Dirk M. Guldi,[c] Stefano Caramori,[g] Carlo Alberto Bignozzi,[g] Andrea Sartorel,[b] and Maurizio Prato[a,h,i]

[a] CNR-ITM and Dipartimento di Scienze Chimiche, University of Padova, INSTM unit of Padova, via F. Marzolo 1, 35131 Padova, Italy;

[b] Center of Excellence for Nanostructured Materials (CENMAT) and INSTM, unit of Trieste, Department of Chemical and Pharmaceutical Sciences, University of Trieste, via L. Giorgieri 1, 34127 Trieste, Italy;

[c] Institute of Inorganic Chemistry, Graz University of Technology, Stremayrgasse 9/IV, Graz 8010, Austria;

[d] Department of Chemistry and Pharmacy & Interdisciplinary Center for Molecular Materials, Egerlandstr. 3, 91058 Erlangen, Germany;

[e] Dipartimento di Scienze Chimiche, Università di Messina and Centro Interuniversitario per la Conversione Chimica dell'Energia Solare, sezione di Messina, Via Sperone 31, 98166 Messina, Italy;

[f] Elettra-Sincrotrone Trieste, Strada Statale 14, km 163.5 in AREA Science Park, 34149 Basovizza, Trieste, Italy;

[g] Department of Chemistry and Pharmaceutical Sciences and CNR-ISOF, University of Ferrara, Via Fossato di Mortara 17, 44121 Ferrara, Italy;

[h] CIC BiomaGUNE, Parque Tecnológico de San Sebastián, Paseo Miramón, 182, 20009 San Sebastián, Spain; [i] Basque Foundation for Science, Ikerbasque, Bilbao 48013, Spain.

Submitted in 2018.

All of Earth's oxygen is the result of water oxidation performed by photosynthetic organisms using solar light as the only energy source. The O_2 necessary for our aerobic life is produced by the photo-cleavage of the extremely stable H-O-H bonds. Making oxygen is exceptionally difficult and lethal for the biological factory, which benefits from a continuous self-repair cycle during photocatalysis. Indeed, and despite the vast bio-diversity footprint, just one specialized protein complex is found in Nature's toolbox as the O_2-photolyzer, shared by all existing photosynthetic organisms: the photosystem II enzyme (PSII). Artificial systems are still far from replicating the complexity of PSII, which in its "core" form is essentially described by the co-localization of multi-Light Harvesting units with the functional Reaction Center (LH-RC). This notion fits the so-called "quantasome" model, focused on the

photocomplex ensemble rather than on the individual tasks of each component. While classical photosynthetic models are generally based on donor-acceptor "photo-dyads" and/or on sensitizer- water oxidation catalyst (WOC) binary combinations, our results reach out to the quantasome archetype. Here we report the self-assembly of multi-perylenebisimide chromophores (PBI) shaped to function by interaction with a state-of-the-art polyoxometalate WOC (Ru_4POM). Convergent characterization evidence points at the formation of $[PBI]_5Ru_4POM$, as the minimal photosynthetic unit, both in solution and on photoelectrodes, showing (i) a red-shifted, light harvesting efficiency (LHE>40%), (ii) favorable exciton accumulation and negligible excimeric loss; (iii) a robust amphiphilic structure; (iv) dynamic aggregation into large 2D-paracrystalline domains. Our results include the X-ray diffraction analysis of a dense, quasi-hexagonal packing of the PBI-quantasome motif ($\{[PBI]_5Ru_4POM\}_n$), showing a striking analogy with the coexistence of fluid and crystalline phases of PSII in the native photosynthetic membrane. Photoexcitation of the PBI-quantasome triggers one of the highest driving forces for photo-induced electron transfer applied so far, fostering ultra-fast charge separation in the ps timescale, and winning over recombination by ca. two orders of magnitude. Such a long lived charge-separated species is likely favored by electron delocalization along the π-backbone of the multi-PBI walls, so that oxygen evolution is the result of sequential hole accumulation at the WOC site. Indeed, photoanodes integrating the PBI-quantasome are found to evolve oxygen with quantitative faradaic yield, and a peak value of quantum efficiency using low energy, "green" photons (λ> 500 nm) similar to PSII-bioelectrodes. The modularity of the building blocks, the simplicity of the non-covalent chemistry and the biomimetic appeal of the quantasome approach, offer a unique opportunity for innovation in Artificial Photosynthesis.

Artificial Photosynthesis (AP) is a long-sought scientific dream and a matter of urgency as Nature will not be efficient enough to feed the world and power its energy in the next decades (*1*). Despite the rapid progress of photovoltaic technology, green plants, algae and photosynthetic bacteria still hold the podium for solar energy conversion, while their efficient emulation by man-made devices awaits a change of paradigm (*2,3*). In this direction, the "quantasome hypothesis" was a decisive step forward for deciphering the function-vs-structure requirements of Natural Photosynthesis (*4*). Since the earliest studies of Emerson and Arnold (1932) and Park and Biggins (1964) (*4*), the quantasome concept identifies the minimal

photosynthetic unit responsible for the "quantum" solar energy conversion, taking place within the chloroplast membrane. This definition applies to photosystems (PS) II and I, the two supercomplexes working in tandem, being specialized for photo-oxidation and photo-reduction respectively, (*2,4*) that despite their wide structural and functional diversity, share the unique "quantasome" essentials: they both integrate a self-assembled light-harvesting (LH) antenna in combination with catalytic co-factors. (*4*) The need of a LH specialized unit is because solar light is a low-density energy source, with few photons hitting a square-nm per second (ca.10 photons nm^{-2} s^{-1}).(*5*) Therefore, the extended cross-section and wavelength absorbance of multi-chromophore antennas (mainly chlorophills) is meant to capture and accumulate enough photon excitation energy required for the chemistry to take place at the reaction center (RC).(*2*) Moreover, the LH units regulate the frequency of the photon conversion events according to the quantum flux (i.e. charge-separation in the range 10^3-10^4 s^{-1}), thus pushing the photosynthetic engine to its full capacity.(*2*) For this task, the number of pigments/chromophores composing the LH antenna exceeds by at least one order of magnitude that of functional/catalytic centers in the quantasome.(*4-6*)

In the PSII quantasome, (dimeric, 450-kDa, 17.2 nm × 9.7 nm dimensions), ca. 30 core-chlorophills surround the functional reaction center (PSII-RC) and trigger the quantized, four-flash photo-oxidation of water by the proximal Mn_4CaO_5 oxygen evolving catalyst (PSII-OEC) (*6).* In this asset, the PSII quantasome is the most efficient photo-electrolizer built so far, converting solar light via a four-electron/four-proton oxidation mechanism ($H_2O \rightarrow O_2 + 4H^+ + 4e^-$ E = 1.23V vs reversible hydrogen electrode, RHE) (2,6), however with the one critical downfall of the fragile protein structure that is responsible for its photo-induced demolition and leaching of the manganese co-factor (*2,6*) occurring every 30 minutes in-vivo. Therefore, the engineering of a synthetic and robust PSII-quantasome is one formidable challenge of photocatalysis, and by far the most ambitious goal of Artificial Photosynthesis (*7-8*).

Eluding the quantasome concept, the majority of PSII-mimetics have been limited to photocatalytic dyads based on a 1:1 conjugation of a light absorber (i.e. a Ru-polypyridine complex) with the water oxidation catalyst (WOC) (*7-8*). The dyad arrangement rules out diffusion-limited electron transfer (ET) (*9-12*), but equally favors intra-dyad back-recombination, so that photocatalysis is generally quenched at its initial take-off, as recombination events are not counter-acted by a proximal LH antenna/exciton accumulation

pool. (*10-12*) While the dyad provides a basic "embryo" of the photosynthetic apparatus, the quantasome model calls for a significantly different approach: the LH components, of selected type and number, together with their spatial organization need to be specifically optimized according to the WOC requirements, with the final aim to leverage its multi-ET mechanism. On the other end, sophisticated multi-chromophore architectures have been synthesized to mimic the natural LH antennas; however these are generally conceived as a self-standing unit, i.e. independently from a co-localized catalytic interface, and turn out to be plagued by inter-chromophore charge and energy transfer side-processes, i.e. competing with productive events involving the WOC moiety. (*13*)

The breakthrough potential of the quantasome model implies that the LH unit is shaped to function based on the WOC structural and mechanistic features, thus following Nature guidelines. The first "artificial quantasome" is reported herein, that is specifically designed for oxygen evolution by the template association of LH-perylenebisimides domains (*14-16*) with the polyoxometalate WOC, known as a bio-inspired analog of the PSII-OEC (Fig.1A and S1) (*9,17*). To this aim, the bis-cationic N,N′-bis(2-(trimethyl-ammonium)ethylene)perylene-3,4,9,10-tetracarboxylic acid bisimide (**PBI**) has been used in combination with the tetra-ruthenate polyanion, $[Ru_4(\mu\text{-}O)_4(\mu\text{-}OH)_2(H_2O)_4(\gamma\text{-}SiW_{10}O_{36})_2]^{10-}$, **$Ru_4$POM**, thus taking advantage of the complementary electrostatic interactions and hydrophobic properties of the molecular building blocks (Fig. S1A-B). This strategy points at the co-localization of PBI-based excitons with **Ru_4POM**: the former provide one of the strongest and robust photo-generated oxidant using visible light ($\lambda > 500$ nm, $E(\mathbf{PBI}^{*/\cdot-}) = 2.20$ V vs NHE) (*16*); the latter provides low overpotential (300-350 mV), exceptionally wide pH-range of activity (pH = 1-7) (*17*); ultra-fast photo-induced ET (ps timescale) (18), and well-defined, water oxidation mechanism (> 4 electron oxidation) (*19*) in solution as well as on conductive nano-carbon supports including graphene (*17*).

The envisaged "quantasome" assembly forms in water, with a definite **$[PBI]_5Ru_4$POM** stoichiometry, where each **Ru_4POM** turns out to be caged within the surrounding walls of a five-fold PBI-corolla, (Fig. 1A and S1D). Converging evidence identifies the **$[PBI]_5Ru_4$POM** complex as the competent photosynthetic unit featuring: (i) a red-shifted, broad absorption cross-section, greatly improving the light harvesting efficiency of photoelectrodes (LHE>40%, $\lambda = 500$ nm), (ii) favorable exciton accumulation and negligible excimeric loss; (iii) a robust amphiphilic structure by effect of the all-inorganic POM template; (iv) dynamic

fluid-to-crystalline organization into two-dimensional (2D) patterns (**{[PBI]$_5$Ru$_4$POM}$_n$**, Fig. 1). The formation of 2D-arrays of the PBI-quantasomes sets a striking analogy with the PSII arrangement within the native photosynthetic membrane (Fig. S2), (*20*). Our results show the rendering of the PBI-quantasome 2D-phase onto nanostructured tungsten oxide photoelectrodes (***nano*WO$_3$|{[PBI]$_5$Ru$_4$POM}$_n$**), confirming oxygen evolution using "green" photons (λ up to 560 nm), with quantitative faradaic yield (>97 %) and quantum efficiency (IQE) up to 1.4 % in close analogy with PSII-bioelectrodes (Table 1).

Characterization of the {[PBI]$_5$Ru$_4$POM}$_n$ photosynthetic assembly

Intercalation of **Ru$_4$POM** deca-anions into aqueous **PBI$_n$** bundles (π–π nano-stacks, Fig. S1) (*14-16*) is probed in solution by conductometric and spectrophotometric titrations, (25 – 100 μM, in 2-20 mM phosphate buffer, pH 7, Fig. S3) displaying sharp isosbestic points at λ = 465, 478, 522, 560 nm (Fig. S3B) and a 5:1 **PBI/Ru$_4$POM** association stoichiometry, in compliance with electroneutrality requirements. The POM-induced exfoliation of **PBI$_n$** colloids, occurs with a progressive shift of Zeta Potential values (ζ-Potential, Fig. S4) from +20 mV to -37 mV, while Dynamic Light Scattering (DLS) analysis shows a corresponding shift of the size distribution, from 500 to 850 nm, indicating a major structural modification of the particles (Fig. S4). Indeed, Wide angle X-ray scattering (WAXS) measurements of aqueous **PBI$_n$** (Fig.1B Inset, bottom left corner, red trace) show a strong suppression and broadening of the prominent PBI peak at q = 17.6 nm^{-1} (ascribed to a π-π-stacking distance of 2π/q = 3.57 Å, Fig.1B Inset, bottom left corner, blue trace) upon **Ru$_4$POM** addition. This is a clear indication of residual PBI π-π stacking coupled with a coherent domain size effect,

that originates from self-assembly on extended length scales (*vide infra*, Fig.1C).

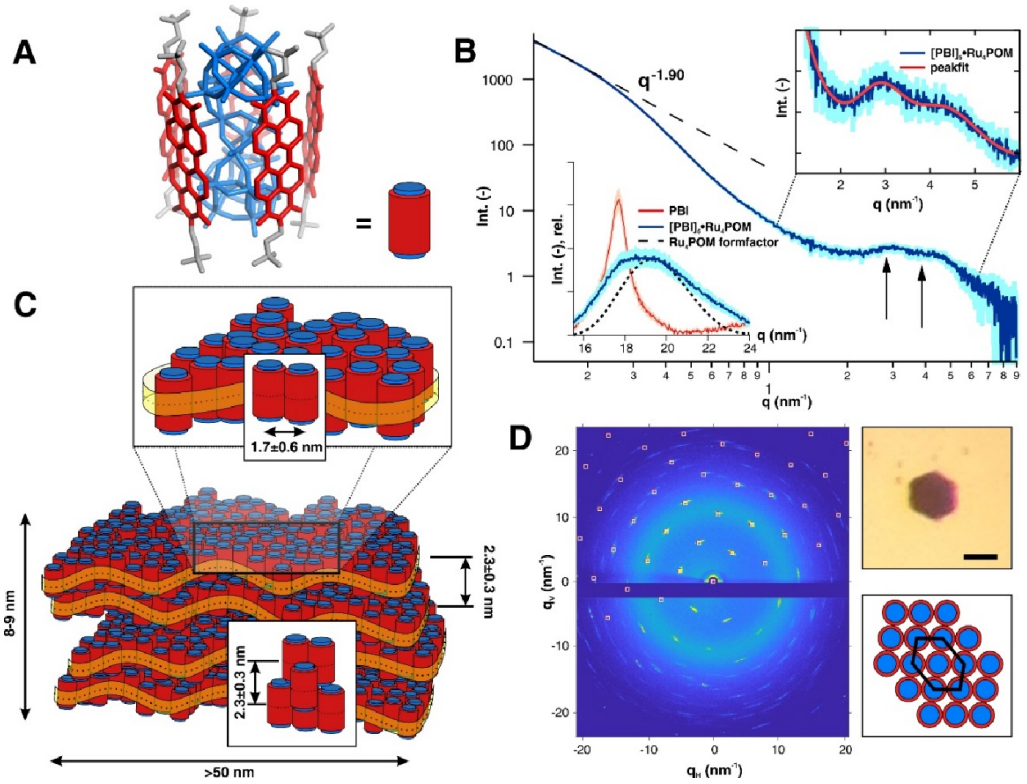

Figure 1. Structural investigation and modeling of {[PBI]$_5$Ru$_4$POM}$_n$ photosynthetic aggregates. (**A**) Figurative representation of the **[PBI]$_5$Ru$_4$POM** building-block [**Ru$_4$POM** = blue framework; **PBI** = red (aromatic body) and grey (alkylammonium tails) framework], shown as a core-shell cylindrical amphiphile [cartoon: **PBI** shell = red cylinder, **Ru$_4$POM** = blue cylinder]. (**B**) Inset, bottom left corner: Wide angle x-ray scattering (WAXS) measurements of 40 mM **PBI** before (red trace) and after (blue trace) the addition of 10mM **Ru$_4$POM** in water, compared to the theoretical **Ru$_4$POM** formfactor scattering (black dotted traces) calculated using CRYSOL (51)). Main graph: Small angle x-ray scattering (SAXS) data for **{[PBI]$_5$Ru$_4$POM}$_n$** (blue) formed upon mixing 20 mM **PBI** with stoichiometric amounts of **Ru$_4$POM** in 20 mM phosphate buffer, pH 7. The low-q Porod slope of -1.9 indicates the formation of a defected 2D lamellar super-structure. Two disordered correlation peaks are visible in the mid-q regime (black arrows): a peak-fitting (red line in the top inset) links these peaks to corresponding d-spacings of 1.7 ± 0.6 nm and 2.3 ± 0.3 nm; the coherent domain size of the 1.7 nm d-spacing is significantly lower than the one corresponding to 2.3 nm, hence, the two peaks are caused by two different structural motifs, in-plane and out-of-plane, respectively (see Supplementary Table S1). (**C**) Multi-scale model representation (cartoon version) of the cylinders packing into stacked nano-lamellae, where the mean molecular out-of-plane distance corresponds to 2.3± 0.3 nm, causing the first correlation peak in the scattering data. Note that the building-blocks are not necessarily confined into each lamella. The zoom-in shows a single lamellar plane, built from the parallel alignment of the cylinders with a mean in-plane distance of 1.7± 0.6 nm. Estimated dimensions of the building-block and center-to-center distances of the **Ru$_4$POM-PBI//PBI–Ru$_4$POM** supramolecular motif within a lamella are reported in Supplementary Fig. S5. (**D**) Reciprocal space map of a hexagonal-shaped, laminar crystalline aggregates of **{[PBI]$_5$Ru$_4$POM}$_n$** (single-crystal like behavior with mosaicity of about 10-15°), separating over time from the solution (upper left right corner – scalebar denotes 25 µm); indexing of the in-plane reflections (see white cubes) yields a strained hexagonal unit-cell (see Supplementary Fig. S7 for reflection labels). A simplified model of the packing arrangement in a single crystallite, shown in the lower right corner.

The molecular structures of both **Ru$_4$POM** and **PBI** have a comparable axial length (1.8-2.1 nm, Fig. S5) and complementary charge distribution localized at the peripheries of the longest

dimension (see the calculated electrostatic potential map, MEP, in Fig. S1), which supports an axial alignment of **PBI** and **Ru_4POM** in their electrostatic assembly. *The resulting supramolecular assembly,* **[PBI]$_5$$Ru_4$POM**, *is thus envisaged as a POM-encapsulated super-complex, in which the inorganic polyanion templates a corolla-like arrangement of five surrounding PBIs* (Fig. 1A, and Fig.S5). (*21*) The co-axial localization of the PBI-corolla / POM building blocks is reminiscent of the PSII-core complex structure, (Fig. S2) (*20*) and is conveniently described as a "core-shell" cylindrical amphiphile which, by effect of the large π-surface area of the PBI outer-walls, is expected to form higher order aggregates in water (Fig. 1C). Indeed, Small angle X-Ray scattering (SAXS) measurements (Fig. 1B) indicate that a paracrystalline phase forms in solution arising from the close packing of the **[PBI]$_5$$Ru_4$POM** units. More in detail: (i) the slope of -1.90, obtained in the low-q regime power law fit, is consistent with self-assembly of **[PBI]$_5$$Ru_4$POM** into a 2D-lamellar superstructure, albeit with a broad defect dislocation (a slope of -2.00 is indicative of an ideal lamellar arrangement, Fig. 1B), and with an approximate thickness of $T = 8.2\ nm$ (Guinier approximation for infinite plate-like particles) (*22*); (ii) the two correlation peaks in the mid-q scattering part, observed around 3 and 4 nm^{-1} (Fig. 1B, top right corner), correspond to molecular d-spacings of 2.3 ± 0.3 nm and 1.7 ± 0.6 nm respectively (Supplementary Table S1), and are readily assigned to **Ru_4POM-Ru_4POM** distances. Considering the molecular dimensions of the **[PBI]$_5$$Ru_4$POM** unit (with an estimated average diameter of ca. 1.5-1.6 nm, Fig. S5), we attribute the d-spacing of 1.7 ± 0.6 nm to a **Ru_4POM···Ru_4POM** motif with intercalated **PBI** pairs at a π-π-stacking distance of 0.3-0.4 nm, arising from an in-plane perpendicular alignment of the **[PBI]$_5$·Ru_4POM** unit within the 2D-nanoplates (Fig. 1C and Fig. S5). The d-spacing of 2.3 ± 0.3 nm is instead ascribed to the mean distance between vertically diffracting planes within the nanoplates, in agreement with the long-axis dimension of **Ru_4POM** (Fig. 1C). Atomic Force Microscopy (AFM) imaging of **{[PBI]$_5$$Ru_4$POM}$_n$** confirms the 2D morphology of the nano-flakes, collapsing into a micro-meter porous network, where the particle sub-structure is still visible, showing a broad size distribution and an average height of ca 9 nm (Fig. S6). Noteworthy, micro-sized hexagonal-shaped crystalline aggregates formed over time (Fig. 1D), showing the expected UV-Vis signature of the PBI-quantasome (Fig. S7). X-ray diffraction studies revealed a single-crystal behaviour with significant mosaicity in reciprocal space and a distinctive in-plane scattering pattern, corresponding to a strained hexagonal lattice (*C*2 cell, approx. dimensions a = 1.5 nm, b = 2.0 nm, see Fig. 1D and Fig. S7). The inferable high-density hexagonal-like arrangement of the PBI-quantasomes in the single crystallites is

consistent with the postulated cylindrical shape and core-shell amphiphilic nature of the **[PBI]$_5$Ru$_4$POM** unit, *(22)*, and could be considered as a thermodynamic sink of the 2D-lamellae dynamics. The coexistence of disordered packings, ordered arrays, and/or mixtures thereof, as found in the native thylakoid membrane (Fig. S2), strengthens the high biomimetic appeal of the artificial PBI-quantasome.(*20*)

Photo-catalytic water oxidation by {[PBI]$_5$Ru$_4$POM}$_n$

The PBI excited state, (E (**PBI*/PBI$^-$**) = +2.20 V vs normal hydrogen electrode, NHE), is expected to leverage multiple ET from **Ru$_4$POM**, with oxidation features in the range 0.75 – 1.02 V, up to the catalytic water oxidation onset at 1.2 V, vs NHE (Fig. S8). (*23*)

Therefore, the ET driving force is significantly higher within the PBI-quantasome than with classical ruthenium polypyridine sensitizers ([Ru(bpy)$_3$]$^{3+/2+}$ = +1.26 vs NHE), (*24*) or with cerium ammonium nitrate (CAN) (+1.75 vs NHE), typically used for water oxidation catalysis (*24*). Indeed, static quenching of the PBI excited-state emission occurs, levelling off at the expected 5:1 PBI/POM association stoichiometry (**PBI** 10 μM, in phosphate buffer, 20 mM, pH 7.0, Fig. S9), while photo-induced oxygen evolution is confirmed in the presence of persulfate ($S_2O_8^{2-}$) as terminal electron acceptor (Fig. 2A, see equations SI.6-SI.10, and energy diagram in Fig. S10, Table S2). In all cases, oxygen evolution by the ternary **PBI/Ru$_4$POM/$S_2O_8^{2-}$** system is observed from the reaction solution that shows the spectroscopic footprint of the **{[PBI]$_5$Ru$_4$POM}$_n$** aggregates (**PBI** 100 μM M, **Ru$_4$POM** added in the range 3-60 μM, $S_2O_8^{2-}$ 1 mM, LED white lamp irradiation, 4.5 mW/cm^2; Fig. 2A, Table S2) (*25*). Moreover, the oxygen evolution kinetics and yield, both reach a maximum plateau value at [**Ru$_4$POM**] ~ 20 μM, i.e. at the expected 5:1 PBI/Ru$_4$POM stoichiometry (Figure 2A). (*26*) *This result clearly identifies the PBI-quantasome assembly as the competent photosynthetic unit responsible for oxygen evolution.*

The PBI-quantasome proves to be exceptionally robust with respect to the Ru(bpy)$_3^{2+}$ benchmark as superimposable Uv-Vis spectra are registered before and after oxygenic turnover confirm (Fig. S13).

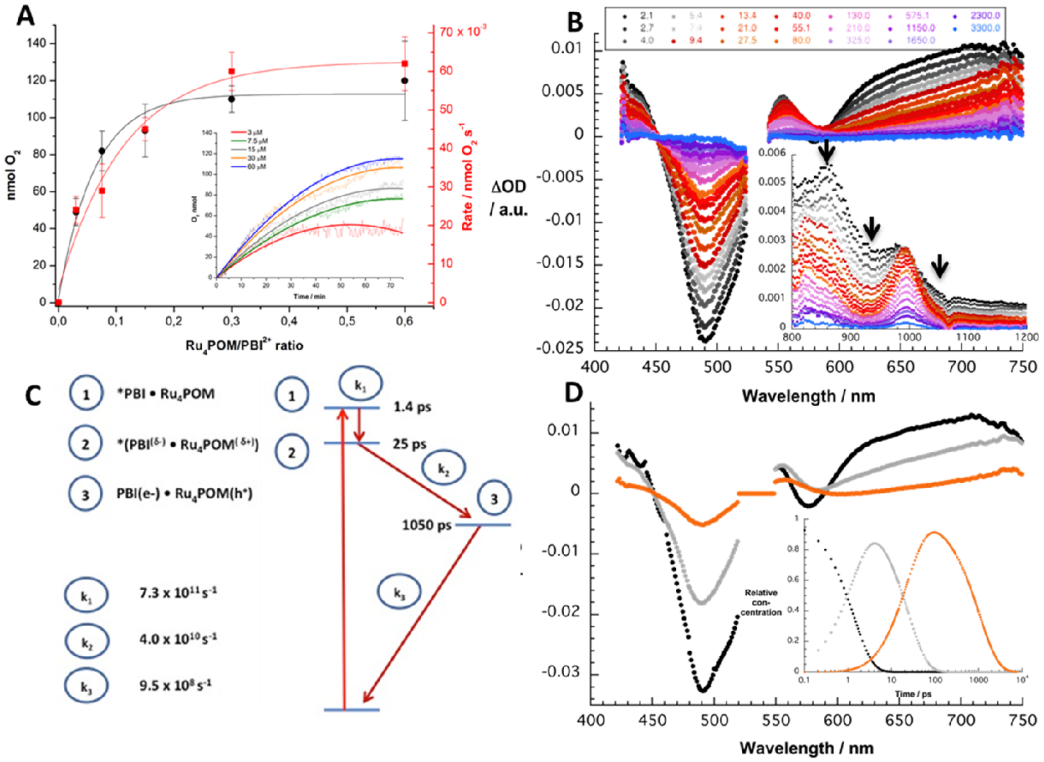

Figure 2. Femtosecond transient absorption (fsTA) dynamics of oxygenic {[PBI]$_5$Ru$_4$POM}$_n$ A. Plot of evolved O_2 (left axis, black plot) and of the initial rate of O_2 production (right axis, red plot) against the Ru$_4$POM/PBI ratio; inset: Oxygen evolution kinetics, with [**PBI**] = 100 µM, [$S_2O_8^{2-}$] = 1 mM, **Ru$_4$POM** (3.0 - 60 µM) in 20 mM phosphate buffer, pH 7, upon irradiation with a LED white lamp (4.5 mW/cm^2). **B**, Temporal evolution and transient dynamics of **{[PBI]$_5$Ru$_4$POM}$_n$**: differential absorption spectra of {[**PBI**]$_5$**Ru$_4$POM**}$_n$ with [**PBI**] = 100 µM and [**Ru$_4$POM**] = 60 µM recorded in phosphate buffer (20 mM, pH 7) with several time delays between 2 ps (red) and 3300 ps (blue) obtained upon femtosecond flash photolysis (530 nm) in the range 400-750 nm. The inset displays the differential absorption spectra in the range 800-1200 nm showing the peak shaped absorption at 990 nm ascribed to the PBI radical anion transient (Fig. S8). **C,** kinetic model used to fit / deconvolve the excited state surfaces of {[**PBI**]$_5$**Ru$_4$POM**}$_n$ at pH 7 via GloTarAn with states 1-3 as described in the main text. **D.** deconvoluted transient absorption spectra in the visible range, associated via GloTarAn analysis to states 1 (black), 2 (grey), and 3 (orange) according to the kinetic model in C; inset shows the time evolution of state population.

Investigation of {[PBI]$_5$Ru$_4$POM}$_n$ Transient States by Time-Resolved Spectroscopy

Oxygen evolution implies that photoexcitation of the PBI-quantasome triggers sequential **PBI$_5$(e$^-$)•Ru$_4$POM(h$^+$)** charge-separation events, leading to multi-hole accumulation at the WOC site, up to the formation of the high valent oxygen evolving intermediate (formally **Ru$_4$POM(nh$^+$)**, Fig. S10). (*19*). This multi-state mechanism, (*19*) is encoded within the quantasome unit, where the number of PBI photo-sensitizers per WOC offers a definite advantage for collecting excitation energy to power sequential ET.

Femtosecond transient absorption (fsTA) spectroscopy was used to probe the unique excited-state dynamics resulting from **{[PBI]$_5$Ru$_4$POM}$_n$**, when compared to aqueous **PBL$_n$**, (Figure 2B and Figures S14). The fsTA spectra of the **PBI$_n$** reference (100 μM in phosphate buffer, 20 mM, pH 7), following a 530 nm laser pulse, display a sharp ground-state bleaching at 500 nm, and formation of the singlet excited state (^{1}***PBI$_n$**) absorption maxima at 590, 700, 850, and 950 nm (Figure S14). Both time resolved multiple wavelength analysis and global fitting (GloTarAn software package, see SI) reveal a monoexponential, short-lived decay for ^{1}***PBI$_n$**.(*27*) In line with previous studies, the 263 ± 10 ps lifetime ($k = 3.8 \pm 0.14 \times 10^9$ s^{-1}, Figure S14) reflects charge recombination following a non-resolvable symmetry-breaking charge separation. (*13,16*)

Very different transient dynamics emerge from **{[PBI]$_5$Ru$_4$POM}$_n$**, (Fig. 2B). At a first glance, the PBI-centered singlet excited state ***PBI•Ru$_4$POM** featuring maxima at 430, 550, 710, and 870 nm is seen to transform, within less than 25 ps, into a new transient species showing positive absorption in the near-IR region at 750, 820 and 990 nm (Fig 2B), that indicates the formation of the **PBI$^{\bullet-}$** radical anion, readily identified by comparison with spectroelectrochemical evidence (Fig S8). (*23*) Moreover, a closer look at the early timescales shows the population of an intermediate state, that still retains the signature of the former excited state, but whose 990 nm maximum infers its definite charge-transfer character. We can conclude that upon photoexcitation, the PBI-quantasome undergoes a three-state cascade where the ***PBI•Ru$_4$POM** singlet excited state decays to a charge transfer excited state ***(PBI$^{(\delta-)}$•Ru$_4$POM$^{(\delta+)}$)** followed by formation of a **PBI(e$^-$)•Ru$_4$POM(h$^+$)** charge-separated state (Fig 2C), as indicated by an appreciable sharpening of the 990 nm maximum marker. (*23*) Ultra-fast energy transfer and charge separation within the PBI-quantasome also explains the fluorescence quenching observed upon its formation (Fig. S9).(*28*)

At variance with the **PBI$_n$** reference, fitting of the **{[PBI]$_5$Ru$_4$POM}$_n$** fs-TA results, on the femto- to nanosecond timescales (GloTarAn software package, Fig. 2D), were thus realized for a sequential " three-species" model. In the cascade, the localized PBI singlet excited state (state 1, 1.4 ± 0.2 ps lifetime, $k_1 = 7.1 \pm 0.1 \times 10^{11}$ s^{-1}) decays to an intermediate charge transfer state (state 2, 25 ± 2 ps lifetime, $k_2 = k_{cs} = 4.0 \pm 0.3 \times 10^{10}$ s^{-1}) which ultimately affords the fully stabilized, charge-separated state (state 3, 1050 ± 5 ps lifetime, $k_3 = k_{cr} = 9.5 \pm 0.05 \times 10^8$ s^{-1}) whose decay to the ground state is about two orders of magnitudes slower than its formation (Fig. 2C).

A different behavior is usually observed for electrostatic assemblies of **Ru4POM** with ruthenium polypyridine sensitizers, where ultra-fast recombination precludes the observation of photo-induced charge separation. (*18*) In contrast, a long-lived charge-separated state within the PBI-quantasome is likely favored by electron delocalization along the π-backbone of the **{[PBI]5Ru4POM}*n*** system after photo-induced injection.(*11*) Furthermore, the PBI-quantasome puts down deactivation processes (symmetry-breaking charge separation, SB-CS, and excimeric emission) generally arising from a multi-chromophore arrangement.(*13*) In this notion, ultra-fast electron-injection by **Ru4POM** outcompetes unproductive inter-chromophore charge/electron transfer (*13*). *We can conclude that the PBI-quantasome is shaped to funnel the exciton energy towards the productive pathway of hole-formation at the catalytic site, by increasing the probability of charge separation per unit time (LH/antenna effect) so to match the slower-boundary of the four-electron mechanism required for oxygen evolution.(29)*

Wiring of {[PBI]5Ru4POM}*n* onto photoanodes

The wiring of a fully integrated photosystem (LH antenna + RC) has been previously demonstrated by loading the native PSII enzyme on mesoporous Indium Tin Oxide electrodes (*meso*-ITO|PSII, Table 1). (*30*) Oxygenic photocurrent is observed for the bio-electrode, showing a peak Incident Photon to Current Efficiency (IPCE = 0.125 %) at 680 nm (i.e. the excitation wavelenght of the PSII-chlorophyll primary electron donor, P680*). This result is still unrivalled by synthetic photoanodes that generally show very low IPCE profiles at irradiation wavelenghts $\lambda > 500$ nm. (*30-32).*

Building on the PBI-quantasome advantage, the **{[PBI]5Ru4POM}*n*** motif has been transferred onto a nanostructured tungsten oxide photoanode (*nano*WO_3 ca. 700 nm film thickness) to accomplish water splitting via regenerative photoelectrochemical cell (PEC) technology, (*30-32)* (Table 1). (*33*)

The resulting photoelectrode (***nano*WO3|{[PBI]5Ru4POM}*n***,) shows the Uv-Vis footprint of **{[PBI]5Ru4POM}*n***, (Fig. S16)(*34,35*), together with a high surface-area/nano-morphology (AFM images in Figure 3A-B), and GISAXS scattering curves / 2D-intensity maps that nicely correspond to the expected hierarchical organization of the photocomplex (compare the scattering profile of Fig. 3B,C with Fig. 1B).

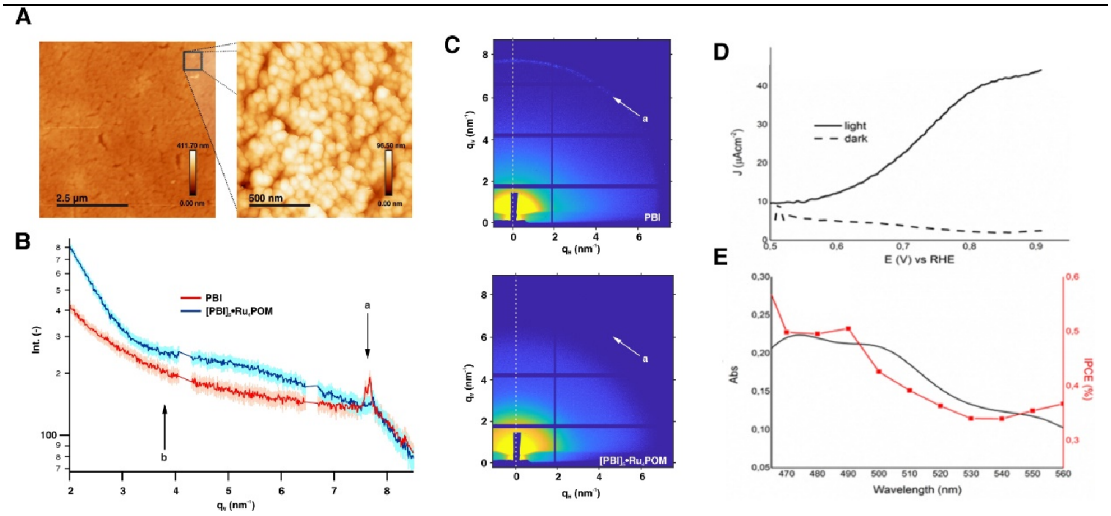

Figure 3: **Characterization of *nano*WO$_3$|{[PBI]$_5$Ru$_4$POM}$_n$ photoanodes. A**. AFM image of **{[PBI]$_5$Ru$_4$POM}$_n$** on nanoWO$_3$ at different magnification, showing a smooth and uniform texture with a porous substructure in the nanometer scale. **B**. GISAXS scattering intensities along vertical cuts at q_H=0 nm^{-1} (see white dotted lines in C), where a distinct **PBI** inherent scattering peak (peak a) is registered, that is strongly reduced for **{[PBI]$_5$Ru$_4$POM}$_n$**, while a broader correlation peak (peak b) arises corresponding to the **Ru$_4$POM–Ru$_4$POM** scattering centres with intercalated, π-π **PBI** doublets (see Figure 1B for comparison). **C**. 2D scattering-images of the GISAXS scattering intensities. **D.** Photocurrent density (solid line) versus dark current density (dashed line) as a function of the applied potential (oxidative scan up to 0.90V vs RHE, scan rate 20 mV sec^{-1}) under simulated solar irradiation (AMG 1.5, 1 Sun, with a cut-off filter at 450 nm), in aqueous $HClO_4$ pH 3, 0.1 M $NaClO_4$; counter electrode: Pt wire; reference electrode: Ag/AgCl. The potential values were then converted to the reversible hydrogen electrode (RHE) according to the equation: E(RHE) = E(Ag/AgCl) + 0.197 + 0.059 x pH. **E**, Action spectrum of the ***nano*WO$_3$|{[PBI]$_5$Ru$_4$POM}$_n$** photoanode showing the incident photon to current conversion efficiency (IPCE, red squares) as a function of the irradiation wavelength and overlapped with the absorption spectra of the ***nano*WO$_3$|{[PBI]$_5$Ru$_4$POM}$_n$** photoanode (black solid line)**.**

The ***nano*WO$_3$|{[PBI]$_5$Ru$_4$POM}$_n$** photoanode (exposed area of 1.5 cm^2) was probed in the potential range from 0.50 to 0.91 V, vs RHE at 20 mV/s scan rate, under irradiation by a solar simulator (AM 1.5 G light, 1 sun, 100 mWcm^{-2}) at $\lambda > 450$ nm to avoid the direct excitation of the semiconductor layer. Compared to the dark scan (J < 5μA cm^{-2}, dashed line in Fig. 3D), the photocurrent response is indicative of fast hole scavenging and catalysis by **{[PBI]$_5$Ru$_4$POM}$_n$** (solid line, Fig. 3D), featuring the onset potential close to the saturation plateau of > 40 μA cm^{-2}, respectively at < 0.60 V and 0.91 V, i.e. with a cathodic shift of ca 0.15 V with respect to the bare *nano*WO$_3$ electrode and far below the expected thermodynamic limit for oxygen evolution (E (O_2/H_2O) = 1.23 V vs. RHE). (33) Noteworthy, the incident photon to current conversion efficiency (IPCE) profile confirms that the action spectrum of the photoanode overlaps with the absorption features of **{[PBI]$_5$Ru$_4$POM}$_n$** (Figure 3E): the peak value of IPCE = 0.50 % corresponds to the expected absorption maxima (470 - 490 nm range) and values of IPCE up to 0.40 % are maintained at $\lambda > 500$ nm, where **{[PBI]$_5$Ru$_4$POM}$_n$** shows a broad absorption tail (Fig. 3E). These results stem from a

favorable optical density (ca. 0.2) of ***nano*WO$_3$|{[PBI]$_5$Ru$_4$POM}$_n$** (roughness factor of ca. 150), *with a maximum Light Harvesting Efficiency (LHE(λ) = 1-10$^{-A(λ)}$) of the order of 40 % (Fig. S16).* (*35*)

Table 1. Photoanode performance metrics and literature benchmark values. All experiments were performed under simulated solar irradiation (AM 1.5G, 1 Sun, cut-off filter at 450 nm, applied bias of 0.90 V vs RHE), in $HClO_4$ (pH 3), 0.1 M $NaClO_4$; counter electrode: Pt wire; reference electrode: Ag/AgCl; potentials are then converted to Reversible Hydrogen Electrode, RHE, using the equation: E (V) vs RHE = E (V) vs Ag/AgCl + 0.197 + (0.0592×pH).

Photoanode	E vs RHE[a] (V)	JMAX[b] (μA cm^{-2})	TOF[c] (s^{-1})	IPCE[d] (%)	APCE[e] (%)	Ref.
***nano*WO$_3$|{[PBI]$_5$Ru$_4$POM}$_n$**	0.91	44	0.026[f]	0.50[g]	1.30[g]	*this work*
***nano*ITO|PSII[h]**	0.94	0.3	0.030[i]	0.12[j]	0.70[j]	(*30*)
***nano*WO$_3$|PBI|IrO$_x$[k]**	0.91	70	-	0.60[l]	0.80[l]	(*36a*)
***nano*TiO$_2$|[Ru(bpy)$_2$(L)]|Ru$_4$POM[m]**	0.54	14	0.003[n]	-	0.11[o]	(*36b*)
***nano*TiO$_2$|[Ru(dpbpy)(L$_1$)$_2$]|Ru$_4$POM[m]**	0.54	55	0.016[p]	-	0.39[o]	(*36b*)

[a]Potential applied in controlled potential electrolysis under irradiation. [b]Maximum photocurrent density observed during the first scan under applied anodic potential and irradiation. [c]Turnover frequency (TOF) determined from the equation TOF = [J_{MAX}/(4×F×l_{WOC})]×FY/100, where J_{MAX} is the maximum photocurrent density, F is the faraday constant = 96485 C mol^{-1}, l_{WOC} is the loading of the water oxidation catalyst, FY is the faradaic Yield of Oxygen production. [d]Incident Photon to Current conversion Efficiency (IPCE). [e]Absorbed Photon to Current conversion Efficiency (APCE) = IPCE(λ)/(1-10$^{-A(λ)}$), where A(λ) is derived from the absorption spectra of the electrodes. [f]up to 0.050 s^{-1} at 1.37 V vs RHE, with l_{WOC} as the loading of Ru$_4$POM = 4.34 nmol cm^{-2}, determined by ICP-OES analysis, and considering the quantitative FY (>97%, Fig. S18). [g]Values recorded at 490 nm. [h]Nanostructured Indium tin oxide (ITO) loaded with PSII; general conditions: pH 6.5 in 40 mM 2-(N-morpholino)ethanesulfonic acid (MES) electrolyte. [i]TOF calculated based on photocurrents obtained at 1.23 V vs RHE. [j]Recorded at 680 nm. [k]Dye sensitized WO_3 with spin coated IrO_2 nanoparticles; general conditions: $HClO_4$ pH 3, 0.1 M $NaClO_4$, illumination under AM 1.5 G with a cut-off filter at 435 nm. [l]Recorded at 470 nm. [m]Dye sensitized *nano*-TiO_2 loaded with Ru$_4$POM; general conditions: pH 5.8 in 80 mM Na_2SiF_6/$NaHCO_3$ buffer electrolyte containing $NaClO_4$ (200 mM), irradiation 455 nm (33 mW cm^{-2}). [n] Calculated from the reported catalyst loading of 10 nmol cm^{-2} and considering the measured FY of 90%. [o] Reported as internal quantum efficiency (IQE). [p]Calculated from the reported catalyst loading of 8 nmol cm^{-2} and considering the experimental faradaic yield of 86%.

Performance metrics for ***nano*WO$_3$|{[PBI]$_5$Ru$_4$POM}$_n$** are reported in Table 1, for benchmarking against relevant photoelectrode configurations. (*30,36*) Inspection of the APCE values, rank the ***nano*WO$_3$|{[PBI]$_5$Ru$_4$POM}$_n$** photoanode at the top position in the series, with ca. a twofold enhancement compared to *nano*ITO|PS II or to *nano*WO$_3$|PBI|IrOx, and outperforming by ca. *one-order of magnitude* the state-of-the art sensitized photoanodes based on Ru$_4$POM (cfr 1.3 % vs 0.11-0.39 %, Table 1). The kinetic advantage of the integrated **{[PBI]$_5$Ru$_4$POM}$_n$** photo-electrocatalyst is further confirmed by the turnover frequency (TOF) obtained under Controlled Potential Electrolysis (CPE) and solar irradiation (see conditions in Table 1), approaching the bio-electrode performance (Table 1), (*30*). Continuous

oxygen production at the ***nano*WO$_3$|{[PBI]$_5$Ru$_4$POM}$_n$** photoanode has been confirmed by a generator-collector bipotentiostatic set-up, showing an overall faradaic yield > 97 % (λ> 450 nm, 0.91 V applied bias vs RHE, for 15 min, Fig. S18).(*37*)

References

1. D. R. Ort et al., Redesigning photosynthesis to sustainably meet global food and bioenergy demand. Proc. Natl. Acad. Sci. U.S.A. 112, 8529-8536 (2015).

2. R. E. Blankenship et al., Comparing Photosynthetic and Photovoltaic Efficiencies and Recognizing the Potential for Improvement. Science 332, 805-809 (2011).

3. J. Barber, Photosynthetic energy conversion: natural and artificial. Chem. Soc. Rev. 38, 185-196 (2009).

4. (a) R. Emerson, W. Arnold, The Photochemical Reaction in Photosynthesis. J. Gen. Physiol. 16, 191-205 (1932); (b) R. B. Park, J. Biggins, Quantasome: Size and Composition. Science 144, 1009-1011 (1964).

5. (a) S. Kundu, A. Patra, Nanoscale Strategies for Light Harvesting. Chem. Rev. 117, 712-757 (2017), (b) Y. Yamamoto, H. Takeda, T. Yui,Y. Ueda, K. Koike, S.Inagaki, O. Ishitani, Efficient light harvesting via sequential two-step energy accumulation using a Ru–Re5 multinuclear complex incorporated into periodic mesoporous organosilica. Chem. Sci., 5, 639-648, (2014).

6 (a) R. Croce, P. Xu, A photo shoot of plant photosystem II. Nature, 534, 42-43 (2016); (b) J. Yano, V. Yachandra, Mn4Ca Cluster in Photosynthesis: Where and How Water is Oxidized to Dioxygen. Chem. Rev. 114, 4175-4205 (2014).

7 (a) M. D. Kärkäs, E. V. Johnston, O. Verho, B. Åkermark, Artificial Photosynthesis: From Nanosecond Electron Transfer to Catalytic Water Oxidation. Acc. Chem. Res. 47, 100-111 (2013); (b) M. D. Kärkäs, O. Verho, E. V. Johnston, B. Åkermark, Artificial Photosynthesis: Molecular Systems for Catalytic Water Oxidation. Chem. Rev. 114, 11863-12001 (2014); (c) S. Berardi et al., Molecular artificial photosynthesis. Chem. Soc. Rev. 43, 7501-7519 (2014).

8 (a) J. D. Blakemore, R. H. Crabtree, G. W. Brudvig, Molecular Catalysts for Water Oxidation. Chem. Rev. 115, 12974-13005 (2015); (b) K. J. Young et al., Light-driven water oxidation for solar fuels. Coord. Chem. Rev. 256, 2503-2520 (2012).

9. (a) A. Sartorel, M. Bonchio, S. Campagna, F. Scandola, Tetrametallic molecular catalysts for photochemical water oxidation Chem. Soc. Rev. 42, 2262-2280 (2013); (b) A. Sartorel, M. Carraro, F. M. Toma, M. Prato, M. Bonchio, Shaping the beating heart of artificial photosynthesis: oxygenic metal oxide nano-clusters. Energy Environ. Sci. 5, 5592-5603 (2012)

10. (a) D. Gust, T. A. Moore, A. L. Moore, Solar Fuels via Artificial Photosynthesis. Acc. Chem. Res. 42, 1890-1898 (2009); (b) D. Gust, Supramolecular photochemistry applied to artificial photosynthesis and molecular logic devices. Faraday Discussions 185, 9-35 (2015).

11 S. Fukuzumi, K. Ohkubo, T. Suenobu, Long-Lived Charge Separation and Applications in Artificial Photosynthesis. Acc. Chem. Res. 47, 1455-1464 (2014).

12. M. R. Wasielewski, Self-Assembly Strategies for Integrating Light Harvesting and Charge Separation in Artificial Photosynthetic Systems. Acc. Chem. Res. 42, 1910-1921 (2009).

13 (a) R. E. Cook, B. T. Phelan, R. J. Kamire, M. B. Majewski, R. M. Young, M. R. Wasielewski, Excimer Formation and Symmetry-Breaking Charge Transfer in Cofacial Perylene DimersJ. Phys. Chem. A, 121, 1607-1615 (2017); (b) Y. Wu, R. M. Young, M. Frasconi, S. T. Schneebeli, P. Spenst, D. M. Gardner, K. E.

Brown, F. Wurthner, J. F.Stoddart, M. R. Wasielewski, Ultrafast Photoinduced Symmetry-Breaking Charge Separation and Electron Sharing in Perylenediimide Molecular Triangles. J. Am. Chem. Soc. 137, 13236-13239 (2015).

14. (a) F. Würthner et al., Perylene Bisimide Dye Assemblies as Archetype Functional Supramolecular Materials. Chem. Rev. 116, 962-1052 (2016). (b) S. Chen, P. Slattum, C. Wang, L. Zang, Self-Assembly of Perylene Imide Molecules into 1D Nanostructures: Methods, Morphologies, and Applications. Chem. Rev., 115, 11967-11998 (2015).

15. (a) Y. Guan, Y. Zakrevskyy, J. Stumpe, M. Antonietti, C. F. J. Faul, Perylenediimide-surfactant complexes: thermotropic liquid-crystalline materials via ionic self-assembly. Chem. Commun. 0, 894-895 (2003); (b) Y. Guan, S.-H. Yu, M. Antonietti, C. Böttcher, C. F. J. Faul, Synthesis of Supramolecular Polymers by Ionic Self-Assembly of Oppositely Charged Dyes. Chem. Eur. J. 11, 1305-1311 (2005).

16. (a) M. Supur, S. Fukuzumi, Photodriven Electron Transport within the Columnar Perylenediimide Nanostructures Self-Assembled with Sulfonated Porphyrins in Water. J. Phys. Chem. C 116, 23274-23282 (2012); (b) M. Supur, S. Fukuzumi, Tuning the photodriven electron transport within the columnar perylenediimide stacks by changing the π-extent of the electron donors. Phys. Chem. Chem. Phys. 15, 2539-2546 (2013).

17 (a) A. Sartorel et al., Water Oxidation at a Tetraruthenate Core Stabilized by Polyoxometalate Ligands: Experimental and Computational Evidence To Trace the Competent Intermediates. J. Am. Chem. Soc. 131, 16051-16053 (2009); (b) F. M. Toma et al., Efficient water oxidation at carbon nanotube–polyoxometalate electrocatalytic interfaces. Nat. Chem. 2, 826-831 (2010), (c) M. Quintana et al., Knitting the Catalytic Pattern of Artificial Photosynthesis to a Hybrid Graphene Nanotexture. ACS Nano 7, 811-817 (2012).

18 (a) M. Orlandi et al., Ruthenium polyoxometalate water splitting catalyst: very fast hole scavenging from photogenerated oxidants. Chem. Commun. 46, 3152-3154 (2010), (b) F. Puntoriero et al., Photo-induced water oxidation with tetra-nuclear ruthenium sensitizer and catalyst: A unique 4 x 4 ruthenium interplay triggering high efficiency with low-energy visible light. Chem. Commun. 46, 4725-4727 (2010); (c) M. Natali et al., Working the Other Way Around: Photocatalytic Water Oxidation Triggered by Reductive Quenching of the Photoexcited Chromophore. J. Phys. Chem. C 119, 2371-2379 (2015); (d) for a relevant comparison with an Ir-based WOC see M. T. Vagnini et al., Ultrafast photodriven intramolecular electron transfer from an iridium-based water-oxidation catalyst to perylene diimide derivatives. Proc. Natl. Acad. Sci. U.S.A. 109, 15651-15656 (2012).

19 S. Piccinin et al., Water oxidation surface mechanisms replicated by a totally inorganic tetraruthenium–oxo molecular complex. Proc. Natl. Acad. Sci. U.S.A. 110, 4917-4922 (2013).

20. S. Scheuring, J. N. Sturgis, Chromatic Adaptation of Photosynthetic Membranes. Science 309 484-487, (2005).

21. The vertical alignment of the PBI and Ru4POM forming the PBI-quantasome would not just maximize the electrostatic interactions between the cationic perylene "shell" and the POM "core", but also encourage intra-molecular contacts of the type W-O···π/W=O···π, W-O···HC(N+)/W=O··· HC(N+) and Ru-OH2···π (Fig.S5). See also A. Nisar, X. Wang, Surfactant-encapsulated polyoxometalate building blocks: controlled assembly and their catalytic properties. Dalton Trans., 2012, 41, 9832-9845.

22. (a) J. M. Seddon, Structure of the inverted hexagonal (HII) phase, and non-lamellar phase transitions of lipids. Biochimica et Biophysica Acta, 1031, 1-69(1990); (b) D. C. Turner, S. M. Gruner, X-ray Diffraction Reconstruction of the Inverted Hexagonal (HII) Phase in Lipid-Water Systems. Biochemistry 31, 1340-1355, (1992).

23. E (PBI*/PBI.-) = E (PBI/PBI.-) + E00, where E00 is the energy of the excited state expressed in eV. The value of E (PBI/PBI.-) = -0.10 V vs NHE, was determined by cyclic voltammetry (CV) and by spectro-electrochemistry analysis performed from -0.26 V to +0.20 V vs NHE, (Fig. S8) showing a progressive bleaching in the 435-517 nm region, positive absorption in the 517-1050 nm region, including a peak-shaped

maximum at 990 nm, and isosbestic points observed at 435 and 517 nm. These features are diagnostic of the PBI.- radical anion formation (Fig. S8). The E (PBI/PBI.-) value is obtained from the inflection point of the sigmoidal fitting of the differential absorbance (ΔOD at 490 and 546 nm) versus applied potential data. E00 is determined from the zero-zero energy emission (Fig. S9).

24. A. R. Parent, R. H. Crabtree, G. W. Brudvig, Comparison of primary oxidants for water-oxidation catalysis. Chem. Soc. Rev. 42, 2247-2252 (2013)

25. Addition of S2O82- anions to {[PBI]5Ru4POM}n does not significantly modify the Uv-Vis spectrum, and the SAXS pattern of the resulting assembly (Fig. S11 and S12).

26. Photocatalysis stops at ca. 5% of persulfate conversion, due to inhibition by the sulfate anion (SO42-) formed as by-product (see the control experiment, entry 6 in Table S2). The quantum yield levels off at the expected 5:1 PBI/Ru4POM stoichiometry (Φ = 0.023, Table S2). This low value can be explained considering that only ca. 10% of the {[PBI]5Ru4POM}n sites are accessible for persulfate association (see discussion in note 29).

27. 1*PBIn coexists with a minor component stemming from monomeric 1*PBI featuring a lifetime of >4 ns.

28. Detection of Ru4POM(h+) at pH 7 is hampered by its low extinction coefficient (see ref 17).

29. The fsTA dynamics obtained with or without persulfate (S2O82-) are almost superimposable, with no variation of the kinetic parameters obtained via global analysis (Fig. S15) The singular exception is observed in the NIR region, in the early 50 ps, for the 990 wavelenght kinetics showing a ca. 10% abatement of the transient absorbance upon addition of S2O82- (0.2, 0.5, and 1 mM). This effect can be explained considering that persulfate association occurs on edge-sites and/or dislocation defects of the {[PBI]5Ru4POM}n assembly, accounting for ca. 10% occupation, as a result of electrostatic repulsion (negative zeta potential of the colloids, Fig. S3) and limited interstitial access within the inter-lamellae space. Therefore, excitation of the photosynthetic aggregates in the presence of persulfate is likely evolving to a mixed transient state with a major component due to the PBI-quantasome excitation (90%) and a minor component (ca. 10%) arising from persulfate associated sites (Fig. S15). The reconstructed kinetic difference spectrum from the 990 nm wavelenght provides an average decay constant of ca 1.0 ± 0.5 ×1011 s-1, which is ascribed to the persulfate charge shift step, (SO4•-, SO42-•PBI•Ru4POM(h+)). This is the nodal point for hole-accumulation at the catalytic site, winning over charge recombination by ca. two orders of magnitude (cfr k3 = kcr= 9.5 ± 0.05 × 108 s-1, Fig. S15). Control experiments performed by substituting persulfate with the spent sulfate by-product, showed no appreciable impact neither on the spectroscopy nor on the kinetics of the charge-separated state.

30. Y.-H. Lai, M. Kato, D. Mersch, E. Reisner, Comparison of photoelectrochemical water oxidation activity of a synthetic photocatalyst system with photosystem II. Farad. Discuss. 176, 199-211 (2014).

31. J. R. Swierk, T. E. Mallouk, Design and development of photoanodes for water-splitting dye-sensitized photoelectrochemical cells. Chem. Soc. Rev. 42, 2357-2387 (2013).

32. (a) J. Y. Kim, G. Magesh, D. H. Youn, Ji-W. Jang, J. Kubota, K. Domen, J. S. Lee, Single-crystalline, wormlike hematite photoanodes for efficient solar water splitting Sci. Rep. 3, 2681; DOI:10.1038/srep02681 (2013). (b) Tae Woo Kim, Kyoung-Shin Choi, Nanoporous BiVO4 Photoanodes with Dual-Layer Oxygen Evolution Catalysts for Solar Water Splitting. Science 343, 990-994 (2014).

33. nanoWO3 shows a suitable conduction band potential, at approximately 0.3 V vs. RHE, similar to the redox potential of the quinone acceptors in PSII (30). The photocatalytic onset for water oxidation is observed at ca. 0.74 V vs. RHE at λ < 420 nm. Photoelectrode potentials are refererred to the reversible hydrogen electrode (RHE) for benchmarking with literature data. Both the photoanode fabrication and PEC experiments were performed in aqueous medium at pH 3 (1 mM HClO4 / 0.1 M NaClO4), which guarantees the optimal WO3 film stability see J. C. Hill, K.-S. Choi, Effect of Electrolytes on the Selectivity and Stability of n-type WO3 Photoelectrodes for Use in Solar Water Oxidation. J. Phys. Chem. C 116, 7612-7620 (2012).

34. The {[PBI]5Ru4POM}n loading on nanoWO3 has been determined upon dissolution of the electrode surface layer, by analysis of the ruthenium content via Inductively Coupled Plasma-Optical Emission Spectrometry (ICP-OES), and by Uv-Vis quantification of the PBI released in solution. In these experiments, the ruthenium content was found 4.34 ± 0.23 nmol/cm2 while the PBI chromophore turned out in the range 16-20 nmol/cm2, which is close to the expected stoichiometry ratio. Noteworthy, the {[PBI]5Ru4POM}n molecular motif is not apparent on lowering the Ru4POM concentration in the casting solution or by using a non-aqueous phase as the casting solution.

35. a considerable absorption shift of red photons for λ> 500 nm is observed with respect to the classical PBI-sensitized electrode (the LHE at 540 nm being ca. twice that of the nanoWO3|PBIn electrode black curve in Fig. S16). Therefore the resulting Internal Quantum Efficiency (IQE) (calculated as Absorbed Photon to current Conversion Efficiency, APCE (%) = IPCE (%)/LHE) turns out to be ca. 1.3%, being exceptionally constant in the 470-540 nm wavelength range (Fig. S17).

36. (a) F. Ronconi et al., Modification of Nanocrystalline WO3 with a Dicationic Perylene Bisimide: Applications to Molecular Level Solar Water Splitting. J. Am. Chem. Soc. 137, 4630-4633 (2015); (b) J. Fielden et al., Water splitting with polyoxometalate-treated photoanodes: enhancing performance through sensitizer design. Chem. Sci. 6, 5531-5543 (2015).

37. The long-term photostability of the nanoWO3|{[PBI]5Ru4POM}n is hardly addressable in the present construction set that would instead require a precise engineering of the surface adhesion properties together with a three-dimensional reconstruction of the phosynthetic lamellae into a 3D-interlocked pattern. In the actual configuration, the photoelectrode suffers from gas-induced mechanical delamination and material-leaching, that occurs under oxygen evolution regime and leads to a ca. 60% photocurrent loss in the first 5 min of photolectrolysis (Figure S18). Noteworthy, {[PBI]5Ru4POM}n arrays are very robust, and fast electron transfer to the encapsulated polyoxometalate is instrumental for photoprotection of the self-assembled dyes.